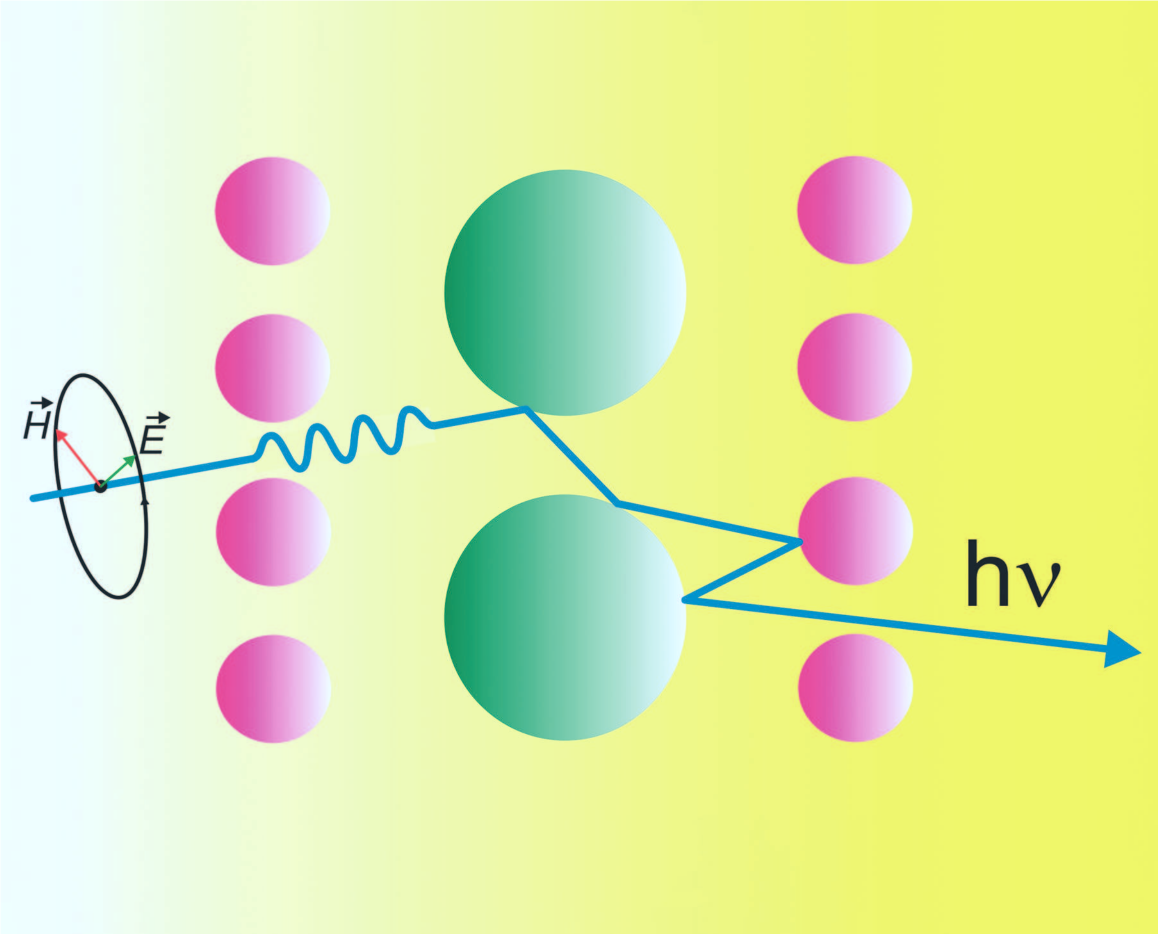

Interaction of physical fields with nanostructured materials

Schlüsseltechnologien / Key Technologies
Band / Volume 211
ISBN 978-3-95806-450-8

Mitglied der Helmholtz-Gemeinschaft

JÜLICH
Forschungszentrum

Schriften des Forschungszentrums Jülich
Reihe Schlüsseltechnologien / Key Technologies Band / Volume 211

Forschungszentrum Jülich GmbH
Institute of Complex Systems
Bioelectronics (ICS-8)

National Taras Shevchenko University of Kyiv
Faculty of Radiophysics, Electronics and
Computer Systems

Interaction of physical fields with nanostructured materials

Contributors

M.V. Petrychuk, V.I. Grygoruk, S.P. Pavlyuk, I.V. Serdeha,
G.S. Felinskyi, V.I. Kanevskii, S.O. Kolienov, S.N. Savenkov,
E.A. Oberemok, I.S. Kolomiets, A.S. Klimov, A.O. Sitnichenko,
V.V. Oliynyk, V.V. Zagorodnii, L.Yu. Matzui, L.L. Vovchenko,
I.A. Gural'skiy, O.I. Kucheriv, M.O. Popov, V.L. Launets,
A.L. Nikytenko, S. Vitusevich

Schriften des Forschungszentrums Jülich
Reihe Schlüsseltechnologien / Key Technologies Band / Volume 211

ISSN 1866-1807 ISBN 978-3-95806-450-8

Bibliografische Information der Deutschen Nationalbibliothek.
Die Deutsche Nationalbibliothek verzeichnet diese Publikation in der
Deutschen Nationalbibliografie; detaillierte Bibliografische Daten
sind im Internet über http://dnb.d-nb.de abrufbar.

Herausgeber und Vertrieb: Forschungszentrum Jülich GmbH
Zentralbibliothek, Verlag
52425 Jülich
Tel.: +49 2461 61-5368
Fax: +49 2461 61-6103
zb-publikation@fz-juelich.de
www.fz-juelich.de/zb

Umschlaggestaltung: Grafische Medien, Forschungszentrum Jülich GmbH

Druck: Grafische Medien, Forschungszentrum Jülich GmbH

Schriften des Forschungszentrums Jülich
Reihe Schlüsseltechnologien / Key Technologies, Band / Volume 211

ISSN 1866-1807
ISBN 978-3-95806-450-8

INTERACTION OF PHYSICAL FIELDS WITH NANOSTRUCTURED MATERIALS

LIST of CHAPTERS

INTRODUCTION

Research results of several important material systems presented in this collective monograph demonstrate a number of characteristic features and unique effects. The main findings are listed below.

1. The interaction between molecules and semiconductor structures allows a new amplification effect to be registered and studied by utilizing a new parameter – characteristic time constant, which is extremely sensitive for the characterization of biomolecular quantity.
2. The effects of the interaction of magnetic, optical and electromagnetic fields with nanostructured composites, semiconductor structures, anisotropic media, magnetic fluid systems, layered structures, phonons of molecular nanocomplexes and nanoinhomogeneities of rough surfaces were established.
3. The fundamental nature of the interaction effects was found as a result of a careful comparison of modeling results with experimental data. The importance of the studies is underlined by the wide range of potential applications.

For the reader's convenience, the presentation of the material is structured as follows. The general content includes only the names of sections. The full content of each section is listed in the text. For the same reason, the list of references is given at the end of each section.

The authors present the material in such a way that the reader can easily view the current state of research in these areas and be able to navigate freely in the text.

Section 1 presents a number of effects registered in semiconductor structures with dielectric coatings as surface potential sensors. In particular, the effects of internal amplification in semiconductor (bio)sensors using single trap phenomena are revealed. The noise characteristics of semiconductor nanoscale sensor structures, the effect of γ-radiation on the noise and transport characteristics of the sensors mentioned above were analyzed. It is demonstrated that effects related to single traps can be used for the detection of troponin biomolecules as indicators of myocardial infarction.

The dynamic processes in formation of the high-ohmic region and its destruction in semiconductor structures were established. It is shown that they strongly depend on power supply value. Pulse response characteristics registered in the structures are compared with steady-state characteristics. The utilization of the frequency as an informative parameter, whose change can be registered with exceptionally great accuracy opens prospects for developing of biosensors with enhanced sensitivity.

Section 2 presents effects studied in fiber-optic noninversion lasers based on Raman gain and optical radiation. Methods of nonlinear optics and Raman scattering for the amplification of light in single-mode fiber light waveguides, fabricated on the basis of fused quartz, were analyzed in detail. The Raman gain profiles were determined using spectra of spontaneous Raman gain and the multimode decomposition of profiles as well as their modeling.

Section 3 describes a new approach for the reduction of the degree of surface heterogeneity (roughness) to the nanometer scale. Known methods of polishing such as chemical-mechanical, vacuum, ion-mechanical etching allow only obtaining roughness in the micrometer range. At the same time the quality of the optical elements depends essentially on the condition of the surface, which has to be prepared with roughness in the nanoscale range. For example, the dielectric surface on which the mirror material is sprayed has to be carefully improved. In this section, the effect of light for subnano polishing surfaces is revealed and analyzed.

Section 4 demonstrates the development of Jones (and Müller) matrix methods to describe the unique polarization properties of the media. The urgent task of modern polarimetry is to analyze complexly the polarization properties of media with complex anisotropy when they simultaneously exhibit dichroic and birefringent properties. In this case, the polarization properties of the investigated medium are the sum of the corresponding Jones (Müller) differential matrices, which describe the infinitely thin layer of the medium.

To characterize finite thicknesses, a vector transport equation that describes the evolution of the light polarization state in an anisotropic medium has to be integrated. The additivity of the homogeneous approach allows unambiguous description of the polarization properties of the studied media, in particular, liquid crystals, cholesterics and twisted nematics for displays.

Section 5 describes the results of studies intended to develop new materials for the effective interaction with electromagnetic fields permitting the control of parameters of microwave electromagnetic radiation. The relevance of such research is dictated by the development of mobile communications, the Internet and digital data networks in order to increase the speed and density of information transmission. This is especially important for current trends towards transformation from the centimeter to the millimeter wavelength range.

The mechanisms of the interaction of microwave radiation with composite materials (CM) fabricated on the basis of structured multi-walled carbon nanotubes are revealed.

Our investigations show that the structuring of carbon nanotubes in composite materials by orienting them using an electric field leads to a significant increase in the interaction of electromagnetic radiation with CM.

The clarification of the behavior of the electrodynamic characteristics of hexaferrites with the addition of various cations (composition materials) showed the possibility of changing their frequency range over wide ranges. The molecular complexes with Re (II) ions applied for the first time in the millimeter range of electromagnetic waves demonstrate unique properties. It was established, that the material parameters can be abruptly changed under the influence of external factors. The studies of the interaction of microwave radiation with materials of different chemical compositions performed at different temperatures allows establishing the features of a new switching effect registered in the composite materials (so-called spin crossovers). This effect is promising for the development of high-speed power switches and filters.

A composite structure consisting of a high-quality dielectric resonator and a layer of magnetically ordered material was investigated. Two classes of magnetic materials, namely a ferromagnetic dielectric (nickel ferrite) and a weak ferromagnet (iron borate), were selected as the ferrite components of the composite resonator. The properties of such two-layer structures in the microwave range were analyzed and ways of controlling the parameters by an external magnetic field were proposed.

The results presented in this monograph were obtained in collaboration with scientists from the Physics and Chemical Faculties of Taras Shevchenko National University of Kyiv, V.Ye. Lashkaryov Institute of Semiconductor Physics, V.I. Vernadsky Institute of General and Inorganic Chemistry, O.O. Chuiko Institute of Surface Chemistry (NAS of Ukraine), as well as with scientists from Azerbaijan, Belarus and Institute of Complex Systems (ICS-8), Forschungszentrum Jülich, Germany.

The key scientific results included in this monograph were obtained while completing the fundamental budgetary topic №16БФ052-04 (reg. № 0116Ш02564) at the departments and laboratories of quantum radiophysics and electrophysics of the Faculty of Radiophysics, Electronics and Computer Systems at Taras Shevchenko National University of Kyiv.

Chapter 1

LIQUID-MEDIATED MOLECULE-SURFACE INTERACTIONS: SEMICONDUCTOR STRUCTURES WITH DIELECTRIC LAYERS FOR SENSOR APPLICATIONS

M.V. Petrychuk, V.I. Grygoruk, S.P. Pavlyuk, S. Vitusevich

CONTENT

List of symbols and abbreviations

List of symbols and abbreviations

FET	field-effect transistor
MOSFET	metal-oxide-silicon field-effect transistor
ISFET	ion-sensitive field-effect transistor
GR	generation-recombination
RTS	random telegraph signal
NW	nanowire
SRH	Shockley-Reed-Hall
SOI	silicon on insulator
PBS	phosphate-buffered saline
SEM	scanning electron microscope

1. Introduction: semiconductor structures with dielectric layer designed for sensors of the surface potential

The rapid progress in understanding of biological objects gathering new insights into the functioning of living organisms at the molecular level has led to increased interest in the development of tools for registration of processes determining by the molecules and even atoms for studies of their specific biochemical reactions in real time. The main component in the registration process determining its success is the transducer element of a biosensor. The properties of this element change under the action of the analyte under study.

Biosensors are devices that include a transducer element specially designed to be sensitive to a biological object. Biosensors usually utilize the formation of an electrical signal uniquely associated with the concentration of molecules being analyzed. The modern concept of the biosensor is in large extent developed due to the ideas of Liland Clarke Jr. and co-authors suggested in 1962 [1]. The authors proposed that enzymes can be immobilized on electrochemical sensors. Such "enzyme" electrodes can expand the range of analytical properties of the biosensor. Subsequently, a significant number of sensitive elements and transducers were proposed for use in the design of biosensors [1]:

Biological components:
Whole organisms
Tissues
Cells
Organelles
Membranes
Enzymes
Ingredients of enzymes
Receptors
Antibodies
Nucleic acids
Organic molecules

Converters:
Potentiometric
Amperometric
Conductometric
Impedance metric
Optical
Calorimetric
Acoustic
Mechanical
Chemical ("molecular electronics")

The most important parameter of a biosensor is sensitivity to the concentration of molecules in a solution. The time required for analysis is another important parameter in obtaining a reliable record of an analyte. The ultimate goal is detection of the adequate response to a single charge in real time. An important characteristic of a biosensor is selectivity, allowing to register a certain type of molecule or set. Usually, this is achieved by the design of a functionalization layer, which enables binding only a certain type of molecule. However, in some cases, the original material can selectively respond to an analyte. In this case is usually used nomograms and/or calibration curves.

The nature of the action of the biological components on the transducer has to be distinguished. This may take a number of forms including the charge or dipole moment of the molecule that is fixed on the sensitized surface of the sensor, the electric pulse on the surface of the cell membrane in the case of a living cell (for example, a neuron), changes in optical absorption or transmission registered in optical spectra, change of the luminescence, or an electromagnetic response in the microwave or terahertz range. Accordingly, an appropriate type of signal recorder has to be selected. The output parameter of a recording system is, as a rule, an analog or digital signal for further computer processing.

1.1. Highly sensitive semiconductor sensor structures

One of the most promising and most commonly used methods of detecting the biological objects, including biological molecules, is potentiometric method that allows one to determine the electrical nature of the molecules, i.e. charge, dipole moment, electrical potential, and also to monitor the change of charge as an impulse response. The fundamental properties of biomolecules can be studied using the same principle of detection as in field-effect transistors (FET), by replacing a metal or semiconductor gate with a liquid gate represented by the electrolyte containing the molecules to be determined. The potential of the liquid gate is changed using a chemically neutral reference electrode. In this case, the conductive channel of the transistor is separated from the liquid gate by a chemically neutral thin dielectric layer or a semiconductor barrier layer. The basic idea of this type of biosensor is to measure the potential as a result of placing biomolecules on a sensitive surface. The output signal is the value of the current I_{DS} in the drain current, which is determined by the parameters of the transistor:

$$I_{DS} = (V_{LG} - V_{th}) \times g_m, \tag{1.1}$$

where V_{LG} is the voltage at the liquid gate, which is applied using the reference electrode, and $g_m = dI_{DS}/dV_{LG}$ is the transistor transconductance. The threshold voltage offset ΔV_{th} is determined either using the following equation:

$$\Delta V_{th} = \frac{\Delta I_{DS}}{g_m}, \tag{1.2}$$

or as a shift of the transconductance characteristic $I_{DS} = f(V_{LG})$,i.e. the difference between the values of V_{LG} before and after the influence of biomolecules at some constant current I_{DS}.

Semiconductor field-effect devices operating in a liquid and sometimes aggressive environment can be fabricated on the basis of different materials and structures. However, silicon-based technology is most frequently used due to its broad mass-production development. Such devices are called ion-sensitive field-effect transistors (ISFETs), the principle of their operation is as follows. The change in surface potential leads to a change in the threshold voltage V_{th}. The amplitude of the current in the channel depends on the value of the surface potential change at a given source-drain voltage applied to the channel. Other transistor characteristics, such as threshold voltage can be also used as informative parameters for determining biosensor sensitivity.

The sensitivity of biosensors fabricated on the basis of semiconductor FET structures depends essentially on the sizes, primarily on the cross-section of the conducting channel with the sensitive surface. Reducing the size of the biosensor allows a signal to be obtained from a small amount of molecules. In cases where the size of the device is about that of the Debye screening radius, it is possible to detect individual molecules. For this reason, the biosensors considered below have the form of nanowires – narrow strips or rods with transverse dimensions of several hundreds, or even dozens, of nanometers. In this case, the electric field of the charged molecule under investigation extends to a significant part of the cross-section of the nanowires, which leads to a considerable modulation of the conductivity of the channel by the biomolecule binding on the sensor surface.

On the other hand, the biosensor should not have too small a surface area, because this reduces the probability of the target molecule binding on the sensitive surface. For this reason, there is a tendency to fabricate the multichannel sensors of sufficient length (several microns) in the form of an array of narrow nanowires. This ensures that the molecules can be registered with high probability and sufficient sensitivity [2].

1.2. Characteristics of low-frequency noise for extracting information parameters of semiconductor biosensor structures

The minimum value of signal registered as the change in the voltage or current of the biosensor under the influence of the reagent is limited by the amount of noise in the frequency band in which the measurement is performed. The noise origin is mainly related to the movement of the charges in the electrolyte, i.e. in an environment that plays the role of the liquid gate of the field-effect transistor and the intrinsic noise of the semiconductor amplifier as well as the molecules attached to the surface [2]. There is a thermal limit, which cannot be overcome by the traditional method of fixing a charge on the surface of the sensor. This is determined by the minimum noise level of the measuring system, which cannot be reduced to zero due to the fundamental nature of the thermal fluctuations. For this reason, the registration of individual charges, and, therefore, individual molecules, is practically impossible. Therefore it is extremely important to find methods for registering a charge not restricted by a thermal limit. This is especially true for the development of solid-state sensors for mass spectrometers. A number of possible solutions can be found to increase the sensor sensitivity, however in the present study two new advanced methods will be considered: the utilization of the noise characteristics sensitive to surface potential changes as the informative parameters and the development of conditions for nonlinear operating modes of the sensors. Also, these two approaches can be combined to obtain a synergistic effect.

1.2.1. Low-frequency noise in semiconductors: models

Noise spectroscopy is widely used to analyze the performance of gate insulators and the electrolyte/insulator interface, which determines the sensor response. However, only a few investigations have been concerned with the use of noise measurements to study the charge processes at the electrolyte/insulator interface. Such charge exchange fluctuations may enable access to information related to molecular bonds and molecular conformational changes. In this case, the noise characteristics can also provide useful information about biosensing processes.

The advantages of noise spectroscopy methods are the simplicity of technical implementation and the possibility of performing research in the state of thermodynamic equilibrium, since the charge movements caused by their own energy can be recorded as the electrical signals. External excitation, such as light, high voltage, applied to the research object or mechanical action on the object, can be omitted for measuring the noise, although additional factors may be useful for the object activation.

In the NW FET structures studied in this chapter, several types of noise that differ in their mechanisms of formation have been found. The noise spectra demonstrate several noise components reflecting the specific mechanism. In general, the frequency spectrum is determined as follows:

$$S_n(f) = \lim_{\Delta f \to 0} \frac{\overline{\Delta n^2(t)}}{\Delta f}, \tag{1.3}$$

where $S_n(f)$ is the spectral density of fluctuations of the magnitude $n(t)$, and $\overline{\Delta n^2(t)}$ is the dispersion of the fluctuations of magnitude $n(t)$ around the central frequency f in the frequency band Δf.

We will below consider the fluctuations of current $I(t)$ or voltage $V(t)$ with the spectral densities $S_I(f)$ and $S_V(f)$, respectively.

The main components of noise in NW FET structures include the following: thermal noise, flicker noise (1/*f* noise) and generation-recombination (GR) noise. Thermal noise component is result of the Brownian motion of free carriers; it is observed for any conductor with an active resistance R and in a wide frequency range it can be determined using the Nyquist formula [3,4]:

$$S_V = 4kTR, \tag{1.4}$$

where k is the Boltzmann constant, and T is the absolute temperature.

From Eq. (1.4) it is follows that the spectral density of the thermal noise does not depend on the frequency. Generation-recombination (GR) noise in semiconductors reflects the random processes of capture and emission of electrons to/from centers with energy in the forbidden zone of a semiconductor. The spectral density of GR noise is described as follows:

$$S_I(f) = \frac{4\overline{\Delta N^2}}{N^2} \frac{I^2 \tau}{1+(2\pi f \tau)^2}, \tag{1.5}$$

where N is the total number of free charge carriers, and τ is time constant of the GR process. The relative dispersion $\overline{\Delta N^2}/N$ and the time constant τ are determined by the concentration of free charge carriers and the characteristics of semiconductor impurity/defect structure, which can be studied using noise spectroscopy. In the case of NW FET structures or any structures in which the traps and free electrons are spatially separated, the value of τ can also depend on the distance between them.

The 1/*f* noise type, or flicker noise, is the noise with a frequency dependence of $1/f^{\gamma}$, where $\gamma \approx 1$ with about $\pm$20% (approximate value) deviation from unity. Flicker noise component can be found in almost all spectra. This component can be distinguished in the spectra with several components. In practice, several GR components according to Eq.(1.5), can be used to describe the 1/*f* noise. This fact was used by McWhorter to suggest the first generally accepted model of flicker noise – the McWhorter model [5]. This model is based on the idea that the 1/*f* noise spectrum can be formed by superposition of a certain number of Lorentzians described by Eq.(1.5) with some distribution of time constant τ. This condition implies the thermo-activating nature of fluctuations with a uniform distribution of activation energies (the Du Pre – van der Ziel model [6,7]). This situation is typical for surface noise, the reason for which is the random transitions of electrons between a semiconductor and traps, uniformly distributed over the oxide layer. This realized most often in MOSFET structures. According to the McWhorter model [5], such noise is described by the expression:

$$S_n = \frac{4\overline{n^2}}{\ln(\tau_2/\tau_1)} \frac{(\text{arctg}\,\omega\tau_2 - \text{arctg}\,\omega\tau_1)}{\omega}, \tag{1.6}$$

where $\overline{n^2}$ is the mean square value of the concentration of free electrons, ω is the angular frequency, τ_1 and τ_2 is the minimum and maximum constant relaxation times (corresponding to the minimum $x = 0$ and the maximum $x = x_{max}$ of the depth of the active traps in the surface dielectric), respectively.

In this case, the constant time of life of electrons in traps located at a depth *x* is equal to:

$$\tau = \tau_0 \exp(a_t x), \tag{1.7}$$

where τ_0 is the constant, and $a_t \cong 10^8$ см$^{-1}$ is the parameter characterizing the tunneling process.

The Du Pre – van der Ziel model is used as the core of many models that explain the noise in some limited situations and predict a fluctuation in the concentration Δn of charge carriers. However, the universal explanation of all manifestations of flicker noise has not been found yet. Not all flicker-noise manifestations can be attributed to concentration fluctuations. In addition, it is not always possible to associate the noise with the traps in the surface dielectric layer of a dielectric-semiconductor structure. For homogeneous samples (both semiconductor and metal), Hooge proposed an empirical formula [8]:

$$S_R(f) = R_0^2 \frac{\alpha_H}{N_{tot}|f|}, \tag{1.8}$$

where $S_R(f)$ is the spectral density of the resistance fluctuations, R_0 is the mean value of the sample resistance, $\alpha_H \cong 2\text{x}10^{-3}$ is the "universal" dimensionless constant, and N_{tot} is the total number of charge carriers in the sample.

It was later demonstrated that α_H can have values in a wide range of quantities. It was decided to regard this as the Hooge coefficient, which is a dimensionless value convenient for comparison of the 1/*f* noise level in different materials and device structures.

1.2.2. Statistical characteristics of low-frequency noise and useful parameters

The informational parameter of the FET biosensors is usually the channel current or threshold voltage, the change of which is an indicator of additional charged particles or biomolecules. As it will be shown below, one of the ways to increase the sensitivity of Si-FET sensors is to use the dynamic characteristics of the generation-recombination charge exchange processes between the conducting channel of the MOS transistor and the traps in the gate dielectric: the time constants of capture τ_c and of emission τ_e [9], which reflect the change of the potential on the surface of the dielectric. A technically feasible way of determining these parameters is to observe charge fluctuations at the single center, which may occur in nanoscale devices. This is another argument in favor of reducing biosensor sizes to tens of nanometers, since at such sizes it is possible to have only one or a few active centers in such a volume.

One of the most attractive phenomena at the nanoscale is the capture/decapture of charge carriers by/from a trap known as the single-trap phenomenon. This typically results in two-level fluctuations of current, also known as the random telegraph signal (RTS) associated with capture/emission processes of charge carriers [10]. If the NW FET has a relatively small size, the capture of charge carriers from the channel by a single trap in the gate oxide determines the strong modulation of the current. The effect is considered promising for the processing of quantum information and mesoscopic electronics [11]. In general, the dynamics of filling a single trap is usually explained statistically in terms of the Shockley-Read-Hall (SRH) theory [12,13].

However, if the shape of the channel is determined by geometric or field factors, the trajectory dynamics deviates from the classical SRH model. It is shown that in the case of the inversion conductivity mode in the transistor channel the deviation can be explained in the framework of the model of the Coulomb blockade energy [14,15]. The energy value of the Coulomb blockade strongly influences the dynamic characteristics of the capture and emission processes of the trap in the dielectric layer in the case of a neutral and repulsive charge state of the trap. As a result of the carrier capture process, the charge state of the trap changes, which, in turn, causes the formation of a screening area near a single trap and affects the entire dynamics of capture. The current flow modulation amplitude can be more pronounced when the trap is located in the area of high field in the channel [11,16].

It should be noted that we registered deviation from the Coulomb blockade model in the case of accumulation conductivity mode and described in detail below. This case was not previously reported in the literature. The voltage applied to the channel V_{DS} during noise measurement was selected in such a way that the NWs operated in the linear region of the output characteristic. Since the characteristics of the capture process of charge carriers depend on temperature, the experiment was performed in the temperature range from 200 to 300 K. The noise spectra of the NW devices exhibit $1/f$ behavior typical of the MOSFET structures [17].

In addition, we registered two-level fluctuations of RTS (Fig.1.1), indicating that the current in the NW FET was modulated by a single trap located near the Si/SiO$_2$ interface in the dielectric layer of the SOI wafer. Characteristic time constants of capture τ_c and emission τ_e processes of carrier exchange with a single center were investigated as a function of the drain current and the gate voltage at different temperatures (Fig.1.2). The value of the capture time constant τ_c depends essentially on the current and, to a lesser extent, on the temperature (Fig.1.2a). At the same time, the value of the emission time constant τ_e is practically independent of the gate voltage and the voltage on the channel. However, it strongly depends on the temperature (Fig.1.2b).

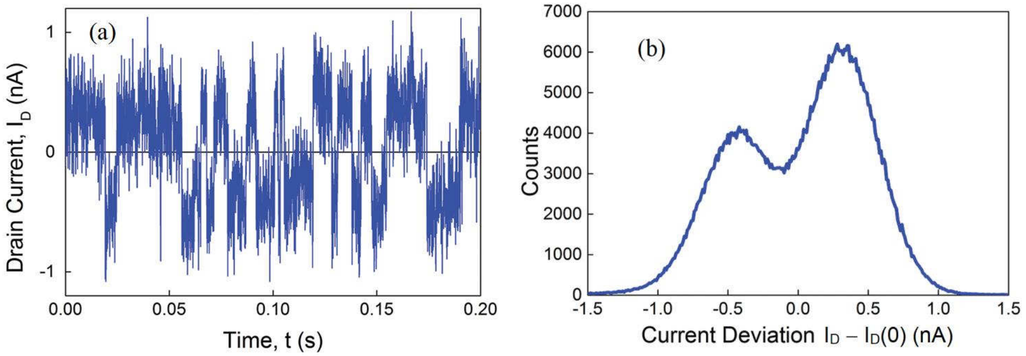

Fig.1.1. (a) Time-dependent RTS noise; (b) two-level RTS noise histogram [18].

The behavior of the capture time constant τ_c and emission time constant τ_e was used to estimate the parameters of a single trap in the gate dielectric of the sample under study. An analysis of the dynamic characteristics of active centers in semiconductors is performed in the framework of the SRH model [12,13], according to which:

$$\tau_c = \frac{1}{\sigma_n v_{th} n} \tag{1.11}$$

$$\tau_e = \frac{1}{\sigma_n v_{th} n_1} \mathrm{e}^{\frac{E_t}{kT}}\,, \tag{1.12}$$

where σ_n is the cross-section of capture, v_{th} is the average thermal velocity, n is the concentration of free electrons in the case of electron capture on the interface Si/SiO$_2$, n_1 is the statistical factor of the *c*-zone for the trap (the concentration of electrons when the Fermi level coincides with the energy of the trap level), E_t is the energy level of the center relative to the bottom of the conduction band, and N_c is the density of electron states at the bottom of the conduction band.

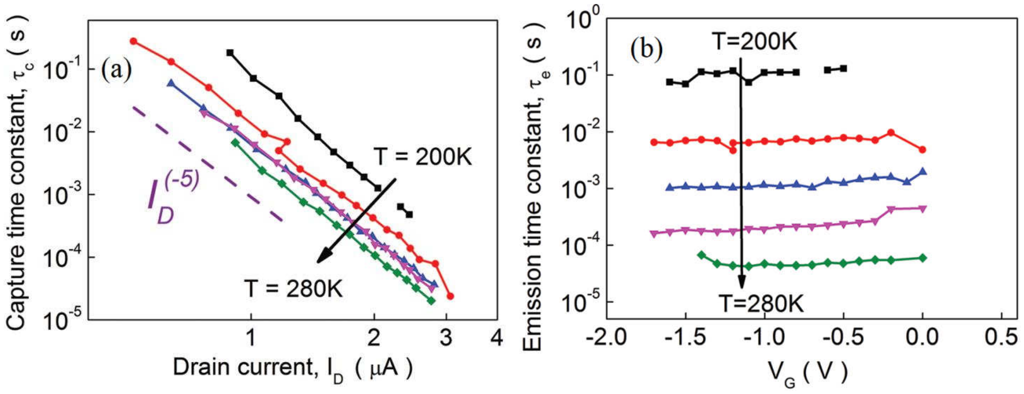

Fig.1.2. (a) Capture time constant τ_c, as a function of the drain current; (b) emission time constant τ_e as a function of the gate voltage V_G measured at different temperatures T (K) [18]

Since the value τ_c varies with the current as I^{-5}, the response to the charge on the sensor surface can be stronger compared to the case of current measurement. This strong dependence can be used to overcome the thermal limit. Clear evidence of this is given by the results of the study presented in [19], which shows that the real changes in the steady-state time τ_c are 3.8 times greater than current changes in similar conditions when changing the pH of the electrolyte.

It is clear that in order to design real biosensors on the basis of Si NW FET it is necessary to introduce/to design an active trap with suitable parameters in the dielectric layer. However, in thermally grown dielectric layer the geometric position and, in general, the presence of the required trap are of a random nature. This fact requires additional measures to increase the probability of finding an appropriate trap to ensure that the fabricated sensor will utilize the single-trap phenomena. In spite of this, in the devices under study we found that also flicker noise can be used to access the molecular dynamic processes in the NW FET structures [2,20,21].

This solution was found by taking into account the fact that the flicker noise spectrum in FETs, according to the McWhorter theory, can be considered as a superposition of a relatively large number of elementary RTS spectra with different characteristic times. In this case the set of such processes with a wide range of other constant times results in $1/f$ noise behavior. If the bonding of an additional charge on the surface of the Si-NW dielectric layer results in a change in the time constant τ_c of the RTS processes due to this charge, then the amplitudes of the RTS spectral component also change (see Eq.(1.5)). In turn, the synchronous change in the amplitudes of the RTS components with different time constant results in the change of the level of the flicker noise spectrum. In addition to this explanation, another strong effect was revealed: the random movement of charged molecules in the electrolyte in the direction perpendicular to the sensor plane leads to fluctuations in the efficiency of the charge influencing the potential displacement in the channel and, as a consequence, leads to fluctuations in the current.

The high sensitivity of the above-described effect can be explained by a strong superlinear dependence of the time constant on the surface potential of a dielectric layer with power equal to (-5) (see Fig.1.2a) compared to (-1) predicted by the standard SRH model. In summary, it can be argued that the well-known high sensitivity of the level of flicker noise to defects in semiconductors can be of the same origin, i.e. superlinear dependence of a number of time constants on the charge influencing the surface potential.

1.3. Investigation of biosensor response to troponin I biomolecules

The possibility of the real application of Si-NW FET as a biosensor was studied using troponin I (cTnI) biomolecules – a specific protein that appears in the bloodstream in the case of acute myocardial infarction (AMI) [22-24]. Such a choice of transducer is determined by the challenge to find the fastest analysis tool for detecting very small amounts of troponin molecules for early-stage diagnostics. It is critical for successful medical treatment to be applied at the earliest possible stage. Of course, such biosensors can be applied to a wide range of analytes with the appropriate choice of functional layer, because the response of the parameters of biosensors based on Si NW does not depend on the nature of charges on the surface, but only on the charge magnitude.

For the practical registration of troponin molecules, a FET biosensor was fabricated as a set of nanowires using CMOS-compatible technology for an SOI wafer. Nanowires have highly doped contact areas for the source and drain (Fig.1.3a, Fig.1.4) [9]. The surface of the nanowires was isolated from the liquid gate by a thermally grown layer of SiO_2. The gate voltage was applied using a Ag/AgCl reference electrode. The negatively charged troponin molecules were introduced into phosphate-buffered saline (PBS) solution that was filled into a volume positioned on the surface of nanowires (Fig.1.3b). The charge of the molecules results in changes of the surface potential, which, in turn, caused the changes in the functional properties of the NW FET structure. In particular, the current and statistical characteristics of the generation-recombination processes at the boundary of the conducting channel and gate dielectric were registered before and after molecular binding on the surface.

Typically, biomolecules in the electrolyte have negative or positive charge, depending on the acidity and concentration of the electrolyte. In this case, the Coulomb interaction of a charged biomolecule with other ions (counterions) (Fig.1.3b), which partially shields the charge of the biomolecule, results in negative total change. The phenomenon of screening in this case reduces the efficiency of the charge of a biomolecule on the potential of a sensitive surface. Numerically, the screening effect can be estimated using a parameter such as Debye's screening length:

$$\lambda_D = \sqrt{\frac{\varepsilon\varepsilon_0 kT}{2N_A e^2 I_C}}, \tag{1.13}$$

where ε is the permittivity of the electrolyte, ε_0 is the dielectric constant, k is the Boltzmann constant, T is the temperature, N_A is the Avogadro number, e is the charge of the electron, $I_C = \frac{1}{2}\sum c_i z_i^2$ is the ionic force, where c_i is the molar concentration of ions i in PBS, and z_i is the charge of the corresponding ion.

The Debye screening radius determines the conditions for the redistribution of charge around the biomolecule. This process can be described by the Stern model [25], according to which a layer of ions directly connected with a biomolecule (the Stern layer) can be distinguished and a diffusion layer in which the electric potential decreases exponentially and the ions are more mobile. It follows from (Eq.(1.13)) that Debye's screening length, and, hence, the sensitivity of the biosensor, increases with a decrease in the concentration of ions in PBS.

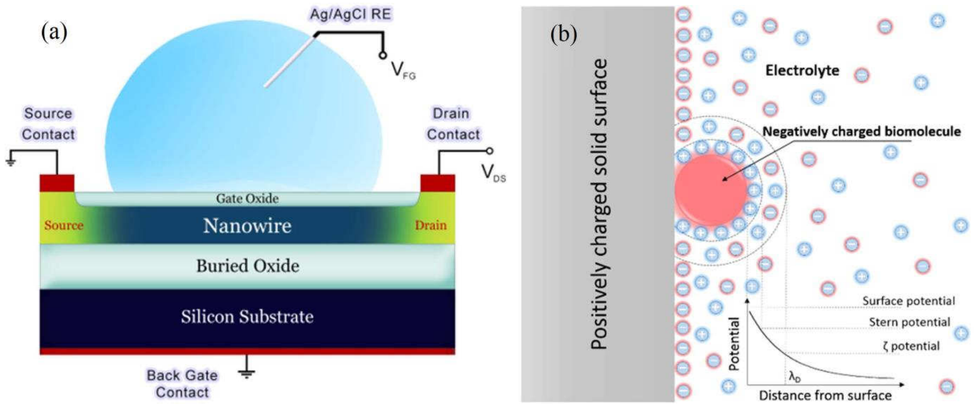

Fig. 1.3. (a) Schematic illustration of the liquid-gated Si NW FET. (b) Schematic presentation of a biomolecule binding to the surface of an NW FET and the potential distribution at the dielectric/bioliquid interface [2].

Since FET NW biosensors react to the charge size on the surface, regardless of the type of charged molecules, to ensure sensitivity to a specific type of molecule, the surface of FETs has to be functionalized by a specific layer that binds only a certain type of biomolecule. This is a multi-stage technological process of the sequential application of monomolecular layers, which provides good adhesion to the dielectric layer SiO_2 (Fig.1.4) and selective bonding with the analyte molecules [2].

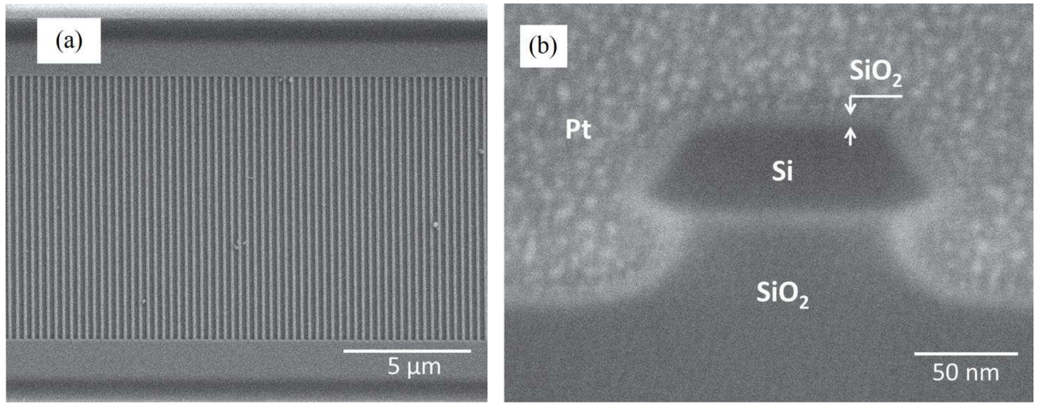

Fig.1.4. (a) High-resolution SEM image of fabricated Si NW array FET. (b) Cross-section of silicon nanowire covered with 8 nm thick SiO_2 layer. A cross-sectional cut through the nanowire was performed using the focused ion beam technique with deposition of a protective Pt layer on top of a silicon nanowire [2].

1.3.1. Shift of transconductance curve in response to troponin molecules

The results of measuring the sensitivity of the biosensor described above to the pH level of the electrolyte are shown in Fig.1.5 [2]. It should be noted that the change in the value of the pH leads to a change in the distribution of charges in a double electric layer on the surface and the surface potential. In this case, the threshold voltage is shifted according to the following relation [26]:

$$V_T = E_{ref} - \psi_0 + \chi_{sol} - \frac{\Phi_{\mathrm{Si}}}{q} - \frac{Q_{it} - Q_b + Q_f}{C_{ox}} + 2\phi_f, \tag{1.14}$$

where E_{ref} is the reference electrode potential, ψ_0 is the surface potential on the boundary of the dielectric/PBS, χ_{sol} is the surface dipole potential of the electrolyte, Φ_{Si} is the silicon output, q is the electron charge, C_{ox} is the capacity of the dielectric layer per unit area, ϕ_f is the difference between the Fermi potentials in doped and intrinsic silicon, $Q_{it}, Q_b and Q_f$ is the volume charge of the exhaustion region, the fixed charge in oxide and charge on the interface Si/SiO$_2$, respectively.

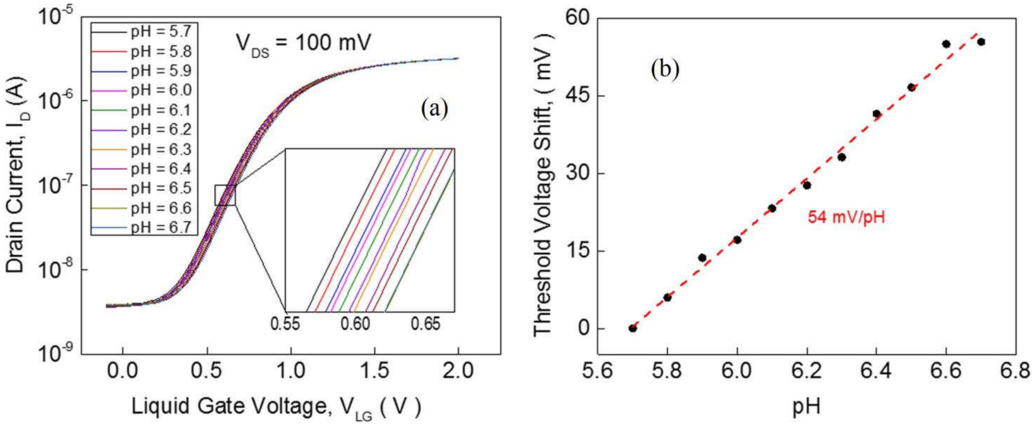

Fig.1.5. (a) Transfer characteristics of Si NW array FET measured in solutions with various pH values. (b) Threshold voltage shift of the Si NW array FET as a function of different pH values [2].

To detect troponin, the surface of the sensor was functionalized according to the technology described in [2]. Different amounts of troponin cTnI were introduced into PBS at pH = 7.4 ($\lambda_D = 7.6$ nm). Initially, the transfer characteristic of the Si NW FET structure was measured in the absence of troponin molecules (left curve in Fig.1.6a).

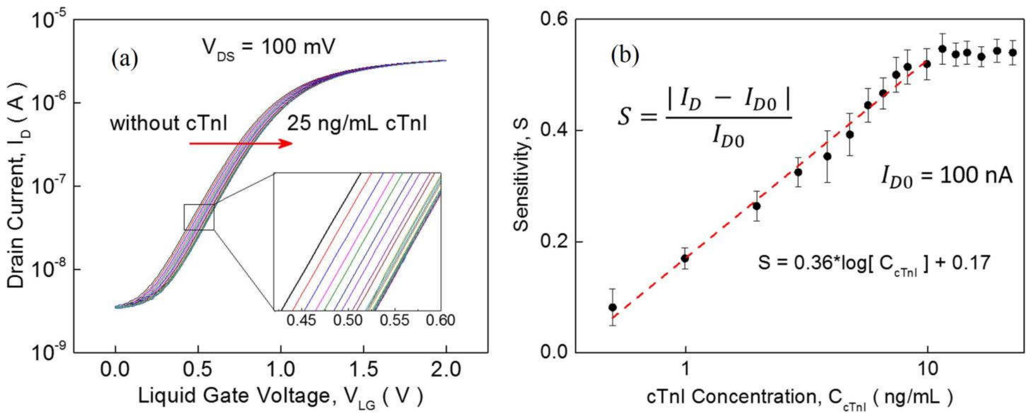

Fig.1.6. (a) Transfer characteristics of the functionalized Si NW FET biosensor for various cTnI concentrations in 1 mM PBS solution. (b) Average sensitivity versus logarithm of cTnI for the values of $I_{D0} = 100$ nA. The dashed line reflects the calibration curve to show the linear-log behavior of device sensitivity [2].

The concentration was increased step by step up to 25 ng/ml, resulting in the set of curves $I_{DS}(V_{LG})$ being shifted to the right, corresponding to depletion of the silicon layer. The results were plotted as a logarithmic dependence of the sensitivity $S = (I_D - I_{D0})/I_{D0}$ on the concentration of troponin in the range from 0.4 to 10 ng/ml (Fig.16b). The saturation of the sensitivity curve at values greater than 10 ng/ml, can be explained by the filling of all antibodies (external functionalization layer) by the troponin molecules.

As follows from the process described above, the biosensor allows detection of an analyte (in this case, troponin) only in the case of increase of its concentration. It is clear that in this case the cost of the device can be high. Thus, the main problem is the development of a method for re-using sensitive elements. Repeated application of the functionalization layer will increase the distance from the biomolecule to the surface of the dielectric, which will inevitably lead to a decrease in sensitivity, meaning that with each subsequent similar operation, the sensitivity will decrease more and more. It is clear that such a decision is suboptimal, and therefore, to achieve an acceptable degree of regeneration, the functionalization layer should be activated after each measurement. A similar process was performed by the authors [27], however, it was not possible to operate the sensor without recalibration.

Fig.1.7 shows the results of measurements before and after regeneration of a sensor that is sensitive to troponin [2]. The regeneration is performed using glycine-HCl buffer.

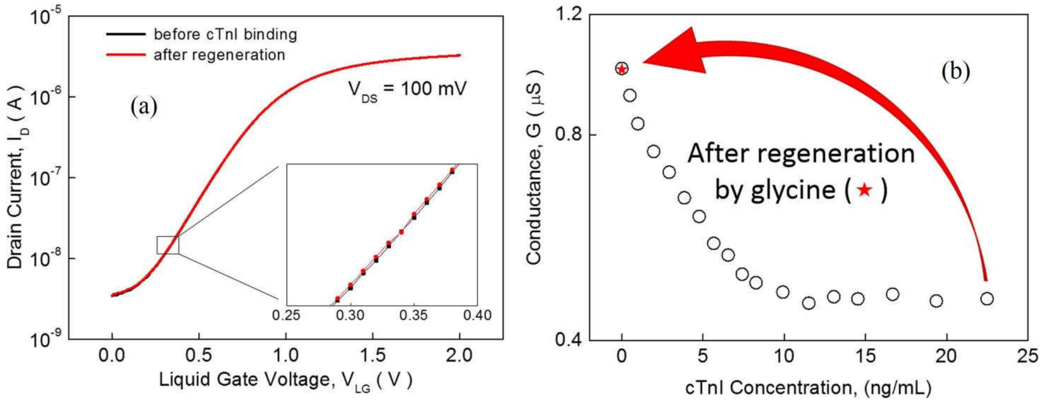

Fig.1.7. (a) Transfer curves before binding of troponin molecules and after application of glycine regeneration solution. (b) Conductance decreases as a function of cTnI concentration for the values of I_{D0} = 100 nA. The conductance returns to the initial level after applying glycine-HCl buffer [2].

The results obtained show almost complete regeneration of the initial state of the biosensor.

1.3.2. 1/f noise level change in response to troponin molecules

The main source of low-frequency noise in MOSFET structures is the random exchange of electrons between the conducting channel and the active traps in the gate dielectric, as discussed above. As a rule, the spectrum of such a noise has $1/f$ frequency dependence, known as flicker noise. However, in the case of devices with a liquid gate, another type of noise is manifested, also with the $1/f$ spectrum, caused by the motion of ions near the surface of the dielectric layer [28]. It should be noted that the random exchange of electrons between traps in a dielectric and an electrolyte cannot result in a significant contribution to the overall noise, as the charge moves at small distances determined by tunneling processes (a maximum of 2 – 3 nm). In this case, the charge on the surface is practically unchanged and does not affect the current in the channel. Fig.8a shows the noise spectra in Si NW before and after the introduction of troponin molecules into a 1 mM PBS solution, which served as a liquid gate (pH = 7.4) [2]. This result is in agreement with the results of [29], however the mechanism of such a noise has not previously been considered and discussed in the literature.

Fig.1.8b shows the value of the Hooge coefficient α_H ,which is a dimensionless parameter that characterizes the level of flicker noise ("noisiness") of the device [8].

As the voltage on the liquid gate increases, the value of α_H decreases to the level of 10^{-4}, which is typical of high-quality MOSFETs [30].

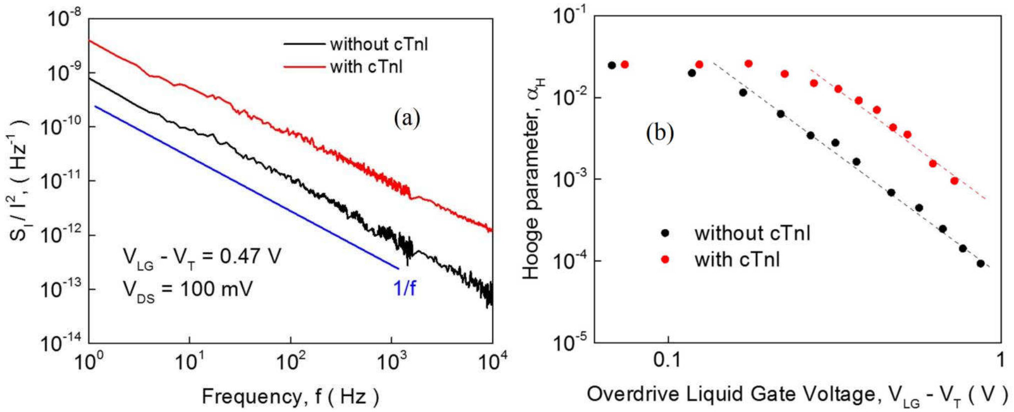

Fig.1.8. (a) Typical noise spectra measured for the liquid-gated Si NW FET at a drain bias of 0.1 V and overdrive gate voltage of 0.47 V before and after cTnI binding. (b) Dimensionless Hooge parameter α_H obtained from $1/f$ noise spectra for solutions with and without troponin molecules as a function of the overdrive liquid gate voltage ($V_{LG} - V_T$) for the same Si NW FET biased at V_{DS} = 100 mV [2].

When the voltage on the liquid gate is reduced, the "noisiness" increases significantly, as shown in Fig.1.8(b), indicating the presence of noise components, depending on the gate potential. Moreover, the difference in the behavior of both the noise and nonnoise characteristics of the biosensor before and after the introduction of troponin is demonstrated in Fig.1.9 [2]. Fig.1.9(a) shows the dependences of the magnitude of the normalized spectral density fS_I/I_D^2, measured at f = 30 Hz, on the value $(g_m/I_D)^2$, where g_m is the slope of the transistor. This dependence of the sensor prior to the introduction of troponin is linear, which corresponds to the model of the fluctuations in the number of carriers of current (the McWhorter model) caused by the exchange of conduction electrons with traps in the dielectric [5,31]. It is typical for n-channel FETs [32]. The dependence upon the addition of negatively charged molecules of troponin has a logarithmic slope (-1.5), which indicates the different nature of the noise. This is also confirmed by the significant difference in the flicker noise spectral density S_I dependence on the liquid gate voltage, while the change of transconductance is very small (see Fig.1.9(b)).

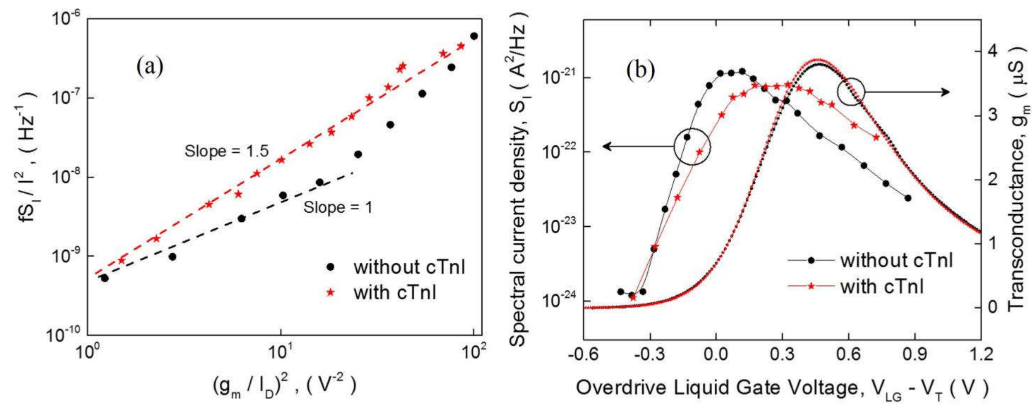

Fig.1.9. (a) The normalized drain current noise of the NW transistor extracted at f = 30 Hz as a function of $(g_m/I_D)^2$. (b) On the left axis, the drain current noise amplitude extracted at f = 30 Hz as a function of overdrive liquid-gate voltage. On the right axis, the transconductance of the Si NW FET extracted from the transfer curves before and after binding of cTnI molecules [2].

If the flicker noise in the MOS structure is described in accordance with the McWhorter model, then the value of the equivalent noise at the gate $S_U = S_I/g_m^2$ should not depend on the voltage on the gate, as we observe in the dependence $S_U = f(V_{LG} - V_T)$ for measurements without the addition of troponin molecules (Fig.1.10(a)) with $V_{LG} - V_T > 0.3$ V. At the same time, after bonding of the troponin molecules, this dependence changes substantially, demonstrating an exponential recession with the change of ($V_{LG} - \mathrm{V}_T$) from 0 to 0.8 V.

It should be noted that despite the presence of other ions in the electrolyte, a significant excess of noise above the level characteristic of MOSFETs, as well as a strong dependence $S_U = f(V_{LG} - V_T)$, only appears when the molecules specific to a specific functional layer on the sensor surface are attached. The level of noise in solutions with different concentrations from 10 mM to 0.1 M without the addition of troponin is the same [33]. This indicates a high selectivity of the noise method for recording of troponin biomolecules.

The increase in biosensor noise when troponin molecules are introduced can be explained by the chaotic movement of charges only in the direction perpendicular to the surface, whereas the parallel motion in the linear mode of the FET structure does not affect the magnitude of the current. The movement of molecules leads to potential fluctuations on the surface of the dielectric, if the molecules approach the surface to the distance about the Debye screening radius, which in our case is close to the distance of the attached troponin molecules from the dielectric.

When a positive voltage is applied, the double electric layer on the border of the dielectric/electrolyte changes its characteristics. This results in the displacement of biomolecules and the noise decreases (see Fig.1.10b,c) [2] .

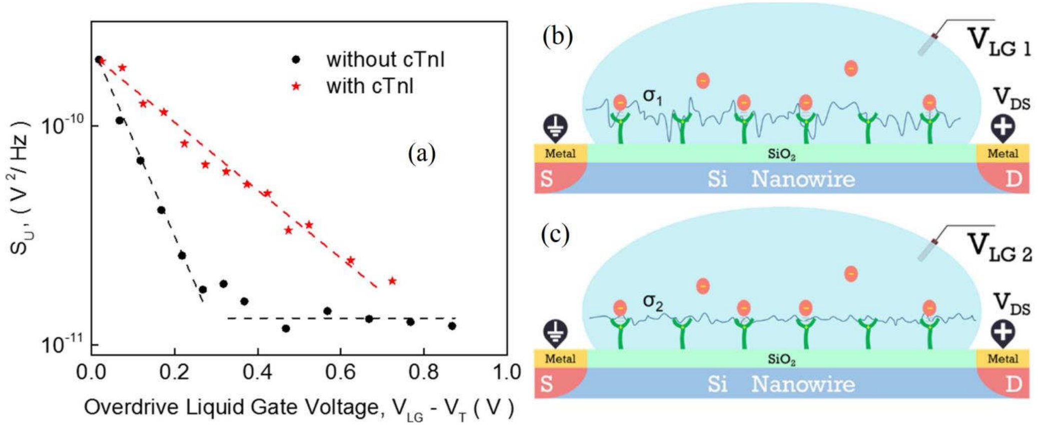

Fig.1.10. (a) Equivalent input noise S_U of the Si NW FET at different liquid gate voltages V_{LG} in 1 mM PBS solution before and after binding of troponin molecules. The lines are guides for the eye. (b) and (c) Schematic presentation of change in charge fluctuations as a function of the applied liquid-gate voltage in solution with troponin molecules for different liquid gate voltages: (b) –V_{LG1}, (c) – V_{LG2} when $V_{LG2} > V_{LG1}$, respectively. Here σ_1 and σ_2 are the dispersion of fluctuations at V_{LG1} and V_{LG2}, respectively [2].

1.4. Methods of fine adjustment of trap parameters to increase the sensitivity of biosensors

1.4.1. Coupling effect: consideration in order to increase the sensitivity of the biosensors

The sensitivity of the biosensors can be improved by utilizing the coupling gate effect as will be shown below. The displacement of the conductive channel in the NW FET structure can be performed by appropriate selection of the liquid and back gate voltages. In our studies, the back gate was realized using a highly doped silicon substrate with a 145 nm oxide layer of SOI wafer [34]. The optimal mode (the maximum value of the slope of the transconductance characteristic for the liquid gate) for the *p*-channel structure was obtained at $V_{FG} = 0$ and the voltage at the back gate $V_{BG} = -10$ V, as shown in Fig.1.11.

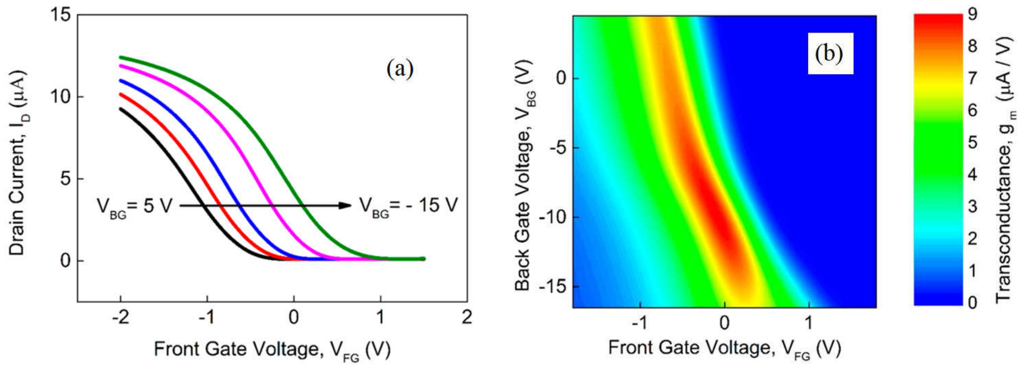

Fig.1.11. (a) Transfer curve of Si NW array FET with 50 nanowires (250 nm in width and channel length of 16 μm), measured at V_{DS} of 1 V and V_{BG}, which varied in the range from 5 to −15 V in steps of 5 V. The direction of V_{BG} changes is shown by an arrow in the figure. (b) Transconductance of the Si NW array FET measured at V_{DS} of 1 V and plotted in a color map as a function of V_{BG} and V_{FG}. Red corresponds to the maximum transconductance [34].

The signal-to-noise ratio (SNR) was measured at the chosen optimal voltage $V_{BG} = -10$ V, (Fig.1.12(a)).

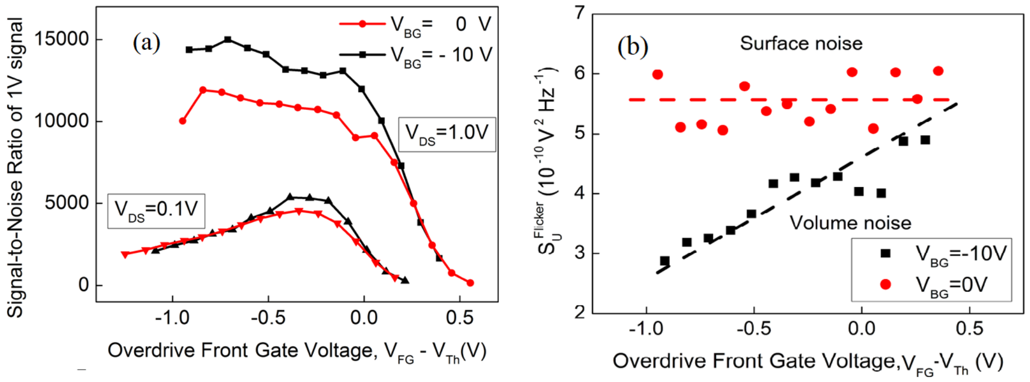

Fig.1.12. (a) Signal-to-noise ratio plotted as a function of overdrive front gate voltage at two drain biases (0.1 and 1.0 V) and different back gate voltages (0 V plotted with red triangles and −10 V plotted with black squares). (b) Equivalent input noise spectral density for 1/*f* component extracted from measured spectra and plotted versus overdrive front gate voltage at drain bias of 0.1 V and different VBG: red circles, 0 V; black squares, (−10 V); red dashed line reflects Su behavior for the case of number fluctuations model of 1/*f* noise; back dashed line reflects proportionality to front gate voltage, typical of the mobility fluctuation model [36]. In the next section, we consider the role of gamma radiation treatment on the parameters of single traps.

As can be seen, in a relatively wide range of V_{FG} voltages, the SNR value at $V_{BG} = -10$ V significantly exceeds the values measured at $V_{BG} = 0$. The noise reduction can be explained by the fact that the main component of the flicker noise at the zero voltage at the back gate is the surface noise and at $V_{BG} = -10$ V the conducting channel shifts from the front surface to the back interface due to the coupling effect [35]. In this case, the effect of surface noise decreases and the total noise level is determined by less intense volume noise. In the next section, we consider the effect of gamma radiation treatment on the parameters of biosensors.

1.4.2. Gamma irradiation as a method of fine-tuning parameters of single traps

One of the most effective tools for changing or improving the internal structure of materials and devices is ionizing radiation, in particular, gamma rays [36-39]. Free electrons and holes generated in a semiconductor under the action of high-energy photons results in change of the native defect structure of the materials, composed a device. Some of defects form metastable centers that can interact with conduction carriers in a random manner. This process can lead to generation-recombination noise according to the McWhorter model. However, there is a reverse process – annihilation of defects and restructuring of the native defect structure as well as formation of more regular distribution in positions of the atoms resulting in reduction of noise intensity. At some values of the radiation dose, the second process prevails, and then as a result of irradiation the semiconductor multilayer structure becomes more perfect. Such a dose is called the optimal dose. For silicon devices this dose is about 10^4 Gy at a photon energy of 1.2 MeV. Another positive effect of such irradiation is the change of the characteristics of active centers, which is used as an informative parameter due to the statistical characteristics of single generation and recombination processes in the biosensors.

The results of a study of the fundamental change in the characteristics of a single active center in the gate dielectric Si NW FET under the action of ionizing radiation treatment are described in [18]. An increase in the number of stable negatively charged centers in the dielectric after the treatment results in a shift of transconductance characteristics. It was shown that the statistical characteristics of the RTS process due to a single trap change after gamma radiation treatment. If before irradiation, the trap was neutral in the underlying state, after irradiation it became attractive (positively charged). This change was caused by a decrease in the concentration of the main charge carriers in the channel, which results in a shift in the Fermi level and the energy depth of the trap (see Fig.1.13). The values of the cross section of trap capture, calculated using the results of measurements of RTS noise at different temperatures before and after irradiation are presented in Table 1.

Table 1. Capture cross sections of the single trap in the Si NW FET transistor before and after gamma irradiation.

T [K]	220	240	260	280
σ_n, cm^2, before irradiation	3.1×10^{-15}	2.9×10^{-15}	3.5×10^{-15}	3.5×10^{-15}
σ_n, cm^2, after irradiation	3.9×10^{-12}	4.9×10^{-12}	4.9×10^{-12}	5.9×10^{-12}

As can be seen, the cross section of capture after irradiation is three orders larger compared to the cross section before the exposure. The fact leads to the conclusion that the main charge state of the trap has been changed. In this respect, gamma radiation treatment may be used to controlling the properties of a single trap in order to obtain the required parameters. This represents the next steps for the development of technology to obtain the biosensors with enhanced sensitivity.

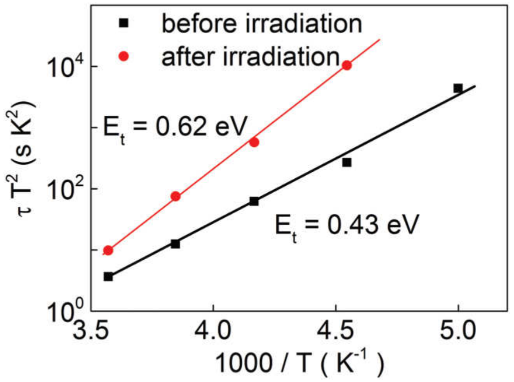

Fig.1.13. Arrhenius plot of the trap before and after gamma irradiation [18]

Thus, it was established, that the proposed method of gamma radiation treatment will allow controlling the properties of a single trap and the time constant of capturing a single trap to be fine-tuned.

1.4.3. Changing the sensitivity of the biosensor using a two-layer silicon structure in the NW FET

In order to control the magnitude of the logarithmic slope of the $\tau_c(I_D)$ characteristic, a Si NW structure with two layers of silicon was proposed, one of which was a low-doped $N_A = (10^{15}\text{cm}^{-3})$, and the other a high-doped (10^{17}cm^{-3}) (Fig.1.14) silicon layer, respectively [40].

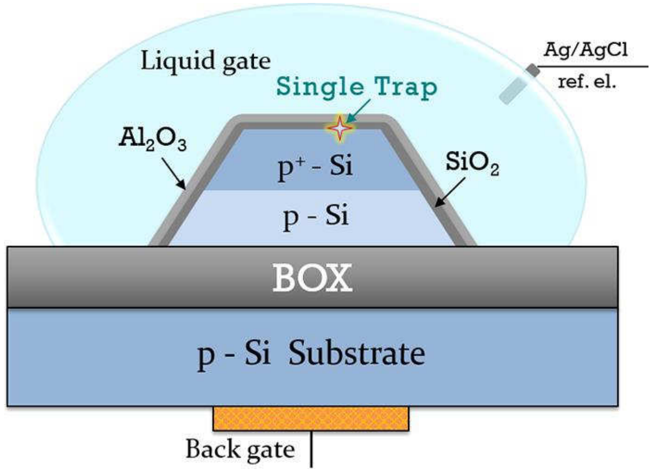

Fig.1.14. Schematic representation of a two-layer structure Si NW [40].

The idea behind such a design was to use the phenomenon of diffusion of charge carriers, which results in trap formation accompanied by the generation-recombination process with the participation of a single trap in the dielectric. Fig.1.15a shows the doping profile of the designed NW FET structure. An SEM image of the structure is shown in Fig.1.15b.

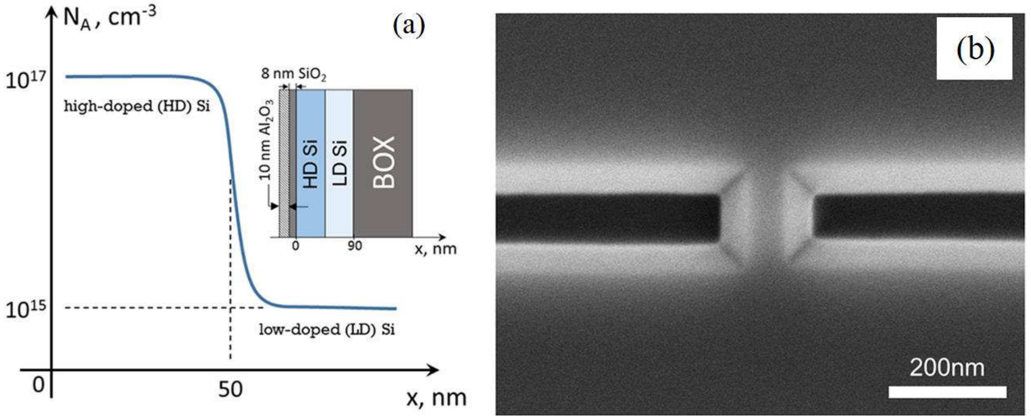

Fig.1.15. (a) Doping profile of two-layer silicon nanowire (schematic). (b) High-resolution SEM image of fabricated Si NW FET [40].

A two-layer structure operating in coupling mode allows us to modify the structure of the conduction channels by manipulating the voltages on the liquid and the back gate. Fig.1.16 shows the results of the simulation of the distribution of the density of free electrons in a two-layered structure using the software package TCAD. By comparing the results of the simulation of transconductance characteristics with experimental data (see Fig.1.16b,c), it can be seen that the main trend is in good agreement with appearance of the second channel revealed as a shoulder in the low range of gate voltages.

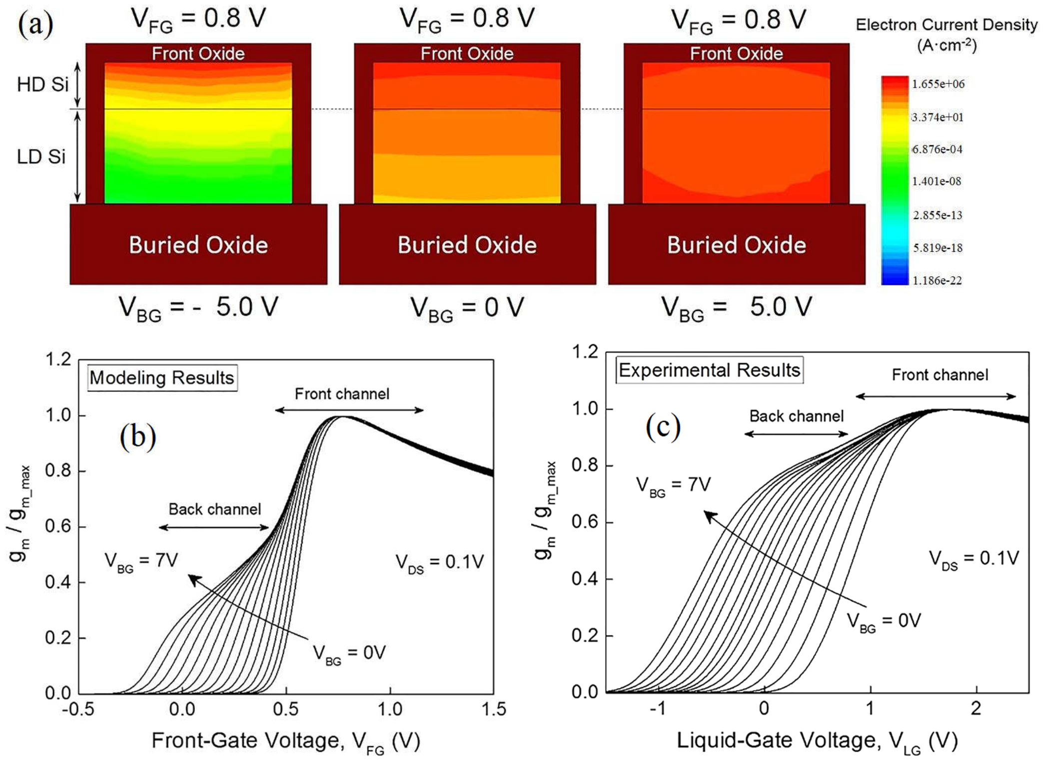

Fig.1.16. (a) Carrier distribution in two-layer Si NW FETs with rectangular cross section (obtained using TCAD software) at front-gate voltage of 0.8 V and various applied back-gate voltages. The black line depicts the conditional boundary between the heavily doped and low-doped silicon layers. (b) The normalized transconductance curves obtained by 3D electrical simulations using TCAD software for a 100 nm wide and 200 nm long Si nanowire at a constant drain-source bias of 100 mV when the back-gate bias is varied from 0 to 7 V in steps of 0.5 V. (c) Experimental normalized transconductance curves obtained from transfer characteristics [40].

The main advantage of the biosensing method is the statistical character of the exchange processes related to a single-trap phenomena in the Si NW FET structure.

This allows achieving high sensitivity and overcoming the thermal limit. It should be remembered that the increase of sensitivity in these devices is achieved by increasing the logarithmic slope of the dependence of the capture time constant on the concentration of free carriers in the channel and the channel current:

$$\tau_c \sim I_D^{-\gamma}. \tag{1.15}$$

The value of γ, which characterizes the deviation of the behavior $\tau_c(I_D)$ from the behavior predicted by the Shockley-Reed-Hall theory ($\gamma = 1$), according to various data in the literature, reaches values of $\gamma = (3 - 5)$ in single-layer structures.

It should be noted that increasing this value is an urgent task for further improving the sensitivity of Si NW sensors. The designed and fabricated two-layer structures allowed us to achieve significant progress in the direction of not only obtaining large quantities of γ values, but also opening up possibilities to control these values in a considerable range [40].

Fig.1.17 shows the results according to which the slope increases with the back gate voltage change from 0 to 3V. The values of the slope from V_{BG} reach values exceeding $\gamma = 10$, with $V_{BG} = 3$ V (see Fig.1.17a and Fig.1.17b). As one can see in Fig.1.17(c) (curves 1 and 2), with the growth of V_{BG}, the sensitivity dependence $I_{\mathrm{D}}/I_{\mathrm{Dmin}}$ on the ionic strength is only slightly improved.

However, by using the RTS noise method, sensor sensitivity $\tau_{\mathrm{c\,max}}/\tau_{\mathrm{c}}$ increases several times (curves 3 and 4), and the application of voltage to the back gate also results in increased sensitivity in good agreement with the increased slope data shown in Fig.1.17 b.

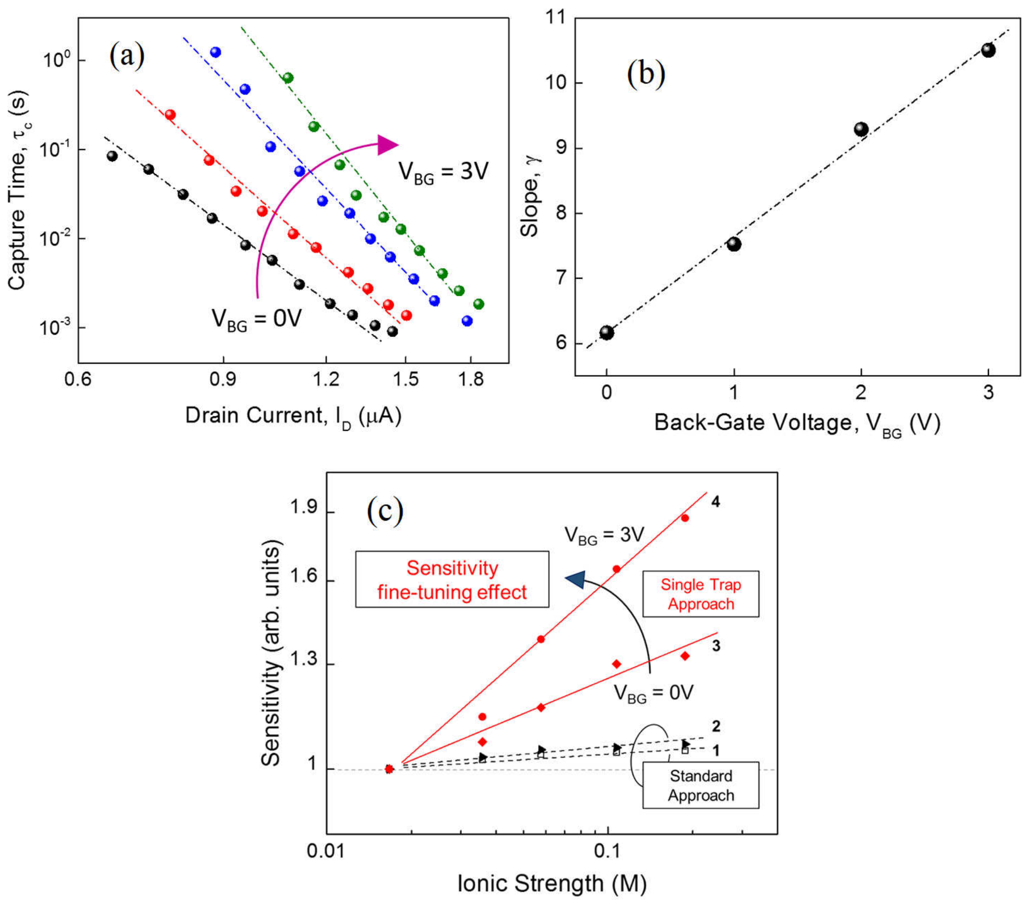

Fig.1.17. (a) Capture time as a function of drain current measured at different back-gate voltages, V_{BG} (V): 0; 1; 2, 3. (b) The characteristic slope γ corresponds to the order of the power function in (Eq.(5.15)) as a function of the applied back-gate voltage. (c) Sensor response to the change of ionic strength of the electrolyte solution in terms of sensitivity extracted for the standard approach I_D/I_{Dmin} shown as dashed lines, 1 − V_{BG} = 0 V; 2 − V_{BG} = 3 V and for the single-trap approach $\tau_{c\ max}/\tau_c$ shown as solid lines, 3 − V_{BG} = 0 V; 4 − V_{BG} = 3 V. Single-trap approach (lines 3 and 4) demonstrates a pronounced fine-tuning effect by gate voltage enabling sensitivity enhancement compared to the standard approach [40].

1.5. Superlinear I-V characteristics of semiconductor structures for highly sensitive registration of changes in surface potential

The internal amplification of response to the action of charges that bind to a sensitive surface can be increased by the use of nonlinear active elements of the biosensors. To do this, we need to find conditions for changing the nonlinear behavior when the charge state of a sensitive surface is changed. With this approach, it is important to obtain a superlinear dependence of the response (current in the channel) on the magnitude of the charge of the molecule being analyzed. Consequently, a charge binding to a sensitive surface results in sublinearity of the *I-V* characteristics. Below we show two possible ways to solve this problem.

The high-electron mobility (HEMT) structure fabricated on the basis of AlGaN/GaN at sufficient length has a sublinear *I-V* characteristic even without an applied gate voltage (Fig.1.18) [41]. The reasons for the appearance of nonlinearity are the saturation of the drift velocity of electrons in strong fields, self-heating, which leads to a decrease in the electron mobility [42], as well as hot carrier effect. The unsaturated chemical bonds in AlGaN material cause the current flow, forming an additional conduction channel. The electrostatic connection between the main and the additional channels leads to the redistribution of the potential and density of the electrons in the main channel [43]. With an increase of the voltage applied to the channel, the response to the change in field distribution increases, which opens the way for the design of extremely sensitive biosensors.

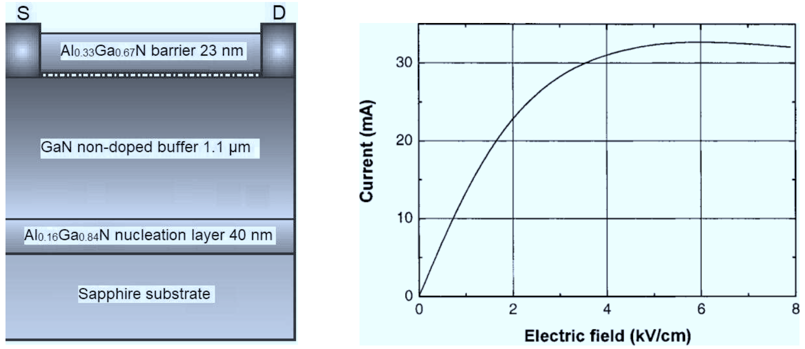

Fig.1.18. Current-voltage characteristic for the device with channel length of 25 µm and width of 100 µm measured at T=300 K. Inset – AlGaN/GaN structure [43].

In contrast to the structure described above, which is based on a degenerate electron gas, in nondegenerate semiconductors, with increasing temperature, the conductivity increases due to an exponential increase in the concentration of current carriers. At very high temperatures, the conductivity increases due to zone-zone generation of electron-hole pairs. The sublinearity of the I-V characteristics of silicon films isolated by a SiO_2 layer grown on the surface is investigated in references [44,45], where the emergence of harmonic and nonharmonic oscillations in extreme currents are registered. The static nonlinear characteristics of $R(I)$ are shown in Fig.1.19.

With a sufficiently high current density, the presence of a negative differential resistance due to self-heating may result in pulsed oscillations of current or even sinusoidal oscillations (Fig. 1.20).

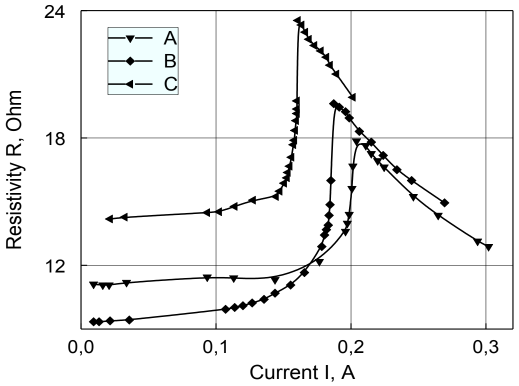

Fig.1.19. Resistance dependence on current in structures of length $L = 8$ μm and different thicknesses 11.9 μm (A), 9.8 μm (B) and 8.4 μm (C).

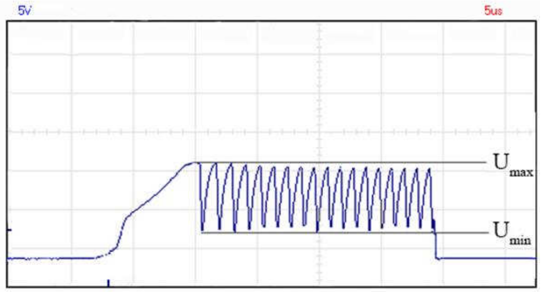

Fig. 1.20. Oscillogram of fluctuations in the silicon structure insulated by a dielectric.

If the static nonlinearity is explained by the increase in conductivity due to self-heating, then the appearance of impulse and sinusoidal oscillations has another origin. Experimental studies [44,45] have shown that the cause of current fluctuations is the periodic formation of a current cord, which shunts the depleted region and discharges its equivalent capacity. The frequency of oscillations is determined by the capacity of the depleted region and the resistance of the depleted part of the channel.

Since the electrical and time characteristics of the oscillations depend on the conductivity of the channel, the change in the surface potential of the FET structure leads to a change in these characteristics, which allows suggesting the structures as sensors sensitive to surface potential. In particular, the importance of this method is the utilization of the frequency as an informative parameter, whose change can be registered with exceptionally great accuracy.

Conclusions

1. Since the decrease in the size of Si NW structures leads to an increase in their sensitivity to the change of the surface electric charge, nano-sized structures are proposed for biosensing applications.

2. The prototype of the Si NW biosensor was designed, fabricated and investigated for the important case of cardiac troponin molecules. An experimental dependence of the value of the shift of the transconductance characteristic on the concentration of troponin was obtained, demonstrating the high quality of the biosensors.

3. A noise spectroscopy method for registering the dynamic behavior of troponin molecules based on flicker noise is proposed. A physical model explaining the charge fluctuations of molecules on the sensitive surface of the sensor was developed.

4. A method for fine adjustment of the parameters of a single trap in a dielectric layer by external excitation using low-dose gamma-radiation treatment is proposed and implemented.

5. The two-layered structure of the Si MW biosensor was investigated. It is demonstrated that by manipulating the voltage on the substrate it is possible to increase the logarithmic slope of the dependence $\tau_c(I_D)$ from (3-5) for single-layered structures to (10.5). This opens up prospects for advanced biosensing applications.

6. It is shown, that with an increase of the voltage applied to the channel, the response to the change in field distribution increases, which opens the way for designing of extremely sensitive biosensors. In addition, the utilization of the frequency as an informative parameter, whose change can be registered with exceptionally great accuracy opens prospects for developing of biosensors with enhanced sensitivity.

References

1. Biosensors: Fundamentals and Applications. Edited by Antony P. F. Turner, Isao Karube, and George S. Vilson . Oxford University Press. – 1987. – 786 p. ISBN 0-19-854724-2.
2. Y. Kutovyi, I. Zadorozhnyi, H. Hlukhova, V. Handziuk, M. Petrychuk, A. Ivanchuk, and S. Vitusevich. Origin of noise in liquid-gated Si nanowire troponin biosensors. Nanotechnology. 29, 175202-1-11 (2018).
3. J. Johnson. Thermal Agitation of Electricity in Conductors. Phys. Rev. 32, 97 (1928).
4. H. Nyquist. Thermal Agitation of Electric Charge in Conductors. Phys. Rev. 32, 110 (1928).
5. A. L. McWhorter. Semiconductor Surface Physics. Ed. R. Kingston. – University of Pennsylvania Press, Philadelphia, 1955. – 413 p.
6. F. K. Du Pre. A suggestion regarding the spectral density of flicker noise. Phys. Rev. 78, N. 5, 615 (1950).
7. A. Van der Ziel. On the noise spectra of semiconductor noise and of flicker effect. Physica. 16, N. 4, 359 –372 (1950).
8. F. N. Hooge. $1/f$ noise is no surface effect. Phys. Lett. A. 29, N. 3, 139–140 (1969).
9. I. Zadorozhnyi, J. Li, S. Pud, M. Petrychuk, S. Vitusevich. Single-trap kinetic in Si nanowire FETs: effect of gamma radiation treatment. MRS Advances. DOI: 10.1557/adv.2016.347 (2016).
10. M. J. Kirton, M. J. Uren. Noise in solid-state microstructures: A new perspective on individual defects, interface states and low-frequency ($1/f$) noise. Adv. Phys. 38, N4, 367 – 468 (1989).
11. M. Xiao, I. Martin, E. Yablonovitch, H. W. Jiang. Electrical detection of the spin resonance of a single electron in a silicon field-effect transistor. Nature. 430, 435 – 439 (2004).
12. W. Shockley and W. T. Read. Statistics of the Recombinations of Holes and Electrons. Phys. Rev. 87, 835 – 842 (1952).
13. R. N. Hall. Electron-Hole Recombination in Germanium. Phys. Rev. 87, 387 (1952).
14. H. Müller, D. Wörle, M. J. Schulz. Evaluation of the Coulomb energy for single-electron interface trapping in sub-μm metal-oxide-semiconductor field-effect transistors. Appl. Phys. 75, N6, 2970 (1994).

15. H. H. Müller, M. J. Schulz. Conductance modulation of submicrometer metal–oxide–semiconductor field-effect transistors by single-electron trapping. Appl. Phys. 79, N8, 4178 (1996).
16. L. K. J. Vandamme, D. Sodini, Z. Gingl. On the anomalous behavior of the relative amplitude of RTS noise. Solid-State Electron. 42, N6, 901 – 905 (1998).
17. Z. Y. Chang, W. M. C. Sansen. Low-Noise Wide-Band Amplifiers in Bipolar and CMOS Technologies. The Springer International Series in Engineering and Computer Science book series. – 1991. – V. 117, 212 pp.
18. I. Zadorozhnyi, J. Li, S. Pud, H. Hlukhova, V. Handziuk, Y. Kutovyi, M. Petrychuk, and S. Vitusevich. Effect of Gamma Irradiation on Dynamics of Charge Exchange Processes between Single Trap and Nanowire Channel. Small. 14, 1702516-1-8 (2018).
19. J. Li, S. Pud, M. Petrychuk et al. Sensitivity Enhancement of Si Nanowire Field Effect Transistor Biosensors Using Single Trap Phenomena. Nano Lett. 14, 3504 – 3509 (2014).
20. Y.Kutovyi, I. Zadorozhnyi, H. Hlukhova, M. Petrychuk, and S. Vitusevich. Low-Frequency Noise in Si NW FET for Electrical Biosensing. Int. Conf. on Noise and Fluctuations (ICNF), 20-23 June 2017, 1-4 (2017).
21. Y. Kutovyi, I. Zadorozhnyi, V. Handziuk, H. Hlukhova, M. Petrychuk and S. Vitusevich. The impact of biomolecules binding on low-frequency noise in Si NW FET biosensors. 8th Int. Conf. on Unsolved Problems on Noise (UPoN-2018), Book of abstracts, 9-30 July 2018, Gdansk, Poland, 35-36 (2018).
22. A. Wu, Y. Feng, R. Moore, F. S. Apple, P. H. McPherson, K. F. Buechler and G. Bodor. Characterization of cardiac troponin subunit release into serum after acute myocardial infarction and comparison of assays for troponin T and I. Clinical Chemistry. 46, 1198–1208, (1998).
23. M. D'Costa, E. Fleming and M. C. Patterson. Cardiac troponin I for the diagnosis of acute myocardial infarction in the emergency department. Am. J. Clin. Pathol..108, N. 5, 550-505, (1997).
24. M. Christ, T. Bertsch, S. Popp, P. Bahrmann, H. Heppner and C. Mueller. High-sensitivity troponin assays in the evaluation of patients with acute chest pain in the emergency department. Clin. Chem. Lab. Med.. 49, N. 12, 1955-1963 (2011).
25. O. Stern. Zur Theorie der electrolytischen Doppelschicht. Zeitschrift für Elektrochemie. 30, 508 (1924).
26. S. M. Sze and K. Ng. Physics of Semiconductor Devices. 3rd (Hoboken, NJ: Wiley). – 1981. – 868 pp.

27. Chiang P-L., Tzu-Chi Chou, Tzu-Heng Wu et al. Nanowire Transistor-Based Ultrasensitive Virus Detection with Reversible. Surface Functionalization. Chem. Asian J. 7, 2073–9 (2012).
28. M. Kuscu and O. B. Akan. Modeling and Analysis of SiNW FET-Based Molecular Communication Receiver. IEEE Trans. Commun. 64, 3708–21 (2016).
29. Q. Guo, T. Kong, R. Su, Q. Zhang, and G. Cheng. Noise spectroscopy as an equilibrium analysis tool for highly sensitive electrical biosensing. Appl. Phys. Lett. 101, 093704 (2012).
30. C. Q. Wei, Y. Z. Xiong, X. Zhou, et al. Investigation of Low-Frequency Noise in Silicon Nanowire MOSFETs in the Subthreshold Region. IEEE Electron Device Lett. 30, 668–671 (2009).
31. I. Zadorozhnyi, J. Li, S. Pud, M. Petrychuk, and S. Vitusevich. Single-trap kinetic in Si nanowire FETs: effect of gamma radiation treatment. MRS Adv. V.1, 3755–3760 (2016).
32. P. Gaubert, A. Teramoto, W. Cheng, et al. Different mechanism to explain the 1/*f* noise in *n*- and *p*-SOI-MOS transistors fabricated on (110) and (100) silicon-oriented wafers. J. Vac. Sci. Technol. B. 27, 394–401 (2009).
33. Y. Kutovyi, I. Zadorozhnyi, H. Hlukhova, M. Petrychuk, and S. Vitusevich. Low-Frequency Noise in Si NW FET for Electrical Biosensing. Proc. Int. Conf. on Noise and Fluctuations (ICNF 2017), 20-23 June 2017, Vilnius, Lithuania. 383-386 (2017).
34. S. Pud, J. Li, V. Sibiliev, M. Petrychuk, V. Kovalenko, A. Offenhäus er, and S. Vitusevich. Liquid and Back Gate Coupling Effect: Toward Biosensing with Lowest Detection Limit. Nano Lett. V. 14, 578−584 (2014).
35. I. Zadorozhnyi, S. Pud, S. Vitusevich, and M. Petrychuk. Features of the Gate Coupling Effect in Liquid-Gated Si Nanowire FETs. Int. Conf. on Noise and Fluctuations (ICNF), 2-6 June 2015 (4 pages).
36. J. Guo, Yu. Li, Sh. Wu, W. Li. The effects of gamma-irradiation dose on chemical modification of multi-walled carbon nanotubes. Nanotechnology. 16, N10, 2385 – 2388 (2005).
37. A. M. Kurakin, S. A. Vitusevich, S. V. Danylyuk, H. Hardtdegen, N. Klein, Z. Bougrioua, B. A. Danilchenko, R. V. Konakova, A. E. Belyaev. Mechanism of mobility increase of the two-dimensional electron gas in AlGaN/GaN heterostructures under small dose gamma irradiation. J. Appl. Phys. 103, 08377 (2008).

38. E. D. Atanassova, A. E. Belyaev, R. V. Konakova, P. M. Lytvyn, V. V. Milenin, V. F. Mitin, V. V. Shynkarenko. Effect of Active Actions on the Properties of Semiconductor Materials and Structures. NTS "Institute for Single Crystals", Kharkiv, Ukraine. – 2007. – 215 p.
39. J. Li, S. A. Vitusevich, M. V. Petrychuk, S. Pud, A. Offenhäusser, B. A. Danilchenko. Advanced performance and scalability of Si nanowire field-effect transistors analyzed using noise spectroscopy and gamma radiation techniques. J. Appl. Phys. 114, 203704 (2013).
40. Yurii Kutovyi, I. Zadorozhnyi, V.Handziuk, H. Hlukhova, N. Boichuk, M. Petrychuk, and S. Vitusevich. Liquid-Gated Two-Layer Silicon Nanowire FETs: Evidence of Controlling Single-Trap Dynamic Processes. Nano Lett. 18, N 11, 7305-7313 (2018).
41. S. A. Vitusevich, S. V. Danylyuk, N. Klein, M. V. Petrychuk, A. E. Belyaev. Power and temperature dependence of low frequency noise in AlGaN/GaN transmission line model structures. Journ. of Appl. Phys. 96, 5625-5630 (2004).
42. S. A. Vitusevich, S. V. Danylyuk, N. Klein, M. V. Petrychuk, A. Yu. Avksentyev, V. N. Sokolov, V. A. Kochelap, A. E. Belyaev, V. Tilak, J. Smart, A. Vertiatchikh, and L. F. Eastman. Separation of hot-electron and self-heating effects in two-dimensional AlGaN/GaN-based conducting channels. Appl. Phys. Lett.82, N 5, 748-750 (2003).
43. B. K. Ridley. Coupled surface and channel transport in semiconductor heterostructures. J. Appl. Phys. 90, N. 12, 6135–6140 (2001).
44. V. N. Dobrovolsky, L. V. Ishchuk, G. K. Ninidze, M. Balucani, A. Ferrari, G. Lamedica. High-Amplitude High-Frequency Oscillations of Temperature, Electron-Hole Pair Concentration and Current in the Silicon-on-Insulator Structures. Journal of Applied Physics. 88, N 11, 6554-6559 (2000).
45. S. P. Pavlyuk, V. I. Grygoruk, V. M. Telega, M. V. Petrychuk, A. V. Ivanchuk. The mechanism of voltage oscillations in a siliceous structure with the occurrence of extreme currents. Journal of Nano- and Electronic Physics. 10, N 4, 04010-1-4 (2018).

Chapter 2

LIGHT AMPLIFICATION BASED ON STIMULATED RAMAN EFFECT AND SPECTROSCOPIC MODELING OF RAMAN GAIN IN SINGLE MODE FIBERS

V.I. Grygoruk, I.V. Serdeha, G.S. Felinskyi, S. Vitusevich

CONTENT

List of symbols and abbreviations

List of symbols and abbreviations

g_R	Raman gain coefficient
EDFA	erbium doped fiber amplifier
FRA	fiber Raman amplifier
SMF	single mode fiber
SSMF	silica single mode fiber
ASE	amplified spontaneous emission
G_R	bandwidth of Raman gain
G	bandwidth of full amplification
DSF	dispersion-shifted fiber
NZDSF	non zero dispersion-shifted fiber (TrueWaveRS^{TM})
DRS	double Railegth scattering
OSNR	optical signal to noise ratio
OSNR$_{ASE}$	optical signal to ASE noise ratio
OSNR$_{DRS}$	optical signal to DRS noise ratio
FWM	four-wave mixing
NF	noise figure
DCF	dispersion compensated fiber
DWDM	dense wave division multiplexing
BER	bit error rate

INTRODUCTION

Optical single-mode fibers based on silica glass as an active medium for amplifiers and non-inversed lasers using the stimulated Raman Effect of light are the object of research described in this chapter. The is to study fundamental properties of Raman light amplification (Raman gain profile, threshold pumping power, and time response function) in Stokes shifted region on the background of Stokes noise in different types of single-mode fibers (SMF).

The research results were obtained using the optical spectroscopy method by measuring amplified spontaneous emission (ASE) at the output of a single-mode silica fiber. The reliability of our data processing is based on both quantum and semi-classical approaches to Raman Effect description and numerical calculation. The original technique for extraction of the Raman gain profiles from the experimental spontaneous spectra is obtained. Furthermore, the spectral decomposition method was applied using standard line form functions by the Levenberg-Marquardt nonlinear regression algorithm and novel numerical methods of approximation.

New knowledge on the amplification dynamics of the coherent signal on the background of stochastic Stokes noise were obtained as a result of our research. It has been found that the main vibrational modes formed the Raman gain profiles of the glass matrix in the different fibers are considerably varied over oscillation parameters. Thus, the average value of the fiber Raman amplifier (FRA) relaxation time,τ_i, is equal to about 300 fs. This opens prospects for practical utilization of Raman photonic devices in the terahertz band. Among the high-priority challenges, which are important for practical applications, are in-depth understanding of the processes of nonlinear Raman amplification and the finding of the physical nature of the FRA noise and the photonic nonlinearity in optical-fiber systems.

The fitting with high accuracy of the Raman gain profile using multimode spectrum decomposition is performed. This allows obtaining the exact approximation of experimental data in a simple analytic form and forms a reliable basis for calculating important FRA parameters.

Modern photonic devices working on the basis of amplified optical radiation using stimulated Raman gain of light are radically advanced in respect of the development of optical transmission tools and information processing. They allow expanding the working frequencies to the terahertz range. This enables the utilization of the femtosecond speed range. Fundamental principles of Raman amplification were established eight decades ago [1–3]. The starting point can be considered as the experimental observation of spontaneous Raman scattering (SRS) of light [4–8].

New effects were registered and described in this chapter when polarized electromagnetic radiation interacts with homogeneous and heterogeneous transparent media in the form of telecommunication fibers that are usually used for optical communication. New knowledge about the dynamics of coherent signal amplification against the background of stochastic Stokes noise was obtained. The results assist in the elimination of the inconsistency of the existing theory with experimental data, in discovering new patterns and improving the theory of the noise parameters of the optical fiber Raman amplifiers (FRA).

Generally, the study of Raman gain in single-mode optical fibers constitutes the fundamental basis for two new branches of photonics. The first branch is represented by the fiber Raman lasers (FRL). Their features are reviewed in [9-17] and many original studies are described in experimental [18-25] and theoretical [26-30] papers. The second direction includes FRA of optical radiation, which is discussed in detail in the next section.

2.1. Results of FRA practical application in ultra-fast optical information systems

The bandwidth of optical data transmission systems now can be increased using two main ways known as the Time Division Multiplexing (TDM) and the Wave Division Multiplexing (WDM). Raman amplification plays a decisive role in both approaches for the practical implementation of such systems.

In the early 1990s, the nonlinearity and cross-distortion in FRA were considered [31-33] as the main limitation factors for increasing the distance between repeaters of the optical signal more than 20 km. It was predicted that the systems will not have more than 30 channels with an optical transmitter on separate wavelengths. It was concluded, according to the theoretical estimations of that time [34-37], that the noise of optical amplifiers and their nonlinearity will not allow increasing the overall throughput of the long-distance communication not only above the limit of 1 Tb/s, but it should be substantially less than 100 Gb/s in practical systems.

This theoretical estimation has been substantially corrected already at the end of last decade as a result of experiments using the FRAs in optical communication systems. The majority of experimental work on multichannel information transmission since 1997 has been demonstrated due to the successful FRA use. The positive results of tests of a multichannel speed line at 100 Gb/s (10 × 10 Gb/s) over the distance of 7200 km were reported in [38] where the linear FRAs were used in 90 km intervals. The high-density system with 32 channels of information transmission at 10 Gb/s rate was demonstrated in [39]. The channels were separated by only 50 GHz (~ 1.7 cm^{-1}) in the optical spectrum of the transmitter frequencies and distributed Raman amplification was applied to each of 80 fiber spans of 80 km long. The total distance of the information stream in the dispersion-shifted fiber was 6400 km using 32 transmitters with wavelengths of about 1.55 μm.

The 1.02 Tb/s speed of information transmission was achieved in [40] using 51 wavelengths in transmitters with 20 Gb/s bit rate per channel. Information pulses were distributed in the form of optical solitons over the total distance more than 1000 km in a standard fiber with a steady change of the refractive index. The FRAs located in 100 km intervals were used in order to maintain the form of solitons and for compensation of the 21 dB propagation losses.

Record 3.28 Tb/s (82×40 Gb/s) total bandwidth of the optical transmission line was reported in 2000 [41]. Such an information transfer rate was obtained in a fiber line with 3×100 km length and using the non-zero dispersion fiber. Both C- and L-telecommunication windows were applied in the line for the first time due to the use of distributed FRAs in conjunction with the 40 Gb/s speed in each channel of the information transmission system. The experimental testing of a high-bandwidth 1.28 Tbps line with 840 km (6x140) length was reported in [42]. This line had 128 channels separated by wavelength with 10.66 Gb/s speed in each channel. Both C + L telecommunication windows were occupied by channels and the FRAs were used in repeaters. Distributed FRAs were used to improve the optical signal-to-noise ratio and to enhance the distance between repeaters up to 140 km. At the same time, the advantages of the distributed FRAs were demonstrated in field conditions [43] with ground-build optical cables. The receiver sensitivity was improved by 3.8 dB for the 600 km (5x120 km) long line and the 10 Gb/s transmission speed with 650 mW pumping power at each site without any apparent damage to the cable service.

In the next research [44] WDM system was implemented using a low noise FRAs and the information was transmitted for 230 km distance without utilization of repeaters. The system had 64 channels (with 40 Gb/s in each) arranged across 50 GHz on the scale of optical frequencies. The information capacity in the amount of 2.56 Tb/s was implemented in the wavelength band of 25.8 nm. The long-distance communication line in the short-wavelength telecommunication S-window was demonstrated in [45] by cascade usage of lumped FRAs for dispersion compensated fibers. The twenty channels that filled the entire S window were transmitted through 10 spans of standard SMF with a total length of 867 km at a data rate of 10.67 Gb/s, with the BER $<10^{-12}$ in each of the channels, which were secured without any additional tools for error correction.

The results of a successful test of the high-speed data transmission line for 2100 km distance with a total bandwidth of 3.2 Tbps was reported in [46]. It had 40 channels with 80 Gb/s per each channel. The application of FRAs located within 100 km intervals in this line ensured the full transparency line for the signal propagation and the bandwidth usage was 0.8 bps/Hz. The numbers of WDM channels distributed by the optical emitters wavelengths are increased to 160 in [47]. The information was transmitted for the 4000 km distance through the fiber with a non-zero dispersion and the channels packaging density on the optical frequencies scale was very high as the distance between the channels was equal to only 25 GHz (<1 cm^{-1}). Even such channels distribution density allowed reliable transmission of the information at a 10.7 Gb/s speed and the total line bandwidth was 1.6 THz. The usage of FRAs located every 100 km allowed to get the OSNR no more than 14.4 dB in all channels at the output line end and it corresponds to the BER=10^{-4}. Significantly reduce the BER and bring it to the level of 10^{-13} may be performed by using the standard methods of error correction and by the application of the Reed-Solomon code {255,329}. However, there was a problem of uneven amplification in the operating FRA band (~ 5 dB) and it was necessary to reduce this value. Increase of the speed to 2.56 Tb/s and prolonger the transmission distance up to 6000 km was successfully demonstrated using FRA [48]. The system had 64 channels with a bit rate of 42.7 GB / s in each. The channels were located in a band of 52 nm (1540-1565 and 1570-1595 nm) separated by 100 GHz. Raman pumping was carried out using 5 wavelengths 1424, 1436, 1449, 1465, and 1494 nm with a total power of 810 mW. After 6000 km, the OSNR value exceeded the 11.3 dB. This allows obtaining the BER $\leq 6\times10^{-14}$ after the error correction. The key role of FRAs in the 192 channels transmission at 10.66 Gb/s in 25 GHz sequential bands across 30 fiber spans with 22 dB (~ 100 km) attenuation was noted in [50]. The number of channels with 40 Gb/s bit rate was brought to 273 in [38], and it allowed to exceed the 10 TB/s limit for a total throughput [51].

Such impressive achievements in the developments of information transmission systems was mainly due to utilization of the FRAs. This allows reconsidering the role of such optical amplifiers for their applications in information systems based on WDM technology [52-56].

At the same time, much attention is being paid to the development of the optical data transmission system using TDM in order to increase the bit rate in a separate channel. The decisive role of the FRAs in such systems, in particular, focused on the 160 Gb/s speed of information transmission was considered in the paper [57].

2.1.1. The physical basis of the high-speed optical data transmission with time-division multiplexing

The optical bandwidth in transmission and processing systems can be extended by the transition to the picosecond time scale of modulation and demodulation elements of optical radiation. These elements perform the input and output high-speed digital information flow into the optical links due to electro-optical conversions. The current state of TDM systems development is characterized by the achievement of the data transmission rate of 160 Gb/s [57-59]. However, there are serious fundamental restrictions on the way to further increase the operation speed. They will be briefly discussed below.

According to current developments of digital data transmission systems, each new generation is characterized by at least double speed increasing and/or often by 4 times the bit rate of the digital stream in the TDM system. Recently, the industrial standards of high-speed fiber-optic systems are considered to provide an information exchange rate of 10 Gb/s or 40 Gb/s. In order to transform electric pulse chains into the optical data stream of digital information the two physical effects are used in such systems namely the electro-optical effect in dielectric crystals [60] and electrical absorption in semiconductors [61, 62].

Fig.2.1 shows the scheme of the optical radiation modulator based on the controlled electrical absorption (EA) using an external field from the signal in the semiconductor material. The modulation of continuous optical waves in the EA modulator is performed due to the displacement (under influence of the electric field) of the signal of the edge of the plasmonic absorption band in semiconductor materials with high mobility of charge carriers such as InGaAsP quaternary compounds. In the absence of the field, the absorber remains transparent, but the absorption of optical radiation reaches 20 dB with the applied negative voltage ~ 3 V. The rather small value of the nominal voltage in the modulator is its main advantage. However, the modulator's drawback is induced frequency variations in modulation pulses. This can significantly affect the dispersion expansion of propagated pulses.

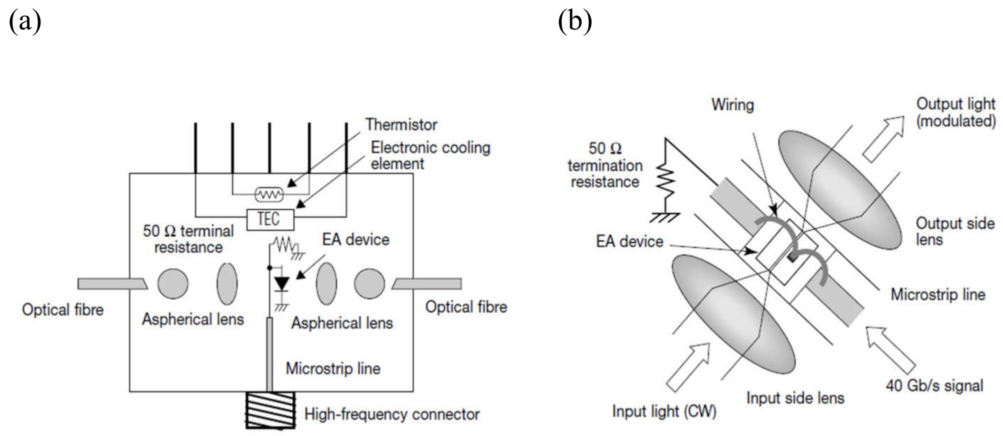

Fig.2.1 Structure (*a*) and mounting (*b*) structure of EA modulator module.

Electro-optical (EO) modulators are free of this disadvantage and potentially have a much wider band of operating frequencies. Physical and technological basis for the development of integrated optical EO modulators was developed in the early 1970s [63] now have wide practical application. In particular, the EO modulator of the type Mach–Zehnder interferometer is used as a standard element for converting sufficiently short electrical impulses into an optical form in high-speed fiber links. However, the voltage values for the EO modulator operation are approximately twice higher than those for the EA modulators. This results in certain complications in the practical application of devices. Therefore, the serial EO modulators based on integrated Mach–Zehnder interferometers are used mainly in systems with the data transfer rate of 10 Gb/s. Spectroscopy research of spontaneous KP in noncentrosymmetric crystals [64-66] allowed to determine electron-lattice contributions to the electro-optical coefficients of a number of EO crystals. Spectroscopy research of spontaneous Raman scattering in noncentrosymmetric crystals [64-66] allowed to determine electron-lattice contributions to the electro-optical coefficients for a number of EO crystals. It was found that the main contributions to all EO coefficients of such as $LiNbO_3$ crystal give certain polar vibrations namely 152 cm^{-1} E-type and 253 cm^{-1} A-type with the highest intensity of lines in the Raman spectra of this crystal [64].

The analysis of the Raman spectra of the Ti-diffused waveguides [66] allows us to estimate the stability of their electro-optical properties. The electro-optical coefficients r_{33} and r_{13} attract the greatest interest in the design of integrated EO devices in $LiNbO_3$. The first one has a maximum value. The electron-vibrational A_1-type oscillations contribute to these coefficients. There were no noticeable changes in the intensity of the transverse Raman lines of the A_1 type and its T-L splitting in the spectra of optical waveguides. This indicates the invariability of the differential components of the Raman tensor and the oscillator strengths. The presence of an optical Ti-diffused waveguide does not change the parameters of the electro-optical soft mode for EO coefficients r_{33} and r_{13} , accordingly.

Thus, the invariance of the frequency position, T-L-splitting and relative intensity of the E-type line 152 cm^{-1} and A-type line 253 cm^{-1} observed in the Raman spectrum allow us to conclude that the parameters of the electrooptical soft mode are invariant in the Ti-diffused waveguides in lithium niobate. The obtained data from the Raman measurements form a reliable basis for solution of a practically important problem of the dispersion of electro-optical coefficients by the frequency of the control electric field.

The electro-optical coefficients dispersion omitting the tensor symbols can be described as [66]:

$$r = A\left\{ \xi + \sum_{m=1}^{N} \frac{\Delta r\left(W_m\right)\omega_m^2}{\omega_m^2 - \omega^2 - i\omega\Gamma_m} \right\}, \tag{2.1}$$

where $A = -4\pi / (n^2_i\ n^2_j)$ is the recalculation coefficient of nonlinear polarizability to EO coefficients, $\Delta r\ (W_m)$ is the contribution of the mth lattice oscillation to the electro-optical effect. All EO contributions were obtained in [64] and dispersion functions were calculated for all electro-optical coefficients for lithium niobate material.

Fig. 2.2 shows the dispersion curves for the real parts of the EO coefficients: r_{13}, r_{33}, r_{42}, and r_{22} at the frequency ω of lattice resonances. The maximum change in the EO coefficients: r_{13} and r_{33} is observed at the frequency of 253 cm^{-1} and in the EO coefficients: r_{42} and r_{22} is registered near 152 cm^{-1}. The changes begins at a frequency of approximately 100 cm^{-1}. The total contribution of oscillations starts from $\omega > 253$ cm^{-1} to r_{13} and r_{33} is no more than 10-15% compared to a contribution of 253 cm^{-1} vibration. Since the electron-ion contribution to EOE in lithium niobate is the main one and the parameters of electrooptic soft modes in Ti-diffused waveguides are invariant than the variance of waveguide EO coefficients, at least in the range of 0-300 cm^{-1}, can be very well described (see curves in Fig. 2.2a, b).

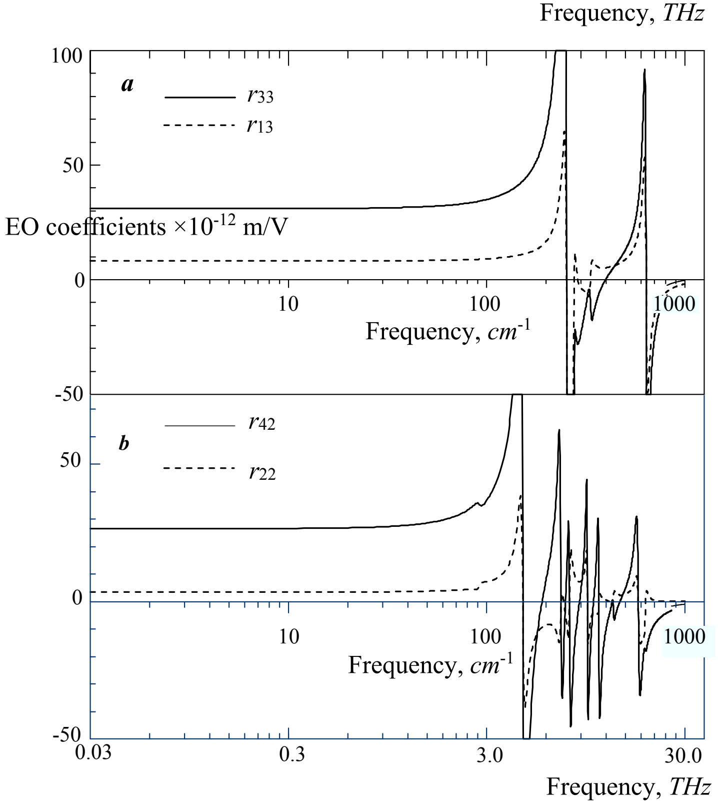

Fig.2.2 Dispersion of electro-optical coefficients of a diffused waveguide in lithium niobate.

The dispersion of the electro-optical coefficients around the dipole vibrations of the crystal lattice is one of the physical limits for increasing the operating frequencies band and the speed of all electro-optical devices. We set the upper limit frequency by allocating a region of 10-100 cm^{-1} where the dispersion of electro-optical coefficients is absent. This frequency limits the operating frequencies band of integral electro-optical devices up to 3 THz.

There are dipole phonon vibrations in the frequency band from 3 THz to 30 THz . They are observed not only in noncentrosymmetric crystals but also in most condensed media. This is result of the extremely high absorption of electromagnetic radiation [67] in the layer width thickness ≤1 micron. For example, the electromagnetic wave attenuation as a function of frequency for a lithium niobate crystal is given in Fig. 2.3. All graphs are shown in Fig. 2.3 in logarithmic scale for both coordinates. They are plotted taking into account all dipole-active oscillations for both polarizations of the electromagnetic wave. Therefore, the slope of the lines in the Fig.2.3 unambiguously indicates the quadratic dependence on the frequency in the range from 0 to about 1 THz. Indeed when the frequency in this interval increases by an order of magnitude the attenuation increases by two orders.

Note that the acceptable level of own losses due to waves propagating in integrated optical devices in particular for the modulation wave in the Mach-Zander interferometer should be ≤1 dB/cm. Such losses level for the modulation of electromagnetic waves as shown in Fig. 2.3 is realized in lithium niobate at frequencies not exceeding 100–300 GHz.

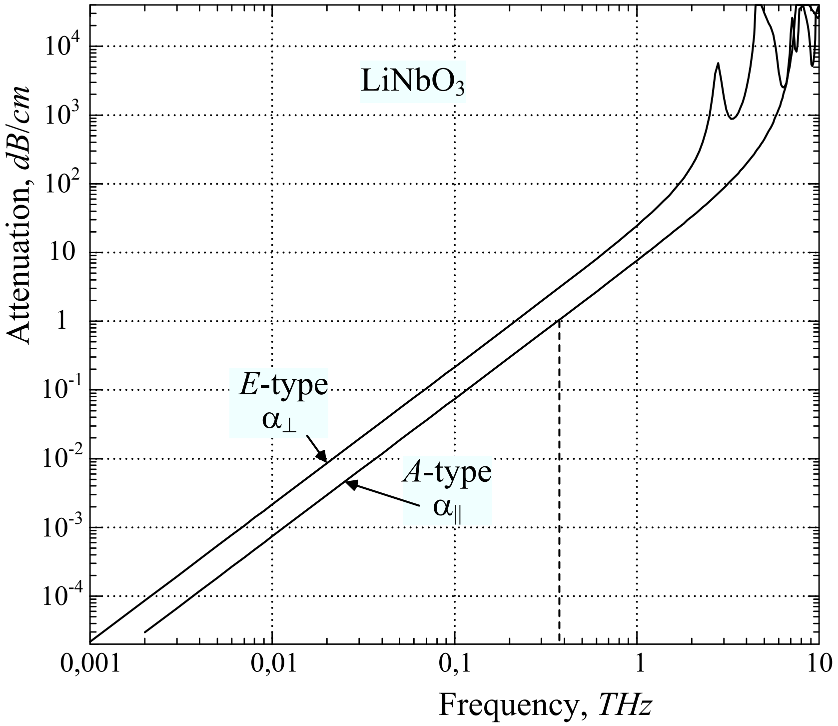

Fig. 2.3. The power attenuation of electromagnetic radiation in the lithium niobate crystal as a function of the frequency. The attenuation is calculated taking into account all polar crystal oscillations for both wave polarizations.

These frequencies are smaller by an order of magnitude than the frequency of the first resonances on the crystal polar oscillations. The attenuation may exceed 10^3 dB/cm when the frequencies exceed the resonant frequencies of the polar oscillations.

In this case, the wave propagation is impossible since the total decay length of the radiation power becomes much smaller than the wavelength. Actually, this reflects that the damping of the modulation wave in $LiNbO_3$ is a fundamental limitation of the operating frequencies band and the specified value of 300 GHz can be regarded as the upper limit frequency for this band. Accordingly, the minimum duration of the propagated electric pulse in this material has to be less than 3 ps. Thus, all spectral frequency components of pulse exceeded the limiting frequency will be "cut off" by absorption of the energy in material.

In general, not only noncentrosymmetric crystals but the overwhelming majority (if not all) of materials with dipole-active molecular oscillations should have an upper limit of the passband in the microwave range. Since these oscillations frequencies are in the range of 100–1000 cm^{-1} (3–30 THz) the attenuation near such resonances is the main physical limitation of increasing the operating frequency of all electron devices without exception, in particular, it is the largest restrictions for electro-optical devices.

It should also be noted that the EO integrated devices implemented in this way can operate in the maximum band 0–40 GHz although it is only a few percents of the potentially possible band. This fact indicates some possibilities for increasing the speed and operating bandwidth of integrated devices based on Ti-diffused waveguides in lithium niobate. On the other hand, solving the problem of practical development of the frequency range in the band of maximum transparency of optical fibers, reaching 200 THz goes beyond the scope of the indicated electro-optical devices and traditional electronics.

As a result of the described limitations of the electronic devices in semiconductor and dielectric materials, the fundamentally other signal processing methods have to be developed with the placement of a single bit information in a time interval that is substantially less than 10 ps with reliable reception of such high-speed signal flows. Such possibilities can be provided by photonic devices that naturally fit fiber optics of active media based on Raman amplification in single-mode fibers. The present stage of the development technique for ultrafast information processing is characterized by a wide utilization of nonlinear fiber optics [68] in practical equipment. The components of receiving and transmitting devices designed for high-speed systems, in particular for a transmission rate of 160 Gb/s, already include components using non-linear fibers [58] including mirror types of fiber-optic loop and other fiber elements.

The study of ways to build high-speed fiber-optic TDM aims not only extending the communication lines bandwidth but it also mainly focused on development of fundamentally new technologies based on photonic devices for the super-fast processing of information streams. To solve the problem of the bandwidth expansion in the telecommunication links, the WDM technology is used.

2.1.2. Wavelengths division multiplexing for bit rate expansion

A simple increment in the number of wavelengths is now successfully applied to maximized use of the optical fiber bandwidth to transmit information with standard speed and the densest channel arrangement on the optical frequency scale. On the way of the multiple channels application by wavelengths division multiplexing (WDM) system there were several challenges:

- noise due to multipass interference (MPI) caused by double Rayleigh scattering (DRS),
- crosstalk as a result of relative intensity noise (RIN) of pumping
- cross-gain modulation (XGM),
- the gain dependent on polarization;
- nonlinear impairments of the optical pulse’s propagation in a single-mode fiber.

Nonlinear perturbations depend on the optical pulse power propagated in the fiber and their nature may be following: self-phase modulation (SPM), cross-phase modulation (CPM), and four wave mixing (FWM).

As proved by practice the FRA used in optical WDM links can significantly moderate the harmful effects of these factors and it may increase the link information capacity. The extremely high values of the optical signal to noise ratio of the FRA and its combination with flexible bandwidth control are resulted in significantly reducing the nonlinear perturbation effects. In such a way, the ultra-long information transmission with high spectral density and minimum cost is implemented. The modern experimental data show the key role of such distributed amplifiers to provide a huge operating band. At the same time, the interval between channels can be reduced to 25 GHz for the long-path transmission of the information at the rate of 10.66 GB/s. Since the accompanied pumping gives a very low equivalent noise ratio, the rather small signal power can be entered in each channel (13 dBm) of transmission fiber and it nevertheless guarantees the high OSNR value. In addition, the low signal power in the channel allows minimizing the potential losses in channel efficiency as a results of decreasing the cross perturbation and inter-channel non-linear interactions that accompanied the Raman gain process.

For example, the practical test of the 20 channels system with channels separation by wavelength in the S-band (between 1493.36 and 1521.77 nm) is demonstrated in [69]. It was allocated in the 200 GHz band for each channel and the digital signal transmission was carried out at a speed of 10.67 Gb/s through ten sections of standard single-mode fiber with a total length of 867 km. The system consists of eleven lumped FRAs on dispersion compensation fibers. There were, as a rule, six split fiber connections on each site and additional lossy elements resulting in an average loss of up to 21 dB per site.

The experimental signals spectrum at the output of 20 channel link is shown in Fig. 2.4. The measured average OSNR value (in the bandwidth of 0.1 nm) was about 20.7 dB. The bit error rate (BER) at such an OSNR level in all channels was $<10^{-12}$ without any errors correction at the transmission rate of 10.67 GB/s in the communication link. These BER values are confirmed by direct OSNR measurements using the threshold variation of the noise spectrum for the steady signal peak power. Almost no distortion caused by dispersion was observed even channels were influenced with the greatest dispersion.

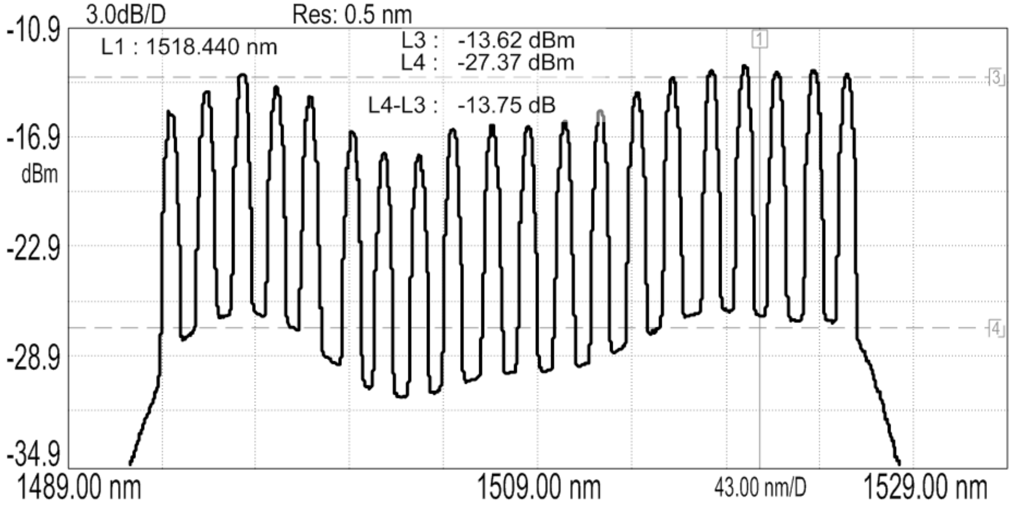

Fig.2.4. The output spectrum at the last cascade of the Raman amplifier in 20 channels fiber link of 867 km long in the S-band. The average optical signal-to-noise ratio (bandwidth is equal to 0.1 nm) is ~ 20.7 dB [69].

The absence of the frequency intermodulation effect between channels at the densest arrangement of WDM transmitters is illustrated in Fig.2.5 [69]. Even five channels were separated by only 50 GHz no intermodulation products between the channels were observed at least below –28 dB in relation to the signal. According to theoretical estimations, when the operating input power in a single channel was set to the maximum (+1 dBm), the self-phase modulation (SPM) of the optical signal pulses results in the greatest deterioration of the system parameters. The SPM perturbation value according to estimations should be not less than 1 dB for any channel of the information transmission link. However, there were no registered the perturbations due to both SPM and cross-phase modulation (CPM) in the experiment.

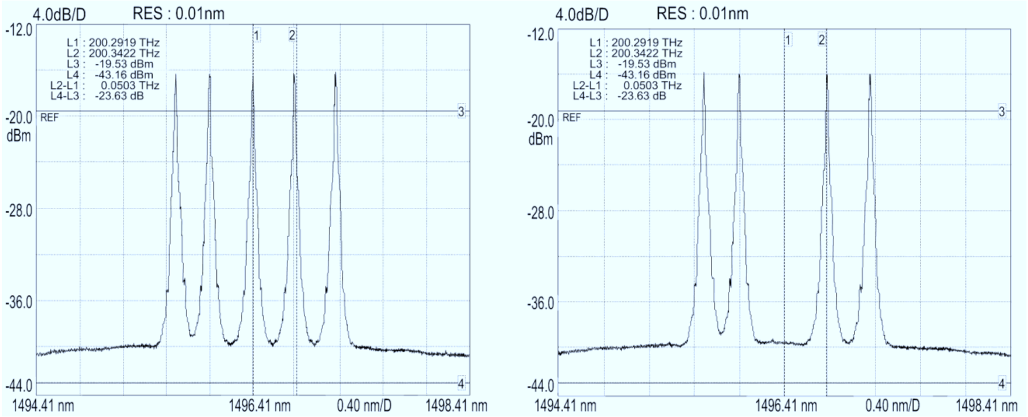

Fig.2.5. The output spectrum of the optical signal in a five-channel line at a speed of 10.67 Gb/s. The channels are spaced at 50 GHz on the frequency scale. The spectrum with all five active channels is shown on the left side and the case of the spectrum with turned off central channel is shown on the right side. No intermodulation products are observed close to the 28 dB level lower than the signal.

Test experimental results of the 192-channel data transmission link through more than 30 sections with 22 dB losses in TrueWave RS-type fiber spans are presented in [49]. The actual transmission distance was 2,400 km in the presence of a variable attenuator but it can reach 3,000 km by extending the distance between repeaters usually achieved in out-door communication links.

The 192 channels were multiplexed in the experimental setup using four polarization-maintaining array waveguide gratings combining groups of 48 CW lasers 100 GHz spaced into four Mach–Zehnder (MZ) modulators. Digital data are formed by two separate pulse pattern generators (PPGs) with bit pattern length equal to (2^{23}–1). All channels are coupled together using 3-dB couplers and fed into the transmission lumped Raman amplifier (LRA). The system simulation on the in-field behavior was peformed for channels separation by 25 GHz and/or 50 GHz.

Multi-pass interference noise has been measured in each span and the related crosstalk is less than –43 dB. It corresponds to a crosstalk level of less than 28 dB at the receiver end. Note that the use of a distributed bidirectional pumping reduces this level.

Considering the little saturation of the propagating Raman gain (less than 1 dB) and the optimized dispersion compensation map the XT induced by XGM can be estimated to be less than 40 dB. The same level of XT has also been estimated due to copropagating pump RIN. Adding up all these contributions the related penalty is less than 1 dB. The main sources of penalties are due to the interaction between SPM and XPM (1 dB) and polarization-dependent gain (2 dB) [49].

Thus, all given experimental data are indicated on the main source of the FRA noise figure and it is the amplified spontaneous emission (ASE). At the same time, the coherent signal after several tens of amplification cycles has a sufficient excess above the ASE level and it ensures the reliable reception of information streams with a satisfactory BER value. In general, the total disadvantages from polarization, interference and nonlinear effects accompanied the amplification of optical radiation in Raman based process, give a fairly small contribution to the OSNR reduction in comparison with the ASE influence.

In summary of this part analysis, we note that the practical FRA application has already become a key technology for the implementation of multichannel fiber-optic links based on WDM technology. However, the unexpectedly high quality of the optical signal after amplification in many FRAs dozens as it actually restores the signal after propagation through relatively long fiber distances raises some questions about the mechanisms for the own noise-generating in such amplifiers. Only the possibility of a signal amplifying through significant space intervals (≥100 km) without full pulse shapes regeneration is radically distinguished the optical amplifiers from their radio analogs and it does not fit into the existing theoretical treatment to the minimum noise parameters of such amplifiers. Considering certain complications regarding the comparison between theory and measurement data, further experimental studies have to be performed to analyze the problem.

2.1.3. Experimental studies of amplified spontaneous emission noise in the FRA

The noise factor F_n is played the central role among the generalized parameters of the signal amplifier quality as it directly influenced the BER in the information streams and it defined as:

$$F_n = \frac{Q_{in}}{Q_{out}}, \tag{2.2}$$

where $Q_{in}=P_{s,in}/P_{n,in}$; $Q_{out}=P_{s,\,out}/P_{n,out}$ is the ratio of the signal power P_s to the noise power P_n (OSNRs) at the input and output of the amplifier, respectively. The noise factor according to definition (2.2) should not depend on the gain coefficient and therefore it can use as generic parameter characterized SNR degradation at the output Q_{out} in comparison with the Q_{in} ratio before the amplifier. For any linear amplifier, the signal and noise power amplification occur with the same gain the factor $F_n > 1$ is due to the presence of own amplifier noise and it reduces Q_{out} with respect to Q_{in}. As a result of such Q regression for the Gaussian distribution of noise peak power, there is a noticeable increase in the BER in the telecommunication system.

Thus the amplifier's noise parameters are decisively influenced on the signal transmission quality and it generally determined the system technical parameters of the information links. All long-term practice of designing and application of earth or space data exchange systems in the microwave diapason indicates the primary role of F_n reduction for reducing the BER in the telecommunication links. If F_n value approaches to the unit for high-quality amplifiers instead of the noise coefficient, it is more convenient to use an equivalent noise temperature parameter T_n:

$$T_n = (F_n - 1)T, \tag{2.3}$$

where T=300K is physical temperature (at 27°C) of the surrounding environment. Using the noise temperature parameter, the real amplifier can be modeled as a perfect device without own noise with an equivalent noise generator connected to its input. Thus, the noise power P_n brought to the amplifier input can be estimated as:

$$P_n = k_B T_n \Delta f_n, \tag{2.4}$$

where k_B is Boltzmann constant, Δf_n is noise bandwidth.

The noise bandwidth is closely interconnected to the amplifier operating band but it may slightly differ in their numerical terms due to the uneven distribution of the noise temperature in the working frequency band. The gain band extension results in inevitable extension of Δf_n due to the increase of the noise power P_n . This significantly reduces the signal quality parameter Q and increases the BER in the data flow. This demands to reduce the transmission distance and completely restore the signal to its original form before signal transmitting to the next part of the required distance.

It should be noted that the temptation of direct transfer of the phenomenological theory results on the noise parameters by analogy with radio frequency and microwave amplifiers to optical amplifiers, in particular to the FRA [70] does not produce the correct results at the end. The paradox of the extremely small frequency of error occurrence in optical data transmission systems which in fact neglected the worked out building principles of radio-relay systems in the microwave range has been paying attention for a long time [71], but the problem is still open.

There are serious doubts regarding the existence of the quantum limit for reducing F_n when one analyzed the parameters of the above-mentioned fiber optic systems [72-74]. For example, a serial amplifier in the satellite antenna converter is considered to be of satisfactory quality if its noise temperature is several dozen Kelvin. Against this backdrop, the theoretically perfect optical amplifier with a noise temperature of 300K looks like an over-optical noise. However, the information transfer at the microwave frequency cannot be realized otherwise than by the scheme of complete signal recovery. So the typical FRA using scheme even for the "ideal" F_n would be simply impossible because the signal should be absorbed by own noises after several sections of the fiber. Therefore, the actual processes of optical amplification of a coherent signal and stochastic noise in a nonlinear system such as the FRA are the subject of experimental research.

Based on the spectroscopic modeling of the Raman amplification processes, in particular, using the actual band model and/or the multimode decomposition of the Raman gain profile, we analyzed the measurement data of amplified spontaneous emission (ASE) spectra. These experimental data allow studing the spectral profile of the effective noise factor. The good agreement of the calculated ASE spectra with the measured curves for the real amplifier noise figure (NF) allowed formulating certain qualitative conclusions regarding the FRA noise parameters. Obviously, the main part of the FRA noise is formed on the segment of the fiber near the pump source since therein the pumping power has the maximum value. The pumping power is attenuated as its propagated through the fiber,i.e. the pumping gradually begins to decrease, therefore the power is not sufficient for efficient ASE generation. This is confirmed by the fact that the average NF slope remains practically constant and it is almost independent of the fiber length at the amplification span. Thus, the NF delta from one edge of the amplification band to another edge is the same as in the ASE distribution. However, spectroscopic modeling allows obtaining only some qualitative estimation of the FRA noise parameters. Therefore, the additional ASE measurements have to be performed to obtain more detailed information about the nature of the noise properties of real fiber optic amplifiers.

2.1.3.1 Method and measurements results of amplified spontaneous emission in counter-pumped FRA

Our experimental ASE studies were performed from the single-mode fiber span in the counter direction to pump using commercial pumping unit with four LD pump sources (1425, 1435, 1455, and 1465 nm) [75]. The maximum pump power was 300 mW per each LD. The experimental setup is shown in Fig. 2.6. Output pump power from each LD through the pump combiner and circulator is directed to the 50 km span of standard single-mode fiber. Pumping source allows independently to fix the output power of each LD in the range from 0 to 300 mW using a digital control unit. ASE power from the fiber after the circulator is registered by an optical spectrum analyzer (OSA). The spectral resolution of OSA was set to 1 nm for all ASE measurements.

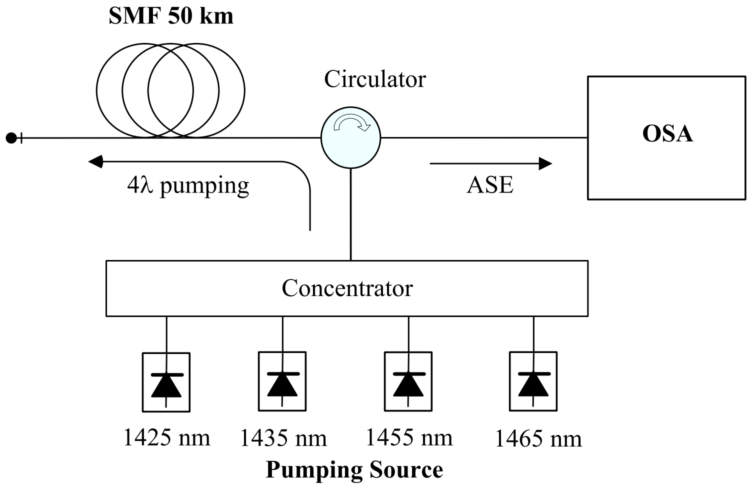

Fig. 2.6. Experimental setup for measurements of amplified spontaneous emission with several pumping sources.

Using four LD wavelengths in the pumping unit in the working amplification mode of the coherent signal can provide a gain bandwidth from 1528 nm to 1562 nm with a guaranteed variations of no more than 0.5 dB [76]. The signal gain can reache value of 25 dB. It depends on the pumping power distribution for each LD and the specific operating conditions, in particular, the type of fiber. The standard SMF of 50 km length under the experimental conditions was pumped in the FRA idle mode, namely without the supply of any optical signals to the input fiber end. Such idle mode of a distributed amplification in the absence of the optical signals combined with the counter pumping allows obtaining the maximum ASE power levels. Therefore, the spectral distribution of the ASE power recorded by the OSA corresponds to the maximum possible level of output FRA optical noise.

The general view of the spectra submitted in Fig. 2.7 has strongly pronounced features in a qualitative interpretation [77] of the well-known spectrum of the spontaneous Raman scattering of light in the silica fibers, looking like a non-uniform continuum in the Stokes shift range from 0 up to 1400 cm^{-1}. The main difference between the spontaneous Raman spectrum and SRS spectral profile is shown as the raised intensity of frequency components with the small Stokes shifts approximately up to 6 THz (200 cm^{-1}). As the term corresponding to the spontaneous Raman scattering contains the phonon density factor of $n_B(\omega)+1$ that considerably exceeds unity at $T = 300$ K in the frequency region less than 200 cm^{-1}, and it infinitely grows when the frequency tends to zero. Really the SRS process does not depend on the phonon density-of-states alternatively to the spontaneous Raman scattering, and accordingly, it does not depend on the temperature.

This fact defines the difference of an observable Raman gain spectrum from the measured spontaneous Raman spectrum which is the most noticable in the small Stokes shift region.

Another feature of the spontaneous Raman scattering is its linearity by nature and thus it does not depend on pump intensity. The spontaneous Raman cross-section remains constant for each studied material, and its numerical value is determined by physical parameters of substance. The presented ASE measurements show that the absolute power cross-section of the Stokes radiation for each of four pump wavelengths varies from $(2.75 \pm 0.08)\cdot 10^{-6}$, when the input LD pump power is 100 mW, up to $(4.3 \pm 0.2)\cdot 10^{-6}$ for the pump power of 300 mW.

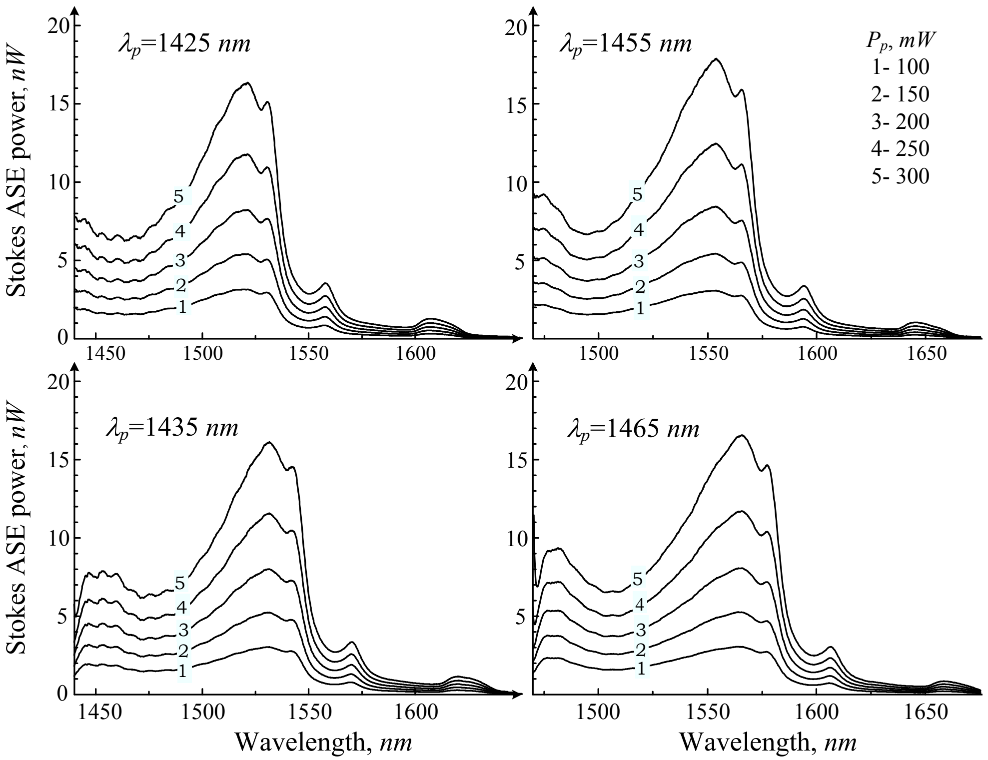

Fig. 2.7. Spectral distribution of Stokes ASE powers measured in counter pump direction and generated with separate pumping sources.

The obtained numerical values for ASE cross-section of the order size $\sim 10^{-6}$ correspond to the quantum efficiency of the spontaneous Raman scattering, but do not correspond to SRS because its quantum efficiency should be higher by approximately 4–5 orders. The absolute ASE cross-section was experimentally determined as the ratio of the total power for the Stokes spectrum integrated over the shifted frequency range from 10 up to 1400 cm^{-1} to the input pump power.

2.1.3.2 Effect of amplified spontaneous emission on the formation of FRA noise parameters

As can be seen the power gain of spontaneous optical noise in the single-mode silica fiber is enough small. The Raman quantum efficiency grows no more than ~40 %, and it corresponds to an increase on/off gain only about 1.9 dB, when the pump powers are varied by 3 times, *i.e.*, from 100 up to 300 mW.

The nonlinearity and the threshold nature of the FRA gain may appear as large amplification of a powerful coherent signal by many times over the amplification of weak incoherent optical noise. This FRA gain nonlinearity causes not only OSNR decreasing at the output, but also allows repeated multiplication [77].

The distribution of the Stokes ASE power generated by a separate LD with λ_p = 1466 nm in counter-pumped FRA is shown in Fig. 2.8 for the frequency domain of the Stokes shift from 0 to 900 cm^{-1} (27 THz). There is a clear tendency on the normalized curves (Fig. 2.8b) the ASE power distribution goes to the Raman gain profile (dotted line) according to increasing power of pumping. The Raman gain profile should be formed by SRS process as zero Kelvin cross-section scattering which is shown by a dotted line in Fig. 2.8b. In contrast to spontaneous Raman scattering, SRS does not depend on phonon density states and, accordingly, does not depend on temperature.

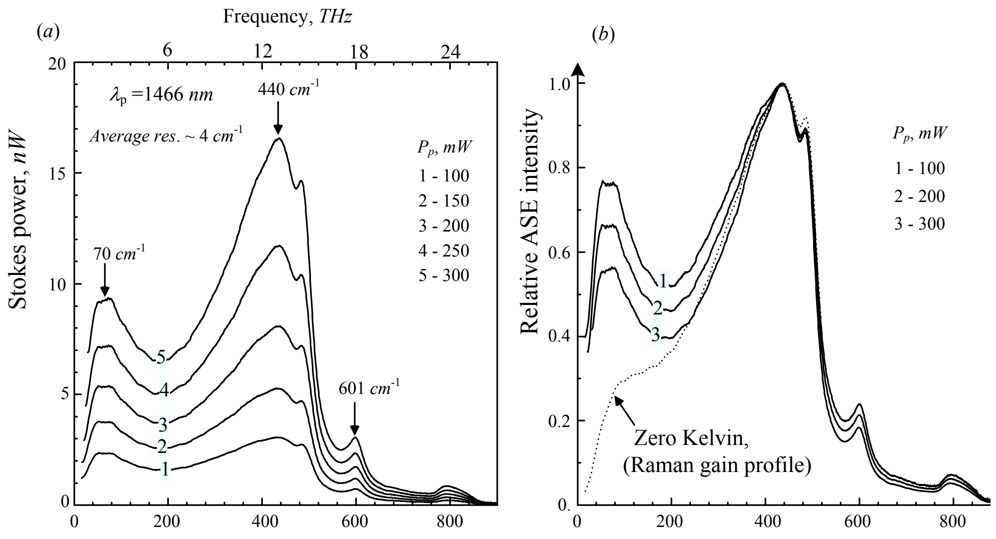

Fig.2.8. Absolute (*a*) and normalized (*b*) Stokes ASE power distributions generated by separate LD λ_p =1466 nm in backward pumped FRA with terahertz bandwidth. Normalized curves (*b*) show the trend of ASE distribution to Raman gain profile (dotted line) when the pump power is increased.

This is the main distinction between the registered Raman gain spectrum and the measured spontaneous Raman spectrum. It explains the obvious tendency of ASE distribution to the structure of the Raman gain profile with increase of pumping power as can be seen in Fig. 2.8b.

The linearity of the spontaneous Raman process excludes the dependence of its cross-section on the pump intensity. As a result, the spontaneous Raman cross-section remains constant for any studied material and the dashed lines in Fig. 2.9 correspond to the power of spontaneous Stokes radiation as a function of pumping power.

Power amplification of spontaneous optical noise in single-mode silica fiber (as can be seen in Fig. 2.9) is in enough small limits. Quantum efficiency of the Raman grows no more than by ~40 %, and it corresponds to on\off amplification approximately on 1.9 dB when the pumping power increases in 3 times: from 100 mW up to 300 mW.

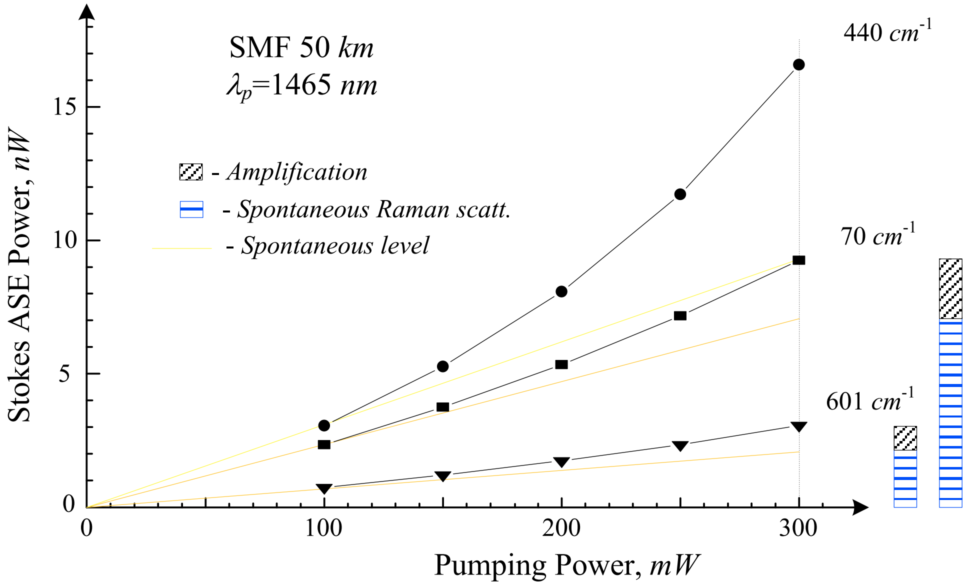

Fig. 2.9. Stokes ASE power as a function of pump power for several peaks in experimental spectra in Fig.2.8a (solid dots). On the right: the diagram shows the Raman gain values, which are only decimal parts in comparison with spontaneous scattering peaks.

This can be explained from the physical point of view as follows [77]. Rather weak ASE generation in the studied pump power range is a result of incoherence Stokes photons exciting due to inelastic scattering of pump photons on a huge amount of molecular phonon vibrations with different frequencies. Therefore, the Stokes radiation in addition to its random phase distribution is registered in a very wide frequency range. Both these facts prevent establishing automatically the phase matching conditions necessary for the coherent accumulation of Stokes radiation which would result in the Raman gain. In other words, Raman interaction in the core of the silica-based optical fiber results in the "spreading" of pump power along the wide spectrum of Stokes frequencies. The condition for obtaining the in-phase Stokes photons with equal frequencies depends on Raman radiation bandwidth, because available pump power is insufficient for effective Raman noise generation. As a result, spectral power distribution of ASE registered corresponds to more spontaneous Raman scattering, instead of SRS.

Using the qualitative interpretation of the above experimental data it should be noted that the Raman amplification is a nonlinear optical process and it appears as result of spontaneous light scattering on molecular vibrations of the medium.

As in all nonlinear processes, the energy transformation efficiency in this process depends on the phase-matching conditions of wave vectors. So the wave vector of the pumping photon should be an exact sum of the wave vectors of the Stokes photon and phonon. The phase synchronization in spontaneous Raman scattering is automatically established by generating a phonon with such a wave vector which in sum with the wave vector of a Stokes photon is exactly equal to the pumping wave vector. The duration of the automatic conditions of phase matching for the predefined Stokes wave and pumping photons is the lifetime of the phonon in the non-equilibrium state and it is equal to τ_2 = 32 fs in the amorphous silica glass [77].

It should be emphasized that the Raman active phonons do not accompany by a dipole moment in materials with a center of symmetry, in particular in a silica glass of optical fiber. Therefore they cannot be directly related to the electromagnetic wave of the same frequency. It is the dipole inactivity of the Raman active phonons that completely protects their equilibrium state from any resonance effect of electromagnetic radiation. As a result, neither thermal electromagnetic radiation nor the difference frequency between the pumping and Stokes frequencies in no way affect the equilibrium distribution of the Raman active phonons, even with the full equality of the frequencies of the thermal photons to the phonon frequency. Linear processes of propagation and attenuation of electromagnetic waves in the fiber do not cause the excitation of the Raman active phonons.

The quantum dynamics of Stokes stimulated Raman scattering indicates the processes realized precisely using non-equilibrium phonons since it does not depend on the phonon density of the equilibrium state. Thus, the Stokes noise generation is possible with so high pumping intensity that guaranteed at least two pumping photons in the time interval of 32 fs during the existence of a non-equilibrium phonon. Only such condition allows amplifying the Stokes wave since the scattering possibility of two coherent photons may be obtained on one phonon, which is generating two identical (and therefore coherent) Stokes photons with equal wave vectors. Resulted phonons pair will repeat the frequency and the direction of the wave vector of the primary phonon. The chain reaction of multiplying non-equilibrium phonons and coherent Stokes photons is the physical cause of the occurrence of stimulated Raman scattering.

In contrast to the described Stokes noise generating mechanism, the non-equilibrium Raman active phonons may continuously arise throughout the signal wave propagation in fiber in the case of an equality of signal wave frequency to the Stokes frequency with respect to pumping radiation. The continuous phonons generation including the phonons with wave vectors matched with the pumping, promotes the chain reaction origin for no equilibrium phonons multiplication. It results in additional coherent Stokes photons. The continuous generation of no equilibrium phonons initiated the Stokes power growth and the number of synchronous Raman active phonons does not depend on the lifetime of a single phonon in an excited state. It leads to a significant reduction of the Raman gain threshold. Therefore, the presence of Stokes wave propagated together with the pumping wave forms a kind of positive feedback that gives an exponential growth of the Stokes wave.

Although abovementioned effect do not fill the gap in the quantitative theoretical description of the Raman amplification of the coherent and stochastic signals from the point of view of phonon dynamics, but it allows to explain the large values of the amplification of the coherent Stokes signal in comparison with the amplification of optical Stokes noise using FRA in silica fibers.

It should be noted that the presented results are obtained without optical signals in the studied single-mode fiber. In signal presence, its coherent power, with the spectral density considerably higher than the Stokes noise density, results in the concurrence process for the pump power during the SRS process. The increase of the pump power for 20-30 dB signal amplification causes the accelerated pump depletion in the propagation process along the fiber, simultaneously reducing the effective length of power accumulation of Stokes noise. Therefore the ASE gain coefficients measured by us in the single-mode silica fiber have the greatest possible quantities and noise power of real FRA don’t exceed the absolute values shown in Fig. 2.7.

The data shown in Fig. 2.9 illustrate that the pure ASE amplification essentially depends on peak power in noise distribution which is defined by the frequency position of the given maximum in the spectrum. The ASE gain coefficients comsiderably grow in the spectrum points with the large intensity as a result of Raman nonlinearity. Simultaneously, the maximal noise amplification remains several times smaller in comparison with nonlinear amplification of the coherent signal. The output SNR after Raman amplifier becomes large in comparison with the case of FRA absence, therefore there is an improvement (even to F<1) of the noise figure of such amplifier.

In summary, the presented experimental results of the noise amplification measurements in the backward pumping FRA with the terahertz working bandwidth definitely show that the real noise figure is essentially below the established limit of 3 dB. There are, at least, two physical reasons based on the fundamental feature of the stimulated Raman process as nonlinear interaction of optical waves. First, the coherent signal with the much larger power than the power of spontaneous Stokes noise is more effectively amplified by the pumping radiation in comparison with the amplification of Stokes radiation with random initial phase distribution. Second, the presence of the Raman threshold leads to essentially narrows effective noise bandwidth and the pumping depletion process decreases the length of coherent accumulation of Stokes noise simultaneously. Therefore even at the absence of input signal, the real ASE gain coefficient in practical FRA sample appears so small that its own amplifier noise differs a little from the spontaneous Raman scattering by the pumping, and its power is approximately –60 dB relatively to the input pumping power. The FRA gain coefficient for a signal essentially exceeds the noise gain coefficient in the investigated range of nominal pumping powers. This reflects that in accordance with Eq.(2.2) there is possibility of increasing Q_{out} in comparison with Q_{in} under certain operating conditions. It is equivalent to value F_n <1 in whole terahertz working frequency bandwidth of such amplifier. The performed estimations based on the direct ASE measurements give an explanation of the reasons for substantial reliability improvement of information transfer using FRA in long-path communication systems.

2.1.4. Improvement of the receiver sensitivity of optical signals and the quality of the digital information transmission

The interesting application results of Raman amplification using the diode pumping source for the modernization of the communication system without any changes in the fiber parameters used for the data transmission were described in [78] published in 1997. It is shown that by increasing the overall signal power one can obtain higher productivity of the communication system as increased both the data transmission speed in one channel and the number of WDM channels. Two methods were used in experiments on the modernization of communication lines, namely: 1) the improvement of the single-channel 2.5 Gb/s system to the transmission rate of 10 Gb/s, and 2) the replacement of a single-channel 10 Gb/s system to the four channels system with total data rate of 40 Gb/s. The increased total signal power by 7.4 dB was obtained in both experiments using the pumping wavelength of 1453 nm and the pump power of ~ 1.0 W launched from the receiver end. The output power can be received more than 1.5 W by application of a cascade fiber Raman laser, pumped from a double-cladding fiber laser and doped by rare-earth elements, which in turn pumped by a conventional line of semiconductor lasers.

The Raman gain is obtained by pumping waves propagated in the opposite direction to the signal along the fiber. This allows increasing the power of the total signal in the communication system. The receiver in these experiments was improved by the use of an additional Raman amplifier. The fiber span of the 123 km length was used with the receiver at the end of the fiber. The input optical amplifier, fiber dispersion compensation module (DCF), the 0.3-nm Fabry-Perot filter, and PIN-type photodetector are included in the receiver. The data recovery and clock rates equipment were set up immediately after the PIN photodetector and it is adjusted accordingly to a data transfer rate of 2.5 Gb/s or 10 Gb/s. The optical fiber directly in front of the receiver used for the Raman amplification was a silica fiber with an average loss of 0.173 dB / km and the group velocity dispersion of 20 ps/nm/km.

The 590 mW, 750 mW, 900 mW and 1000 mW pumping powers were used for the Raman amplification. The value of the input power equal to the power in the receiver -32.5 dBm in the absence of the Raman gain is used as the reference value for the measurements. For peak pumping power of 1000 mW peak amplification was 28.1 dB.

The signal power change throughout the wavelength range from 1547.0 nm to 1562.5 nm was 1.3 dB. The pumping wavelength was 1453 nm chosen for maximum amplification in the wavelength range between 1550 nm and 1560 nm in a standard fiber with a Raman gain of 3.3×10^{-4} $m^{-1}\cdot W^{-1}$. The Raman gain coefficients are usually higher for other fibers types in particular for fibers with shifted dispersion it is two to three times higher. Accordingly, the lower pumping power is required to achieve the same gain in such fibers.

The first experiment shows an increase in the transfer rate from 2.5 Gb/s to 10 Gb/s in a single-channel system at 20.2 dBm input power. The span of dispersion-shifted fiber 74.8 km long was used at the transmitting end of the line. The specialized fiber had a slightly larger wavelength of zero-dispersion. It was used to eliminate the modulation instability. Measured BER parameters in the system operated without Raman gain with the data transfer rate of 2.5 Gb/s are shown in Fig. 2.10 by solid triangles.

The power at the receiver provided the BER of 10^{-9} was –43.4 dBm. The measured BER values are shown by solid black circles in Fig. 2.10 for the 10 Gb/s data transmission system that used the same fiber span and dispersion compensation but without the Raman gain. The error rate of 10^{-9} is obtained for the power at the receiver input –39.5 dBm. Accordingly, the speed transfer of such a system from 2.5 Gb/s to 10 Gb/s leads to the loss of receiver sensitivity to value about 3.9 dB. Such transmission speed change should result in the deterioration of sensitivity on value of 6 dB at the permanent levels of optical noise and relative bandwidth of the optical filter. However, the self-phase modulation in conjunction with the positive slope of the dispersion somewhat improves the sensitivity at the data transmission rate of 10 Gb/s. Note that such system behavior is entirely within the scope of the noise theory for electronic amplifiers. Indeed the own noise power is increased proportionally to the increase of the working band according to Eq. (2.4); Thus, it reduces the *Q* (OSNR) and ultimately increases the frequency of errors in the information flow.

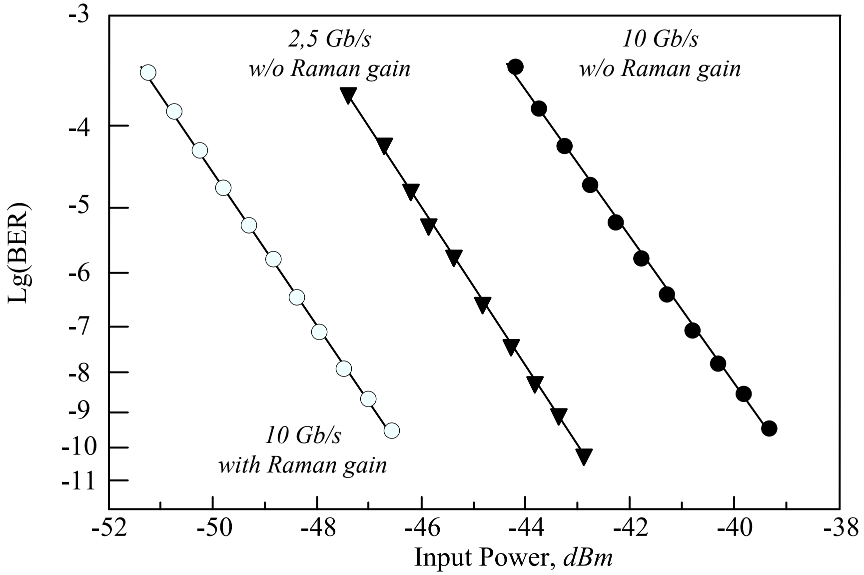

Fig.2.10. The BER is measured as a function of the power in the receiver channel at 2.5 Gb/s without the Raman gain, as well as for a channel of 10 Gb/s with and without Raman gain at a pump power of 1000 mW [78].

The measured BER values at a data rate of 10 Gb/s with the Raman gain are shown by the open circles in Fig. 2.10. The BER is shown as a function of the equivalent power at the input of the receiver. The equivalent power corresponds to the power that would flow to the receiver input when there is no amplification. Thus an effective sensitivity can be determined and directly compared with the sensitivity measured at 2.5 Gb/s and 10 Gb/s without Raman gain. Using Raman gain the sensitivity is improved by 7.4 dB to –46.9 dBm at the pump power of 1 W. Therefore the FRA application in the existing communication system designed for 2.5 Gb/s data rates extends its throughput to 10 Gb/s without any fiber infrastructure modifications. Moreover, the additional excess of signal power over the noise level in the system up to 3.5 dB is demonstrated in this experiment. Reducing the BERs after FRA application actually reflects that such an optical amplifier allows improving signal visibility over optical noise background in contrast to electronic amplifiers.

The increase of the Q parameter after the FRA use is in agreement with the conclusion that the coherent signal gain is significantly higher than the stochastic noise amplification from the previous subsection. The outlined results show there are real values of $F_n < 1$ obtained in the experimental conditions for the direct use of the noise factor definition in Eq. (2.2).

The increase of the signal-to-noise ratio Q due to FRA is used in [65] to increase the number of data transmission channels maintaining a stable and acceptable level of error rate. The measured error rate as a function of the received power in each of four channels of 10 Gb/s with Raman gain by pump power of 1000 mW is shown in Fig. 2.11.

The signal was propagated in this experiment through the fiber span 123 km long with an input power no more than –15 dBm and it is eliminated the fiber nonlinearity effects. The signals wavelengths were 1552.6, 1555.3, 1557.0, and 1558.5 nm respectively. The measured sensitivities for error rates 10^{-9} in channels 1, 2, 3 and 4 were (– 45.1); (– 45.2); (– 45.2) and (– 45.1) dBm, respectively. The spread of 0.1 dB is within the measurement uncertainty. The open squares show the BER performance for a single 10-Gb/s channel at a wavelength of 1555.3 nm indicating a sensitivity of –45.1 dBm. The single-channel result without Raman gain is shown in the Fig.2.11 for comparison by solid squares, and it exhibits a sensitivity of (– 37.7) dBm. The BER performance with Raman gain is improved by 7.4 dB independently of the number of channels.

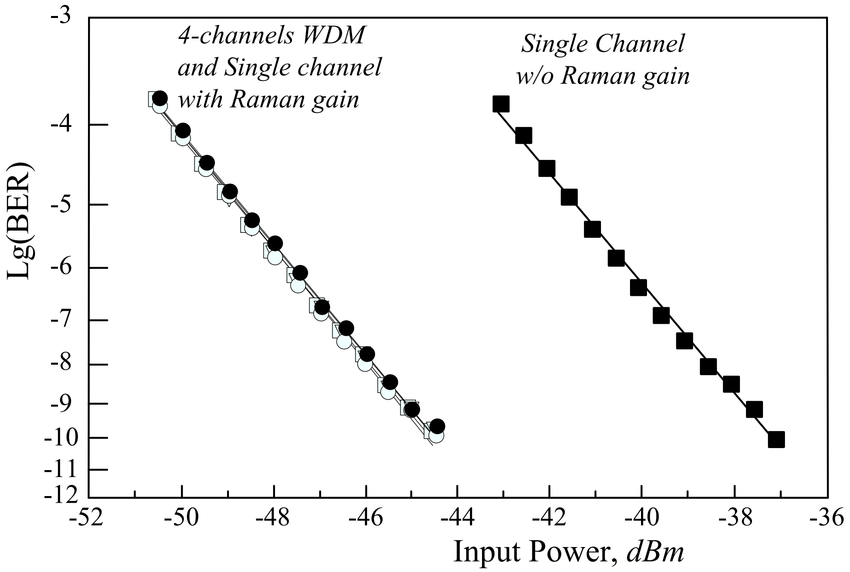

Fig. 2.11. The measured BER performance as a function of the input received power in a single channel for the data rate of 10 Gb/s with the presence and absence of Raman gain, as well as in the 4-channel system of 10 Gb/s with Raman amplification. The Raman pump power is 1 W. The equivalent power at the input of the receiver is shown in dBm for the case of Raman gain [78].

Generally, upgrades in capacity of the existing communication systems (either by TDM or WDM in the described experiments) were performed at least four times only using the Raman gain. As a result, it is shown experimentally that the actual increase in total signal power by 7.4 dB in the TDM system allows increasing the data transmission speed from 2.5 Gb/s to 10 Gb/s and the single-channel transmission can be expanded from 10 Gb/s up to four channels of 10 Gb/s each in the WDM system. Raman gain was a rather attractive method of upgrading existing communication systems, which does not require any changes in the fiber subsystem.

Fig. 2.12 shows the eye pattern in the one channel of the 192-channel data transmission system after the 30 x 22 dB of True Wave RS-type fiber spans [49]. Recall the eye pattern method is a fairly simple and elegant way of directly observing the error rate in digital systems especially at high speeds of information processing. This method consists of the oscilloscope observation of the test pseudorandom sequence of pulses passed through the amplifier. The digital information stream is simulated by the pseudorandom sequence with roughly equal numbers of zeroes and units. Each binary flow number corresponds to a high or low signal level within the one clock cycle. If the horizontal scan speed is set to observe the duration of one period of clock frequency for the entire screen width, then the tracks from the positive and negative pulses can form the characteristic figure which looks like an eye (Fig.2.12).

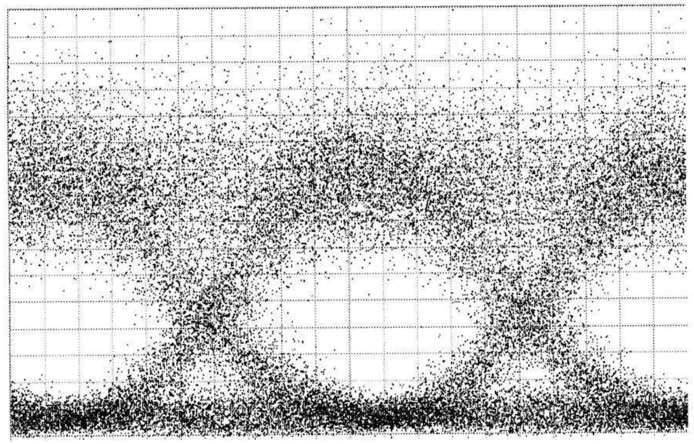

Fig.2.12. The eye pattern for one channel of the 192-channels data transmission system after the 2500 km fiber length and passing in total the 90 FRAs without restoring the initial waveforms [49].

The oscilloscope has high sharpness without blurring in the absence of noise and interference. If the random noise at the signal background is presented than the signal tracks are blurred with increase of the noise level, so the eye image seems to be closed. It is not only the generalized and very apparent picture of the received signal quality is obtained but it also allows the direct quantitative measurements of the BER performance using the random variables ensemble with the number of elements of the pseudorandom sequence. It is clear from the eye pattern (Fig.2.12) after the signal passed over 2500 km fiber long. It is gained in general by 90 FRAs without distortion the initial signals form. There are very small distortions caused not only by dispersion and nonlinear effects but also by the noise of optical amplifiers. The experimentally detected OSNR for all 192 channels was in the range between 11 dB and 15 dB and it corresponds to the BER performance in the range of 10^{-4} to 10^{-8} without error correction in the channel. Figuratively speaking FRAs open the new opportunities in respect of the range and speed of the optical telecommunication systems.

Thus, the optical nonlinearity of Raman gain is radically distinguished this photonic process both from the electromagnetic waves amplification in the radio frequencies range and from the amplifiers of the traditional laser type based on the population inversion of the electronic energy levels of impurity centers. The Raman gain nonlinearity is resulted in the much larger efficiency of the pumping energy conversion into a coherent signal compared with the amplification of the spontaneous Stokes noise. It is the unique feature of stimulated Raman. It appeares in the pump nominal modes without exceeding the self-excitation threshold and allows for the optical signals regeneration i.e. the power amplification of a coherent Stokes wave significantly exceed the optical noise level.

In fact, the OSNR improving at the FRA output uniquely leads to the values $F_n < 1$. According to Eq. (2.3) the FRA noise temperature should be negative. It may cause the reduction of noise power according to Eq. (2.4) at the FRA input.

On the other hand, a certain "exotics" accompanied the Eqs. (2.2) – (2.4) applied to the FRA description reflect the following. If these phenomenological parameters are formally applied to the description of a substantially nonlinear process, and this by definition does not fit into the linear theory then the unusual values of the noise parameters appear due to the difference in the transmission coefficients for the coherent signals and the stochastic noise.

In addition, such FRA noise parameters do not have a single-valued numerical expression for the pumping unit separately from the transmission line. Both the main amplification factors as for signal and for noise depend on a very large number of factors: the fiber type, the pumping direction (direct or reverse), the pump method (lumped or distributed) as well as the power, quantity, and channel multiplex density of the signals, and other parameters of communication lines. In general, with respect to the FRAs the indicated parameters almost completely loose their generalizing role as a basis for comparison of the quality of the device, which may rise the question about the appropriateness of their use.

At the same time, a great application success of the Raman amplification of optical signals for ultra-long data transfer in terrestrial conditions with record data exchange rates has quite promising prospects of wide penetration in adjacent areas of signal processing.

2.2. Modeling of Raman gain profiles in single-mode fibers based on the silica glass

A detailed analysis of the threshold conditions and the working generation band of FRL based on GeO_2-doped single-mode fibers we performed in [79]. Now our calculation technique is described in this subsection and the numerical results of the spectroscopic analysis of the Raman gain profile for a number of other single-mode fibers based on silica glass are given in the Stokes shift region from 0 to 1400 cm^{-1}.

2.2.1. Theoretical basics of spontaneous and stimulated Raman scattering in optical fibers

Spontaneous Raman scattering (SRS) occurs as an interaction result between the optical wave field and the vibration of separate molecular nanocomplexes in amorphous compounds forming the optical fiber core.

2.2.1.1. Oscillatory model of Raman active vibrations of molecular nanocomplexes in amorphous glass

The most common fiber type (the "pure" SiO_2 fiber) is fabricated on the basis of silica glass SiO_2 with small impurities of germanium GeO_2 into the fiber core to form a waveguide. It should be noted that this is a standard fiber, commonly referred to as "pure" SiO_2 fiber, but it actually contains several volume percents of GeO_2 impurities inducing the formation of a region of an increased refractive index. The change in the refractive index of a single-mode fiber core relative to the cladding layer is about $\Delta n \sim 10^{-2}$, as a rule. It depends on the GeO_2 impurity concentration. At the same time, a small amount of germanium impurities allows attributing this most common type of fiber to pure SiO_2 (hereinafter the quotes symbols will be omitted). When the GeO_2 concentration in the core is increased up to 25%, the observed Raman gain coefficient increases more than an order of magnitude in accordance with the increase of the stimulated Raman cross-section in the spectrum of molecular oscillation modes nearby 440 cm^{-1} peak. Because of the sharp increase in the Raman amplification this type of fiber is referred to a separate class called Raman fiber or GeO_2-doped fiber. It is used as a working active medium for the vast majority of modern Raman lasers.

The glass of both fiber cores is rather complicated since it is formed by amorphous compound from molecular nanocomplexes containing Si–O–Si, Si–O–Ge (Fig.2.13), and seldom Ge–O–Ge bonds. The elastic bond of an oxygen atom with two adjacent silicon or germanium atoms are considered in the modeling of Raman processes. Since the oxygen atom is lighter than other atoms often it is assumed [68] the vibrations of this type of atoms forms the harmonic oscillators system for the Raman process. Although the oscillating spectrum of molecular nanocomplexes is clearly not limited to oscillations of only oxygen atoms, it is efficient to quantitatively describe the features of Raman gain on the background of spontaneous scattering using the model of one oscillating mode.

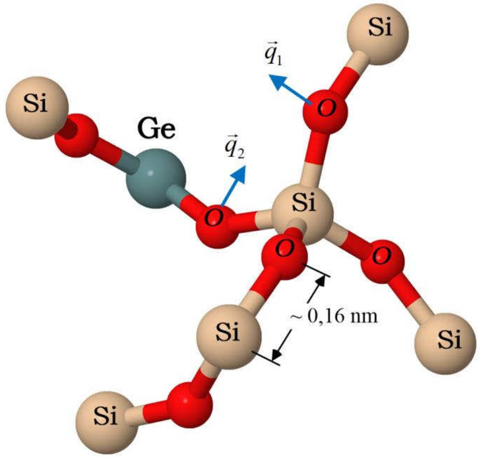

Fig.2.13. Near order in the formation of amorphous glass from molecular nanocomplexes containing Si–O–Si and Si–O–Ge bond types

In the case of most probable inelastic scattering of an optical radiation field photon on this oscillation, the oscillator energy increase. Simultaneously with the decrease of the incident photon energy the scattered light (Stokes wave) acquires a lower optical frequency. Its frequency shifts accordingly to the phonon oscillation frequency of mentioned molecular nanocomplexes. The spontaneous Raman cross-section does not depend on the intensity of excitation radiation and differs from zero in the centrally symmetric glass only for non-polar oscillations.

The relaxation of the excited oscillator to the future equilibrium position in irregular amorphous compounds, such as glass, occurs very fast (at femtosecond intervals) through various interaction processes with other oscillators. Therefore the renewal of the equilibrium state of glass occurs almost instantaneously. As a result, the spontaneous Raman cross-section turns out to be temperature-dependent due to the Bose factor of the phonon population on the oscillator’s energy levels.

In the presence of the Stokes wave which can be an external optical signal, the stimulated Raman process is registered in the exponential growth of the Stokes wave power propagated through the fiber. The conversion efficiency of the pumping power into the Stokes wave due to Raman amplification is proportional to the pumping wave intensity. Therefore, in order to characterize the dynamics of the Raman gain process, it is introduced the gain coefficient of the electromagnetic wave propagated in the fiber instead of the scattering cross-section.

Within our work we utilize the results of stationary Raman theory in fibers for quantum and semi-classical approaches and the Raman amplification process is described by continuous waves for both pumping wave and signal wave. This approximation is proved to be correct for the experimental data interpretation even for relatively short pulses of subpicosecond duration and for signal frequencies extending up to several dozen GHz, taking into account the rapid relaxation of the fiber's phonon system,

2.2.1.2.Quantum dynamics of spontaneous and stimulated light scattering on phonons

In terms of quantum dynamics, the elementary act of Raman scattering corresponds to the fact that a photon with an angular frequency ω_p is inelastically scattered on a molecule and two events can occur: i) Stokes and ii) anti-Stokes processes. The Stokes process consists in the appearance of a phonon with an angular frequency ω_v resulting in the photon with a lower angular frequency $\omega_s = \omega_p - \omega_v$. In the case of an anti-Stokes process, an incident photon receives the phonon energy and, after the scattering process, acquires higher $\omega_{as} = \omega_p + \omega_v$ angular frequency. These events may be occurred spontaneously or be stimulated by photons at Stokes or anti-Stokes frequencies.

Based on the quantum approach the dynamic equation for the change of the number of photons n_s with frequency ω_s in the process of inelastic light scattering (spontaneous + stimulated) depending on the photons propagation *z*-distance along the fiber has been obtained [68] in first-order perturbation theory in the form:

$$\frac{dn_s}{dz} = A\left[n_s n_p - n_s n_\upsilon + (n_\upsilon + 1) n_p \right], \tag{2.5}$$

where n_p is the number of pumping photons, n_υ is the number of phonons of molecular oscillations of a fiber core. Due to the fast relaxation of molecular oscillations, we can assume that n_υ is maintained under conditions of thermodynamic equilibrium, i.e., the population n_υ is determined by Bose-Einstein distribution:

$$n_\upsilon = [\exp(\hbar\omega_\upsilon / k_B T) - 1]^{-1}, \tag{2.6}$$

where $\hbar = h / 2\pi$ is the Plank constant, k_B is the Boltzmann constant, T is the absolute temperature, and the coefficient A in Eq. (2.5) has the form:

$$A = \left|\frac{\partial\alpha}{\partial q}\right|^2 \frac{\pi\hbar^2}{4V^2 Nm\varepsilon_s\varepsilon_p v}\rho(\hbar\omega_f)\frac{\omega_p\omega_s}{\omega_v}, \tag{2.7}$$

where $\partial\alpha/\partial q$ is the differential polarizability of a molecule determined by a derivative of the polarizability, α, by the displacement coordinate, q; m is the effective mass associated with the vibration, N is the number of oscillators in the interaction volume V, ε_s and ε_p is dielectric permittivity for Stokes and pumping waves, respectively (they are given in scalar approximation); $v = c/\sqrt{\varepsilon_s/\varepsilon_0}$ is the phase velocity of Stokes wave, c is the light velocity in vacuum, ε_0 is the dielectric constant, and $\rho(\hbar\omega_f)$ is the density of final states, in which the system may find itself after the scattering. The density involves the sum of contributions from all possible final states.

The density of states $\rho(\mathrm{h}\omega_f)$ is a parameter of the quantum theory. This parameter is difficult to calculate directly especially in the case of an irregular medium of the amorphous fiber core since it requires the determination of all electron-vibrational energy levels of each molecule. In addition, this density depends on the phonon dumping which through molecular transitions returns the system from the final state to the initial one. There are many processes that return the system to a state of thermal equilibrium.

In spite of the difficulties associated with finding of the exact solution of the quantum Eq. (2.5), a number of important conclusions regarding the physical features of the Raman amplification of a Stokes photon on the background of spontaneous Raman scattering can be performed as it is the main source of Stokes noise in the processes of nonlinear Raman amplification of optical radiation. The first positive term, $n_s n_p$, in square brackets of the right-hand side Eq.(2.5) is responsible for the exponential growth of Stokes photons due to stimulated Raman effect in the process of photons propagation along the z-direction of the fiber. The second term, $-n_s n_v$, describes the own attenuation of Stokes photons. Finally, the third term, $(n_v + 1)n_p$, describes the spontaneous Raman scattering since with a given pumping, $n_p = \mathrm{const}$, the number of Stokes photons does not change at any fixed length, *l,* of the fiber. For the next data analysis, two differences between the processes of spontaneous and stimulated Raman scattering have to be specified.

Firstly, the intensity of the stimulated radiation does not depend on the temperature in contrast to the spontaneous radiation, for which the factor $n_v + 1$ has essential temperature dependence in accordance with Eq. (2.6). Secondly, the occurrence of stimulated Raman scattering has a threshold nature since for the small pumping photons number, $n_p << n_v$, and if the spontaneous Raman scattering is neglected then according to Eq.(2.5), $dn_s / dz < 0$, i.e. Stokes photons are absorbed during the propagation process. The attenuation of Stokes waves stops at $n_p = n_v$, therefore the stimulated Raman scattering will be noticeable over the background of spontaneous Stokes noise at $n_p > n_v$.

It should be noted that in the case of usage of certain phenomenological models for $\rho(\hbar\omega_f)$ to describe the distribution of vibrational energy levels of a molecule, the results of the quantum description of the process practically coincide with the results of the classical approach.

2.2.1.3. Classical electrodynamics of light scattering processes in single-mode fibers

According to classical description considered in this subsection, the Lorentz-type form of Raman line can be obtained. Therefore, classical electrodynamics under conditions of the homogeneous broadening of vibrational energy levels in a system containing N oscillators allows to use of the Lorentz-form line for the quantum mechanical value $\rho(\mathrm{h}\omega_f)$. Moreover, in amorphous fibers when the orientation of the molecular nanocomplex relative to the neighbor's environment is wholly random, then the broadening of an oscillatory level becomes heterogeneous and the oscillatory level can acquire the Gaussian form.

In order to describe the Raman scattering in an optical fiber in terms of classical electrodynamics, the analysis should be limited by one-mode field scattering. The full-electric field in the case of Raman gain can be considered as the sum of two monochromatic waves, one at the pump frequency ω_p, and the other at the scattered wave frequency ω_s, which under the amplification coincides with the signal frequency. Next, the corresponding indices s and p are used to indicate the signal and pumping waves. If we restrict ourselves to the most common types of fibers in our consideration, namely, to those with weak waveguide properties then the electric field can be devided into the transverse part $R^i(r)$, (where $i = s, p$, and $r = \sqrt{x^2 + y^2}$) and the function of z: $E_i(z)$. Then the full electric field can be described as :

$$\begin{aligned}\vec{E} = \vec{e}^{\,p} E^{p}(z) R^{p}(r) \exp\{i(\beta_p z - \omega_p t)\} + \\ + \vec{e}^{\,s} E^{s}(z) R^{s}(r) \exp\{i(\beta_s z - \omega_s t)\} + c.c.\end{aligned} \tag{2.8}$$

where $\vec{e}$ is the unit polarization vector, and β_i is the propagation constant; it is determined by the solving eigenvalue problem of the waveguide $[\nabla_{\perp}^{2} + (\varepsilon_i / \varepsilon_0)(\omega_i^{2} / c^{2})]R^{i} = \beta_i^{2} R^{i}$, where $\nabla_{\perp}$ is the two-dimensional Laplace operator. The abbreviation c.c. in Eq. (2.8) denotes a complex conjugation from the previous expression.

The polarization induced by the electric field is equal to the density of the dipole moment and has the form

$$P_i = P_i^{L} + P_i^{NL} = n_0 \xi_{ij}^{0} E_j + n_0 \frac{\partial \xi_{ij}}{\partial q_k} q_k E_j = \alpha_{ij}^{0} E_j + \frac{\partial \alpha_{ij}}{\partial q_k} q_k E_j \, , \tag{2.9}$$

where $n_0 = N / V$ is the concentration of molecules, vector $\vec{q}$ describes the displacement of the oscillating mass in a molecule from the equilibrium position, $\alpha_{ij} = n_0 \xi_{ij}$ is the macroscopic polarizability of the scattering medium, which is the sum of all-dielectric susceptibilities ξ_{ij} of individual molecules in the unit volume, and by repeated indices in Eq. (2.9) form the sum of components. The first term in the right-hand part describes Rayleigh scattering and the second term describes Raman scattering and the tensor $\alpha_{ijk} = \partial \alpha_{ij} / \partial q_k$ is the Raman tensor. In terms approved to the description of non-linear optical phenomena $P_i^{L} = \chi_{ij}^{(1)} E_j$ and then $\chi_{ij}^{(1)} \equiv \alpha_{ij}^{0}$. In the case of the isotropic core of an optical fiber as well as for other media with an inversion center then $\chi_{ijk}^{(2)} \equiv 0$. Therefore, for the description of the stimulated Raman process in fibers the nonlinear polarization should have the form:

$$P_i^{NL} = \varepsilon_0 \chi_{ijkl}^{(3)} E_j E_k E_l \, . \tag{2.10}$$

The relationship between the nonlinear susceptibility of the third order $\chi_{ijkl}^{(3)}$ and the Raman tensor $\alpha_{ijk} = \partial \alpha_{ij} / \partial q_k$ may be considered as follows. The vector $\vec{q}$ is depended on $\vec{E}$ in the form (2.8) for the case of the stimulated Raman effect. The synchronous external force $\vec{F}$ is result of the corresponding combination of pumping fields and Stokes wave and it is excited the resonant behavior of this oscillation. This vector $\vec{q}$ is described by the equation of the forced harmonic oscillator:

$$\frac{d^2\vec{q}}{dt^2}+2\Gamma\frac{d\vec{q}}{dt}+\Omega_{0v}^2\vec{q}=\frac{\vec{F}}{m}, \qquad (2.11)$$

where Γ is the damping constant, and Ω_{0v} is the self-resonant frequency of the harmonic oscillator without attenuation, *m* is the effective mass of the oscillator. Note that the homogeneous Eq. (2.11), must have quasi-periodic solutions only in the case of weakly damped oscillation $\Omega_{0v}<\Gamma$, and its resonance frequency is equal to $\Omega_v=\sqrt{\Omega_{0v}^2-\Gamma^2}$, i.e. it decreases under the attenuation influence[81]. To solve the equation (2.11) the shift $\vec{q}$ is expressed as:

$$\vec{q}=\vec{Q}e^{i(\beta_v z-\omega_v t)}+\text{c.c.}, \qquad (2.11)$$

where β_v and ω_v is the wavenumber and the current frequency of forced oscillations of the dumped phonon mode, respectively. As the Raman active vibration is dipole-inactive in the case of an isotropic medium of the fiber core the external force F_k vector components should have the form [68]:

$$F_k=\frac{1}{2}\frac{\partial\alpha_{ij}}{\partial q_k}E_jE_i. \qquad (2.12)$$

The resonance of stimulated oscillation for the fields in the form Eq.(2.8) will be realized to obey synchronization conditions as a result of energy and momentum conservation laws:

$$\begin{aligned}\omega_p&=\omega_s+\omega_v,\\ \beta_p&=\beta_s+\beta_v.\end{aligned} \qquad (2.13)$$

Leaving only the synchronous components for the force in EQ.(2.13) in the product of fields as in Eq.(2.9) we obtain:

$$F_n=\frac{1}{2}R^p(R^s)^*\frac{\partial\alpha_{kl}}{\partial q_n}E_k^p(E_l^s)^*e^{i(\beta_v z-\omega_v t)}+c.c.=F_0e^{i(\beta_v z-\omega_v t)}+c.c., \qquad (2.14)$$

which allows us to find the solution of Eq. (2.11) in the form:

$$\vec{Q} = \frac{\vec{F}_0}{m}\frac{1}{(\Omega_v^2-\omega_v^2)-(2i\omega_v\Gamma)} + c.c. \tag{2.16}$$

and the induced polarization at the frequency ω_s may be expressed from equations Eq.(2.8) and (2.9) in two equivalent forms as the amplitude at the oscillatory term $\exp\{i(\beta_s z-\omega_s t)\}$ as follows:

$$\begin{aligned} P_i^{\omega_s} &= \frac{N}{2mV}\frac{R^s\left|R^p\right|^2}{(\Omega_v^2-\omega_v^2)+(2i\omega_v\gamma)}\cdot\left[\frac{\partial\alpha_{ij}}{\partial q_n}\left(\frac{\partial\alpha_{kl}}{\partial q_n}E_k^p\right)^* E_l^s E_j^p\right] = \\ &= 6\varepsilon_0\left|R^p\right|^2 R^s\left[\chi_{ijkl}^{(3)}E_j^p(E_k^p)^* E_l^s\right] \end{aligned} \tag{2.17}$$

with the complex conjugation at $-\omega_s$ frequency. Thus, the expression for the susceptibility tensor of the third order $\chi^{(3)}$ is:

$$\chi_{ijkl}^{(3)} = \frac{N}{12m\varepsilon_0 V}\frac{1}{(\Omega_v^2-\omega_v^2)+(2i\omega_v\Gamma)}\cdot\sum_n\frac{\partial\alpha_{ij}}{\partial q_n}\left(\frac{\partial\alpha_{kl}}{\partial q_n}\right)^*, \tag{2.18}$$

or

$$\chi_{ijkl}^{(3)} = b_{ijkl}\frac{1}{(\Omega_v^2-\omega_v^2)+(2i\omega_v\Gamma)} = b_{ijkl}\cdot\tilde{\varphi}(\omega_v), \tag{2.19}$$

where the tensor components are

$$b_{ijkl} = \frac{N}{12m\varepsilon_0 V}\sum_n\frac{\partial\alpha_{ij}}{\partial q_n}\left(\frac{\partial\alpha_{kl}}{\partial q_n}\right)^*, \tag{2.20}$$

and they do not depend on Stokes shift frequency ω_v, in contradiction with the complex function: $\tilde{\varphi}(\omega_v)$ describing the resonant behavior of the third-order susceptibility $\chi^{(3)}$ near own frequencies Ω_v of the molecular oscillations.

Thus, the Eq. (2.17) gives the quantitative expression of the nonlinear relationship between the Stokes wave and the pumping wave when they are simultaneously propagating along z-direction of the fiber. Then the amplitude of the Stokes electric field $\vec{E} = \vec{E}^s = \vec{e}^s E^s(z)R^s(r)\exp\{i(\beta_s z-\omega_s t)\}$ will be slowly changing in z-direction due to the smallness of components $\chi_{ijkl}^{(3)}$ and $\alpha_{ijk} = \partial\alpha_{ij}/\partial q_k$.

Therefore the term $\partial^2 \vec{E}^s / \partial z^2$ may be neglected, and the wave equation for the amplitudes of each Stokes component of scattered waves may be presented as:

$$\frac{\partial E_i^s}{\partial z} R^s = \frac{3\omega_s^2}{c^2 \beta_s} i R^s \left| R^p \right|^2 \left[\chi_{ijkl}^{(3)} E_j^p (E_k^p)^* E_l^s \right]. \qquad (2.21)$$

In practice, the most important is the dynamic equation for power $P^s = 2\varepsilon_0 n_s c \int_A \left| E^s E^p \right|^2 dA$, where A is the cross-section area of the fiber. It can be obtained directly from Eq.(2.21) in the form [9]:

$$\frac{dP^s}{dz} = \gamma_R P^s = g_R P^p P^s. \qquad (2.22)$$

This expression describes the exponential Raman amplification of the Stokes wave in single-mode fibers.

2.2.1.4. Spectral Raman gain profile

The gain coefficient of the Stokes wave power γ_R occurs to be directly proportional to the pumping power $\gamma_R = g_R P^p$ whereas the gain coefficient g_R depends only on the fiber parameters in the form:

$$g_R = -\frac{3\omega_s^2}{\varepsilon_0 n_p c^3 \beta_s} \frac{1}{A_{eff}^{ps}} \frac{\mathrm{Im}\left[\chi_{iiii}^{(3)} + \chi_{ijji}^{(3)} \right]}{2}, \qquad (2.23)$$

where A_{eff}^{ps} is an effective area of the overlap of the pumping and the signal:

$$A_{eff}^{ps} = \frac{\int_A \left| R^p \right|^2 dA \int_A \left| R^s \right|^2 dA}{\int_A \left| R^p \right|^2 \left| R^s \right|^2 dA}. \qquad (2.24)$$

The Raman gain coefficient g_R is a function of the Stokes shift frequency ω_υ. If we assume that Raman tensor components are the real numbers $\alpha_{ijk} = \alpha_{ijk}^*$, then according to Eq.(2.19) and Eq.(2.23) this dependence can be represented as:

$$g_R(\omega_\upsilon) = g_{R\max} \frac{4\omega_\upsilon^2 \Gamma^2}{(\Omega_\upsilon^2 - \omega_\upsilon^2)^2 + 4\omega_\upsilon^2 \Gamma^2} = g_{R\max} \varphi(\omega_\upsilon). \qquad (2.25)$$

The function $g_R(\omega_v)$ is called the Raman gain profile. The profile Eq. (2.25) has a resonant dependence of the damped oscillator (Lorentz type) since it is obtained for a single oscillator model of an individual molecule. Total oscillatory energy levels in the ensemble of oscillators are expanded and the form factor $\varphi(\omega_v)$ may remain as Eq.(2.25) in the case of a homogeneous broadening. With random distributing of the molecular movement orientation relative to the surroundings the vibrational levels broadening becomes heterogeneous and the form-factor $\varphi(\omega_v)$ has the form:

$$\varphi(\omega_v) = g_{R\max} \exp\left[-\frac{(\Omega_v - \omega_v)^2}{\Gamma^2}\right] \tag{2.26}$$

and it belongs to Gaussian type.

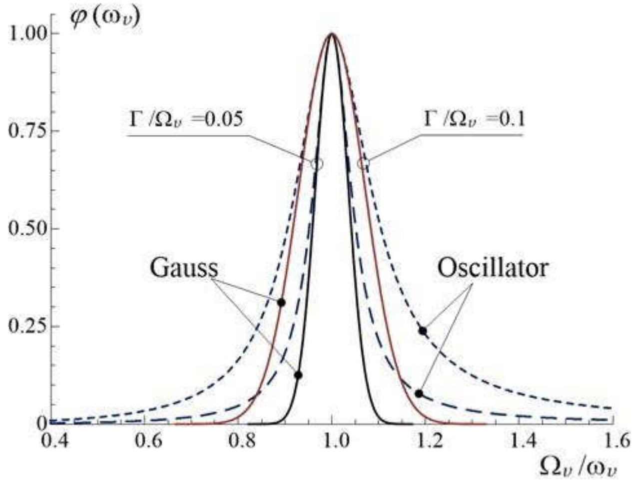

Fig.2.14. Normalized form factors for Raman gain profiles: Gaussian profile (solid line) and profile of the decay oscillator (dotted line) for $\Gamma/\Omega_v = 0.05$ and $\Gamma/\Omega_v = 0.1$.

Both profiles Eq.(2.25) and Eq.(2.26) are presented in Fig.2.14 for two values of the relative phonon's dumping, namely for Γ/Ω_v =0.05 and 0.1. The broadening is mostly heterogeneous in such amorphous materials as glass and next we continue to use Gaussian components Eq.(2.26) in order to decompose the complex Raman spectra in optical fibers.

2.2.1.5. Raman gain features and their relation to spontaneous scattering

In fact, the difference between the Raman spectrum and the frequency Raman gain profile in single-mode silica fibers was found by the analysis of the quantum dynamic Eq. (2.6). Since the energy of n photons with frequency ω in its numerical expression is equal to the spectral power density then the number n actually determines the power of monochromatic radiation in the unit frequency interval around ω. According to the quantum approach the monochromatic power is interpreted as the number of photons in one longitudinal mode of optical radiation. This allows us to find relation between the Raman gain profile and the spontaneous Raman cross-section based on the dynamics of Stokes and pumping photons.

First of all the absence of the temperature dependence of the Raman amplification allows connecting the frequency profile $g_R(\omega_\upsilon)$ with the spontaneous cross-section in such a way that the cross-section $\sigma_0(\omega)$ at zero temperature corresponds to the Raman gain value [94,95]. Thus, $g_R\,(\omega_\upsilon)$ takes the form:

$$g_R(\omega_\upsilon) = \sigma_0(\omega_\upsilon) \cdot \frac{\lambda_s^3}{c^2 h\, A_{eff}^{ps} n_p^2}, \tag{2.27}$$

where λ_s is the Stokes wavelength, c is the speed of light, h is the Planck's constant.

Frequency dependence of the refractive index n_p in the frequency region of Stokes shift is weak, therefore it can be neglected.

The Raman cross-section $\sigma_T(\omega_\upsilon)$ measured at a temperature T, is referred to a zero Kelvin cross-section $\sigma_0(\omega_\upsilon)$ as:

$$\sigma_0(\omega_\upsilon) = \sigma_T(\omega_\upsilon) / [n_B(\omega_\upsilon, T) + 1], \tag{2.28}$$

where $n_B(\omega_\upsilon, T)$ is the Bose-Einstein factor Eq.(2.6).

Another difference between the stimulated and the spontaneous Raman processes is the amplification of the coherent Stokes wave during the stimulated Raman process whereas the entire Stokes shift region is incoherent optical noise at the spontaneous process. Experimental studies of the noise statistics of amplified spontaneous emission (ASE) have been performed in [84]. It is confirmed the Bose-Einstein distribution for the noise nature appeared as ASE in the fiber Raman amplifiers.

Fig. 2.15 shows the scattering cross-section $\sigma_T(\omega_\upsilon)$ in the spontaneous Raman spectra as a function of temperature T and Raman gain profile corresponding to zero-Kelvin cross-section $\sigma_0(\omega_\upsilon)$ for fiber-based on pure silica SiO_2. Some idealization of the picture in Fig. 2.15 utilizes the fact that the basic profile obtained for T = 300 K was considered unchanged over the whole range of temperatures from 77 K to 500 K.

In practice, the description is complicated because the profile can have the noticeable features due to the change in the dumping constant Γ and the shift of resonant frequencies Ω_v of the damped oscillator of the molecules in the fiber core. As a result of strong decrease of temperature the dumping,Γ, as a rule, decreases by several times. This leads to the greater separation of individual phonon modes of the oscillatory spectrum.

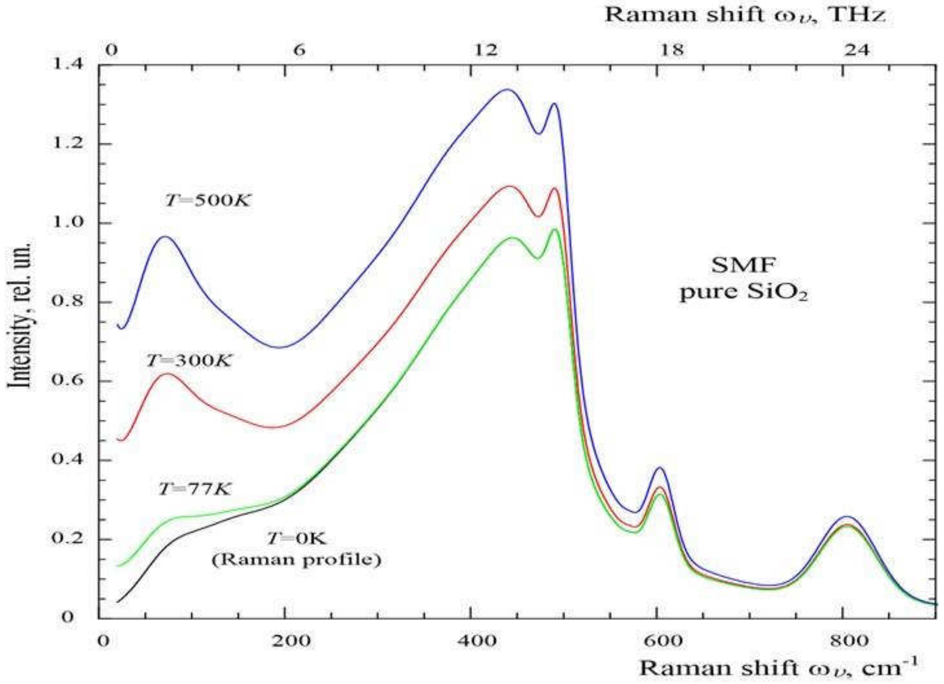

Fig. 2.15. The scattering cross-section in the spontaneous Raman spectra as a function of temperature and Raman gain profile corresponding to zero Kelvin cross-section $\sigma_0(\omega_v)$.

According to Eq.(2.11) the frequency shift $\Omega_\upsilon = \sqrt{\Omega_{0\upsilon}^2 - \Gamma^2}$ with respect to the frequency of a non-dumping oscillator Ω_{0v} will be negligible with $\Gamma << \Omega_{0v}$. However, the shift will be noticeable for highly damped low-frequency oscillations, and with $\Gamma > \Omega_{0v}$ the oscillation completely disappears from the phonon spectrum. At the same time, the difference between the spectra of the Raman scattering and the Raman amplification shown in Fig.2.15 is observed experimentally at least near the room temperature when the pumping power does not exceed several hundred milliwatts.

Note that such pumping regimes for the single-mode fiber are nominal for optical FRA and they are close to the lasing threshold in FRL.

According to Eqs.(2.27) – (2.28) and the data shown in Fig.2.15 the significant difference between the spontaneous Raman spectra and the Raman gain profile in pure SiO_2 fibers, in particular at T = 300 K, should be observed only in the frequency range of the Stokes shift less than 500 cm^{-1}, where the thermal population factor of phonons is considerably greater than one unit. The thermal population factor for Stokes phonons in the higher-frequency region (> 500 cm^{-1}) can lost its frequency dependence. It does not practically differ from one, and therefore the spontaneous Raman spectrum coincides with the Raman gain profile.

Thus the multiple growths of the cross-section $\sigma_T(\omega_v)$ for Stokes shifts less than 200 cm^{-1} regarding to the Raman gain allows detecting the spontaneous Raman scattering, i.e. incoherent Stokes noise in the optical spectrum of silica fiber. On the other hand, this feature of the Raman processes was considered by us as the basis for the method to determine Raman gain profiles by the spontaneous Raman spectra in other types of fibers mainly based on silica glass.

2.2.1.6. Absolute transparency and lasing threshold due to Raman gain in optical fibers

To determine the threshold of Raman gain it is sufficient to consider the simplest case of the interaction between one pumping wave and one Stokes wave. Then, the intensity of both waves in the quasi-continuous approximation and taking into account the slowly changed wave amplitudes during their propagation along the fiber (z coordinate) is described by the system of two coupled equations:

$$\frac{dI_s(z,\omega)}{dz} = g_R(\omega) I_p(z) I_s(z,\omega) - \alpha_s I_s(z,\omega), \tag{2.29}$$

$$\frac{dI_p(z)}{dz} = \frac{\omega_p}{\omega_s} g_R(\omega) I_p(z) I_s(z,\omega) - \alpha_p I_p(z), \tag{2.30}$$

where α_s and α_p is the term taking into account fiber losses at the Stokes and pumping frequencies, respectively; $g_R(\omega)$ is the Raman gain coefficient, I_p is the pump intensity, I_s is the Stokes wave intensity.

Equations (2.29) – (2.30) obtained from Maxwell equations and they have derived by analogy to the Eq. (2.22). It should be noted that the variable frequency ω of both interacting waves is included in Eq. (2.29) and Eq.(2.30) as a parameter. In respect to the frequency dependence of the variable functions and coefficients in these equations we apply the following approximations. The width of the pumping line can be considered infinitely narrow compared to the Stokes radiation band. In other words, the pump remains localized at its frequency ω_p, and $I_p(z,\omega) = I_p(z,\omega)\big|_{\omega=\omega_p} = I_p(z)$. It does not depend on the frequency at any point z along the fiber. In fact, the system of Eqs. (2.29) – (2.30) describes the Raman interaction of monochromatic pumping waves and Stokes radiation.

The wave coupling degree, at any given frequency ω within the irregular continuum of Stokes shifted frequencies, is determined by the values of functions $g_R(\omega) = g_{R\max}\varphi(\omega_\upsilon)$ considering the attenuation of both waves. It is determined by absorption coefficients $\alpha_{s,p} = \alpha_{s,p}(\omega)$. The function $g_R(\omega)$ is shown in Fig. 2.15 at $T=0$ for a single-mode pure SiO_2 fiber. The dependence $\alpha_{s,p}(\omega)$, as a rule, is rather weak. Next, we consider the absorption coefficients α_s and α_p to be constant and they are frequency-independent in Eqs. (2.29) and (2.30).

From Eq. (2.29) one can directly obtain the condition of absolute transparency of the fiber. This corresponds to the lasing threshold of the Raman gain process. Since the pumping power $P_p(\omega)$ may be expressed using the pump intensity $I_p(\omega)$ and the fiber effective area A_{eff}, then the equality $dI_s/dz = 0$ taking into account the inequality ($dP_s(\omega)/dz>0$) gives the following quantitative expression [79]:

$$P_p^{th} = \frac{\alpha_s A_{eff}}{\tilde{g}_R(\omega)} = \frac{\alpha_s}{g_R(\omega)}, \tag{2.31}$$

where $\tilde{g}_R[m/W]$ and $g_R[(W\cdot km)^{-1}]$ is the equivalent form of the Raman gain coefficients referred to the intensity I_p and the power P_p, respectively. The Eq. (2.31) determines the spectral function of the full transparency of the fiber, i.e. $P_p^{th} = P_p^{th}(\omega)$ corresponds to the boundary condition when the material of the fiber core begins its transformation from the natural state with the Stokes wave attenuation to a state in which the Stokes wave is amplified by the pumping power. Usually for P_p^{th} its minimum value at $g_R(\omega_{\max}) = g_{R\max}$ is choosed. The advantages of such a definition of the amplification threshold are as follows.

The value of pumping power P_p can be obtained at a certain point z of the fiber as a result of measurements or calculations. Then, the direct verification of the inequality $P_p > (<) P_p^{th}$ with the known constant α and function $g_R(\omega)$ allow us to determine not only the frequencies in which the condition of full transparency of the fiber is fulfilled but also the amplification (generation) band. This modeling for TiO_2 doped fiber is described in section 2.3.

Thus, using Eq. (2.31) and available experimental data for Raman gain profile $g_R(\omega)$ one can directly calculate the lasing threshold as a function of the frequency (or wavelength) in the region of Stokes shifted frequencies for an arbitrary wavelength of the pumping source. According to Eq.(2.25) and Eq. (2.26) the gain profile $g_R(\omega)$ of a particular oscillatory mode may be described by simple line-form functions, namely by oscillatory (Lorentz) type and/or Gaussian type. However, real fibers have such a complex gain profile that the satisfactory shape of the function $g_R(\omega)$ may be obtained by the special modeling. The multimode decomposition model of the Raman gain profile and the results of its application using Gaussian type components for a number of fibers are described in the next section.

2.2.2. Raman gain in single-mode fibers based on the fused silica

Our analysis of Raman gain profiles is performed using the experimental spectra of spontaneous Raman scattering. A general view of the Raman spectra is shown in Fig.2.16a for single-mode fibers with different dopants in the core, namely for fibers from "pure" SiO_2, for GeO_2, and for TiO_2 doped, as well as for phosphorus-silicate fibers (with P_2O_5 impurities). The Raman spectra in all-optical fibers based on silica glass demonstrate several peaks as a result of the overlapping of strongly extended modes of the oscillating spectrum.

Because of the large difference in the scattering cross-sections, the spectrum of pure SiO_2 in Fig.2.16 for the convenience of comparison with other fiber spectra in particular relatively to GeO_2 doped fiber is shown with amplitude increased by ≈ 8 times. Both types of silica fibers are the most investigated ones and their Raman gain coefficients are well known. Thus, they are used in our work to calibrate the absolute gain values for other types of silica fibers, such as TiO_2 and P_2O_5 doped fibers.

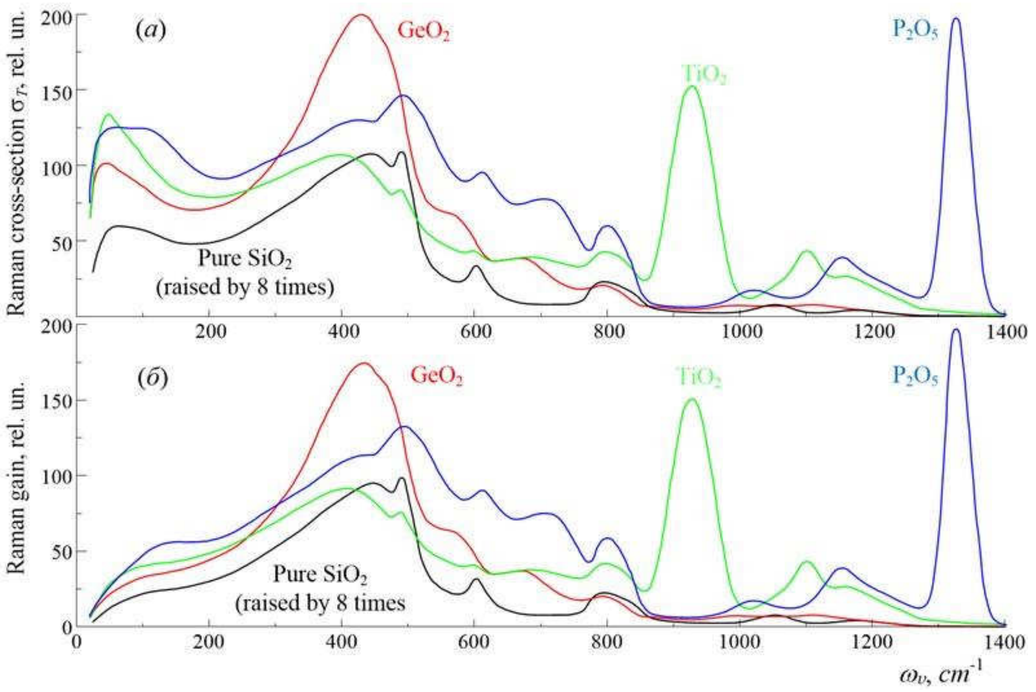

Fig.2.16. Raman spectra (*a*) and Raman gain profiles (***b***) in singlemode fibers based on fused silica.

TiO_2 and P_2O_5 doped fibers are recently developed, when they were considered as an active medium for nonlinear optical amplification. Therefore they are less studied. The advantages of phosphorus-silicate fibers were demonstrated in [10] as an example of cascade FRL generation using a Stokes shift of 1330 cm^{-1} in the molecular vibration spectrum of this fiber core. The application of these fibers may be used for the entire area of Stokes shifts, in particular, the frequency range ~ 500–1500 cm^{-1}. In [10] we analyze in detail the Raman gain profiles for these single-mode fibers in such a wide frequency range of the Stokes shift.

The preliminary theoretical analysis of the Raman scattering processes forms the basis for the direct determination of Raman gain profile from the experimental Raman spectrum, from its part that does not depend on temperature. Then we can use the spectroscopic technique for determination of Raman gain profile in an analytical form. It is based on the multimode decomposition of the complex spectrum in a definite region of Stokes shift frequencies.

Note that the amorphous nature of silica glass significantly complicates the solution of such rather standard spectroscopic problems in almost every case of optical fiber and their general solutions have not been obtained yet. However, we succeeded to find a special solution to this problem in a number of individual cases, in particular, for the case of TiO_2 doped fiber [85]. We obtained an analytical expression for the Raman gain profile in phosphoric silicate fiber, which opens explicit prospects for the utilization of the material as an active medium for fiber nonlinear optics in modern devices.

2.2.2.1. Determination of Raman gain profiles by spontaneous spectra in silica fibers

Our method for the accession of Raman gain profile from the spontaneous spectra is based on the expressions Eq.(2.27) and Eq.(2.28) and on the separation from spontaneous spectra their components corresponding to zero temperature (on Kelvin scale) spectra of their own molecular oscillations. It does not depend on the absolute temperature of the fiber. The results of such processing of spontaneous spectra of all investigated fibers are shown in Fig. 2.16.

The Raman gain profiles differ mainly from the spontaneous Raman spectrum by the significant decreasing in the absolute intensity of low-frequency components due to the spectral distribution of the Bose factor of the phonon population Eq.(2.6).

Indeed at the frequency corresponding to the wavenumber of 20 cm^{-1} the spectral density of spontaneous noise is 11 times larger than the Raman gain at T = 300K. This difference between Raman gain profiles and the spontaneous spectra becomes ~ 13-14% at the frequency~ 440 cm^{-1}, where Raman gain coefficients reach their maximum for pure SiO_2 and GeO_2 doped fibers. Moreover, the ratio of the spectral density of the Stokes noise to the Raman amplification decreases below 1% level only at frequencies exceeding 880 cm^{-1} at room temperature. Therefore, the absolute maxima of the Raman gain coefficients for TiO_2 and P_2O_5 doped fibers (located at frequencies of 930 cm^{-1} and 1330 cm^{-1}, respectively), are practically coincided with the values of the differential Raman cross-section at least for typical surrounding temperatures $T \leq 300K$.

The normalized Raman gain profiles separated from the experimental spontaneous spectra for the Stokes shift region of 0–1400 cm^{-1} (0–42 THz) are shown in Fig. 2.17 for SMF fabricated from silica glass: *a* – for pure SiO_2; *b*, *c*, *d* – for GeO_2, TiO_2 and P_2O_5-doped fibers, respectively. The values of the gain coefficients at the maximum frequency points of the Raman profile were obtained in [80], namely g_{Rmax}= 0.4 $(W\times km)^{-1}$ for pure SiO_2 and g_{Rmax}= 6.3 $(W\times km)^{-1}$ for specialized Raman fiber with the GeO_2 dopant concentration in the core up to 25%. We supplemented the data of work [68] by extending the Stokes shifts region up to 1400 cm^{-1} as it is shown in Fig.2.17*a*,*b*.

The estimation of g_{Rmax} values for TiO_2 and P_2O_5 doped fibers was performed by comparison of the absolute intensity of main spectral components in the experimental Raman spectra because they are unambiguously related to the corresponding Raman gain profiles.

According to this estimation, g_{Rmax}= 4.8 (W×km) $^{-1}$ is achieved at Stokes shift frequency of 930 cm^{-1} for TiO_2 doped fiber. In P_2O_5 doped fiber, the maximum value of Raman gain coefficient according to data [11] reaches 90% of the gain in GeO_2-doped fiber and therefore should be equal to $g_{Rmax} = 5.7$ $(W×km)^{-1}$ at the Stokes shift frequency ω_{max} = 1330 cm^{-1}.

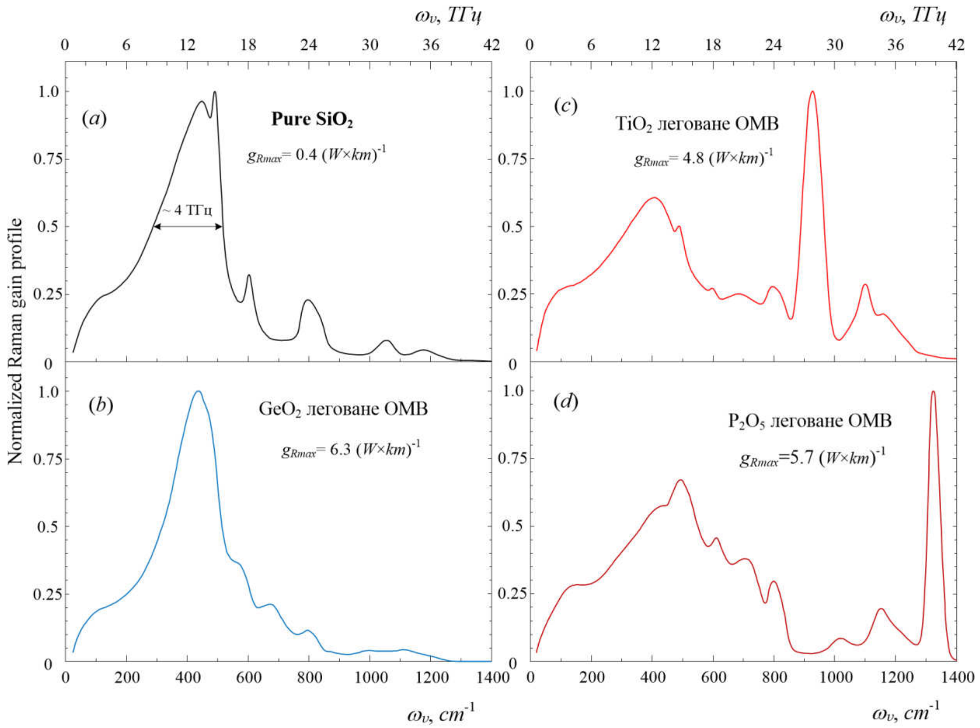

Fig.2.17. Normalized Raman gain profiles of silica fiber in the Stokes shift region 0–1400 cm^{-1} (0–42 THz)

The absolute value of g_{Rmax} together with the normalized Raman gain profiles unambiguously determines the magnitude of the nonlinear signal gain at the given point of the Stokes shift band. Despite the listed numerical values of g_{Rmax} can vary slightly depending on the technological fiber features affected on their effective area. The estimations allow us to obtain a quantitative representation about the nonlinear-optical properties of the fiber core of the investigated silica glass and its chemical composition.

All Raman gain profiles shown in Fig.2.17 can be conventionally divided into two almost equal spectral regions. The first one is from 0 to 700 cm^{-1} . It contains the main maxima of Raman gain from the base material of the fiber core, i.e. the silica glass. The second region is from 700 cm^{-1} to 1400 cm^{-1} can be assigned to the dopant oscillatory spectrum since its small intensity of Raman bands can be observed in both pure SiO_2 and in the standard GeO_2 strongly doped fiber. In contrast, the bands contained the Raman gain maximum in the other two samples: TiO_2 and P_2O_5 doped fibers are located in the second, i.e. impurity region. However, both impurities TiO_2 and P_2O_5 simultaneously considerably perturb the phonon spectrum in the first low-frequency region too. The absolute intensity of these molecular vibrations increase by several times compared with pure SiO_2.

Because of the irregularity of the quasi-continuous vibrational spectrum and the "diffuse" nature of Raman lines as their width may exceed 100 cm^{-1} with a strong overlap in Raman spectra of silica glass, the special methods of spectroscopic modeling of Raman gain profile have to be used. The simulation basis represented by the theory, described in Sec.2.1 use the following: the Stokes shift frequencies in the Raman process are placed within the line of spontaneous Raman scattering from each of the oscillatory modes of the fiber core material.

2.2.2.2 Multimode decomposition of Raman gain profiles

The reliability of the multimode decomposition method for Raman gain profiles is proved by the several formation peculiarities of phonon spectra in different types of glass noted in many papers [9–11,82,83]. In particular, although the profile of the refractive index changes in the fiber core repeats the distribution of the dopant concentration the Raman gain spectra of the germanosilicate fibers, the spectra are not a simple mixture of the spectra of pure SiO_2 and germanium glass GeO_2 [80]. The essential deformations of Raman gain profiles in one glass type relative to the other type are observed in practice. It indicates a significant change in all the vibration parameters: amplitude, frequency position and damping constant. Moreover, Raman gain coefficients of some germanosilicate composites can significantly exceed the values obtained for both pure components of this glass.

The significant expansion of oscillatory spectrum bands of molecular oscillations of more than 100 cm^{-1} is typical for materials based on amorphous glass. Thus, the Stokes region in each fiber is converted into a regular continuum (Fig.2.16 and Fig.2.17). Therefore it practically impossible to split into the frequencies of individual oscillating modes. The analysis of the spontaneous Raman spectra of pure SiO_2 in the Stokes region between 0 and 900 cm^{-1} was presented in [82]. Authors found at least 10 separate components by the careful analyzing the observed spectrum features as the maxima positions, slopes and pedestals available in the spectrum and these components were classified as Gaussian type. The decomposition into Gaussian components in pure SiO_2 fiber core was performed for Raman gain profile in the Stokes shift region up to 1400 cm^{-1}.

The oscillatory dynamics of molecular nanocomplexes of the amorphous fiber core is in the formation basis of Raman gain profiles. Thus, the profiles can be modeled as a system of harmonic oscillators forced by the external and rather powerful pumping wave. In the Eq. (2.28) the frequency dependence of the effective area A_{eff}^{ps}, the refractive index n_p, and also the dependence of the Raman gain coefficient g_R on the Stokes wavelength λ_s are neglected. Rather weak and monotonic dependence of g_R on the pumping frequency just on the Stokes wavelength is often referred to Raman gain scaling by the pumping wavelength [70]. It can be obtained from the spectroscopic simulation of Raman gain profile. In fact, the main frequency dependence in Raman gain profile is due to imaginary part of the nonlinear polarizability $\chi^{(3)}$ Eq.(2.23) namely by the resonant denominator Eq.(2.19) in the phonon harmonic oscillator. The oscillating mode lineform can be described using the form factor Eq.(2.25) or the Gaussian function Eq.(2.26).

The physical sense of the Gaussian decomposition procedure of the Raman gain spectrum is substantiated by the amorphous of the core material in all investigated fibers. Due to the amorphous nature of both fused silica and other fibers, each dumped oscillator Eq.(2.11) with a resonance of the vibrational coordinate $\vec{Q}$ at the frequency Ω_υ [according to Eq.(2.16)] has an arbitrary orientation relative to its neighbors and it introduced stochastic perturbations to this oscillator frequency. As a result, we should expect the formation of a Gaussian profile for the superposition of a large number of narrow spectral maxima with a normal distribution of random values of these oscillators frequencies. Therefore, we have decomposed all Raman gain profiles into several spectral components of Gaussian type:

$$g_R(\omega) = g_{R\max} \cdot \sum_{i=1}^{N_m} A_i \exp\left[-(\omega-\omega_{v,i})^2 / \Gamma_i^2\right] = g_{R\max} \cdot \varphi(\omega) \qquad (2.32)$$

where $\varphi(\omega)$ is the analytic function from the frequency ω, corresponding to normalized Raman gain profile, $g_{R\max}$ is the maximum value of the Raman gain coefficient; N_m is the number of components; A_i and $\omega_{v,i}$ is the amplitude and central frequency *i-th* Gaussian component, respectively. $\Gamma_i = \Delta\omega_i / (2\sqrt{\ln 2}) \approx 0,6\Delta\omega_i$, where $\Delta\omega_i$ is the full width at half of the maximum for the *i-th* Gaussian profile, which is usually used in spectroscopy.

The main task of the decomposition is to achieve the best fitting of the form factor $\varphi(\omega)$ to the experimental Raman gain profile of each fiber presented in Fig.2.17*a-d*. The problem in practice was solved by finding an optimal set of $3\times N_m$ parameters from Eg.(2.31) using the computer procedure of nonlinear approximation by the Levenberg-Marquardt method.

This method uses the algorithm to search for the minimum sum of the least squares by the method of rapid descent to quadratic minimization of deviations of experimental points from the function $\varphi(\omega)$ defined by Eq.(2.32). With the proper choice of the initial approximation, this method allows us to obtain very good practical results in approximating Raman amplification spectrum throughout Stokes shift frequency range from 0 to 1400 cm^{-1}.

The numerical values of multicomponent decomposition parameters are presented in Table 1 and the approximation accuracy of experimental profiles for all 4 SMF types is demonstrated in Figs.2.18-2.21.

The decomposition procedure is represented with two aspects: fundamental and applied, taking into account these formation features of rather complex Raman gain profiles in amorphous fibers. At first, it is the spectroscopic aspect and the decomposition is considered as a possible method to divide the density of oscillatory states of molecular nanocomplexes into well-defined contributions. In the second applied aspect of decomposition the goal is set up the possibly simplest function $g_R(\omega)$ corresponding to the experimental Raman gain profile with maximum precision.

The numerical data of the spectroscopic decomposition are presented in Table 1. They can serve as interpretation basis of the phonon spectra peculiarities of the fiber cores forming the Raman gain profiles. For example, all Raman bands (in Fig.2.18) in pure SiO_2 with frequencies less than 1053 cm^{-1} or 1180 cm^{-1} belong mainly to fundamental one-phonon oscillations [70]. The area of multi-phonon overtones and composite tones extends from the line with a frequency of 1180 cm^{-1} or 1460 cm^{-1} to a frequency of 2600 cm^{-1} and above. It remains unclear whether the 1180 cm^{-1} line is one- or two-phonon state.

The main asymmetric maximum of the Raman gain in the pure SiO_2 (Fig.2.18) at frequency 440 cm^{-1} is formed according to our data from at least three of the most intense Gaussian components indicated in Table 1 as G3 $\rightarrow$ 359 cm^{-1}, G4 $\rightarrow$ 408 cm^{-1} and G5 $\rightarrow$ 465 cm^{-1} with dumping constants of 182 cm^{-1}, 68 cm^{-1} and 49 cm^{-1}, respectively.

Table 1. Results of multimode decomposition of Raman gain profiles in silica fibers. The parameter $\delta = (I_G - I_0)/I_0 \cdot 100\%$ is presented to evaluate of the approximation accuracy, where I_G and I_0 are the corresponding integral intensities of the calculated and measured Stokes spectra.

mode no.	Pure SiO_2			GeO_2			TiO_2			P_2O_5		
	A	ω_v, cm^{-1}	Γ, cm^{-1}	*A*	ω_v, cm^{-1}	Γ, cm^{-1}	*A*	ω_v, cm^{-1}	Γ, cm^{-1}	*A*	ω_v, cm^{-1}	Γ, cm^{-1}
1	0.07	71	39	0.04	48	25	0.11	67	38	0.05	72	35
2	0.12	128	67	0.09	89	53	0.13	130	75	0.13	131	67
3	0.54	359	182	0.18	179	102	0.53	381	215	0.53	437	268
4	0.25	408	68	0.49	360	119	0.09	418	56	0.04	410	31
5	0.35	465	49	0.68	448	80	0.07	493	14	0.17	502	47
6	0.32	496	17	0.08	481	21	0.03	599	16	0.11	618	31
7	0.01	571	8	0.25	573	43	0.19	712	94	0.21	716	55
8	0.16	605	19	0.21	670	71	0.21	811	41	0.21	810	32
9	0.06	625	336	0.09	796	48	1.01	928	44	0.08	1025	63
10	0.18	806	43	0.04	996	175	0.13	1097	26	0.19	1159	53
11	0.07	1053	39	0.02	1133	81	0.17	1135	115	0.08	1240	32
12	0.04	1180	60				0.02	1173	20	1.02	1329	27
	$\delta=0.6 \cdot 10^{-4}$ %			$\delta=0.04$ %			$\delta=0.3$ %			$\delta=0.1$ %		

The second peak of Raman gain in pure SiO_2 at frequency ~ 495 cm^{-1} (Fig.2.18) is formed by a rather stable corresponding phonon mode G6 with dumping constant equal to 17 cm^{-1} (~ 50 GHz). It should be noted that the lifetime of this oscillation almost an order of magnitude longer than the lifetime of its neighboring modes. This allows maintaining stable synchronization conditions Eg.(2.9) required for coherent amplification of the Stokes wave in the single-pass Raman amplification process. This may be an argument to explain the results of previous experiments [72] where the maximum of single-pass amplified Stokes wave is observed just at 495 cm^{-1} frequency of Stokes shift with the pulse pumping of kilowatt power.

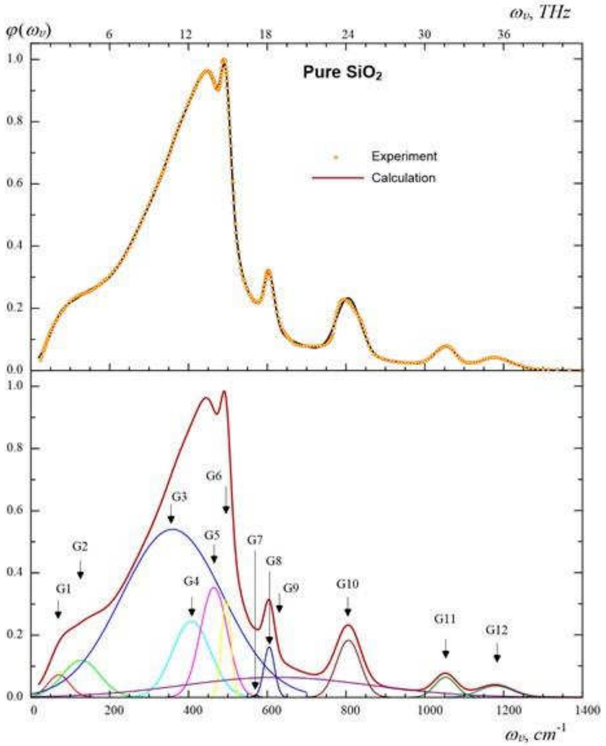

Fig.2.18. The decomposition results of Raman gain profile in the pure silica fiber in the Stokes shift region 0–1400 cm^{-1} (0–42 THz).

The gain profile (Fig.2.19) in Raman fiber (doped with ~ 25% GeO_2) notably differs from the profile (Fig.2.18) in pure SiO_2 and Gaussian components were sufficient for its decomposition. The main deformation of Raman gain profile is due to the sharp increase in the relative intensity of mode G5 → 448 cm^{-1} . This can be explained as a result of the coupling of two separate modes G4 and G5 observed in the spectrum of pure SiO_2. This is confirmed by the average value of oscillation frequency and the extension of the entire band.

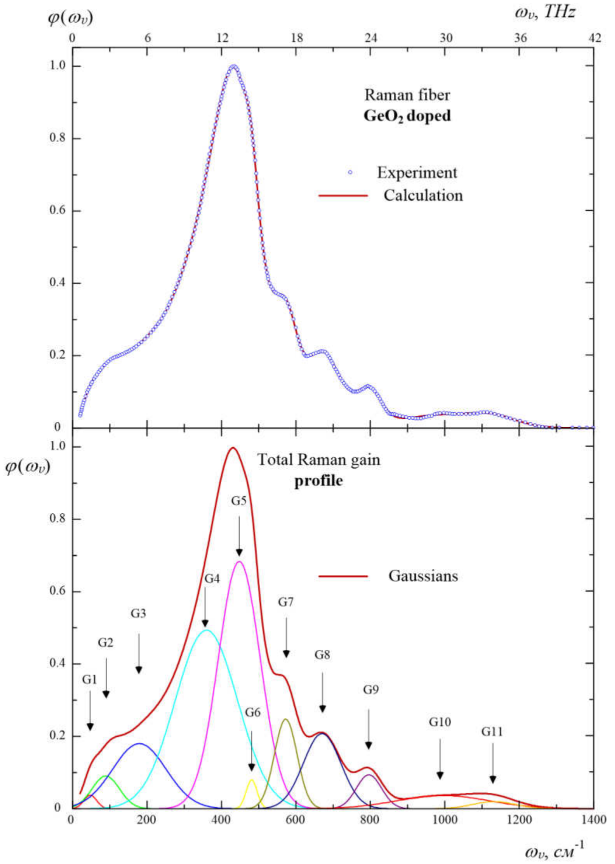

Fig.2.19. 11-modes decomposition of Raman-gain profiles in germanosilicate fiber in the Stokes shift region 0–1400 cm^{-1} (0–42 THz).

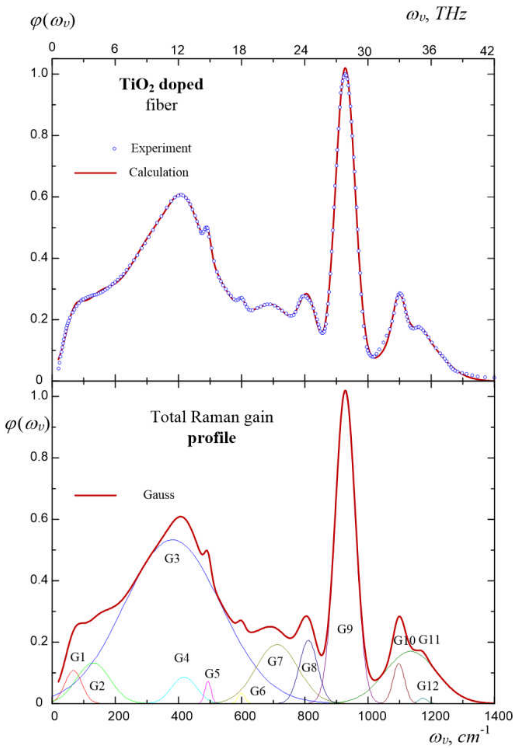

Fig.2.20. 12 modes decomposition of Raman-gain profiles in TiO2 doped fiber in the Stokes shift region 0–1400 cm^{-1} (0–42 THz).

The narrow 481 cm^{-1} line becomes more damped, its frequency is lowered on 15 cm^{-1}, the relative intensity is reduced by 4 times, and therefore this mode slightly affects the spectral profile. The low-frequency profile slope is formed by two main components G3 $\rightarrow$ 179 cm^{-1} and G4 $\rightarrow$ 306 cm^{-1} with dumping constants of 102 cm^{-1} and 119 cm^{-1}, respectively. The result of such profile rearrangement with GeO$_2$ dopants in the fiber core is separate and rather wide maximum in the 410--450 cm^{-1} region with a simultaneous notable increase in the value g_{Rmax}.

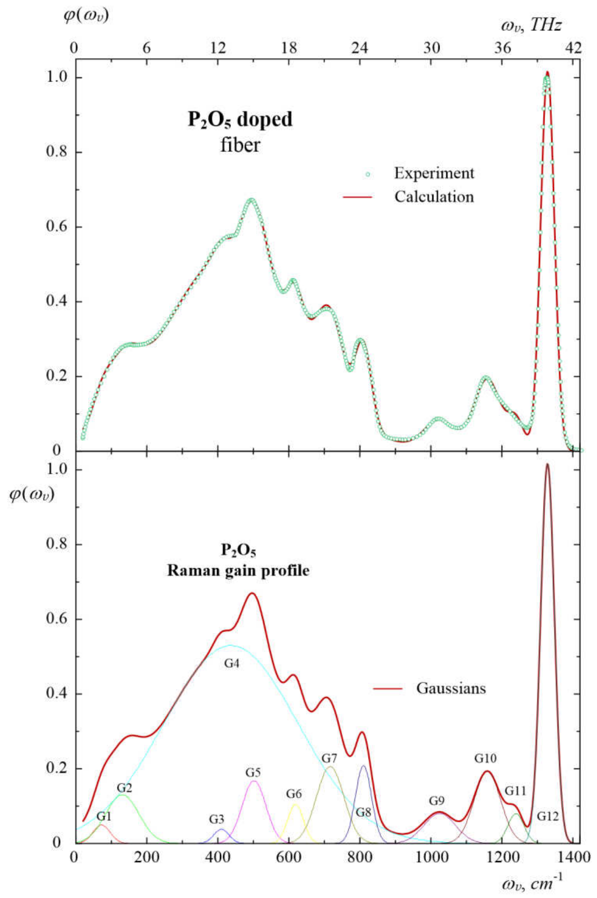

Fig.2.21. Decomposition of Raman-gain profiles in P_2O_5 doped fiber in the Stokes shift region 0–1400 cm^{-1} (0–42 THz).

Raman gain profile in TiO_2 doped fiber together with 12 Gaussian components of its decomposition are shown in Fig.2.20. The most powerful oscillatory mode G9 → 928 cm^{-1} with dumping constant of 44 cm^{-1} is located in the impurity region of Stokes shifts. Relatively slight dumping, as for amorphous materials, reflects relatively large transparency of TiO_2 doped glass for the propagation of optical phonons at frequencies $\omega_\upsilon = 930\ cm^{-1} = 28$ THz. On the other hand, the full width of this band of Raman gain is greater than 2 THz. This is enough for many applications. In addition, the phonon spectrum of the glass matrix is noticeably rebuilt by the impurities and its structuration consists in the formation of a powerful oscillatory mode G3 → 381 cm^{-1} with dumping constant equal to 215 cm^{-1}. As a result, the Raman gain coefficient is much higher compared to pure SiO_2 in the actual Stokes shift area from 100 cm^{-1} to 600 cm^{-1} (3–18 THz).

The result of the decomposition of Raman gain profile in P_2O_5 doped fiber is shown in Fig.2.21. The influence of the P_2O_5 impurity on the formation of Raman gain profile in silica glass has a lot of similarities to features obtained for TiO_2 with certain quantitative differences. The main maximum of Raman gain coefficient is provided by the oscillating mode G12 $\to$ 1329 cm^{-1} with dumping constant equal to 27 cm^{-1}. According to our data, the significant contribution to Raman gain in the domain of the own phonon spectrum of the glass matrix gives mode G4 $\to$ 437 cm^{-1} with dumping constant equal to 268 cm^{-1}. This significantly expands the spectral range of applications of P_2O_5 doped fiber.

In general, the determination of the dumping constant Γ_i for all Gaussian components allows us to quantitatively estimate the damping degree and the lifetime of molecular vibrations because they determine the shape of the Raman spectrum in the doped glass. A common feature of all fibers based on silica glass is the presence of fundamental vibrations with a damping constant $\Gamma_i \sim 100$ см$^{-1}$ = 3 THz. Consequently, the attenuation of the principal oscillatory modes, forming the Raman gain profiles in the fibers, gives the value of the characterized time $\tau_i \simeq 1/\Gamma_i \simeq 0{,}3\cdot 10^{-12}$ s for the renewal time of the thermodynamic equilibrium or the transients time for Raman amplifiers and lasers. On the one hand, the femtosecond scale of the relaxation time of the Raman processes provides the possibility of the practical use of FRA and FRL in the terahertz band of operating frequencies. On the other hand, this time interval specifies the limits of the applicability of the quasi-stationary approximation, and, consequently, Eqs. (2.29) – (2.30) for the simulation of telecommunication systems with terabit carrying capacity.

However, the presence of a large number of vibrational modes that strongly overlap does not practically allow directly to separate the Raman bands in the experimental spectrum in all investigated objects. It does not complicate the computational procedure due to the possibility of an unambiguous interpretation of the obtained results. With the proper choice of the initial approximation for the decomposition using 10-15 Gaussian components the convergence of the Levenberg – Marquard method is provided in real-time and it does not require any extraordinary computational resources. However, the optimal set of decomposition parameters obtained as a result of the calculations cannot be guaranteed as the only possible set.

In spite of the decomposition uncertainty may cause certain complications in the fundamental interpretation of the vibrational states of molecular complexes, it practically does not affect the applied aspect of the presented calculations. It should be noted that the overwhelming majority of experimental points of the measured spectrum are directly placed on the approximation curves of all Raman gain profiles. Moreover, the deviation of the calculated curves $g_{R\max}$ from φ (ω) exceeding 1% have only individual unit points of the experimental spectrum at small values of g_R. From the point of view of the application of the presented model, we can assume that the approximation is practically exact, since the mean square deviation is about an order of magnitude smaller than the typical measurement accuracy and spectral processing, as it can be seen from the comparison of the data depicted in Fig.2.18–2.21, respectively.

Indeed the ratio of the integral intensities of the calculated I_G and the measured I_0 Stokes spectrum $\delta = (I_G - I_0)/I_0 \cdot 100\%$ given in Table 1 is significantly less than 1% for all investigated fibers. All integration of functional dependencies for data in Table 1 was performed in the range from 0 to 1400 cm^{-1}.

Note that the determination of accuracy of the Raman gain profiles will be of fundamental importance in the simulation of the Raman photonic devices. For example, it describes the telecommunication systems containing 192 channels with wavelength division [49] or even 273 channels [50] and it may have the pumping source with more than 10 wavelengths. Consequently, the system of Eqs. (2.29) – (2.30) becomes a system for several hundred Stokes waves with a dozen pumping waves. In addition the correlation between the coefficients of amplification and attenuation in form Eq. (2.31) will determine the singular points in which the fundamental solution of each differential equation changes fundamentally. Therefore, regardless of the solution algorithms of such complex systems, any systematic errors in the definition of $g_R(\omega)$ cause various kinds of calculations instability and they are becoming simply unacceptable. In particular, this explains the unsatisfactory results of the simulation of multichannel FRA systems in the case of neglecting the frequency dependence $g_R(\omega)$ or its approximation by the very simple functions of the triangle type.

Thus, the spectral Raman gain profile is a key parameter for describing the process of Raman light amplification and its determination forms the fundamental basis for the design of both high-performance FRAs and FRLs with a band expanded up to 13 THz in the most common fibers based on silica glass.

2.2.3. Simulation results of the Raman gain profile and their application

First of all, we note that in the literature (see [11]), the Raman gain coefficient is sometimes given in dB/(W·km) and its numerical terms differ from the above introduced $g_R(\omega)$. The value g_0 is calculated as:

$$g_0\left[dB/\left(km \cdot W\right)\right]=\frac{G\left[dB\right]}{L_{eff} \cdot P} \tag{2.33}$$

by the measured value of the so-called on/off gain, G [dB], of the weak signal (the ratio of the signal power between the on pumped and off pumped states). Here P is the pump power, and effective fiber length $L_{eff} = [1 - \exp(-\alpha_p L)]/\alpha_p$, where α_p is the optical fiber loss on the pumping wavelength.

Since for large L, the relation $\alpha_p L >> 1$, then $L_{eff} \simeq 1/\alpha_p$. Note that the Eq. (2.33) is based on the weak signal assumption. It is actually used an approximate solution of the system Eqs.(2.28)–(2.29) for a fixed pump when the pump power depletion is neglected [68]. Furthermore the measured values of g_0[dB/(km·W)] are dependent not only on their own Raman gain, but also on additional linear parameters for pump power, optical fiber losses over pumping wavelength, and so on. Therefore, it is often necessary (except the recalculation from g_0 into g_R) to take into account the corrections for above restrictions for accurate use of g_0[dB/(km·W)] term in the simulation of optical waveguide gain processes, in particular when the system of Eqs.(2.28) – (2.29) is used. The invariance of the profile $g_R(\omega)$ with respect to the linear fiber parameters and the pumping features, allows more suitable simulation for the Raman photonic devices.

The most significant differences between the spontaneous and stimulated Raman spectra in the low-frequency Stokes shift region as were discussed in detail (see sec.2.1.5) are very useful for experimental studies of FRA noise parameters. In particular, amplified spontaneous emission has been analyzed in idle mode FRA (without an external optical signal) [86], [87] and the mixture of amplified and spontaneous noise is observed at the output of the investigated fiber. When the pump power is increased, an exponential growth in the amplified noise over a non-coherent Stokes noise background independent of pumping is observed. By a careful analysis of the deformation of the noise spectra under the pumping influence, we separate the coherent amplified Raman noise from the background of spontaneous Stokes noise as this discussed in more detail in [88], [89].

On the other hand, the extremely wide frequency band of the single Raman gain profile, such us for pure SiO_2 is ~ 4 THz = 130 cm^{-1} (Fig.2.17a) represents the basis of modern technology for FRA design with a unique wide band of operating frequencies. Using pumping on several wavelengths high-quality FRA of light in the band exceeding 10 THz with a very low level of noise was demonstrated [77], [90]. The completely fiber-based implementation of 10 FRL is presented in [90] where 6λ FRL provides uniform amplification of Stokes waves in C + L transparency windows and the internal resonator on the fiber Brag's grating in the Raman (GeO_2-doped) fiber performs a 4-fold Stokes conversion on ~420 cm^{-1} of the pumping wavelength from 1100 nm to 1347 nm. A certain alternative to GeO_2 doped fiber, in our opinion, can form a fiber with TiO_2 dopant [85].

Fig.2.22 shows the modeling results of full transparency function Eq.(2.31) in TiO_2 doped fiber at $\lambda_p = 1.35$ μm. These results demonstrate the possibility of forming several lasing areas. In particular, at relatively low pumping power equal to $P_p = 18$ dBm it is possible, as one can see in Fig.2.22 to form at least four bands of laser generation across the wavelength range from 1.37 μm to almost 1.6 μm. Note that such wide tuning range of the FRL generation line almost twice exceeds the band of standard Raman fiber, mainly due to the impurity domain on the Raman gain profile in TiO_2 doped fiber.

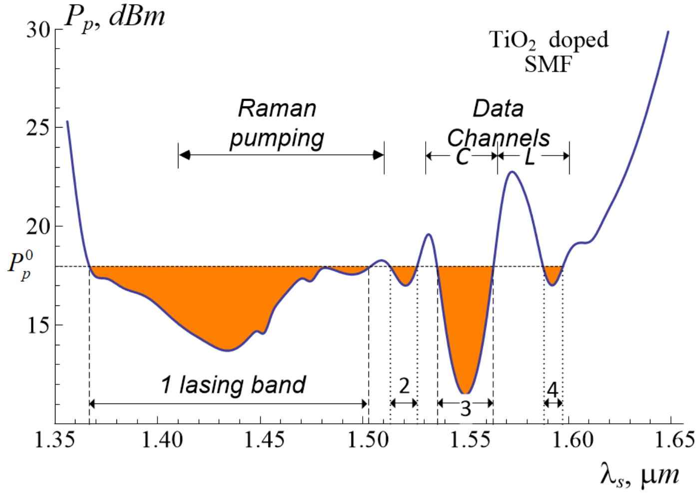

Fig.2.22. Four lasing bands are formed in TiO_2 doped fiber at $\lambda_p = 1.35$ μm and pumping power P_p = 18 dBm

From the practical point of view, the obvious advantages of TiO_2 of doped fibers include the possibility of obtaining a laser generation both at the FRA pumping wavelengths and the carrier information signals in the transparency windows of the telecommunication fibers.

Several application examples of the doped single-mode fibers as FRA active media are given in [10]. The output power (in a fiber Raman laser with a Bragg gratings resonator using phosphor silicate fiber with the content of P_2O_5 of 13% molecular weight (Δn = 0.011) and the 200 m length) was 2.3 W at λ_s = 1240 nm with a pump power of 3.5 W on 1.06 μm (Nd^{3+}). Hence the quantum efficiency was realized equal to 77% using Stokes shift frequency of 1330 cm^{-1}. Simultaneously, there are even more important applications, as indicated data in Fig. 2.17 for the Raman gain profiles in doped fibers for both multiwave FRL and for ultra-wideband Raman amplification of optical signals.

Conclusions

Spectroscopic features of Raman gain profiles in four types of single-mode fibers based on silica glass are analyzed by their extraction from the experimental spontaneous spectra with successful multimode decomposition using Gaussian type components. The method's justification is based on the oscillatory model of the Raman active vibrations of molecular nanocomplexes in amorphous glass taking into account both quantum and semiclassical approaches. It is shown that the temperature changes of the Raman spectra are concentrated in the low-frequency region. The spontaneous spectral density is more than an order of magnitude larger than the corresponding components of the Raman gain profile at frequencies $\leq 20\ cm^{-1}$. However, their difference became practically invisible at frequencies above 800 cm^{-1}.

It has been found that the nonlinear spectrum of the Raman amplification is strongly excited by alloying dopants, at least one order of magnitude larger compared with the changes of linear parameters of the fiber's core, because the corresponding changes in the refractive index are $\Delta n \simeq 0.01$. The Raman gain profiles are strongly deformed due to the significant restructuring of the vibrational spectra of molecular nanocomplexes of fibers cores under the influence of relatively small dopant concentrations. As a result of the Gaussian decomposition using 12 components in pure SiO_2, P_2O_5 and TiO_2, and using 11 components in GeO_2 doped fiber. It has been found (when forming the Raman gain profiles) that the main vibrational modes of the glass matrix in the fibers are considerably varied over all oscillation parameters. These changes variate several times in amplitude and they are in the range of a few tens of cm^{-1} at definite frequency and damping constant. Therefore, the average value of the relaxation time,τ_i, of the stimulated Raman processes is equal to about 300 fs. Firstly, this provides the possibility of practical use of Raman amplifiers and light generators in the terahertz band of operating frequencies. Secondly, such a femtosecond time interval indicates the fundamental limit of the quasi-stationary approximation applicability, namely, for the basic coupled equations described the nonlinear wave interactions in Raman effect for the modeling of telecommunication systems with terabit capacity.

The decomposition allows us to obtain an almost exact approximation for the experimental data. It provides a reliable basis for calculating the main FRA parameters. A simple analytic form of approximating functions in the form of a linear combination of exponential functions is an essential advantage of the presented method. It may be useful for the gain parameters modeling, in particular for determining the spectral density of optical noise, for lasing bands definition using given pumping parameters, for optimizing the size of the group delay in the multiwave pumped FRAs and for the design of advanced devices.

The work was performed with partial financial support from the Ministry of Education and Science of Ukraine (Reg No 0116U002564) during the implementation of the budget theme №16БФ052-04 at the Kyiv Taras Shevchenko National University.

References

1. G. Landsberg, L. Mandelstam. Eine neue Erscheinung bei der Lichtzertreuung. Naturwissenschaften. B. 16, 557 (1928).
2. G. Landsberg, L. Mandelstam. New light scattering phenomenon (preliminary announcement). Journal of the Russian Physico-Chemical Society. Part physical. 60, 335–338 (in russian) (1928).
3. G. S. Landsherg, L. I. Mandelstam. Über die Lichtzerstrenung in Kristallen. Zs. Phys. B. 50, 769 (1928).
4. C.V. Raman, K. S. Krishnan. A New Type of Secondary Radiation. 121, 501 (1928).
5. C.V. Raman. A Change of Wave-laugh in Light scattering. Nature. 121, 619 (1928).
6. C. V. Raman, K. S. Krishnan. The Optical Analogue of the Compton Effect. Nature. 121, 711 (1928).
7. C. V. Raman, K. S. Krishnan. The Negative Absorption of Radiation. Nature. 122, 12 (1928).
8. C. V. Raman. A new radiation. Ind. J. Phys. 2, 387 (1928).
9. P. A. Korotkov, G. S. Felinskyi. Fiber Raman CW lasers. Ukr. J. Phys. Rev. 3, N2, 126–150 (in ukrainian) (2006).
10. E. M. Dianov and A. M. Prokhorov. Medium-power CW Raman fiber lasers. IEEE J. Sel. Top. Quant. Electr. 6, N6, 1022–1028 (2000).
11. E. M. Dianov. Advances in Raman Fibers. J. Lightwave Techn. 20, N8, 1457–1462 (2002).
12. P. D. Dragic, M. Cavillon, and J. Ballato. Materials for optical fiber lasers: A review. Appl. Phys. Rev. 5, 041301 (2018).
13. W. Shi, Q. Fang, X. Zhu, R. A. Norwood, and N. Peyghambarian. Fiber lasers and their applications. Appl. Opt. 53, 6554–6568 (2014).
14. D. J. Richardson, J. Nilsson, and W. A. Clarkson. High-power fiber lasers: current status and future perspectives. J. Opt. Soc. Am. B27, B63–B92 (2010).
15. M. N. Zervas and C. A. Codemard. High power fiber lasers: a review. IEEE J. Sel. Top. Quantum. Electron. 20, 219–241 (2014).
16. P. Zhou, H. Xiao, J. Leng, J. Xu, Z. Chen, H. Zhang, and Z. Liu. High-power fiber lasers based on tandem pumping. J. Opt. Soc. Am. B34, A29–A36 (2017).
17. P. Ma, H. Zhang, L. Huang, X. Wang, P. Zhou, and Z. Liu. Kilowatt-level near-diffraction limited and linear-polarized Ytterbium-Raman hybrid nonlinear

amplifier based on polarization selection loss mechanism. Opt. Express. 23, N20, 26499–26508 (2015).

18. E. M. Dianov, I. A. Bufetov, M. M. Bubnov, et. al. Three-cascaded 1407-nm Raman laser based on phosphorus-doped silica fiber. Opt. Lett. 25, N6, 402–404 (2000).
19. A. A. Demidov, A. N. Starodumov, X. Li, A. Martinez-Rios, H. Po. Three-wavelength Raman fiber laser with reliable dynamic control. Opt. Lett. 28, N17, 1540–1542 (2003).
20. Z. Xiong, N. Moore, Z. G. Li, and G. C. Lim. 10-W Raman fiber lasers at 1248 nm using phosphosilicate fibers. J. Lightwave Techn. 21, N10, 2377–2381 (2003).
21. E. M. Dianov, et al. CW bismuth fibre laser. Quantum Electronics. 35, N12, 1083–1084, http://dx.doi.org/10.1070/QE2005v035n12ABEH013092 (2005).
22. M. Tan, P. Rosa, S. T. Le, Md. A. Iqbal, I. D. Phillips, and P. Harper. Transmission performance improvement using random DFB laser based Raman amplification and bidirectional second-order pumping. Opt. Express. 24, 2215–2221, DOI:10.1364/OE.24.002215 (2016).
23. L. E. Nelson, X. Zhou, B. Zhu, M. F. Yan, P. W. Wisk, and P. D. Magill. All-Raman-amplified, 73 nm seamless band transmission of 9 Tb/s over 6000 km of fiber. IEEE Photon. Techn. Lett. 26, 242–245 (2014).
24. Q. Xiao, P. Yan, D. Li, J. Sun, X. Wang, Y. Huang, and M. Gong. Bidirectional pumped high power Raman fiber laser. Opt. Express. 24, N6, 6758–6768 (2016).
25. Y. Feng, L. R. Taylor, and D. B. Calia. 150 W highly-efficient Raman fiber laser. Opt. Express 17, N26, 23678–23683 (2009).
26. M. Rini, I. Cristiani, and V. Degiorgio. Numerical modeling and optimization of cascaded CW Raman fiber lasers. IEEE J. Quant. Electr. 36, N10, 1117–1122 (2000).
27. S. D. Jackson and P. H. Muir. Theory and numerical simulation of nth-order cascaded Raman fiber lasers. J. Opt. Soc. Am. B. 18, N9, 1297–1306. (2001).
28. S. D. Jackson. Theoretical characterization of Raman oscillation with intracavity pumping of fiber lasers. IEEE J. Quant. Electr. 37, N5, 626–634 (2001).
29. I. Syuaib, M. Asvial, and E. T. Rahardjo. Modeling of ultra-long span bidirectional Raman transmission link using three-segment hybrid fiber core structure. Photonics 6. 18, doi:10.3390/photonics6010002 (2019).
30. W. S. Pelouch. Raman amplification: An enabling technology for long-haul

coherent transmission systems. J. Lightwave Technol. 34, 6–19 (2016).

31. R. G. Waarts, A. A. Friesem, E. Lichtman, et. al. Nonlinear effects in coherent multichannel transmission through optical fibers. Proc. IEEE. 78, N8, 1344−1368 (1990).
32. A. R. Chraplyvy. Limitations on lightwave communications imposed by optical-fiber nonlinearities. J. Lightwave Techn. 8, N10, 1548−1557 (1990).
33. M.-S. Kao, J. Wu. Extending transmission distance of high-density WDM systems using post transmitter fiber Raman amplifiers. J. Lightwave Techn. 9, N3, 394–399 (1991).
34. A. R. Chraplyvy, R. W. Tkach. What is the actual capacity of single-mode fibers in amplified lightwave systems? IEEE Photon. Techn. Lett. 5, N6, 666−668 (1993).
35. Evolution of stimulated Raman crosstalk in wavelength division multiplexed systems. D. N. Christodoulides, R. B. Jander. IEEE Photon. Techn. Lett. 8, N12, 1722−1724 (1996).
36. M. Zirngibl. Analytical model of Raman gain effects in massive wavelength division multiplexed transmission systems. Electron. Lett. 34, N8, 789−790 (1998).
37. S. Bigo, S. Gauchard, A. Bertaina, J. P. Hamaide. Experimental investigation of stimulated Raman scattering limitation on WDM transmission over various types of fiber infrastructures. IEEE Photon. Techn. Lett. 11, N6, 1041−1135 (1999).
38. M. Nissov, C. R. Davidson, K. Rottwitt, et al. 100 Gb/s (10×10 Gb/s) WDM transmission over 7200 km using distributed Raman amplification. In: Integrated Optics and Optical Fibre Communications, 11th International Conference on, and 23rd European Conference on Optical Communications (Conf. Publ. No.: 448), Edinburgh, UK, 22-25 Sep 1997, 09/22/1997 -09/25/1997. 5, 9–12 (1997).
39. N. Takachio, H. Suzuki, H. Masuda, M. Koga. 32×10 Gb/s distributed Raman amplification transmission with 50-GHz channel spacing in the zero-dispersion region over 640 km of 1.55-μm dispersion-shifted fiber. In: Optical Fiber Communication Conference, 1999, and the International Conference on Integrated Optics and Optical Fiber Communication. OFC/IOOC '99. Technical Digest, San Diego, CA, USA, 02/21/1999 -02/26/1999. – PD9/1-PD9/3 Suppl. (1999).
40. D. Le Guen, S. Del Burgo, L. Moulinard, D. Grot, M. Henry, F. Favre, T. Georges. Narrow band 1.02 Tbit/s (51×20 Gbit/s) soliton DWDM transmission over 1000 km of standard fiber with 100 km amplifier spans. In: Optical Fiber

Communication Conference, 1999, and the International Conference on Integrated Optics and Optical Fiber Communication. OFC/IOOC '99. Technical Digest, San Diego, CA, USA, PD4/1-PD4/3 Suppl. (1999).

41. T. N. Nielsen, A. J. Stentz, K. Rottwitt, D. S. Vengsarkar, Z. J. Chen, P. B. Hansen, J. H. Park, K. S. Feder, S. Cabot, S. Stulz, D. W. Peckham, L. Hsu, C. K. Kan, A. F. Judy, S. Y. Park, L. E. Nelson, L. Gruner-Nielsen. 3.28-Tb/s transmission over 3×100 km of nonzero-dispersion fiber using dual C- and L-band distributed Raman amplification. IEEE Photon. Technol. Lett. 12, N8, 1079–1081 (2000).
42. T. Terahara, T. Hoshida, J. Kumasako, H. Onaka. 128×10.66 Gbit/s transmission over 840 km standard SMF with 140 km optical repeater spacing (30.4 dB loss) employing dual-band distributed Raman amplification. Opt. Fiber Comm. Conf., 2000, Baltimore, MD, USA, 03/07/2000 -03/10/2000. 4, 251–253 (2000).
43. L. D. Garrett, M. Eiselt, R. W. Tkach, et. al. Field demonstration of distributed, Raman amplification with 3.8 dB Q-improvement for 5×120 km transmission. Optical Fiber Comm. Conf., 2000, Baltimore, MD, USA, 03/07/2000 - 03/10/2000. 4, 293–295 (2000).
44. T. Miyakawa, I. Morita, K. Tanaka, H. Sakata, N. Edagawa. 2.56 Tbit/s (40 Gbit/s × 64 WDM) unrepeatered 230 km transmission with 0.8 bit/s/Hz spectral efficiency using low-noise fiber Raman amplifier and 170 μm^2-$\boldsymbol{A_{eff}}$ fiber. In: Optical Fiber Communication Conference and Exhibit, 2001. OFC 2001. 4, PD26, 1–3 (2001).
45. A. B. Puc, M. W. Chbat, J. D. Henrie, N. A. Weaver, H. Kim, A. Kaminski, A. Rahman, H. Fevrier. Long-haul WDM NRZ transmission at 10.7 Gb/s in S-band using cascade of lumped Raman amplifiers. In: Optical Fiber Communication Conference and Exhibit, 2001. OFC 2001. 4, PD39, 1–3 (2001).
46. G. C. Gupta, L. L. Wang, O. Mizuhara, R. E. Tench, N. N. Dang, P. Tabaddor, A. Judy. 3.2-Tb/s (40 ch × 80 Gb/s) Transmission With Spectral Efficiency of 0.8 b/s/Hz Over 21 100 km of Dispersion-Managed High Local Dispersion Fiber Using All-Raman Amplified Spans. IEEE Photon. Technol. Lett. 15, N7, 996–998 (2003).
47. L. Leng, S. Stulz, B. Zhu, L. E. Nelson, B. Edvold, L. Gruner-Nielsen, S. Radic, J. Centanni, A. Gnauck. 1.6-Tb/s (160×10.7 Gb/s) Transmission Over 4000 km of Nonzero Dispersion Fiber at 25-GHz Channel Spacing. IEEE Photon. Technol. Lett. 15, N8, 1153–1155 (2003).

48. M. Morisaki, H. Sugahara, T. Ito, and T. Ono. 2.56-Tb/s (64 42.7 Gb/s) WDM transmission over 6000 km using all-Raman amplified inverse double-hybrid spans. IEEE Photon. Technol. Lett. 15, N11, 1615–1617 (2003).
49. F. Di Pasquale, F. Meli, E. Griseri, A.Sguazzotti, C. Tosetti, and F. Forghieri. All-Raman transmission of 192 25-GHz spaced WDM channels at 10.66 Gb/s over 30×22 dB of TW-RS fiber. IEEE Photon. Technol. Lett. 15, N2, 314–316 (2003).
50. K. Fukuchi et al. 10.92-Tbit/s (273 × 40 Gb/s) Tripleband/ Ultra-dense WDM Optical-repeated Transmission Experiment. OFC2001. – PD (2001).
51. K. Fukuchi. Wideband and ultra-dense WDM transmission technologies toward over 10-Tb/s capacity. In: Optical Fiber Communications Conference, A. Sawchuk, ed., Vol. 70 of OSA Trends in Optics and Photonics (Optical Society of America, 2002), paper ThX5. Anaheim, California, March 17 (2002).
52. K. Rottwitt, M. Nissov, F. Kerfoot. Detailed analysis of Raman amplifiers for long-haul transmission. In: OFC’98 Technical Digest. TuG1, 30–31 (1998).
53. N. Takachio, H. Suzuki. Application of Raman-distributed amplification to WDM transmission systems using 1.55-μm dispersion-shifted fiber. J. Lightwave Technol. 19, N1, 60–69 (2001).
54. K. H. Seo, J. S. Lee. Signal transmission analysis of backward-pumped fiber Raman amplifiers. IEEE Photon. Technol. Lett. 14, N7, 932–934 (2002).
55. H. Suzuki, N. Takachio, H. Masuda, K. Iwatsuki. Super-dense WDM transmission technology in the zero-dispersion region employing distributed Raman amplification. J. Lightwave Technol. 21, N4, 973–981, (2003).
56. J. C. Bouteiller, J. Bromage, H. J. Thiele, L. E. Nelson, K. Brar, S. Stulz. An optimization process for Raman-amplified long-span transmission. IEEE Photon. Technol. Lett. 16, N1, 326–328 (2004).
57. Z. Xu, Ka. Rottwitt, C. Peucheret, P. Jeppesen. Optimization of pumping schemes for 160-Gb/s single-channel Raman amplified systems. IEEE Photon. Technol. Lett. 16, N1, 329–331 (2004).
58. K. Fujii. Development of an ultra-high-speed optical signal processing technology - for practical implementation of a 160Gbit/s optical communication system. Oki Techn. Rev. Is.204, 72, N4, 70–75 (2005).
59. T. Ito, S. Fujita, E. L. Taillandier de Gabory, K. Fukuchi. Improvement of PMD Tolerance for 110Gb/s Pol-Mux RZ-DQPSK Signal with Optical Pol-Dmux Using Optical PMD Compensation and Asymmetric Symbol-Synchronous Chirp. In: Optical Fiber Communication Conference, OSA Technical Digest (CD)

(Optical Society of America, 2009), paper OThR5. San Diego, California, March 22 (2009).

60. Y. Ogawa, T. Izumi. 10 Gbit/s Lithium Niobate Modulator Driver. Oki Techn. Rev. Iss. 211, 74, N3, 74–77 (2007).
61. K. Nagai, H. Wada. 40 Gb/s EA modulator. OKI Techn. Rev. Iss. 190, 69, N2, 64–67 (2002).
62. T. Kimura. GaAs IC set for optical transmission module – From 10 Gb/s to 40 Gb/s. OKI Techn. Rev. Iss. 190, 69, N2, 68–71 (2002).
63. I. I. Kondilenko, P. A. Korotkov, G. S. Felinskyi. Integrated Electro-Optic Light Modulators. Quantum Electronics, Kiev. Naukova Dumka (ISSN 0368-7155), 9, 60–77 (1980).
64. P. A. Korotkov, G. S. Felinskyi. Investigation of the mechanism of a linear electro-optical effect by spectroscopy. Quantum Electronics. Kiev, Naukova Dumka (ISSN 0368-7155). 22, 66–80 (1982).
65. I. I. Kondilenko, P. A. Korotkov, G. S. Felinskyi. Dielectric properties of non-centrosymmetric crystals and their relationship with Raman scattering. Quantum Electronics. Kiev. Naukova Dumka (ISSN 0368-7155). 21, 49–64 (1981).
66. I. I. Kondilenko, P. A. Korotkov, V. A. Klimenko, G. S. Felinskyi. Raman spectra of a Ti-diffuse planar waveguide in lithium niobate. Optics and Spectroscopy. 49, N5, 1011–1013 (1980).
67. P. A. Korotkov, G. S. Felinskyi. Research of negative dielectric permeability area in the media without inversion center. Bulletin of University of Kyiv. Series: Physics & Mathematics. 2, 162–171 (2008).
68. V. I. Grygoruk, P. A. Korotkov, G. S. Felinskyi. Nonlinear and laser processes in optical fibers. Kyiv: Polygraphic Center “Kyiv University”, –576 p. – 2008.
69. M. N. Islam. Raman amplifiers for telecommunications. IEEE J. Sel. Top. Quant. Electr. 8, N3, 548–559 (2002).
70. H. A. Haus. Noise figure definition valid from RF to optical frequencies. IEEE J. Sel. Top. Quant. Electron. 6, N2, 240–247 (2000).
71. C. H. Henry and R. F. Kazarinov. Quantum noise in photonics. Rev. Mod. Phys. 68, N3, 801–853 (1996).
72. Y. Yamamoto. Noise in amplifiers. J. Lightwave Techn. 21, N11, 2895–2915 (2003).
73. H. A. Haus. Optimum noise performance of optical amplifiers. IEEE J. Quant. Electron. 37, N6, 813–823 (2001).

74. C. R. S. Fludger, V. Handerek, R. J. Mears. Fundamental noise limits in broadband Raman amplifiers. In: Optical Fiber Comm. Conf. and Exhibit, OFC 2001, 1, MA5-1- MA5-3 (2001).
75. G. S. Felinskyi. Noise of spontaneous emission in fiber Raman amplifier with terahertz working bandwidth. New Technologies (ISSN 1810-3049), 3, 21, 72–80 (2008).
76. G.S.Felinskyi. Amplified spontaneous emission measurements and noise figure of the distributed fiber Raman amplifiers with terahertz bandwidth. Proc. 4th Int. Conf. on Advanced Optoelectronics and Lasers, CAOL 2008, September 29 – October 4, Alusta, Crimea, Ukraine, 140–142 (2008).
77. P. A. Korotkov, G. S. Felinskyi. Forced-Raman-scattering-based amplification of light in one-mode quartz fibers. Ukr. J. Phys. Reviews, 5, N2, 103–169 (Ukr) (2009).
78. P. B. Hansen, L. Eskildsen, S. G. Grubb, et. al. Capacity upgrades of transmission systems by Raman amplification. IEEE Photon. Techn. Lett. 9, N2, 262–264 (1997).
79. G. S. Felinskyi, P. A. Korotkov. Raman threshold and optical gain bandwidth in silica fibers. Semicond. Phys. Quant. Electr. Optoelectr. 11, 360–363 (2008).
80. J. Bromage, K. Rottwitt, M. E. Lines. A method to predict the Raman gain spectra of germanosilicate fibers with arbitrary index profiles. IEEE Photon. Techn. Lett. 14, 24–26 (2002).
81. L. D. Landau, E. M. Lifshitz. Mechanics. 1 (4rd ed.)., §26. (Nauka, 1988 – 216 p) [ISBN: 5-02-013850-9] (1976).
82. G. E. Walrafen, P. N. Krishnan. Model analysis of the Raman spectrum from fused silica optical fibers. Appl. Opt. 21, N3, 359–360 (1982).
83. K. Rottwitt, J. Bromage, A. J. Stentz et al. Scaling of the Raman gain coefficient: applications to germanosilicate fibers. J. Lightwave Technol. 21, N7, 1652–1662 (2003).
84. K. X. Liu, E. Garmire. Understanding the formation of the SRS Stokes spectrum in fused silica fibers. IEEE J. Quant. Electron. 27, N4, 1022–1030 (1991).
85. G. S. Felinskyi, I. V. Serdeha, V. I. Grygoruk. TiO_2-doped single-mode fiber as active material for Raman lasers. Key Engineering Materials, doi:10.4028/www.scientific.net/ KEM.753.173, 753, 173–179 (2017).
86. G. S. Felinskyi. Noise measurement of the backward pumped distributed fiber Raman amplifier. Photoelectronics. 18, 16–23 (2009).
87. G. S. Felinskyi, M. Dyriv. Signal-to-noise analysis in a counter-pumped fiber Raman amplifier. Optica Applicata 44, N4, 493–501 (2014).

88. G.S. Felinskyi, M. Dyriv. Noise suppression phenomenon in fiber Raman amplifier. Measur. Sci. Rev. 15(3) 107-110 (2015).
89. G. S. Felinskyi, M. Y. Dyriv. Noise gain features of fiber Raman amplifier. Adv. OptoElectron. Volume 2016, Article ID 5843636, 7 pages, dx.doi.org/10.1155/2016/5843636, (2016).
90. M. D. Mermelstein, C. Horn, S. Radic, C. Headley. Six wavelength Raman fiber laser for C- and L-band Raman amplification and dynamic gain flattening. Electron. Lett. 38, 636–638 (2002).

Chapter 3

LIGHT EFFECT FOR SUBNANO POLISHING OF QUARTZ COVERED WITH LAYER OF SODIUM HYPOCHLORITE AQUEOUS SOLUTION

V.I. Grygoruk, V.I. Kanevskii, S.O. Kolienov, S. Vitusevich

CONTENT

List of symbols and abbreviations

List of symbols and abbreviations

SHAS	sodium hypochlorite aqueous solution
SPP	surface plasmon polariton
h	the height of surface peaks
T	the width of calculation cell
k_0	free space wavenumber
$\mathbf{k}_{ev}$	wavevector of evanescent field
$\mathbf{E}$	electric field strength vector
$\mathbf{E}_{ev}$	evanescent field strength vector
$\mathbf{P}_{in}$	Poynting vector of incident field
Q	filling factor of quartz rough surface profile which consists of periodically repeated triangular peaks and troughs
δ	standard deviation of rough surface height
$\boldsymbol{\varepsilon}_r$	tensors of relative complex dielectric permittivity
λ_{in}	wavelength of laser radiation in a vacuum
$\boldsymbol{\mu}_r$	tensors of relative complex magnetic permeability
θ_{in}	incident angle of laser radiation
θ_{cr}	critical angle of total internal reflection
σ	correlation length of rough surface

INTRODUCTION

A new approach for subnano polishing of the quartz rough surface using the optimal near field method is suggested and analyzed. The analytical and numerical results of light scattering by a rough surface of quartz covered with a layer of sodium hypochlorite solution are presented at light excitation from the quartz side. The finite-element approach is used to solve the Helmholtz two-dimensional vector equation. The distribution of the electric field strength and the Poynting vector along the "quartz – solution" interface using the numerical model for three types of the quartz surface profile shape were calculated, namely: a sinusoidal profile, a random profile with a Gaussian spatial correlation function and a profile in the form of peaks and troughs with a triangular shape. It is shown that regardless of the quartz surface profile shape, the maximum efficiency of subnano polishing is achieved under the following conditions: refractive index of the quartz should be higher than the refractive index of the solution; the angle of light incidence on the quartz surface should be equal to the critical angle of total internal reflection; the standard deviation of roughness should be negligible (less of 10 nm). In this case, the maximum energy of the field is localized near the profile peaks, and the minimum is localized near the profile troughs. Simulation results using a sinusoidal surface profile allow evaluating the effect of separate spatial spectrum frequencies of a random surface profile on the evanescent field parameters. It is determined that some profile spatial frequencies have the resonance at the incident radiation wavelength. It is shown that the complexity of numerical calculations can be reduced by replacing the random quartz surface profile using a Gaussian spatial correlation function by a regular profile in the form of triangular peaks and troughs that repeat periodically for analysis of light scattering processes at the "quartz – solution" interface.

An important characteristic of many optical elements is the degree of their surface irregularity (roughness). There are several methods that reduce surface roughness, such as (a) chemical-mechanical polishing [1], (b) vacuum ion beam etching [2], (c) use of near-field polishing [3]. In the last case, the procedure for photochemical sub-nano-polishing of the surface is as follows. A quartz plate, which has a nanometer level of surface roughness, is located on a horizontal surface of a quartz triangular prism (Fig. 3.1). A thin layer of sodium hypochlorite aqueous solution (SHAS) is applied to a quartz plate surface. The refractive index of SHAS should be less than the refractive index of the quartz plate. This solution is unstable due to its natural properties. In an acidic medium, a large percentage of molecular chlorine forms in it.

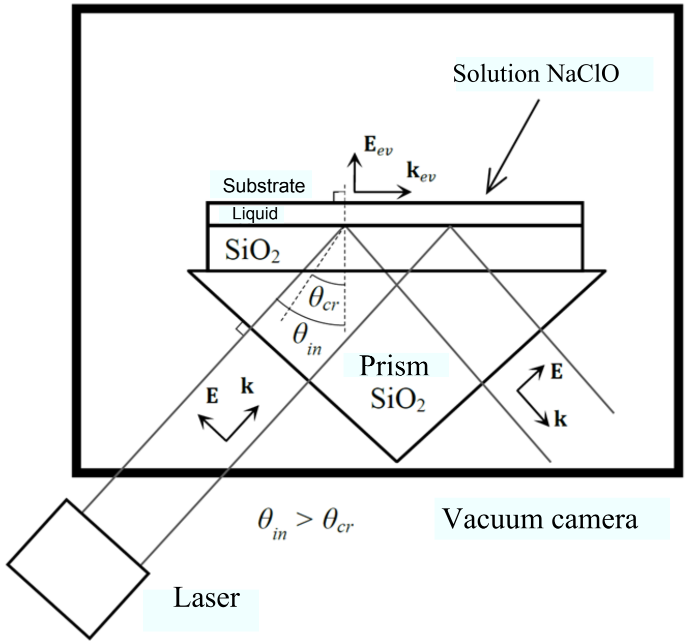

Fig. 3.1. The general scheme of photochemical sub-nano-polishing of the rough surface of quartz, where k_{ev} and E_{ev} is the wavevector and the strength vector of the evanescent field, respectively. θ_{in} is the incident angle of laser radiation on the upper surface of the quartz substrate, θ_{cr} is the critical angle.

When irradiating a lateral face the laser beam passes through the prism, falls to the plate and partially reflects from the upper side of the plate. When the reflection process occurs at an angle greater than the angle of total internal reflection, an evanescent field is formed above the upper surface of the plate. This field reduces sharply when moved away from the plate surface and contributes to photodissociation of molecular chlorine, which is contained in the SHAS near the surface. As a result, atomic chlorine and its ions are formed in regions of the increased strength of an evanescent field, which increases in the area of the peaks of nano-irregularities. On being polarized in an external electromagnetic field these products are attracted to the plate surface which is also polarized by the field.

As shown in [4], under the action of electromagnetic radiation, the interaction of atomic chlorine with the quartz plate surface is more active in the region of the peaks. It leads to local quartz etching and therefore reduces the roughness of the sample surface.

Thus, the problem of sub-nano-polishing of the quartz rough surface can be divided into three parts: (a) the calculation of parameters of the evanescent field in the near zone of nano-irregularities of quartz rough surface covered with the thin layer of the SHAS; (b) the quantum-chemical calculation of the interaction of products of photodissociation of molecular chlorine with the silica surface; (c) the description of results of the comprehensive experiment on near-field polishing of quartz surface.

In the first part, which is discussed in this work, it is necessary to solve several actual tasks: (i) the analysis of electrical component configuration in electromagnetic radiation along the “quartz-SHAS” interface, which provides necessary conditions for the effective etching of quartz surface in the area of peaks and the absence of such etching in the area of troughs; (ii) a determination of the conditions for ensuring the necessary electric field contrast on the sample surface, which is obviously related to the shape of the sample surface and its roughness parameters, as well as to the wavelength of electromagnetic radiation; (iii) the choice of the optimal profile shape of “quartz-SHAS” interface, that allows to adjust the degree of complexity of the obtained results with the accuracy required to gain them.

This section considers three profile types of the quartz rough surface: a sinusoidal profile, the profile in the form of triangular peaks and troughs and a random profile that has a Gaussian spatial correlation function. This enables us to determine the influence of the profile shape on the strength and contrast of the evanescent field along the “quartz-SHAS” interface.

According to the given paper, a sinusoidal profile allows understanding better the connection between the field parameters and the spatial frequency of the surface profile function. It can be used for the analysis of more complex surfaces since any surface can be represented as a set of sinusoidal profiles of different spatial frequencies [13]. A study of the profile described by a random function which includes a Gaussian spatial correlation function actually shows a connection between the parameters of the evanescent wave propagating along the “quartz-SHAS” interface with a spatial spectrum of this surface profile. Consideration of the profile in the form of triangular peaks and troughs allows us to combine the trivial approach (in the first case) with the attempt to take into account all components of the spatial spectrum (in the case when the profile has a Gaussian spatial correlation function).

This gives an opportunity to obtain a simplified solution of the problem which describes the effect of electromagnetic radiation on a rough surface of quartz, and to provide the necessary accuracy of the results.

The work performed is supported by the Foundation for Fundamental Research of Ukraine (grant F76/29-2018).

3.1. Electric field strength analysis of the evanescent wave near the plane interface of two media under conditions of the total internal reflection

The aims of this section are: (i) a description of an analytical method for calculating the distribution of electromagnetic field in the case when a plane wave falls to the plane “quartz-SHAS“ interface at the angle which is not less than the angle of total internal reflection; (ii) a description of a numerical model which represents that distribution; (iii) an analysis of test results on the basis of the distribution of Poynting vector near the plane interface between two media obtained by using the abovementioned models; (iv) verification of the numerical model by calculating the reflection coefficient when a plane wave is scattered by the “quartz-golden film-SHAS“ interface.

3.1.1. Analytical model

Figure 3.2 shows the schematic image of an electromagnetic wave behavior near the plane “quartz-SHAS“ interface in the case, when (i) $n_1 \geq n_2$, where n_1, n_2 are refractive index of the quartz and SHAS, respectively; (ii) the incident angle θ_{in} of the given wave at the specified interface is greater than the angle of total internal reflection θ_{cr} (the critical angle of incidence); (iii) the incident electromagnetic wave has TM polarization. Note that the refracted wave has the angle of refraction that exceeds 90 degrees and becomes imaginary. It is shown schematically by a dotted line in Fig. 3.2. Consider the analytical procedure of an electromagnetic field distribution calculation in the cell (Fig. 3.2) when the incident angle of an electromagnetic wave on the specified interface is not less than the angle of total internal reflection.

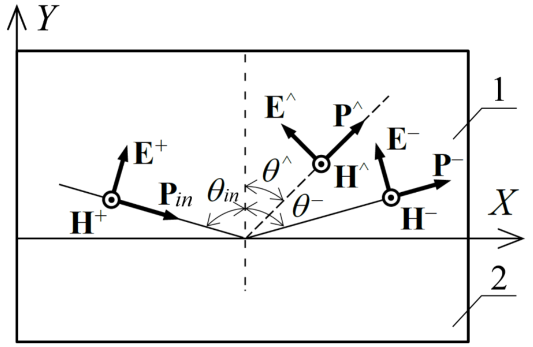

Fig. 3.2. The two-dimensional cell used for the analytical calculation of the electromagnetic field distribution when the TM-plane wave falls to the plane “quartz-SHAS” interface at the θ_{in} angle that is greater than the θ_{cr} angle of total internal reflection where the regions 1 and 2 is the area of the quartz plate and SHAS with refractive indices $n_1 \geq n_2$, respectively; H^+, H^-, $H^\wedge$ is the strength of magnetic field of incident, reflected and refracted waves, respectively; E^+, E^-, $E^\wedge$ is the strength of electric field of incident, reflected and refracted waves, respectively; θ_{in}, θ^-, $\theta^\wedge$ is the angle of incidence, reflection and refraction of the corresponding waves, respectively; P_{in}, P^-, $P^\wedge$ is the Poynting vector of incident, reflected and refracted waves, respectively.

According to Fig. 3.2 there are expressions for the projections of the electromagnetic wave vectors **E** and **H.**

1. *For the incident wave*:

$$E_x^+ = E^+ \cos(\theta_{in}) \cdot exp\left[-i\left(k_{1x}x - k_{1y}y\right)\right], \tag{3.1}$$

$$E_y^+ = E^+ \sin(\theta_{in}) \cdot exp\left[-i\left(k_{1x}x - k_{1y}y\right)\right], \tag{3.2}$$

$$H_z^+ = (E^+/Z_1) \cdot exp\left[-i\left(k_{1x}x - k_{1y}y\right)\right], \tag{3.3}$$

where $Z_1 = Z_c/n_1$ is the quartz wave resistance, Z_c is the vacuum wave resistance, $k_{1x} = k_1 \sin(\theta_{in})$, $k_{1y} = k_1 \cos(\theta_{in})$ are projections of wavevectors on the coordinate axes, k_1 is the wavenumber, which corresponds to the incident wave.

2. *For the reflected wave*:

$$E_x^- = -E^- \cos(\theta_{in}) \cdot exp\left[-i\left(k_{1x}x + k_{1y}y\right)\right], \tag{3.4}$$

$$E_y^- = E^+ \sin(\theta_{in}) \cdot exp\left[-i\left(k_{1x}x + k_{1y}y\right)\right], \tag{3.5}$$

$$H_z^- = (E^-/Z_1) \cdot exp\left[-i\left(k_{1x}x + k_{1y}y\right)\right], \tag{3.6}$$

where $\theta_{in} = \theta^-$ according to the first Snell's law.

3. *For the refracted wave*:

$$E_x^\wedge = -E^\wedge \cos(\theta^\wedge) \cdot exp\left[-i\left(k_{2x}x + k_{2y}y\right)\right], \tag{3.7}$$

$$E_y^\wedge = E^\wedge \sin(\theta^\wedge) \cdot exp\left[-i\left(k_{2x}x - k_{2y}y\right)\right], \tag{3.8}$$

$$H_z^\wedge = (E^\wedge/Z_2) \cdot exp\left[-i\left(k_{2x}x + k_{2y}y\right)\right], \tag{3.9}$$

where $Z_2 = Z_c/n_2$ is SHAS wave resistance, $k_{2x} = k_2\sin(\theta^\wedge)$, $k_{2y} = k_2\cos(\theta^\wedge)$ are projections of wavevectors on coordinate axes, k_2 is the wavenumber corresponding to the refracted wave and the ratio $\cos(\theta^\wedge) = i\sqrt{\left(\frac{n_1}{n_2}\sin(\theta_{in})\right)^2 - 1}$ obtained from the second Snell's law provided that (i) $\theta_{in} \geq \theta_{cr}$, (ii) the angle $\theta^\wedge$ is complex.

Thus, the distribution of the electromagnetic field above the "quartz-SHAS" interface (Fig. 3.2, $Y > 0$) is obtained by summing up the incident and reflected waves, taking into account the shift of the reflected wave relative to the incident wave. So, the reflected wave is represented in the form:

$$E^- = E^+ \cdot exp[-i2\psi_0], \tag{3.10}$$

where $2\psi_0$ is the phase shift of the reflected wave relative to the incident wave, and a formula for it was obtained in [5]:

$$\psi_0 = \text{arctg}\left(\frac{\sqrt{\sin^2(\theta_{in}) - (n_1/n_2)^2}}{(n_1/n_2)^2\cos(\theta_{in})}\right). \tag{3.11}$$

As a result, we get expressions for the projections of the electromagnetic wave vectors **E** and **H** above the "quartz-SHAS" interface:

$$E_x = 2iE^+ \cos(\theta_{in}) \sin(k_{1y}y - \psi_0) \cdot exp[-i(k_{1x}x - \psi_0)], \tag{3.12}$$

$$E_y = 2E^+ \sin(\theta_{in}) \cos(k_{1y}y - \psi_0) \cdot exp[-i(k_{1x}x - \psi_0)] \ , \tag{3.13}$$

$$H_z = 2(E^+/Z_1) \cos(\theta_{in}) \sin(k_{1y}y - \psi_0) \cdot exp[-i(k_{1x}x - \psi_0)] \, . \tag{3.14}$$

The relations for the projections of the electromagnetic wave vectors **E** and **H** under the surface of the total internal reflection (Fig. 3.2, $Y < 0$) are obtained based on the relations (3.7) - (3.9)

$$E_x^\wedge = -iE^\wedge \sqrt{\left(\frac{n_1}{n_2}\sin(\theta_{in})\right)^2 - 1} \cdot e^{k_2 y\sqrt{\left(\frac{n_1}{n_2}\sin(\theta_{in})\right)^2-1}} \cdot e^{-ik_2\frac{n_1}{n_2}x\cdot\sin(\theta_{in})}, \tag{3.15}$$

$$E_y^\wedge = E^\wedge \frac{n_1}{n_2}\sin(\theta_{in}) \cdot e^{k_2 y\sqrt{\left(\frac{n_1}{n_2}\sin(\theta_{in})\right)^2-1}} \cdot e^{-ik_2\frac{n_1}{n_2}x\cdot\sin(\theta_{in})}, \tag{3.16}$$

$$H_z^\wedge = \frac{E^\wedge}{Z_2} \cdot e^{k_2 y\sqrt{\left(\frac{n_1}{n_2}\sin(\theta_{in})\right)^2-1}} \cdot e^{-ik_2\frac{n_1}{n_2}x\cdot\sin(\theta_{in})} \, . \tag{3.17}$$

Note that the amplitudes of the fields H^+, H^-, $H^\wedge$, E^+, E^-, $E^\wedge$ are determined (up to constant which is defined by the power of the incident wave P_{in}) from the boundary conditions on the “quartz-SHAS“ interface ($Y = 0$).

$$E_x^+(+0) = E_x^-(+0) = E_x^\wedge(-0) \, , \quad H_z^+(+0) = H_z^-(+0) = H_z^\wedge(-0) \, . \tag{3.18}$$

Thus, the expressions (3.12) - (3.17) allow obtaining the distribution of the Poynting vector in the two-dimensional region (Fig. 3.2) analytically. This provides finding the flow of the plane wave energy in the calculated region assuming that the total internal reflection from the plane “quartz-SHAS“ interface takes place. This reflects that the features of the rough surface of quartz were not taken into account.

3.1.2 Numerical model

Now we have to describe a two-dimensional numerical model. It allows getting the distribution of the electromagnetic field strengths in the calculated region (Fig. 3.2) provided that the plane TM wave falls to a plane “quartz-SHAS“ interface and the incident angle θ_{in} is not less than the critical angle θ_{cr}. This approach is also acceptable for a partial verification of calculations obtained by using analytical and numerical models.

The upper and lower horizontal lines of the two-dimensional cell (Fig. 3.2) are selected as the source and receiver of incident radiation, respectively. The right and left sides of the calculation cell are limited by the vertical lines, along which periodic boundary conditions are performed. The region 1 is volumetric quartz, which has the refractive index equal to $n_1 = 1.5168$, and we neglect losses here. The region 2 is the SHAS, whose refractive index is equal to $n_2 = 1.37$, and we neglect losses here too.

The distribution of the electric field strength in the regions 1-2 (Fig. 3.2) is calculated on the basis of the solution of the homogeneous Helmholtz equation [6]:

$$\vec{\nabla} \times \left[\boldsymbol{\mu}_r^{-1} \cdot \left(\vec{\nabla} \times \mathbf{E}\right)\right] - k_0^2 \boldsymbol{\varepsilon}_r \cdot \mathbf{E} = 0\,, \tag{3.19}$$

where $\boldsymbol{\varepsilon}_r$, $\boldsymbol{\mu}_r$ is second-order tensors of relative complex dielectric and magnetic permeabilities, respectively. We assume that the objects which are in the calculation cell do not have magnetic properties ($\boldsymbol{\mu}_r = 1$). Also, we neglect the field of chloride ions, which are formed as a result of molecular chlorine photodissociation.

To solve the equation (3.19), we choose the finite-element approach which consists of the Galerkin method and the finite element method [7], in fact. Triangles were used as vector finite elements.

Note that the source and receiver of optical radiation (horizontal lines on Fig. 3.2) on the outside of the calculation cell are limited by absorbing layers that simulate the radiation conditions at infinity [6,7]:

$$\lim_{\mathrm{r}\to\infty} r\left(\frac{\partial \mathbf{E}}{\partial r} + jk_0\mathbf{E}\right) = 0\,, \tag{3.20}$$

where r is the distance between the point of beam scattering and the observation point located in the far observation zone; k_0 is the wavenumber in free space.

The numerical realization of the radiation conditions (3.20) was carried out by applying a local approximation, in which the method of absolutely absorbing layers was selected [8, 9]. As a light source is used a plane TM-wave polarized in the incident plane and scattered at the “quartz-SHAS“ interface. The direction of its motion is represented by Poynting vector **P** directed at an angle θ_{in} to the Y axis, and E-wave falls from the quartz side to the mentioned interface.

The calculation of electrical and magnetic field strengths in the optical range is sufficient to obtain all other output parameters, in particular, to obtain a reflection coefficient R in the case when, for example, a film of gold is placed between a surface of quartz and SHAS (Fig. 3.2). In this case:

$$R = \left(\frac{E_{out}^{av}}{E_{in}^{av}}\right)^2 , \tag{3.21}$$

where E_{in}^{av} and E_{out}^{av} is the mean values of the complex amplitudes of electric field strength vectors along the upper horizontal line of the calculation cell in the case of incident and reflected waves, respectively.

Optical constants for gold (n and η, where n is the refractive index, η is the absorption index) were taken from work [10]. According to [10] in the range of wavelengths λ from 400 to 650 nm, the real part of the dielectric constant $\varepsilon'(\lambda) = n^2 - \eta^2$ has the singularity: $\varepsilon'(\lambda) \leq 0$. So, there are conditions for the appearance of plasmon resonance on the gold surface when the scattering of plane electromagnetic wave take place (in the specified range of wavelengths).

Thus, the numerical solution of Eq. (3.19) allows obtaining the Poynting vector distribution in the calculated two-dimensional region (Fig. 3.2) with the necessary accuracy. Note that the numerical model (as it will be shown below) allows calculating successfully Poynting vector flows in the 2D area, which includes predefined “quartz-SHAS“ interface.

3.1.3. Verification of numerical and analytical models

3.1.3.1. Calculation of the Poynting vector

The numerical and analytical models of light scattering on the plane “quartz-SHAS” interface allow obtaining the distribution of electric and magnetic fields strength in the 2D cell independently (Fig. 3.2). Thus, it is possible to obtain the distribution of the Poynting vector flow in this domain. The Poynting vector allows describing the phenomenon of total internal reflection at the “quartz-SHAS” interface unambiguously.

Taking into account that the strengths of electric and magnetic fields can be written in the form:

$$\mathbf{E} = \frac{1}{2}\left(\mathbf{E}_m e^{j\omega t} + \mathbf{E}_m^* e^{-j\omega t}\right); \quad \mathbf{H} = \frac{1}{2}\left(\mathbf{H}_m e^{j\omega t} + \mathbf{H}_m^* e^{-j\omega t}\right),$$

then the Poynting vector can be presented as:

$$\mathbf{P} = \mathbf{P}_{av} + \mathbf{P}_{var}, \quad \mathbf{P}_{av} = \frac{1}{2}\mathrm{Re}([\mathbf{E}_m \mathbf{H}_m^*]), \quad \mathbf{P}_{var} = \frac{1}{2}\mathrm{Re}\left([\mathbf{E}_m \mathbf{H}_m]e^{j2\varphi(t)}\right), \quad (3.22)$$

where $\varphi(t) = \omega t$ is the phase of the incident wave; ω is the cyclic frequency; t is time; $\mathbf{E}_m$, $\mathbf{E}_m^*$, $\mathbf{H}_m$, $\mathbf{H}_m^*$ is the complex amplitudes of vectors $\mathbf{E}$ and $\mathbf{H}$ and their complex conjugate values, respectively; $\mathbf{P}_{av}$ is the mean value of the energy density during the period of fluctuation of the incident wave (the active power); $\mathbf{P}_{var}$ is the variable component of energy density (the reactive power).

Note that the Eqs (3.22) allow describing a wave process that propagates along the *X* coordinate, as well as a standing wave along the *Y* coordinate.

Figure 3.3 shows the distribution of the flows of the Poynting vector in the calculation cell (Fig. 3.2) for the incident wavelength $\lambda_{in} = 500$ nm and the initial phase $\varphi(t = 0) = 0$. The distributions are calculated using the analytical model (3.12) ‑ (3.17) under the condition of the total internal reflection from the plane "quartz-SHAS" interface, $(n_1 \geq n_2,\ \theta_{in} \geq \theta_{cr})$, and for (a) $\theta_{in} = \theta_{cr} = 65^{\circ}$, (b) $\theta_{in} = 70^{\circ}$. These results are in good agreement with data, obtained using the numerical model Eqs.(3.19)–(3.20) with the accuracy up to the constant.

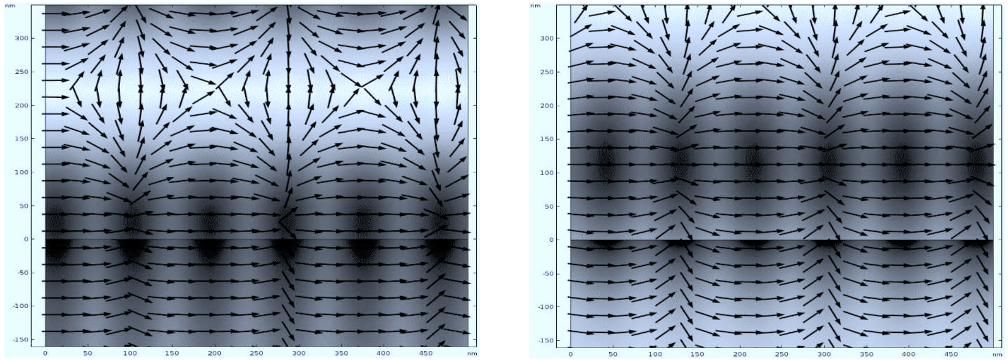

a *b*

Fig. 3.3. Two-dimensional distribution of Poynting vector flows (*arrows*) and values of this vector (*gray background*) in the calculation cell, computed using the analytical model under conditions of the total internal reflection from the plane "quartz-SHAS" interface $(n_1 \geq n_2, \theta_{in} \geq \theta_{cr})$, $\varphi(t = 0) = 0$, $\lambda_{in} = 500$ nm, for (a) $\theta_{in} = \theta_{cr} = 65^{\circ}$, (b) $\theta_{in} = 70^{\circ}$.

From Fig. 3.3 data the following conclusions can be made which are well-matched with the conclusions obtained in [5]: (i) the wave process propagates along the X coordinate when the phase of the incident wave changes; (ii) there is a standing wave along the Y coordinate; (iii) an increase in the incident angle θ_{in} causes an increase in the phase shift which, in turn, changes the distribution of the flows of the Poynting vector (the extremums of the standing wave shift along the Y axis); (iv) the incident wave partially penetrates into the volume of the solution. It decays exponentially with distance from the interface according to Eq. (3.15) and Eq.(3.16) of the analytical model. Note that the identity of the results for the analytical and numerical models in the future allows, at a qualitative level, to explain wave processes near the interface in the case when the standard deviation of the quartz surface roughness is negligibly small.

3.1.3.2. The Kretschmann effect: the calculation of reflection coefficient

Another way to verify the correctness of data obtained using numerical model is to calculate the reflection coefficient R (see Eq.(3.21)) in the case when a gold film with thickness d is placed between the quartz sample and the SHAS. In such a case, as shown in Fig. 3.4, we have different dependences of the reflection coefficient R on the incident angle θ_{in} of wave incidence for the specified wavelength and for the different thickness of the gold film.

Figure 3.4 shows the dependences of the reflection coefficient R on the angle of incidence wave at wavelength: $\lambda_{in} = 500$ nm for different thicknesses of the gold film: $d = 1$ nm (curve 1), $d = 20$ nm (curve 2), $d = 30$ nm (curve 3), $d = 50$ nm (curve 4). Note that for a fixed thickness of the film, by adjusting the angle of wave incidence, it is possible to satisfy the conditions of surface plasmon-polaritons (SPP) excitation at the “gold film – SHAS” interface. In this case the tangential components of a photon and a plasmon wave vectors on the gold film rough surface have to be aligned. The minimum of the reflection coefficient R (other parameters are unchanged) corresponds to the mentioned conditions for the excitation of the SPP and, consequently, to the maximum possible transformation of the incident wave energy into the SPP [11,12]. Very thin gold film contributes to the accelerated attenuation of the SPP (enhanced reverse re-emission). The thick gold film contributes to accelerated attenuation of the SPP (increased absorption in the thickness of the film). The zero value of the reflection coefficient R corresponds to the optimal conditions for the SPP excitation, when the energy of the incident wave is equal to the energy of the surface plasmon.

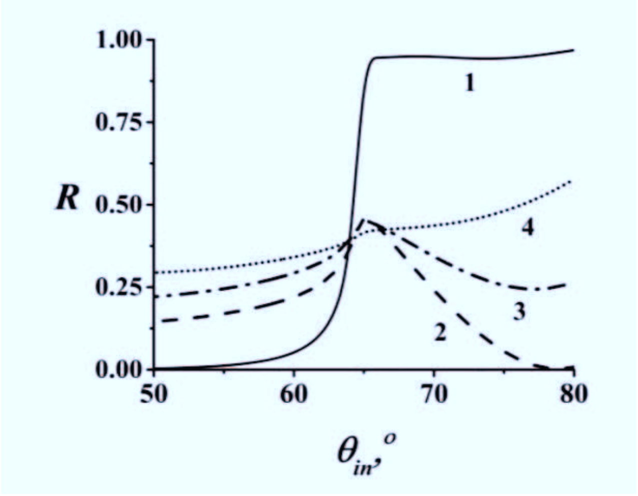

Fig. 3.4. Dependences of the reflection coefficient on the angle of wave incidence for wavelength $\lambda_{in} = 500$ nm and different thicknesses of the gold film: $d = 1$ nm (*curve* 1), $d = 20$ nm (curve 2), $d = 30$ nm (*curve* 3), $d = 50$ nm (*curve* 4).

Summary

The analysis of the field distribution in the calculation cell allows to find the following features. Excluding areas near the "quartz-SHAS" interface, the distribution of Poynting vector flows in the calculation cell, taking into account the rough surface of quartz, in general, does not depend on the parameters of this surface in the case when: (i) the wave falls to a surface with a lower refractive index, and in the case when the incident angle is not less than a critical angle; (ii) the length of the incident wave is considerably greater than the standard deviation of the roughness height and the length of the correlation of the quartz rough surface; (iii) the standard deviation of the quartz surface roughness is insignificant.

3.2. Computation of the evanescent wave parameters in the near zone of quartz rough surface with a sinusoidal profile shape covered with a layer of sodium hypochlorite aqueous solution

The aim of this section is twofold (i) to describe a numerical method for calculating the distribution of an electromagnetic field in the case when a plane wave falls on the quartz rough surface coated by SHAS and the profile of this surface has a sinusoidal shape; (ii) an analysis of the results obtained in terms of understanding the connection between parameters of an electromagnetic field and a spatial frequency of the surface profile which has a sinusoidal shape.

3.2.1. Numerical model features

Let's consider the modified 2D cell presented in Fig. 3.2, in which the "quartz-SHAS" interface has a sinusoidal shape now. Fig. 3.5 shows a 2D cell for calculating the evanescent field parameters in the near-field region of nano-irregularities of the quartz rough surface coated by SHAS. The top and bottom sides (regions 1, 4) of the calculation cell are limited by absorbing layers. The right and left sides of the calculation cell are limited by vertical lines, along them periodic boundary conditions are realized. Region 2 is the volumetric quartz. Region 3 is the SHAS. The distances t, S_1, h, S_2 and w in the figure is the thickness of the absorbent layer, the distance between the upper absorbing layer and the middle line of the "quartz-SHAS" interface, the height of peaks on the quartz surface, the distance between the middle line and the lower absorbing layer, the width of the cell, respectively. $\mathbf{P}_{in}$, θ_{in} is the Poynting vector and the angle under which the plane TM-wave scattered by the "quartz-SHAS" interface, respectively.

To improve the accuracy of the results, four periods of quartz rough surface with a sinusoidal shape in the 2D cell was placed.

Figure 3.5 indicates the height h of quartz surface peaks with a sinusoidal shape, as a parameter of roughness. It is known that the sinusoidal rough surface has the standard deviation δ equal to $h/2\sqrt{2}$. Note that the distances S_1 and S_2 between the middle line of the rough surface and absorbing layers are taken larger than the double length of the incident wave in free space.

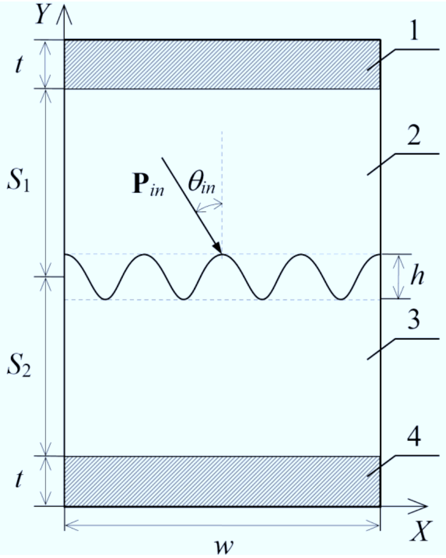

Fig. 3.5. The two-dimensional cell used for the calculation of evanescent field parameters in near-field nanoinhomogeneities of sinusoidal quartz rough surface coated by SHAS, *w* is the calculation cell width.; 1,2,3,4 is the upper absorbing layer; the quartz layer; the SHAS layer; the lower absorbing layer, respectively.

It was shown in [13] that there is a direct connection between the light scattering spectrum on a rough surface and the roughness parameters of this surface, namely, the standard deviation of the surface height δ and the correlation length of the rough surface σ. In the case, when the random function of the surface shape has a correlation function with a Gaussian distribution, this relation can be described as

$$|s(\Delta k_x)|^2 = \frac{1}{4\pi}\delta^2\sigma\exp\left(-\frac{\sigma^2(\Delta k_x)^2}{4}\right), \tag{3.23}$$

where $s(\Delta k_x)$ is the energy spectrum of scattered light, which is actually the energy spatial spectrum of the rough surface (as it will be shown in this chapter, this fact occurs only in the case when $\theta_{in} = \theta_{cr}$, i.e. when the profile of the electric field along the "quartz-SHAS" interface repeats the spatial profile of the quartz rough surface), and Δk_x is the projection of the change in the light wave vector on the *X*-axis, corresponding to the spatial frequency of the rough surface profile.

This dependence, represented on a logarithmic scale, shows a linear relationship between the values of the function $|s(\Delta k_x)|^2$ and an argument Δk_x, that allows obtaining the parameters δ and σ directly.

In the case of a sinusoidal surface, the relation (3.23) is transformed into the form [13]:

$$|s_1(\Delta k_x)|^2 = \left(\frac{h}{4}\right)^2 \left|\hat{\delta}(\Delta k_x - g) + \hat{\delta}(\Delta k_x + g)\right|, \tag{3.24}$$

where $\hat{\delta}$ is the delta function and $g = 2\pi/T$ corresponds to the spatial frequency of the surface with a specified period T.

Thus, if we decompose the random function of the rough surface having a Gaussian correlation function into Fourier series, then this rough surface can be simulated by a set of sinusoidal surfaces with specified spatial frequencies g for which the heights h are determined from the Eq. (3.24) under the condition that $|s_1(g)| = |s(g)|$. In this case, the amplitude of the sinusoidal surface can be associated with the parameter δ, and the period that for our model is equal to $T = w/4$, also can be associated with the length of the correlation σ, which corresponds to the value of the argument for which the quartz rough surface correlation function decreases by *e* times.

We consider that the contrast of the evanescent field between peaks and troughs of a rough surface along the "quartz-SHAS" interface (Fig. 3.5) can be determined by the relation: $K = |E_1 - E_2|/(E_1 + E_2)$, where E_1, E_2 are the averaged amplitudes of the evanescent field, relative to the middle line of the mentioned interface profile, in the region of all peaks and troughs, respectively, Thus, the main idea of implementing the scattering of an incident wave at the "quartz-SHAS" interface with a sinusoidal profile is the possibility to study the dependence between the field parameters in the near-zone of this interface and the spatial frequency of the quartz rough surface at the specified value of the incident wavelength λ_{in}. At the same time, in the linear approximation ($\delta \ll \lambda_{in}$, $\sigma \ll \lambda_{in}$, $\theta_{in} = \theta_{cr}$, $K \sim \sigma$, δ) the integral characteristics of the electromagnetic field (for example, the contrast *K*) can be determined by the superposition of the field parameters formed by the individual spectral components of the spatial spectrum of the random rough surface, which is described by the Eq. (5.23). To perform the calculations, the special software was developed that implements the solution of Maxwell's equations using the finite element method.

3.2.2. Results and analysis

Fig. 3.6 shows the distribution of the electric field strength along the “quartz-SHAS” interface at the different incident angles. There are two phenomena in the case when the angle of incidence is equal to $\theta_{in} = 0°$: (i) on the one hand, the distribution of Poynting vector flows in the calculation cell is formed independently of the presence of a quartz rough surface, with the exception of areas near the “quartz-SHAS” interface; (ii) on the other side, the existence of roughness near the indicated interface, according to the second Snell’s law, enforces Poynting vector flows to change their configuration. Meanwhile, the comparison of the spatial roughness profile (Fig. 3.5) and the distribution of the electric field along the spatial profile (Fig. 3.6) shows that the minimum values of the field strength are formed in the regions of peaks of the rough surface, and the minimum values are formed in the regions of troughs. In this case, the regions of peaks act like nano-lenses, which scatter the Poynting vector flows. The regions of troughs act like nano-lenses, which concentrate the Poynting vector flows. Thus, the photodissociation of chlorine molecules will take place in the regions of troughs, which corresponds to an effective increase in the rough surface area.

The above statements are confirmed by numerical experiments on the basis of the two-dimensional model described above. With $\theta_{in} = \theta_{cr} = 65°$, the situation is fundamentally different. In this case, the maximum values of the field strength are formed in the regions of the roughness peaks, and the minimum value of the field strength is formed in the regions of the roughness troughs. Thus, according to Fig. 3.5 and Fig. 3.6, the spatial profile of the quartz rough surface and the curve of the electric field strength will repeat each other, i.e. photodissociation of chlorine molecules will take place in the regions of the peaks of the quartz rough surface. Thus, the quartz etching occurs mainly in the regions of the peaks, rather than the troughs. It should be noted that the electromagnetic wave scattered by a rough surface at a critical angle. The light excitation of the sample under other angles, as it is shown above, is inappropriate in terms of nano-polishing of the rough surface of quartz.

Increasing the incident angle, when $\theta_{in} > \theta_{cr}$, leads to a phase shift of the reflected wave relative to the incident wave (see (3.11)), which is observed when analyzing the curves 3 and 4 in Fig. 3.6.

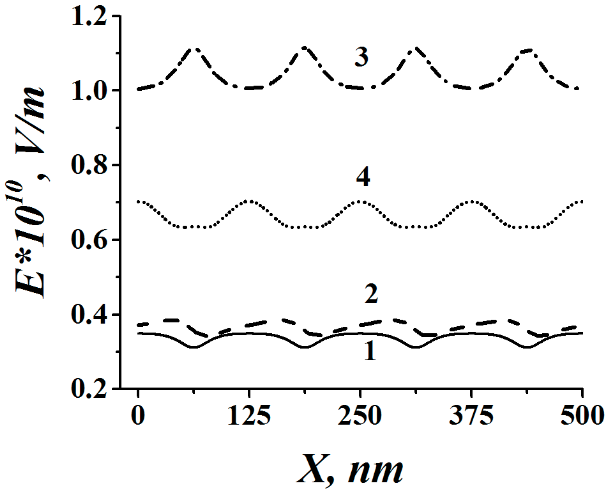

Fig. 3.6. The distribution of electric field strength along the “quartz-SHAS” interface at different values of the incident angle θ_{in}: $\theta_{in} = 0°$ (curve 1), $\theta_{in} = 30°$ (curve 2), $\theta_{in} = 65°$ (curve 3), $\theta_{in} = 80°$ (curve 4). Wavelength in vacuum: $\lambda_{in} = 500$ nm, the height of quartz surface peaks: $h = 28.2$ nm, the critical incident angle: $\theta_{in} = \theta_{cr} = 65°$, the correlation length of the quartz rough surface: $\sigma = 23.7$ nm.

When the incident angle of the beam (which allows performing nano-local etching of quartz) has been determined, the next step is to find out in what range of h parameter value is reasonable to perform nano-polishing. Fig. 3.7 shows the distribution of electric field strength along the “quartz-SHAS” interface at different values of the quartz surface peaks height h, when the angle of plane wave incidence is equal to $\theta_{in} = 65°$. According to Fig. 3.7, at different values of the parameter h, the distribution of the maximums and minimums of electric field strength along the interface does not change and generally repeats the profile shape of quartz rough surface. However, as will be shown below, with $h = 84.6$ nm the dependence of the field contrast on the profile height (in all range of profile height variation) becomes nonlinear and the distribution of the amplitude values of the field strength will be no longer proportional to the distribution of the profile height, which in turn will not provide uniform etching of the rough surface. Numerical calculations show that near-field nano-local etching of quartz (the rough surface of quartz is in the form of a sinusoid) is reasonable to perform when the parameter $h \leq (20 - 30)$ nm.

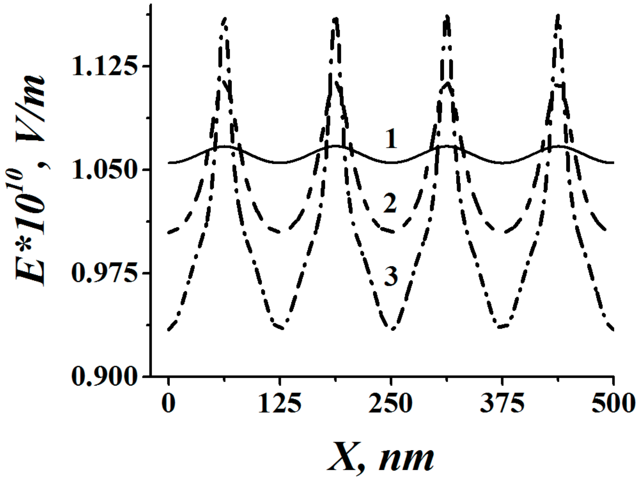

Fig. 3.7. The distribution of electric field strength along the “quartz-SHAS” interface at different values of the height of quartz surface peaks: $h = 2.82$ nm (curve 1), $h = 28.2$ nm (curve 2), $h = 84.6$ nm (curve 3). The wavelength in vacuum: $\lambda_{in} = 500$ nm, the incident angle: $\theta_{in} = 65°$, the correlation length of the rough quartz surface: $\sigma = 23.7$ nm.

Fig. 3.8 shows the distribution of the active component of the Poynting vector $\mathbf{P}_{av}$ (curve 1) and the total component of the same vector $\mathbf{P}$ along the “quartz-SHAS” interface. It depends on the incident wave phase φ, where $\varphi = 0$ (curve 2); $\varphi = \pi/4$ (curve 3); $\varphi = 3\pi/7$ (curve 4). Note that the distribution of the oscillation amplitude of the vector $\mathbf{P}_{av}$ along the “quartz-SHAS” interface is similar to the distribution of the oscillation amplitude of the vector $\mathbf{E}$ (suppose $K \sim h$) and repeats the shape of the surface profile, when the sample is excited by light at the critical angle. On the other hand, the Poynting vector $\mathbf{P}$ consists of the sum of the vectors $\mathbf{P}_{av}$ and $\mathbf{P}_{var}$, therefore it depends on the phase φ of the incident wave that changes in time (Fig. 3.8). Thus, with the change in the phase of the incident wave, its maximum value (the crest of the vector $\mathbf{P}$ distribution) drifts along the “quartz-SHAS” interface creating optimal conditions for sub-nano-polishing along the entire surface. At the same time, the profile peaks are polished at a higher intensity compared to the troughs, due to the higher average value of the active component of the energy density of the Poynting vector $\mathbf{P}_{av}$.

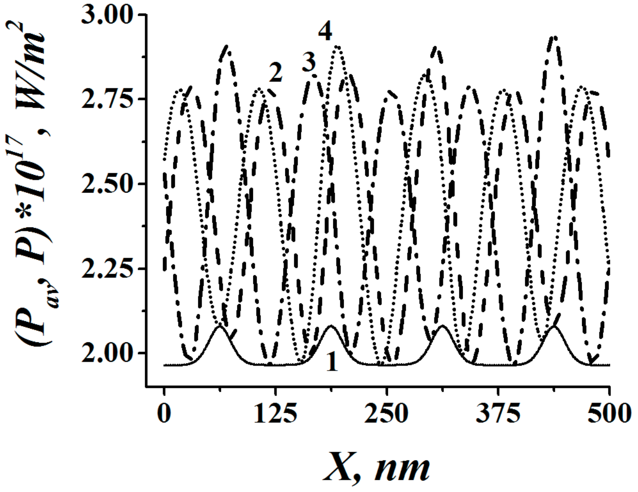

Fig. 3.8. The distribution of the active component of the Poynting vector $\mathbf{P}_{av}$ (curve 1) and the total component of the Poynting vector **P** along the "quartz-SHAS" interface as a function of the incident wave phase φ, where $\varphi = 0$ (curve 2); $\varphi = \pi/4$ (curve 3); $\varphi = 3\pi/7$ (curve 4). Wavelength in vacuum: $\lambda_{in} = 500$ nm, values of the quartz surface peaks height: $h = 28.2$ nm, the incident angle: $\theta_{in} = 65°$, the correlation length of rough quartz surface: $\sigma = 23.7$ nm.

The aim of this section is to show the possibility of nano-polishing of the rough surface of quartz covered with SHAS. Fig. 3.9*a* shows the distribution of the active component of the Poynting vector $\mathbf{P}_{av}$ (curve 1) and the total component of the Poynting vector **P** in the perpendicular direction to the "quartz-SHAS" interface as a function of the incident wave phase φ, where $\varphi = 0$ (curve 2); $\varphi = \pi/4$ (curve 3); $\varphi = 3\pi/7$ (curve 4) in the direction crosseing the interface in a maximum of the peak. Fig. 3.9*b* shows similar dependencies in a perpendicular direction passing through a minimum of the trough. Comparison of dependencies in Fig. 3.9 confirms the previously obtained fact that such nano-etching is performed more effectively in the regions of peaks than troughs when the incident angle of wave is equal to the critical angle.

From Fig. 3.8 and Fig. 3.9 one can conclude that under the condition of total internal reflection (i) the energy transfer occurs mainly along the horizontal coordinate (running waves are observed), (ii) the energy is practically not transmitted along the vertical coordinate (standing waves are observed), (iii) the reflected wave is partially penetrates SHAS volume decaying exponentially in the solution as afunction of distance from the interface.

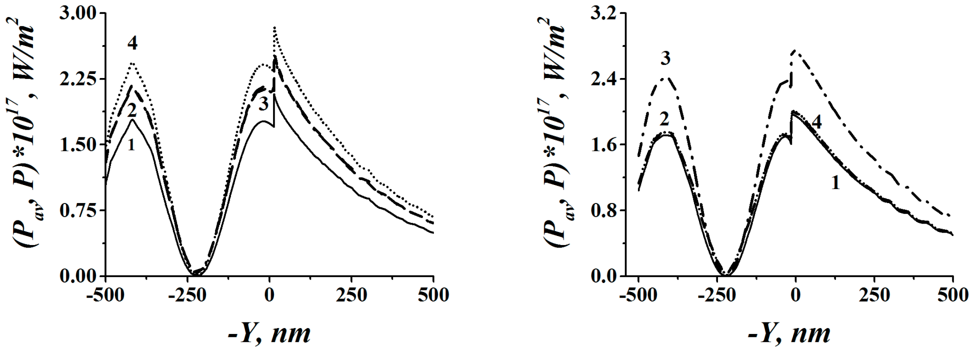

a *b*

Fig. 3.9. The distribution of the active component of the Poynting vector $\mathbf{P}_{av}$ (curve 1) and the total component of the Poynting vector **P** in the perpendicular direction to the “quartz-SHAS” interface as a function of the incident wave phase φ, where $\varphi = 0$ (curve 2); $\varphi = \pi/4$ (curve 3); $\varphi = 3\pi/7$ (curve 4). The perpendicular direction passes through the (a) peak; (b) trough. Wavelength in vacuum: $\lambda_{in} = 500$ nm, values of the quartz surface peaks height: $h = 28.2$ nm, the incident angle: $\theta_{in} = 65°$, the correlation length of the quartz rough surface: $\sigma = 23.7$ nm.

Fig. 3.10*a* shows the contrast *K* of the evanescent field at the “quartz-SHAS” interface as a function of correlation length of the rough surface σ of the quartz plate, determined for the standard deviation $\delta = 0.7$ nm (corresponding to the height of peaks (troughs) of quartz surface $h = 2$ nm) for different incident wavelengths $\lambda_{in} = 400$ nm (curve 1), $\lambda_{in} = 500$ nm (curve 2) and $\lambda_{in} = 600$ nm (curve 3). The correlation length increase with decrease of the contrast because in this case, the surface of quartz becomes more plane. The small changes in the *K* value in comparison with curve 1 can be associated with the spatial resonance of the incident wave on a rough sinusoidal surface. Note that in general curves 1-3 coincide, i.e. the contrast practically does not depend on the incident wavelength when the standard deviation δ is insignificant.

Thus, assuming that the parameter *K* is the integral characteristic of the field in the calculation cell and using Fig. 3.10*a* data, the relationship between the distribution of the field in the mentioned cell and the spatial frequency of the rough surface of quartz at the constant height *h* of peaks of the quartz sinusoidal surface can be established.

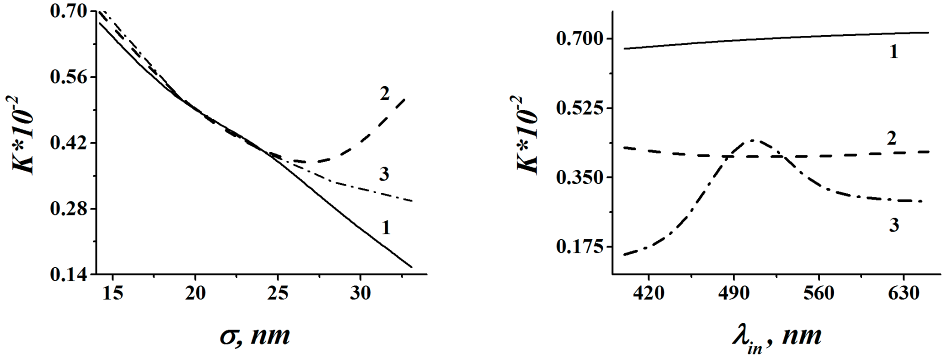

a *b*

Fig. 3.10. The contrast *K* of the evanescent field at the “quartz-SHAS” interface as a function of (a) the correlation length of the quartz rough surface σ, determined for the standard deviation δ= 0.7 nm (corresponding to the height of peaks (troughs) of the quartz surface h = 2 nm) for different lengths of the incident wavelength λ_{in} = 400 nm (curve 1), λ_{in} = 500 nm (curve 2), λ_{in} = 600 nm (curve 3) and the incident angle θ_{in} = 65°;
(b) the incident wavelength λ_{in} , determined for different correlation lengths of the quartz rough surface σ= 14.2 nm (curve 1), σ= 23.7 nm (curve 2), σ= 33.1 nm (curve 3) and the incident angle θ_{in} = 65°.

Fig 3.10*b* shows the contrast *K* of the evanescent field at the “quartz-SHAS” interface as a function of the incident wavelength λ_{in}, determined for the correlation length of the quartz rough surface σ= 14.2 nm (curve 1), σ= 23.7 nm (curve 2), σ= 33.1 nm (curve 3). Curves 1-3 practically do not depend on the incident wavelength (the small variations in the value of *K* (curve 3) also probably are assigned to the spatial resonance of the incident wave on a rough surface of the sinusoidal shape), when the standard deviation δ is less than (20-30) nm. This confirms the conclusion obtained for Fig. 3.10*a*: in this case, the contrast is practically independent of the incident wavelength.

Fig 3.11 shows the contrast *K* of the evanescent field at the “quartz-SHAS” interface as a function of the height *h* of quartz surface peaks, determined for the incident wavelength λ_{in} = 500 nm for profiles with the same spatial frequency, corresponding to the correlation length of the sinusoidal quartz surface σ= 23.7 nm. Obviously, the contrast value *K* increases with the increase of the parameter *h*. When the range of the argument corresponds to a linear change in the value of *K*. This allows using the effective control of the quartz etching process. From Fog.3.11 data it follows that to realize this etching, it is necessary to limit the height of peaks *h* to about 28 nm, which corresponds to a standard deviation of 10 nm for the sinusoidal surface.

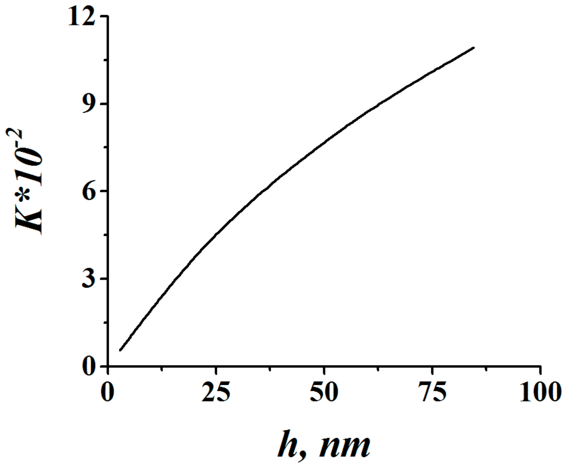

Fig. 3.11. The contrast *K* of the evanescent field at the "quartz-SHAS" interface asa function of the height h of quartz surface peaks, obtained for λ_{in} = 500 nm, θ_{in} = 65° for profiles with the same spatial frequency, corresponding to the period *T* = 125 nm (σ= 23.7 nm), of the sinusoidal quartz surface.

Fig. 3.12. shows the contrast *K* of the evanescent field at the "quartz-SHAS" interface, obtained for λ_{in} = 500 nm, θ_{in} = 65°, as a function of the height h of the peaks of the quartz surface, corresponding to different spatial frequencies of the spectrum of a randomly rough surface having Gaussian shape of the correlation function with the specified length of correlation σ= 14.2 nm and the standard deviation of surface profile δ= 10 nm. In this case, each spatial harmonic corresponds to its own correlation length σ and the height h of the quartz surface peaks. At the same time, the height h of each harmonic was determined according to Eq. (3.23), and the harmonics were selected in such a way that their frequencies were within the width of the spatial spectrum function Eq.(3.23).

Thus, the dependence showed in Fig. 3.12 gives an opportunity to analyze the contribution of various spatial frequencies of the spectrum of the rough surface to the contrast *K* of the evanescent field. The presented dependence shows that the contribution of various harmonics is approximately the same in almost the entire range of investigated frequencies. The abrupt change in the right side of the dependence shown in Fig. 3.12, can be associated with the spatial resonance of the incident wave on the sinusoidal rough surface which has already been mentioned earlier (Fig. 3.10).

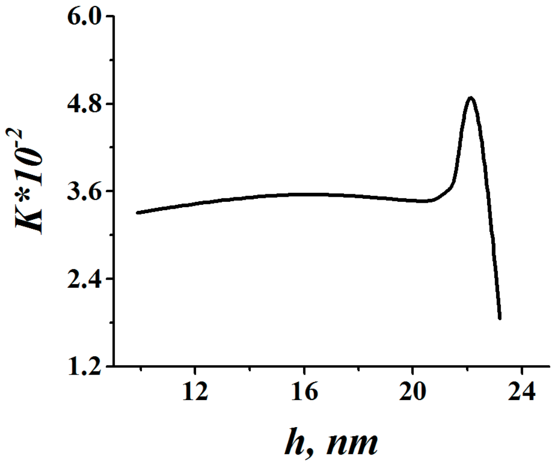

Fig. 3.12. The contrast K of the evanescent field at the "quartz-SHAS" interface, obtained for λ_{in} = 500 nm, θ_{in} = 65°, as a function of the height h of quartz surface peaks, corresponding to different spatial frequencies of the spectrum of a randomly rough surface having Gaussian shape of the correlation function at σ= 14.2 nm and δ= 10 nm.

Fig. 3.13 shows the two-dimensional distribution of the amplitude of evanescent field strength (gray background) and the Poynting vector flows (arrows), obtained for the height of peaks of the sinusoidal surface h = 28.2 nm, the incident angle θ_{in} = 65°, the wavelength λ_{in} = 500 nm, the width of the calculation cell w = 500 nm. As can be seen from the figure: (i) the distribution of field strength in the near zone of the "quartz-SHAS" interface repeats the shape of quartz surface, (ii) the Poynting vector flows (throughout the calculated region, as well as in Figure 3.3) indicate that the energy transfer occurs mainly along the horizontal coordinate; the energy is practically not transmitted along the vertical coordinate; the reflected wave partially penetrates SHAS volume decaying exponentially in the solution with distance from the interface.

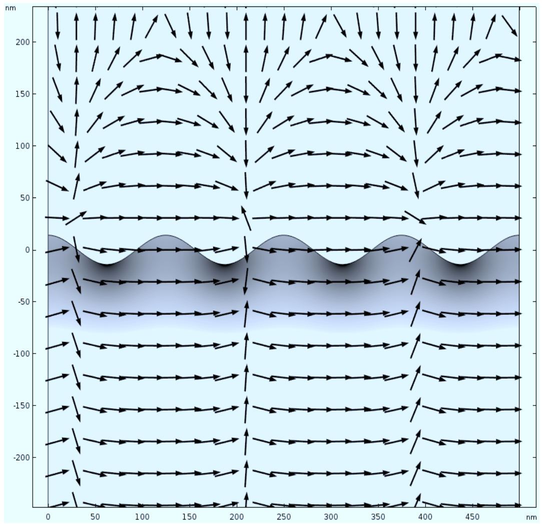

Fig. 3.13. The two-dimensional distribution of the amplitude of the evanescent field strength (gray background) and the flows of the Poynting vector (arrows), obtained fro the height of peaks on the sinusoidal surface $h = 28.2$ nm, the incident angle $\theta_{in} = 65°$, the wavelength $\lambda_{in} = 500$ nm, the width of the calculation cell $w = 500$ nm, the correlation length of sinusoidal quartz surface $\sigma =$ 23.7 nm.

Summary

As a result of the analysis of the propagation of a light wave that falls to the surface of a sinusoidal quartz plate (it propagates from the quartz side) the relation of the contrast of the field formed by the incident wave with a single spatial frequency of the quartz surface profile is obtained. It is determined that the contribution of each spectral component of the spatial spectrum of a randomly rough surface having Gaussian form of the correlation function is almost identical within the width of the spatial spectrum of this surface, except for the spatial frequencies which have the resonance with the wavelength of incident radiation. This gives an idea of the possibility of the practical application of this phenomenon, for example, for the photochemical sub-nano-polishing of the quartz surface.

Thus, under the condition of a total internal reflection of light ($\theta_{in} = \theta_{cr} = 65°$), when the standard deviation of the surface profile is insignificant (below 10 nm) and the incident wavelength is much larger than the correlation length of the sinusoidal quartz surface, the light scattering by quartz surface with sinusoidal profile determines the following effects: flows of energy (the Poynting vector flows) have reaction on a roughness only near the quartz surface. As the phase of the incident wave changes, its maximum amplitude value (crest) drifts along the "quartz-SHAS" interface, creating optimal conditions for sub-nano-polishing of this surface. At the same time, the amplitude of the energy oscillations in the region of peaks is greater than in the region of troughs. The transfer of energy occurs mainly along the horizontal coordinate. There is practically no energy transfer along the vertical coordinate. The reflected wave partially penetrates SHAS volume decaying exponentially in the solution with distance from the interface.

3.3 Computation of evanescent wave parameters in the near zone of quartz rough surface, covered with a layer of sodium hypochlorite aqueous solution, which has a profile described by the random function having a Gaussian spatial correlation function

The aim of this section is twofold: (i) a description of the peculiarities of the numerical model of light scattering by a rough surface of a quartz coated by SHAS with a profile described by a random function having a Gaussian spatial correlation function; (ii) reviewing the results of the simulation of indicated scattering in order to obtain the relation between parameters of the electromagnetic field and parameters of the spatial spectrum of the quartz rough surface profile having a Gaussian spatial correlation function.

3.3.1. Numerical model features

Let's consider the modified 2D cell presented in Fig. 3.2, in which the "quartz-SHAS" interface now has a shape described by a random function. Fig. 3.14 shows the 2D cell for calculating the parameters of the evanescent field in the near-field region of the quartz rough surface in which the "quartz-SHAS" interface is a one of random profile realized using a Gaussian spatial correlation function. The description of the calculated area (Fig. 3.14) is similar to the description of the calculation cell (Fig. 3.5), except the following features: (i) the profile of the quartz rough surface is characterized by roughness parameters δ and σ; (ii) there are no signs of pre-processing (polishing) of the quartz surface, i.e. there is no dominance of peaks or troughs.

To create the mentioned profile, the following features were taken into account: (i) the random amplitudes of the spectral components of the spatial profile spectrum have a standard law of normal probability distribution; (ii) random phases of the spectral components of the spatial profile spectrum have a uniform probability distribution in an interval from 0 to 2π; (iii) the distribution of the amplitudes of the spectral components in the spatial spectrum of rough surface profile with a specified correlation length is defined by a filtering function having the form of Gauss function. In this case, the Gauss filtering function is determined in accordance with Eq. (3.23). Note that in this case, the correlation length of the rough surface of quartz corresponds to the value of the correlation function argument, at which this correlation function decreases by a factor of e.

For the calculations, the special software was developed that implements the solution of Maxwell's equations using the finite element method.

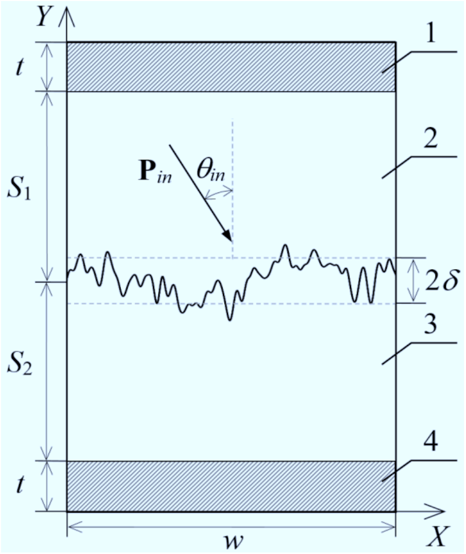

Fig. 3.14. The two-dimensional cell used to calculate evanescent field parameters in the near-field region of the quartz rough surface coated by SHAS with a profile described by a random function. 1,2,3,4 is the region of the upper absorbing layer, the quartz layer, the layer of the SHAS, the region of the lower absorbing layer, respectively.

3.3.2 Results and analysis

Fig. 3.15 shows the distribution of electric field strength along the “quartz-SHAS” interface (the scale is located on the left side) at the different incident angles: $\theta_{in} = 0°$

(curve 1), θ_{in} = 65° (curve 2), θ_{in} = 80° (curve 3). Fig. 3.15 also shows the distribution of the profile height h along this interface (the scale is located on the right side, curve 4), which is measured from the middle line. This profile form is described by the random function, which has a Gaussian correlation function with parameters: standard deviation δ= 10 nm, length of the correlation σ= 13.5 nm. All the graphs of electric field strength were obtained for the incident wavelength in a vacuum λ_{in} = 500 nm.

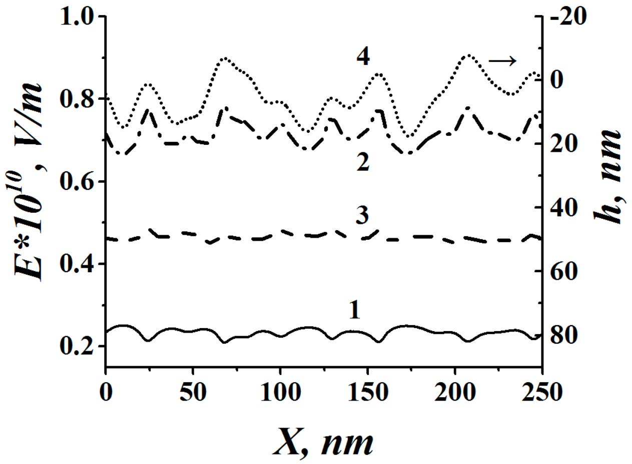

Fig. 3.15. The distribution of electric field strength along the "quartz-SHAS" interface (the scale is located on the left side) at the different incident angles: θ_{in} = 0° (curve 1), θ_{in} = 65° (curve 2), θ_{in} = 80° (curve 3). The distribution of the profile height h (curve 4) along interface (the scale is located on the right side), which is described by the random function which has a Gaussian correlation function with parameters: δ= 10 nm, σ= 13.5 nm. The incident wavelength: λ_{in} = 500 nm.

When the incident angle is equal to critical (θ_{in} = 65°), the spatial profile and the curve of the field strength along the "quartz-SHAS" interface will repeat each other. Thus, the spatial profile (curve 4) and distribution of the field (curve 2), in general, will repeat each other, therefore the maximums and minimums of the field will match with the peaks and troughs of the spatial profile. Thus, photodissociation of chlorine molecules will take place in the peak areas of quartz rough surface and therefore the surface will be etched mainly in the peak areas but not in the troughs. The excitation of the sample by light at other angles, as can be shown by the comparison of the spatial profile of the sample with the corresponding distributions of electric field strength along this interface, is inappropriate in terms of nano-polishing of the quartz rough surface, because the maximums and minimums of the field will no longer match with the maximums and minimums of the profile. Thus, the realization of nano-etching of the quartz rough surface, covered by SHAS, has to be performed with by excitation of the sample by light at a critical angle.

When the incident angle of the beam is determined, it is necessary to find out in what range of δ parameter it is reasonable to perform nano-polishing. Fig. 3.16 shows the distribution of the electric field strength along the "quartz-SHAS" interface with a profile described by the random function, which has a Gaussian correlation function, at different values of the quartz surface height standard deviation δ, when the angle of plane wave incidence is equal to $\theta_{in} = 65°$ and incident wavelength $\lambda_{in} = 500$ nm. According to Fig. 3.16, at different values of δ parameter the distribution of maximums and minimums arrangements of the electric field strength along the interface does not change its own location and generally repeats the shape of quartz rough surface profile.

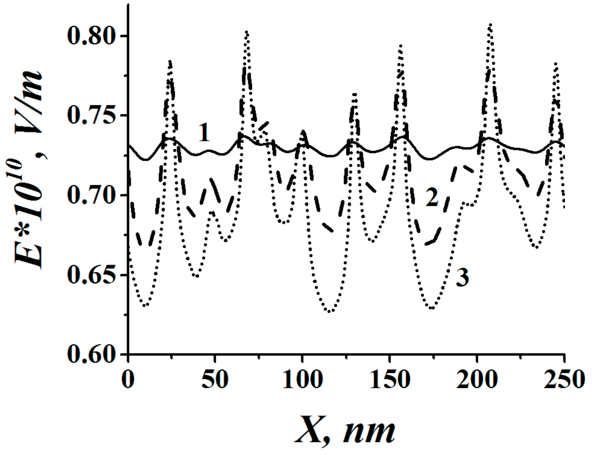

Fig. 3.16. The distribution of the electric field strength along the "quartz-SHAS" interface with a profile described by the random function, which has a Gaussian correlation function, at different values of the quartz surface height standard deviation: $\delta = 1$ nm (curve 1), $\delta = 10$ nm (curve 2), $\delta = 30$ nm (curve 3). The incident wavelength: $\lambda_{in} = 500$ nm, the incident angle: $\theta_{in} = 65°$, the correlation length of the quartz rough surface: $\sigma = 13.5$ nm.

However, as it will be shown below (Fig. 3.20), with $\delta > 10$ nm the dependence of the field contrast becomes nonlinear, which in turn will allow providing uniform etching of the rough surface. Numerical calculations show that near-field nano-local etching of quartz is reasonable to perform with parameter $\delta \leq 10$ nm.

Fig. 3.17 shows the distribution of the active component of the Poynting vector $\mathbf{P}_{av}$ (curve 1) and the total component of the same vector **P** along the “quartz-SHAS” interface which depend on the incident wave phase φ, where $\varphi = 0$ (curve 2); $\varphi = \pi/4$ (curve 3); $\varphi = 3\pi/7$ (curve 4) for the profile described by the random function, which has a Gaussian correlation function, with parameters: standard deviation δ= 10 nm, length of the correlation σ= 13.5 nm. The angle of plane wave incidence $\theta_{in} = 65°$ and incident wavelength $\lambda_{in} = 500$ nm.

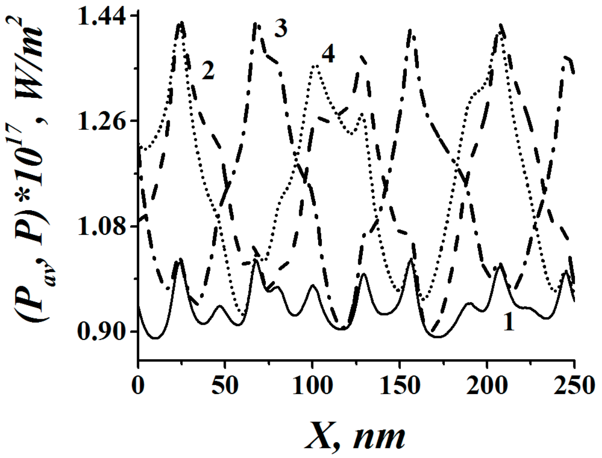

Fig. 3.17. The distribution of the active component of the energy density of the Poynting vector $\mathbf{P}_{av}$ (curve 1) and the total component of the energy density of the Poynting vector **P** along the “quartz-SHAS” interface obtained for different the incident wave phases φ, where $\varphi = 0$ (curve 2); $\varphi = \pi/4$ (curve 3); $\varphi = 3\pi/7$ (curve 4), for the profile described by the random function which has a Gaussian correlation function with parameters: δ= 10 nm, σ= 13.5 nm. The angle of plane wave incidence $\theta_{in} = 65°$ and incident wavelength $\lambda_{in} = 500$ nm.

Note that the distribution of the oscillation amplitude of the vector $\mathbf{P}_{av}$ along the “quartz-SHAS” interface is similar to the distribution of the oscillation amplitude of the vector **E** (suppose $K \sim h$) and repeats the shape of the surface profile, when the sample is excited by light at a critical angle. On the other hand, the Poynting vector **P** consists of the sum of vectors $\mathbf{P}_{av}$ and $\mathbf{P}_{var}$, therefore, it depends on the phase φ of the incident wave that changes in time (Fig. 3.17). Thus, with the change in the phase of the incident wave, its maximum value (the crest of the vector **P** distribution) drifts along the “quartz-SHAS” interface creating optimal conditions for sub-nano-polishing along the entire surface.

The fact of the nano-etching possibility of this surface should be clarified since it is necessary to perform etching the peaks, but not the troughs. Fig. 3.18*a* shows the distribution of the active component of the Poynting vector $\mathbf{P}_{av}$ (curve 1) and the total component of the Poynting vector **P** in the perpendicular direction to the "quartz-SHAS" interface as a function of the incident wave phases φ, where $\varphi = 0$ (curve 2); $\varphi = \pi/4$ (curve 3); $\varphi = 3\pi/7$ (curve 4) in the direction crossed the interface in a maximum of the peak. Fig. 3.18*b* shows similar dependencies in a perpendicular direction passing through a minimum of the trough. Comparison of dependencies shown in Fig. 3.18 demonstrates that the nano-etching is performed more effectively in the regions of peaks than troughs, when the incidence angle is equal to the critical angle, as a result of the higher average value of the active component of the Poynting vector $\mathbf{P}_{av}$.

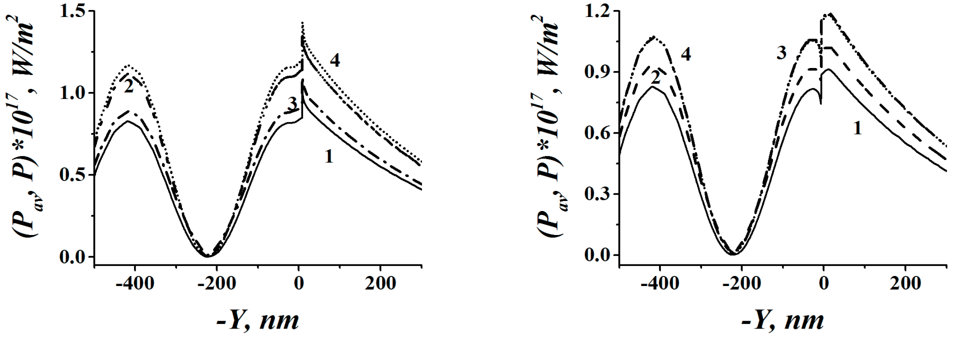

a *b*

Fig. 3.18. The distribution of the active component of the Poynting vector $\mathbf{P}_{av}$ (curve 1) and the total component of the Poynting vector **P** in the perpendicular direction to the "quartz-SHAS" interface obtained for different the incident wave phases φ, where $\varphi = 0$ (curve 2); $\varphi = \pi/4$ (curve 3); $\varphi = 3\pi/7$ (curve 4). The perpendicular direction passes through the (a)peak ; (b) the trough. Wavelength in vacuum: $\lambda_{in} = 500$ nm, the standard deviation of the quartz surface height: $\delta = 10$ nm, the incident angle $\theta_{in} = 65°$, the correlation length of the quartz rough surface :$\sigma = 13.5$ nm.

Considering data of Fig. 3.17 and Fig. 3.18 allows to conclude that under the condition of total internal reflection (i) the energy transfer occurs mainly along the horizontal coordinate (running waves are observed), (ii) the energy is practically not transmitted along the vertical coordinate (standing waves are observed), (iii) the reflected wave is partially penetrates SHAS volume decaying exponentially in the solution as a function of distance from the interface.

Fig. 3.19a shows the contrast K of the evanescent field, averaged over the ensemble of realization, at the “quartz-SHAS” interface with a profile described by the random function, which has a Gaussian correlation function, as a function of the length of the surface correlation σ of the quartz plate, provided that the standard deviation $\delta = 1$ nm and the incident angle $\theta_{in} = 65°$ for different scattered wavelengths: $\lambda_{in} = 400$ nm (curve 1), $\lambda_{in} = 500$ nm (curve 2) and $\lambda_{in} = 600$ nm (curve 3). The contrast K decrease with increase of the correlation length σ, because in this case, the quartz surface becomes more flat. In addition, the contrast is almost independent of the incident wavelength, when the standard deviation is small.

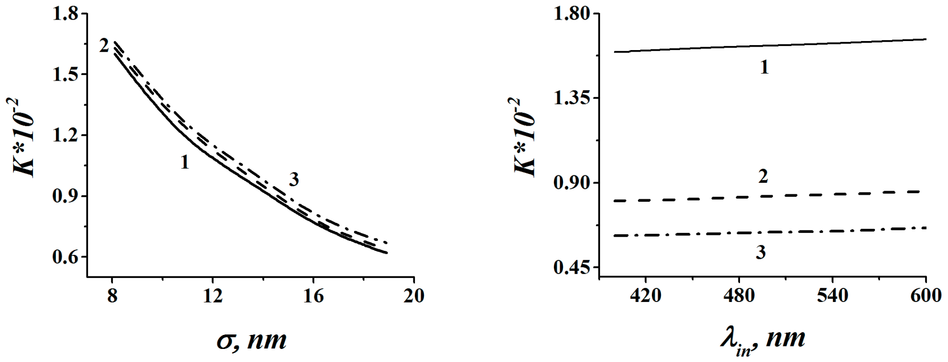

a *b*

Fig. 3.19. The contrast K of the evanescent field, averaged over the ensemble of realization, at the “quartz-SHAS” interface with a profile described by the random function, which has a Gaussian correlation function, as a function of (a)the length of the surface correlation σ of the quartz plate, obtained for the standard deviation $\delta = 1$ nm and the incident angle $\theta_{in} = 65°$ for different scattered wavelengths $\lambda_{in} = 400$ nm (curve 1), $\lambda_{in} = 500$ nm (curve 2), $\lambda_{in} = 600$ nm (curve 3);

(b) the different incident wavelengths λ_{in}, obtained for the correlation length of the quartz rough surface $\sigma = 8.1$ nm (curve 1), $\sigma = 13.5$ nm (curve 2), $\sigma = 18.9$ nm (curve 3).

Fig 3.19b shows the contrast K of the evanescent field, averaged over the ensemble of realization, at the “quartz-SHAS” interface as a function of the incident wavelength λ_{in}, obtained for the standard deviation $\delta = 1$ nm and the correlation length of the quartz rough surface $\sigma = 8.1$ nm (curve 1), $\sigma = 13.5$ nm (curve 2), $\sigma = 18.9$ nm (curve 3). Curves 1-3 practically do not depend on the incident wavelength, when the standard deviation δ is small. This confirms the conclusion obtained for Fig. 3.19a.

Fig 3.20 shows the contrast K of the evanescent field at the “quartz-SHAS” interface with a profile described by the random function, which has a Gaussian correlation function, plotted as a function of the standard deviation δ of quartz surface height, obtained for λ_{in} = 500 nm, the correlation length of the quartz rough surface σ= 13.5 nm, the incident angle θ_{in} = 65°. It is evident, that the contrast value *K* increases with the increase of the parameter δ. When the range of variation of the argument corresponds to a linear change in the value of *K*, it is possible to control effectively the etching process of quartz. It follows from the Figure 3.20 that to realize this possibility the standard deviation of the surface height should not exceed the 10 nm.

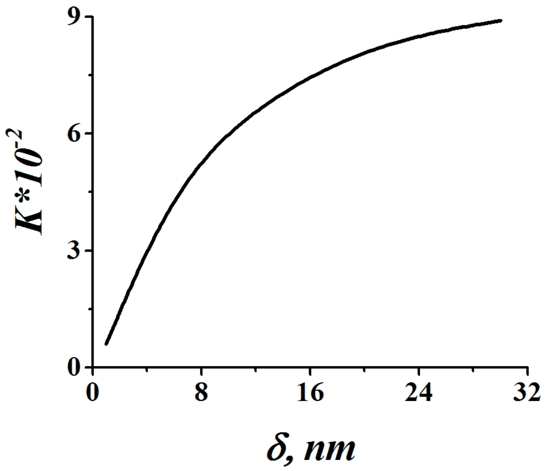

Fig. 3.20. The contrast *K* of the evanescent field at the "quartz-SHAS" interface with a profile described by the random function, which has a Gaussian correlation function, plotted as a function of the standard deviation δ of the quartz surface height, obtained for λ_{in} = 500 nm, the correlation length of the quartz rough surface σ= 13.5 nm, the incident angle θ_{in} = 65°.

Summary

The propagation of a light wave that incident onto the surface of a quartz plate from the quartz side with a profile described by the random function, which has a Gaussian correlation function, is analyzed. As a result, the dependence of the contrast of the field formed by the incident wave on a width of the spatial spectrum of the rough surface is obtained. This allow suggesting the practical application of this phenomenon, for example, for the photochemical sub-nano-polishing of the quartz surface.

Thus, under the condition of a total internal reflection of light ($\theta_{in} = \theta_{cr}$ = 65°), when the standard deviation of the surface profile is small (below 10 nm) and the incident wavelength is much larger than the correlation length of the sinusoidal quartz surface, the light scattering by quartz surface with sinusoidal profile determines the following findings: flows of the energy (the Poynting vector flows), caused by the incident wave, influence on a roughness only near the quartz surface. As the phase of the incident wave changes, its maximum amplitude value (crest) drifts along the “quartz-SHAS” interface, creating optimal conditions for sub-nano-polishing of this surface. In this case, the amplitude of the energy oscillations in the peak regions is larger compared to those in the trough regions. The transfer of energy occurs mainly along the horizontal coordinate. There is practically no energy transfer along the vertical coordinate. The reflected wave partially penetrates SHAS volume, decaying exponentially in the solution as a function of distance from the interface.

It should be noted that the feature of light scattering on a rough surface with a random profile should be calculated for a large number of realizations of the roughness profile. Accordingly, it requires a significant amount of data for calculations and, as a result, a long time for simulations. As it will be shown in the next section, the solution can be found in a form of a certain function of the quartz rough surface profile as periodically repeating peaks and troughs that would be equivalent to the quartz rough surface with a random profile function in terms of the contrast of the evanescent field.

3.4. Calculation of evanescent wave parameters in the near zone of quartz rough surface, covered with a layer of sodium hypochlorite aqueous solution, which has a profile in the form of periodically repeated triangular peaks and troughs

The aims of this section is twofold: (i) to describe the features of the numerical model of light scattering by a quartz rough surface coated by SHAS with a profile in the form of triangular peaks and troughs which are periodically repeated; (ii) to analyze the results of the simulation of indicated scattering in order to obtain the relation between parameters of the electromagnetic field and parameters of the specified form of a rough surface.

The main factors that prompted a further search for an equivalent model of the scattering of light on a quartz rough surface covered by SHAS with a profile described by a random function are following (i) the calculations based on one realization of the random profile do not allow to obtain accurate results (to obtain reliable results with the target accuracy, it is necessary to perform the calculations for a large number of such realizations); (ii) the width of the calculation cell should be sufficient to take into account the basic spatial harmonics and to obtain the required resolution in the spatial spectrum of the surface (in our case not less than 1 μm); (iii) the construction of a calculation grid near a rough surface requires a large number of finite elements. This requires a significant efforts in calculations, as a result, we suggested an idea for the simplification of a model of a quartz rough surface, coated with SHAS.

3.4.1. Numerical model features

Consider the modified numerical model presented in Fig. 3.2, in which the "quartz-SHAS" interface now has a profile in the form of periodically repeated peaks and troughs with a triangular shape. That profile form is selected for the following reasons: (i) the rough quartz surface without any features of pre-processing (polishing) of the quartz surface is considered, i.e. there are no dominance of peaks or troughs; (ii) the triangular form of peaks or troughs is one of the simplest forms of simulation of a quartz rough surface whose spatial spectrum can be well approximated by the spectrum of a random rough surface having a Gaussian correlation function; (iii) numerical simulation of the field distribution along a surface having peaks and troughs in the form of triangles is simpler and more efficient compared to other more complex forms.

Fig. 3.21 shows a two-dimensional cell for calculating the parameters of the evanescent field in the near-field region of the quartz rough surface with a profile in the form of peaks and troughs of triangular form.

The description of the calculated region (Fig. 3.21) is similar to the description of the calculation cell (Fig. 3.5), except for the following features: (i) parameters of roughness: the height h and the width a of a peak is denoted in Fig 3.21, a trough has the same parameters; (ii) the correlation length σ for such surface should be determined by the same principles as the correlation length of a random rough surface, whose spatial spectrum corresponds to Eq. (3.23); (iii) the replacement of a random spatial signal by a periodical one, which has specified width, leads to the occurrence of the filling factor of that periodic signal Q, whose value is chosen as follows: $Q = w/2a$; (iv) parameters of the quartz rough surface: h and $T = w/2$ can be directly related to the standard deviation of a rough surface height δ using the ratio:

$$\delta = h\sqrt{\frac{a}{3T}} = \frac{h}{\sqrt{3Q}} \tag{3.25}$$

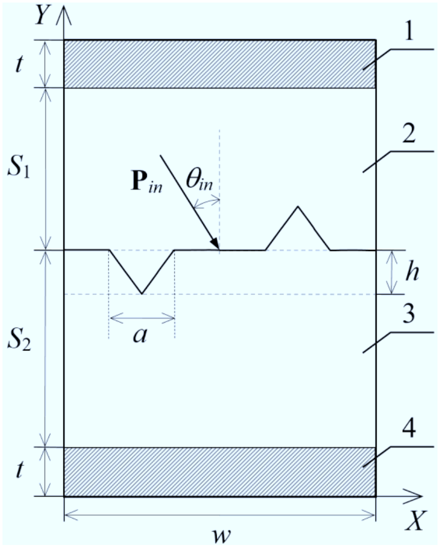

Fig. 3.21. Two-dimensional cell for calculating the parameters of the evanescent field in the near-field region of the quartz rough surface coated by SHAS with a profile in the form of peaks and troughs of triangular form. 1,2,3,4 is the region of the upper absorbing layer, the quartz layer, the layer of the SHAS, the region of the lower absorbing layer, respectively.

Note that in this case, the correlation length σ of the quartz rough surface corresponds to the value of the correlation function argument, at which this correlation function decreases in e times. In this case, the spatial energy spectrum $|s(\Delta k_x)|^2$ of a signal corresponding to the form of triangular peaks and troughs, which are periodically repeated, has the Gaussian shape of the spatial spectrum of a randomly rough surface if (i) their correlation lengths σ are equal; (ii) the height of the triangles h coincides with the standard deviation δ of a random rough surface. This allows us to assume that the results of calculations obtained for a rough surface in the form of triangular peaks and troughs replace the results obtained for a randomly rough surface with a spatial spectrum approximated by the Gauss function [13], if the choice of parameter Q is correct.

To perform the calculations, the special software was developed that implements the solution of Maxwell's equations using the finite element method.

3.4.2 Results and analysis

Fig. 3.22 shows the 2D evanescent field strength distribution (gray background) and the Poynting vector flows (arrows), obtained for the height of the triangular peaks and troughs of the quartz surface equal to $h = 35$ nm, when the incident angle $\theta_{in} = 65°$, the incident wavelength $\lambda_{in} = 500$ nm, the width of the calculation cell $w = 250$ nm, the filling factor of the triangular peaks and troughs of the quartz surface $Q = 4$. As can be seen from the Fig.3.22: (i) the distribution of the field strength in the near zone of the "quartz-SHAS" interface repeats the shape of the quartz surface, (ii) the flows of the Poynting vector (Fig. 3.22) indicate that the energy transfer occurs mainly along the horizontal coordinate; the energy is practically not transmitted along the vertical coordinate; the reflected wave partially penetrates in SHAS volume, decaying exponentially with distance from the interface. Flows of the energy (the Poynting vector flows) have a reaction on a roughness only near the quartz surface. In the case represented by Fig. 3.22 the field is more concentrated in the top region of the peaks.

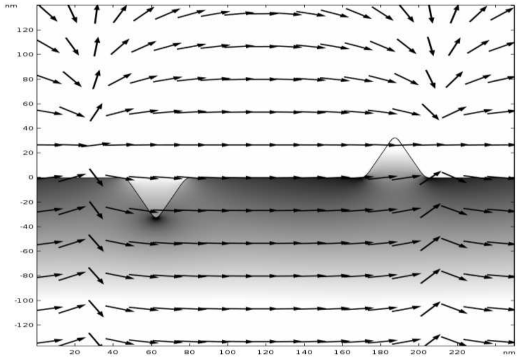

Fig. 3.22. The two-dimensional distribution of the amplitude of the evanescent field strength (gray background) and the flows of the Poynting vector (arrows), provided that the height of the triangular peaks and troughs of the quartz surface equal to $h = 35$ nm, then the incident angle $\theta_{in} = 65°$, the incident wavelength $\lambda_{in} = 500$ nm, the width of the calculation cell $w = 250$ nm, the filling factor of the triangular peaks and troughs of the quartz surface $Q = 4$.

Fig. 3.23 shows the distribution of electric field strength along the "quartz-SHAS" interface with a profile in the form of periodically repeated triangular peaks and troughs, obtained for different values of the incident angle θ_{in}. In this case, as well as for Fig. 3.6, one can conclude that the nano-etching of the quartz rough surface covered with SHAS should be performed when the sample is irradiated by light at a critical angle.

Fig. 3.24 shows the distribution of electric field strength along the "quartz-SHAS" interface with a profile in the form of periodically repeated triangular peaks and troughs at different values of the quartz surface peaks height h, when the angle of plane wave incidence is equal to $\theta_{in} = 65°$, the filling factor of the triangular peaks and troughs of the quartz surface $Q = 4$. According to Fig. 3.24, at different values of the parameter h, the distribution of the maximums and minimums of electric field strength along the interface does not change its own location and generally repeats the shape of the quartz rough surface profile.

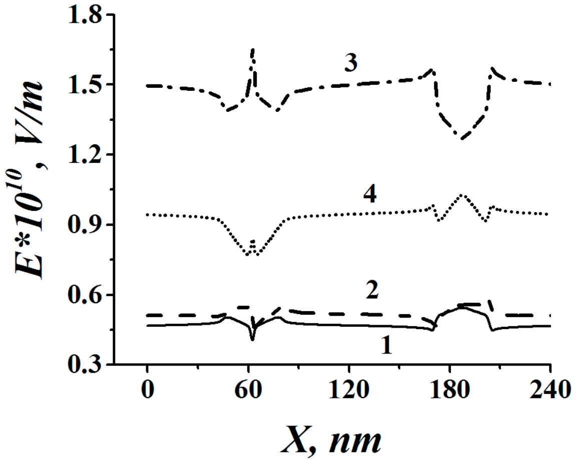

Fig. 3.23. The distribution of the electric field strength along the "quartz-SHAS" interface with a profile in the form of periodically repeated peaks and troughs with a triangular shape, obtained for different values of the incident angle: $\theta_{in} = 0°$ (curve 1), $\theta_{in} = 30°$ (curve 2), $\theta_{in} = 65°$ (curve 3), $\theta_{in} = 80°$ (curve 4). The incident wavelength $\lambda_{in} = 500$ nm, the height of triangular peaks and troughs of the quartz surface $h = 35$ nm, the filling factor of triangular peaks and troughs of the quartz surface $Q = 4$.

However, as it will be shown below (Fig. 3.28), with $h = 105$ nm the dependence of the field contrast on the profile height becomes nonlinear and the distribution of the amplitude values of the field strength is not proportional to the distribution of the profile height. As a result, it is not possible to provide uniform etching of the rough surface. Numerical calculations show that near-field nano-local etching of quartz (provided that the rough surface of quartz is in the form of triangular peaks and troughs, which periodically repeated) is reasonable to perform when the parameter $h \leq 35$ nm. Note that compared to the case described in Fig. 3.7, the effectiveness of nano-etching is much better, the field is more concentrated in the top region of the triangular peaks.

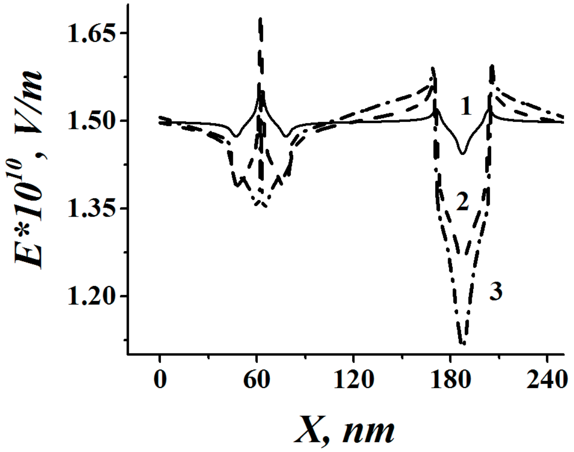

Fig. 3.24. The distribution of the electric field strength along the “quartz-SHAS” interface with a profile in the form of periodically repeated triangular peaks and troughs, obtained for different values of the quartz surface peaks height: $h = 3.5$ nm (curve 1), $h = 35$ nm (curve 2), $h = 105$ nm (curve 3). The incident wavelength $\lambda_{in} = 500$ nm, the incident angle: $\theta_{in} = 65°$, the filling factor of the triangular peaks and troughs of the quartz surface $Q = 4$.

Fig. 3.25 shows the distribution of the active component of the Poynting vector $\mathbf{P}_{av}$ (curve 1) and the total component of the Poynting vector $\mathbf{P}$ along the “quartz-SHAS” interface obtained for different incident wave phases φ, where $\varphi = 0$ (curve 2); $\varphi = \pi/4$ (curve 3); $\varphi = 3\pi/7$ (curve 4), for a profile in the form of periodically repeated triangular peaks and troughs. In this case, as well as for Fig. 3.8, it is possible to state that with the change in the phase of the incident wave, its maximum value (the crest of the vector $\mathbf{P}$ distribution) drifts along the “quartz-SHAS” interface creating optimal conditions for sub-nano-polishing along the entire surface. At the same time, Fig. 3.26 shows that the profile peaks are polished at the high intensity.

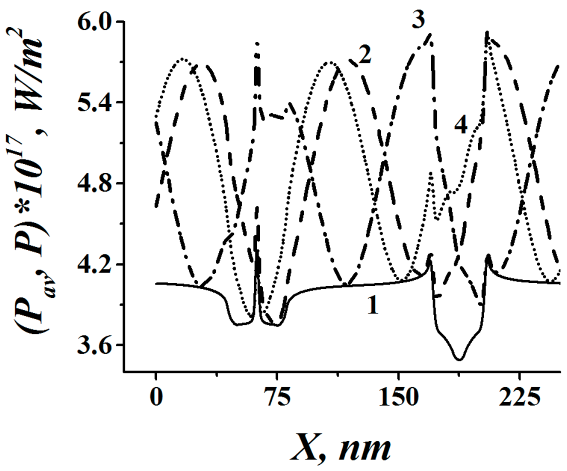

Fig. 3.25. The distribution of the active component of the Poynting vector $\mathbf{P}_{av}$ (curve 1) and the total component of the Poynting vector **P** along the "quartz-SHAS" interface obtained for different incident wave phases φ, where $\varphi = 0$ (curve 2); $\varphi = \pi/4$ (curve 3); $\varphi = 3\pi/7$ (curve 4), for a profile in the form of periodically repeated triangular peaks and troughs. The incident wavelength $\lambda_{in} = 500$ nm, the height of the triangular peaks and troughs of the quartz surface $h = 35$ nm, the incident angle: $\theta_{in} = 65°$, the filling factor of the triangular peaks and troughs of the quartz surface $Q = 4$.

Fig. 3.26*a* shows the distribution of the active component of the energy density of the Poynting vector $\mathbf{P}_{av}$ (curve 1) and the total component of the energy density of the Poynting vector **P** in the perpendicular direction to the "quartz-SHAS" interface, obtained for different incident wave phases φ, where $\varphi = 0$ (curve 2); $\varphi = \pi/4$ (curve 3); $\varphi = 3\pi/7$ (curve 4) and that direction crosses the interface in a maximum of the peak. Fig. 3.26*b* shows similar dependencies in a perpendicular direction passing through a minimum of the trough. Analysis of dependencies in Fig. 3.26*a* and in Fig. 3.26*b* confirms the fact that such nano-etching is performed more effectively in the regions of peaks than troughs when the incident angle is equal to critical angle: the profile peaks are polished at the high intensity compared to the case of troughs, due to the higher average value of the active component of the Poynting vector $\mathbf{P}_{av}$. By comparison of data shown in Fig. 3.9 and Fig. 3.26, one can conclude that nano-etching is more effective when the quartz surface has a profile in the form of triangular peaks and troughs which are periodically repeated.

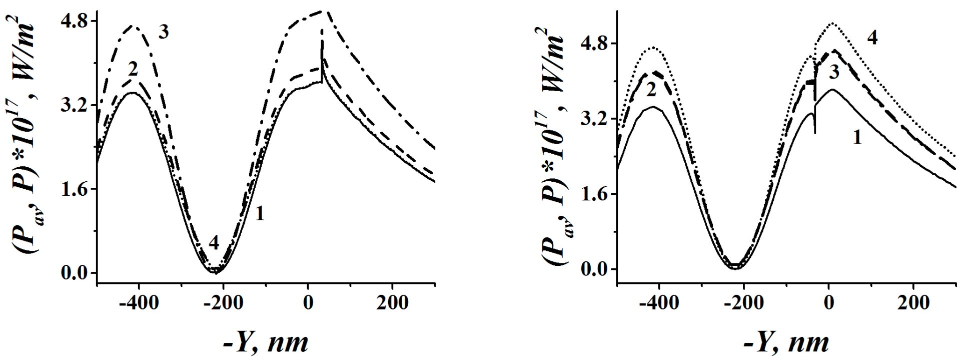

a *b*

Fig. 3.26. The distribution of the active component of the Poynting vector $\mathbf{P}_{av}$ (curve 1) and the total component of the Poynting vector **P** in the perpendicular direction to the “quartz-SHAS” interface, obtained for different incident wave phases φ, where $\varphi = 0$ (curve 2); $\varphi = \pi/4$ (curve 3); $\varphi = 3\pi/7$ (curve 4). The perpendicular direction passes through the peak (*a*); trough (*b*). Wavelength in vacuum: $\lambda_{in} = 500$ nm, the height of the peaks of the quartz surface: $h = 35$ nm, the incident angle: $\theta_{in} = 65°$, the filling factor of the triangular peaks and troughs of the quartz surface $Q = 4$.

Considering the data shown in Fig. 3.25 and Fig. 3.26 (like it was for Fig. 3.8 and Fig. 3.9) allows to conclude that under the condition of total internal reflection (i) the energy transfer occurs mainly along the horizontal coordinate (running waves are observed), (ii) the energy is practically not transmitted along the vertical coordinate (standing waves are observed), (iii) the reflected wave partially penetrates SHAS volume, decaying exponentially in solution as it moves away from the interface. Thus, the flows of the energy caused by the incident wave have a reaction on a roughness only near the quartz surface. This influence is more significant when the profile has a form of periodically repeated triangular peaks and troughs compared to the case of a sinusoidal profile shape.

Fig. 3.27*a* shows the contrast *K* of the evanescent field at the “quartz-SHAS” interface with a profile in the form of periodically repeated triangular peaks and troughs as a function of the correlation length σ of the quartz plate, obtained for different standard deviation $\delta = 0.29$ nm (it corresponds to the height of the peeks (troughs) of the quartz surface $h = 1$ nm) and the incident angle $\theta_{in} = 65°$ for the incident wavelengths $\lambda_{in} = 400$ nm (curve 1), $\lambda_{in} = 500$ nm (curve 2) and $\lambda_{in} = 600$ nm (curve 3). The contrast *K* decreases with the correlation length increase because in this case, the surface of quartz becomes more flat. Also, the contrast practically does not depends on the incident wavelength, when the standard deviation δ is small.

Fig 3.27*b* shows the contrast *K* of the evanescent field at the "quartz-SHAS" interface with a profile in the form of periodically repeated triangular peaks and troughs as a function of the incident wavelength λ_{in}, obtained for the standard deviation δ= 0.29 nm (it corresponds to the height of peaks (troughs) of the quartz surface *h* = 1 nm) and the incident angle $\theta_{in} = 65°$ for different lengths of the surface correlation of the quartz plate σ= 14.2 nm (curve 1), σ= 23.7 nm (curve 2), σ= 33.1 nm (curve 3). Curves 1-3 practically do not depend on the incident wavelength, when the standard deviation δ is small. This confirms the conclusion obtained for Fig. 3.27*a*.

The comparison of the dependencies presented in Fig. 3.27 and Fig. 3.19 shows that at the same lengths of correlation, the contrast of the evanescent field for a randomly rough surface and for a surface in the form of triangular peaks and troughs has close values.

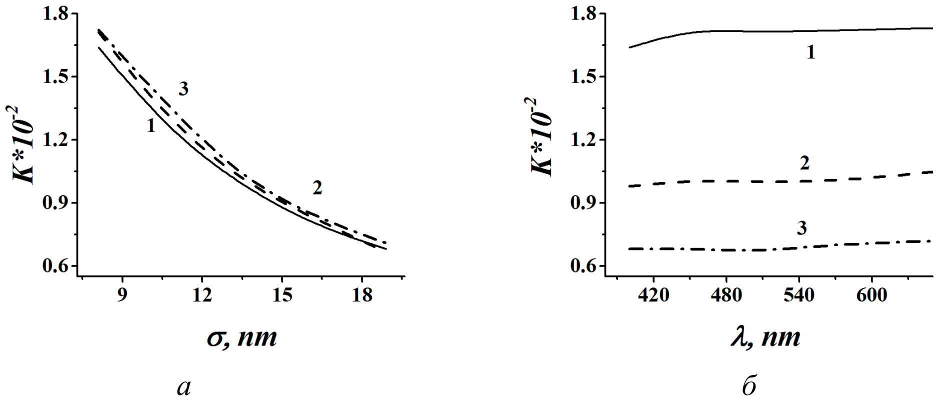

Fig. 3.27. The contrast *K* of the evanescent field at the "quartz-SHAS" interface with a profile in the form of periodically repeated triangular peaks and troughs as a function of (a) the length of the surface correlation σ of the quartz plate, obtained for the incident wavelength λ_{in} = 400 nm (curve 1), λ_{in} = 500 nm (curve 2), λ_{in} = 600 nm (curve 3);

(b) as a function of the incident wavelength λ_{in}, obtained for the length of the surface correlation of the quartz plate σ= 8.1 nm (curve 1), σ= 13.5 nm (curve 2), σ= 18.9 nm (curve 3). The standard deviation δ= 0.29 nm, the incident angle $\theta_{in} = 65°$, the filling factor of the triangular peaks and troughs of the quartz surface *Q* = 4.

This can be explained by the fact that the spatial spectrum of harmonics of a surface with triangular peaks (troughs) has the form close to the Gaussian shape of the random surface spectrum. Note that in this case, the filling factor of the triangular peaks (troughs) $Q = 4$.

Fig 3.28 shows the contrast K of the evanescent field at the "quartz-SHAS" interface with a profile in the form of periodically repeated triangular peaks and troughs asa function of the quartz surface peaks (troughs) height h, obtained for the incident wavelength $\lambda_{in} = 500$ nm, the length of the quartz rough surface correlation $\sigma = 13.5$ nm, the filling factor of the triangular peaks and troughs of the quartz surface $Q = 4$.

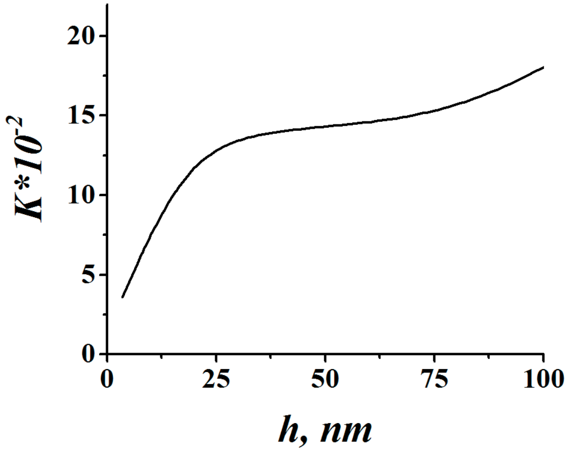

Fig. 3.28. The contrast K of the evanescent field at the "quartz-SHAS" interface with a profile in the form of periodically repeated triangular peaks and troughs as a function of the quartz surface peaks (troughs) height h, obtained for the incident wavelength $\lambda_{in} = 500$ nm, the length of the quartz rough surface correlation $\sigma = 13.5$ nm, the incident angle $\theta_{in} = 65°$, the filling factor of the triangular peaks and troughs of the quartz surface $Q = 4$.

Obviously, the contrast value K increases with the increase of the parameter h . At the same time, other parameters remain constant. When the range of variation of the argument corresponds to a linear change in the value of K, it allows effectively controlling the quartz etching process. As it follows from the figure 3.28 to realize this etching process, the height of the peaks h should be limited. Comparison of the dependences presented in Fig. 3.28 and Fig. 3.11, allows noting that the wave-like dependence in Fig. 3.28, is due to a more sharp change in the surface shape. The linear section of contrast change is within the range of changes in the height of peaks for $h \leq 20$ nm. Thus, the total change in the height of the surface profile from the lowest to the highest point for the given rough surface profile is in good agreement with the range of height change within the same linear section for the sinusoidal profile.

Fig 3.29 shows the contrast K of the evanescent field at the "quartz-SHAS" interface with a profile in the form of periodically repeated triangular peaks and troughs as a function of the quartz surface peaks filling factor Q, provided that the incident wavelength $\lambda_{in} = 500$ nm, the length of the quartz rough surface correlation $\sigma = 13.5$ nm, the incident angle $\theta_{in} = 65°$:(curve 1) for the cases when the standard deviation ($\delta = 1$ nm) is a constant; (curve 2) when the triangular peak height (h = 1 nm) is a constant.

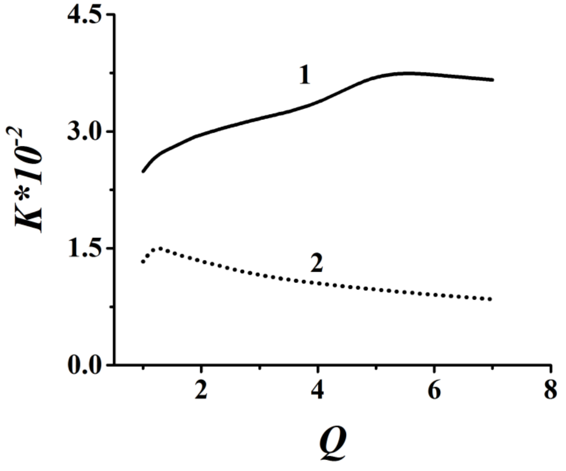

Fig. 3.29. The contrast K of the evanescent field at the "quartz-SHAS" interface with a profile in the form of periodically repeated triangular peaks and troughs as a function of the filling factor of the triangular peaks and troughs of the rough surface Q, obtained for the incident wavelength: $\lambda_{in} =$ 500 nm, the length of the quartz rough surface correlation: $\sigma = 13.5$ nm, the incident angle: $\theta_{in} =$ 65°, in cases when the standard deviation: ($\delta = 1$ nm) is a constant (curve 1) or when the triangular peak height (h = 1 nm) is a constant (curve 2).

In the first case (curve 1) at a constant width of the peaks (troughs) a, the height of peaks (troughs) $h = \delta\sqrt{3Q}$ as well as the width of the calculation cell w decrease with decrease of the parameter Q. Thus, with the decrease of the parameter Q, the surface becomes more flat, the number of harmonics in the spatial spectrum of the rough surface decreases and, as a result, the contrast also decreases. In the second case (curve 2) with the constant width a of peaks (troughs), the standard deviation $\delta = h/\sqrt{3Q}$ decrease, but the width of the calculation cell w increases with increase of the parameter Q . Thus, with the increase of the parameter Q, the surface becomes more flat and, as a result, the contrast also decreases.

The value of the parameter Q should be chosen in such a way that the number of harmonics forming the spatial spectrum of the profile in the form of triangular peaks (troughs) is sufficient to approximate the envelope of this spectrum to the Gaussian function of a random rough surface spectrum and to provide the contrast of the evanescent field near the “quartz-SHAS” interface that is the same for both types of surfaces. In both cases, the lengths of the correlation should be the same. The standard deviation of peaks height, when the profile is described by a random function, and the height of the peaks, when the profile has a triangular shape, should be identical too.

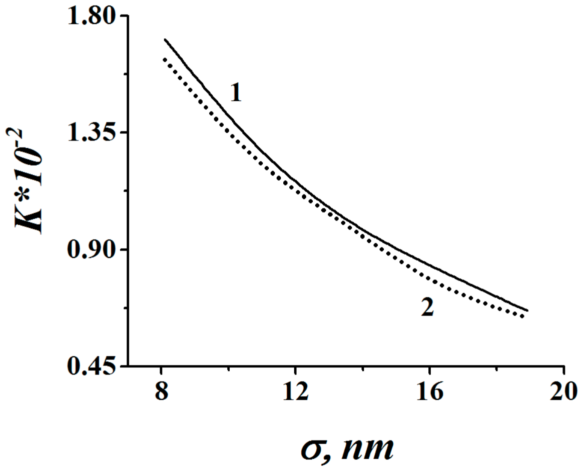

Fig. 3.30. The dependences of the evanescent field contrast K at the “quartz-SHAS” interface as a function of the correlation length of the quartz rough surface, obtained for a random surface profile with δ= 1nm (curve 1) and a triangular surface profile with the filling factor Q = 4 and the height of peaks (troughs) h = 1nm (curve 2) when the incident wavelength λ_{in} = 500 nm and the incident angle θ_{in} = 65°.

Thus, from Fig. 3.29 one can conclude that to achieve a better agreement of the contrast values shown in Fig. 3.19 and Fig. 3.27, the parameter $Q = 4$ should be selected when these requirements are satisfied. Fig. 30 presents the comparison of the dependences of the evanescent field contrast K at the “quartz-SHAS” interface as a function of the correlation length of the quartz rough surface, are obtained for a random surface profile with δ= 1nm (curve 1) and a triangular surface profile with the filling factor Q = 4 and the height of peaks (troughs) h = 1nm (curve 2) when the incident wavelength: $\lambda_{in} = 500$ nm and the incident angle: $\theta_{in} = 65°$.

Summary

The profile in the form of periodically repeated triangular peaks and troughs has been used to calculate the parameters of the evanescent field in the near-zone of the nano-irregularities of the rough surface of quartz, covered with SHAS. The value of the filling factor Q of the selected quartz rough surface profile was chosen. The contrast of the surface with such a profile is equal to the contrast for a randomly rough surface whose spatial spectrum is described by the Gaussian function with parameters corresponding to the following conditions: the height of triangular peaks (troughs) should be equal to the standard deviation of the random surface profile. The lengths of the correlation of such surfaces should be the same. Calculations show that the contrast for the profiles, which correspond to Fig. 3.19 and Fig. 3.27, coincide when the value of the filling factor is equal: Q = 4.

As a result of the analysis of the propagation of a light wave that insident onto the surface of a quartz plate with a profile in the form of periodically repeated triangular peaks and troughs, the relation of the contrast of the field formed by the incident wave with parameters of that rough surface is obtained. This allows suggesting the method of the nano-local etching of the quartz surface with a specified profile shape.

By using the light to excite the rough surface, from the side of quartz, under the condition of a total internal reflection of light ($\theta_{in} = \theta_{cr}$), in the case when the standard deviation of the surface profile is insignificant ($\delta \leq$ 10 nm) and the incident wavelength is much larger compared to the profile correlation length in the form of periodically repeated triangular peaks and troughs, the following results were obtained:

1) Energy transfer occurs mainly along the horizontal coordinate (running waves are observed); there is no energy transfer along the vertical coordinate (standing waves are observed); the reflected wave partially penetrates SHAS volume, decaying exponentially in solution with distance from the interface.

2) The flows of the energy (Poynting vector) caused by the incident wave have a reaction on a roughness only near the quartz surface.

3) Variation in the phase of the incident wave causes the change of the position of the Poynting vector maximum value that drifts along the "quartz-SHAS" interface. The amplitude of the energy fluctuations in the region of peaks is larger compared to those in the region of troughs. It creates optimal conditions for sub-nano-polishing of this surface.

4) A proper choice of the parameter *Q* allows the simulation of light scattering processes on a quartz rough surface by using a profile in the form of triangular peaks and troughs, which are periodically repeated, instead of a profile which is described by a random function that has a Gaussian spatial correlation function. This significantly reduces the complexity of numerical calculations.

Conclusions

The main condition for ensuring the high efficiency of photochemical nano-etching of a quartz surface, covered with SHAS, is the formation of an appropriate configuration of the evanescent electromagnetic field above the surface where the maximum field energy is concentrated near peaks of the relief, and the minimum is arranged near troughs of the relief. In this case, the process of the peaks etching is more intense than troughs etching, which, in turn, leads to a decrease in the height of the surface roughness.

The results obtained in this chapter show that there is a direct relationship between the parameters of the evanescent field occurring near the rough surface and the surface roughness parameters when the surface is exposed by a plane monochromatic electromagnetic wave. At the same time, one of the main criteria that ensures the conformance of the configuration of the evanescent field to the shape of the surface relief is the correct choice of the incident angle of light. In particular, at a critical angle of incidence, when the surface is excited by light from the quartz side and the conditions of total internal reflection are performed, the spatial distribution of the amplitude of the evanescent field formed along the surface matches with the shape of the surface relief, in such a way, that the maximums of the field are formed in the location of the surface peaks, and the minimums fields are arranged in the location of the troughs.

At the same time, the energy flows caused by the incident wave influence on a roughness only near the quartz surface. As the phase of the incident wave changes, its maximum amplitude value (crest) drifts along the "quartz-SHAS" interface. In this case, the amplitude of energy oscillations in the region of the peaks is larger than those in the region of the troughs, and that creates the optimal conditions for sub-nano-polishing of the surface. These findings as well as ensuring the linearity of the etching process, is possible only if the correlation length of the quartz rough surface and the standard deviation of the surface profile height are smaller compared to the wavelength of the incident electromagnetic radiation.

One of the important criteria for achieving high efficiency of the nano-etching process is the assurance of a big contrast of the evanescent field. Therefore, when studying the relationship between surface roughness parameters and field energy characteristics, the contrast over the surface of quartz was considered as a field parameter. To find such a relationship, the investigation of the interaction of the incident radiation field with the test quartz surface with a sinusoidal shape, for different values of the oscillation period and relief height was performed. As a result, the dependence of the contrast of the evanescent field on the correlation length and the peak (trough) height of the quartz surface for different spectral components of the spatial spectrum of the rough surface has been obtained. It was determined that the contribution of each spectral component of the spatial spectrum of a randomly rough surface, which has Gaussian form of the correlation function is almost identical in the range of the spatial spectrum width of this surface, except for the spatial frequencies, which have the resonance with the incident radiation wavelength. In addition, it was found that the dependence of the field contrast on the peaks (troughs) height of the quartz rough surface remains linear if the height of the sinusoidal profile does not exceed 20-30 nm.

During the study of the roughness with a random surface shape, it was determined that the contrast of the evanescent field significantly depends on the correlation length and standard deviation of the quartz rough surface profile height. It was found that the dependence of the field contrast on the height of profile peaks remains linear if the standard deviation of the surface height does not exceed 10 nm.

However, in the case of simulation with a random shape of surface relief to obtain reliable results, it is necessary to perform calculations for a large number of realization of the random surface function. This results in a problem associated with a significant efforts of calculations and thus with the time of results obtaining.

Therefore, for the simulation of processes associated with the formation of an evanescent field near the rough “quartz-SHAS” interface, we applied the idea of replacing a random profile of the quartz surface with the equivalent function of a regular profile, which provides similar integral energy characteristics of the evanescent field (first of all, it is the contrast of the field) with the corresponding parameters of the correlation length and the height of the surface relief.

As the equivalent function, the dependency that describes the profile of the relief in the form of periodically repeated triangular peaks and troughs can be considered. In this case, the height of peaks (troughs) should be equal to the standard deviation of the equivalent random rough surface. The width of peaks (troughs) should be the same as the length of correlation of this surface, which is determined at the level $1/e$ from the maximum of its correlation function.

As a result of the studies, it was found that, in terms of the formation of a similar contrast of evanescent field above the surface, the rough surface of quartz in the form of triangular peaks and troughs can be equivalent to a random rough surface with a Gaussian correlation function with the corresponding parameters of the length of the correlation and the height of the surface profile, if the filling factor of triangular peaks and troughs following on the quartz surface is chosen correctly.

The optimal value of the filling factor, at which the same contrast is achieved for both a random surface profile and a surface in the form of triangular peaks and troughs, should be close to 4. It follows from the comparison of both contrast dependences of the evanescent field along the surface of the mentioned profiles.

Thus, the use of a rough surface in the form of periodically repeated triangular peaks and troughs instead of a randomly rough surface significantly reduces the complexity of numerical calculations during the simulation and gives an understanding of nano local-etching of the real quartz surface profile.

References

1. I. Ali, S. R. Roy, G. Shinn. Chemical-mechanical polishing of interlayer dielectric: a review. Solid State Technology. 10, 63–69 (1994).
2. G. F. Ivanitskii, V. I. Petrov. Ionno-plasmennaya obrabotka materialov (M.: Radio I Svjas, 1986) [Ion-plasma processing of materials] (Moscow: Radio and Communication, 1986) (in Russian).
3. Japan patent JP2014-022411A. Etching method using near-field light / Otsu Genichi, Yatsui Takashi, Nomura Ko. Publ. 03.02.2014 (2014).
4. W. Nomura, T. Yatsui, M. Ohtsu. Nonadiabatic Near-Field Optical Polishing and Energy Transfers in Spherical Quantum Dots. Progress in Nano-Electro-Optics VII. Berlin: Springer-Verlag (Springer Series in Optical Sciences), 155, 113–130 (2010)
5. Adams, M. J. An Introduction to Optical Waveguides, John Wiley & Sons, 1981.
6. J. L. Volakis, A. Cbatterjee, L. C. Kempel. Finite Element Method for Electromagnetics, IEEE Press. – 1998. – 344 p.
7. J. Jin. The Finite Element Method in Electromagnetics. Second Edition. – New York: Wiley. – 2002.
8. W. C. Chew, W. C. Weedon. A 3D perfectly matched medium from modified Maxwell’s equations with stretched coordinates. Microwave Opt. Tech. Lett. 7, 599–604 (1994).
9. Z. S. Sacks, D. M. Kingsland, R. Lee, J. F. Lee. A perfectly matched anisotropic absorber for use as an absorbing boundary condition. IEEE Trans. Antennas, 43, N12, 1460-1463 (1995).
10. P. B. Johnson, R. W. Christy Optical Constants of the Noble Metals. Phys. Rev. B. 6, N12, 4370–4379 (1972).
11. L. Novotny, B. Hecht. Principles of Nano-Optics. Cambridge University Press. – 2012.
12. M. Quinten. Optical Properties of Nanoparticle Systems: Mie and Beyond., Willey – VCH Verlag&Co. KGaA, Weinhein. – 2011. – 348 p.
13. H. Raether. Surface Plasmons on Smooth and Rough Surfaces and on Gratings. Springer-Verlag. – 1988. – 140 p.

Chapter 4

INTERACTION OF ELECTROMAGNETIC RADIATION WITH LINEAR ANIZOTROPIC MEDIUM: JONES MATRIX OF THE LINEAR ANIZOTROPY

S.N. Savenkov, E.A. Oberemok, I.S. Kolomiets, A.S. Klimov, A.O. Sitnichenko,
S. Vitusevich

CONTENT

INTRODUCTION

It is known that the challenge of the finding the eigenvalues and eigenvectors of a given matrix for describing interaction of light with a medium plays an important role not only in the matrix analysis [1,2] but also in fundamental physics. This can be explained by the fact that definitions of physical properties of different classes of media used in polarimetry, remote scattering, radar polarimetry, crystal-physics, and electrodynamics are mainly based on the determination of the input types of polarization that do not change with the propagation of light in the studied medium. They are called the eigenpolarizations. The values characterizing the changes of intensity or/and phase of light with eigenpolarizations are called the eigenvalues.

For example, birefringence [3-6] is the phenomenon of certain medium in which an incident beam of light is split into two beams, called an ordinary beam and an extraordinary beam, which are orthogonally polarized. Wherein, ordinary and extraordinary beams propagate in the medium under consideration with different phase velocities. The polarization of ordinary and extraordinary beams is called eigenpolarizations. If the eigenpolarizations are linear, circular or in general elliptical and propagate in the medium with different phase velocities, then this medium is characterized by linear, circular or elliptical birefringence, respectively. The fact that the eigenpolarizations propagate in a given medium with different phase velocities reflects: the eigenvalues are phase multipliers.

If (linear, circular or elliptical) eigenpolarizations are differently absorbed during propagation in the medium, then this medium is characterized by (linear, circular, or elliptical) dichroism. In this case, the fact that the eigenpolarizations are differently absorbed during propagation reflects: the eigenvalues are real multipliers.

Eigenpolarizations may be non-orthogonal [4,7-9], different [10], and may coincide. In the latter case, the medium is characterized by degenerate anisotropy [11-13]. In the general case, eigenvalues are complex factors. This reflects that the eigenpolarizations can both propagate with different phase velocities and also be absorbed in various ways.

In this respect, it should be noted that all matrices of, using Jones terminology [14,15], elementary types of anisotropy are characterized by orthogonal eigenpolarizations.

Indeed, linear phase anisotropy (or linear birefringence) is described by Jones matrix:

$$\mathbf{T}^{LinPh}=\begin{pmatrix}\cos^2\alpha+\sin^2\alpha\exp(-i\Delta) & (1-\exp(-i\Delta))\cos\alpha\sin\alpha\\ (1-\exp(-i\Delta))\cos\alpha\sin\alpha & \sin^2\alpha+\cos^2\alpha\exp(-i\Delta)\end{pmatrix}, \tag{4.1}$$

where Δ ($0\le\Delta\le 2\pi$) and α ($-\pi/2\le\alpha\le\pi/2$) is the value and the azimuth of linear phase anisotropy, respectively.

Circular phase anisotropy (or circular birefringence) is described by Jones matrix:

$$\mathbf{T}^{CirPh}=\begin{pmatrix}\cos\varphi & \sin\varphi\\ -\sin\varphi & \cos\varphi\end{pmatrix}, \tag{4.2}$$

where φ ($0\le\varphi\le 2\pi$) is the value of circular phase anisotropy. Structurally matrix Eq.(4.2) coincides with the plane rotation matrix [5,6].

Linear amplitude anisotropy (or linear dichroism) is described by Jones matrix:

$$\mathbf{T}^{LinAmp}=\begin{pmatrix}\cos^2\gamma+P\sin^2\gamma & (1-P)\cos\gamma\sin\gamma\\ (1-P)\cos\gamma\sin\gamma & \sin^2\gamma+P\cos^2\gamma\end{pmatrix}, \tag{4.3}$$

where P $(0\le P\le 1)$ and γ ($0\le\gamma\le 2\pi$) is the value and the azimuth of linear amplitude anisotropy, respectively.

Circular amplitude anisotropy (or circular dichroism) is described by Jones matrix:

$$\mathbf{T}^{CirAmp}=\begin{pmatrix}1 & -iR\\ iR & 1\end{pmatrix} \tag{4.4}$$

where R ($-1\le R\le 1$) is the value of circular amplitude anisotropy.

Here Jones matrices Eqs.(4.1) and (4.2) are unitary and Jones matrices Eqs.(4.3) and (4.4) are Hermitian ones. All these four Jones matrices of elementary types of anisotropy are characterized by orthogonal eigenpolarizations.

Anisotropy of arbitrary non-depolarizing or deterministic [16,17] medium can be considered as a combination of four elementary types of anisotropy [18,19].

Thus, the Jones matrix of the arbitrary deterministic medium [19] can be described by the product of the matrices Eqs.(4.1)-(4.4)

$$\mathbf{T}^{Gen} = \mathbf{T}^{CirPh}\mathbf{T}^{LinPh}\mathbf{T}^{LinAmp}\mathbf{T}^{CirAmp} \tag{4.5}$$

The Jones matrix Eq.(4.5) is characterized by elliptical non-orthogonal eigenpolarizations and complex eigenvalues. The solution of the spectral problem for the Jones matrix of an arbitrary medium Eq.(4.5) has not been studied in detail today.

Thus, the main aim of this chapter is to develop and study the Jones matrix of arbitrary medium characterized by linear anisotropy, i. e., by linear eigenpolarizations on the basis of the generally accepted definitions of the physical properties of deterministic anisotropic media and the solution of the spectral problem. The chapter is organized as follows. We discuss the using of the spectral problem in polarimetry in Section 1, where we also obtained the Jones matrix for the general case of linear anisotropy and the Jones matrices for the cases of orthogonal linear eigenpolarizations as well as degenerate anisotropy in terms of eigenvalues and eigenpolarizations. Jones matrices for the same types of linear anisotropy in terms of anisotropy parameters are obtained in Section 2. Several analytical and experimental examples demonstrating and discussing the obtained results, followed by conclusions given in Section 3.

4.1. Jones matrix of linear anisotropy in terms of eigenvalues and eigenpolarizations

If the polarization of light is described by the Jones vector [5]:

$$\mathbf{E} = \begin{pmatrix} E_x \\ E_y \end{pmatrix}, \tag{4.6}$$

then the polarization of light after its interaction with anisotropic medium can be found :

$$\mathbf{E}^o = \mathbf{T}\mathbf{E}^i, \tag{4.7}$$

where $\mathbf{E}^i$, $\mathbf{E}^o$ is the Jones vectors of the input and output light, respectively. Here $\mathbf{T}$ is the 2×2 Jones matrix with complex elements describing studied medium:

$$\mathbf{T} = \begin{pmatrix} T_{11} & T_{12} \\ T_{21} & T_{22} \end{pmatrix}. \tag{4.8}$$

In this case the spectral problem can be represented as follows:

$$\mathbf{TE}^e = V\mathbf{E}^e, \tag{4.9}$$

where V and $\mathbf{E}^e$ is eigenvalue and eigenpolarization of the matrix $\mathbf{T}$, respectively.

To describe the eigenpolarizations of the Jones matrix, it is convenient to use complex value which was introduced by Poincare [20]:

$$\chi = \frac{E_y^e}{E_x^e}. \tag{4.10}$$

Then eigenpolarizations and eigenvalues are related with Jones matrix elements:

$$V_{1,2} = \frac{1}{2}\left(T_{22} + T_{11} \pm \sqrt{(T_{22} - T_{11})^2 + 4T_{12}T_{21}}\right), \tag{4.11}$$

$$\chi_{1,2} = \frac{T_{22} - T_{11} \pm \sqrt{(T_{22} - T_{11})^2 + 4T_{12}T_{21}}}{2T_{12}}. \tag{4.12}$$

The inverse problem using the Jones matrix of studied medium $\mathbf{T}$ can be reconstructed on the basis of its eigenpolarizations and eigenvalues:

$$\mathbf{T} = \mathbf{DVD}^{-1}, \tag{4.13}$$

where $\mathbf{D}$ is the matrix which columns are formed by the eigenpolarizations of $\mathbf{T}$:

$$\mathbf{D} = \begin{pmatrix} 1 & 1 \\ \chi_1 & \chi_2 \end{pmatrix}, \tag{4.14}$$

and $\mathbf{V}$ is diagonal matrix whose non-zero elements are the eigenvalues of $\mathbf{T}$:

$$\mathbf{V}=\begin{pmatrix}\exp(-a_1+ib_1) & 0\\ 0 & \exp(-a_2+ib_2)\end{pmatrix}, \tag{4.15}$$

where $a_{1,2}$ and $b_{1,2}$ is the real values, corresponding to the dichroic and birefringent "behavior" of the studied medium, respectively.

Using the fact that the Jones matrix can be normalized by any of its non-zero elements, we have:

$$\mathbf{V}=\begin{pmatrix}1 & 0\\ 0 & P\exp(-i\delta)\end{pmatrix}, \tag{4.16}$$

where P and δ is the values of linear amplitude and phase anisotropy, respectively. They can be defined as:

$$\begin{cases}P=\exp(a_1-a_2)\\ \delta=b_1-b_2\end{cases}. \tag{4.17}$$

Eq.(4.13) can be presented in expanded form:

$$\mathbf{T}=\frac{-1}{\chi_{e1}-\chi_{e2}}\begin{pmatrix}1 & 1\\ \chi_{e1} & \chi_{e2}\end{pmatrix}\begin{pmatrix}V_1 & 0\\ 0 & V_2\end{pmatrix}\begin{pmatrix}\chi_{e2} & -1\\ -\chi_{e1} & 1\end{pmatrix}. \tag{4.18}$$

or as follows [10]:

$$\begin{aligned}
t_{11}&=\frac{1}{\chi_{e1}-\chi_{e2}}\left(V_2\chi_{e1}-V_1\chi_{e2}\right),\\
t_{12}&=\frac{1}{\chi_{e1}-\chi_{e2}}\left(V_1-V_2\right),\\
t_{21}&=-\frac{\chi_{e1}\chi_{e2}}{\chi_{e1}-\chi_{e2}}\left(V_1-V_2\right),\\
t_{22}&=\frac{1}{\chi_{e1}-\chi_{e2}}\left(V_1\chi_{e1}-V_2\chi_{e2}\right).
\end{aligned} \tag{4.19}$$

It should be noted that the spectral decomposition Eq.(4.18) and Eq.(4.19) are valid only in the case when the eigenvalues $V_{1,2}$ are equal, the eigenpolarizations $\chi_{1,2}$ do not coincide, i. e., in the case of non-degenerate anisotropy.

The relations Eq.(4.19) will be used below to obtain an explicit form of Jones matrices based on their eigenvalues and eigenpolarizations as a function of anisotropy parameters Δ, α, φ, P, γ, R Eqs.(4.1)-(4.4).

In the following Sections, we will obtain the Jones matrices of media characterized by orthogonal, non-orthogonal, and degenerate linear eigenpolarizations.

4.1.1. Orthogonal linear eigenpolarizations

For the case of orthogonality of linear eigenpolarizations we have:

$$\begin{cases} \chi_1 = \tan\theta \\ \chi_2 = -\cot\theta \end{cases} \tag{4.20}$$

Substituting Eq.(4.20) into Eq.(4.19) and taking into account the arbitrariness of the eigenvalues Eq.(4.17) we have the Jones matrix of medium under consideration as follows:

$$\mathbf{T}^{Lin}_{orth} = \begin{pmatrix} \cos^2\theta + P\exp(-i\delta)\sin^2\theta & (1-P\exp(-i\delta))\cos\theta\sin\theta \\ (1-P\exp(-i\delta))\cos\theta\sin\theta & \sin^2\theta + P\exp(-i\delta)\cos^2\theta \end{pmatrix} \tag{4.21}$$

The Jones matrix Eq.(4.21) is the model of a medium characterized by linear orthogonal eigenpolarizations.

Using Eqs.(4.1), (4.3), and relations:

$$\mathbf{T}^{LinAm}(\alpha, P_1)\mathbf{T}^{LinAm}(\alpha, P_2) = \mathbf{T}^{LinAm}(\alpha, P_1P_2) \tag{4.22}$$

$$\mathbf{T}^{LinPh}(\alpha, \Delta_1)\mathbf{T}^{LinPh}(\alpha, \Delta_2) = \mathbf{T}^{LinPh}(\alpha, \Delta_1 + \Delta_2) \tag{4.23}$$

$$\begin{aligned} &\mathbf{T}^{LinAm}(\alpha, P)\mathbf{T}^{LinPh}(\alpha, \Delta) = \mathbf{R}(-a)\mathbf{T}^{LinAm}(0, P)\mathbf{R}(\alpha)\mathbf{R}(-a)\mathbf{T}^{LinPh}(0, \Delta)\mathbf{R}(\alpha) = \\ &= \mathbf{R}(-a)\mathbf{T}^{LinAm}(0, P)\mathbf{T}^{LinPh}(0, \Delta)\mathbf{R}(\alpha) = \mathbf{R}(-a)\mathbf{T}^{LinPh}(0, \Delta)\mathbf{T}^{LinAm}(0, P)\mathbf{R}(\alpha) = , \\ &= \mathbf{R}(-a)\mathbf{T}^{LinPh}(0, \Delta)\mathbf{R}(\alpha)\mathbf{R}(-a)\mathbf{T}^{LinAm}(0, P)\mathbf{R}(\alpha) = \mathbf{T}^{LinPh}(\alpha, \Delta)\mathbf{T}^{LinAm}(\alpha, P) \end{aligned} \tag{4.24}$$

with the rotation matrix $\mathbf{R}(\alpha)$:

$$\mathbf{R}(\alpha)=\begin{pmatrix}\cos\alpha & \sin\alpha\\ -\sin\alpha & \cos\alpha\end{pmatrix}, \tag{4.25}$$

we finally get:

$$\mathbf{T}^{Lin}_{orth}(\alpha,\delta,P)=\mathbf{T}^{LinAm}(\alpha,P)\mathbf{T}^{LinPh}(\alpha,\delta)=\mathbf{T}^{LinPh}(\alpha,\delta)\mathbf{T}^{LinAm}(\alpha,P). \tag{4.26}$$

Taking into account Eqs.(4.1) and (4.3) we can obtain:

$$\begin{aligned}&\mathbf{T}^{LinAm}(\alpha,P_1)\mathbf{T}^{LinAm}(\alpha,P_2)\cdot\ldots\cdot\mathbf{T}^{LinAm}(\alpha,P_n)\mathbf{T}^{LinPh}(\alpha,\Delta_1)\mathbf{T}^{LinPh}(\alpha,\Delta_2)\cdot\ldots\cdot\mathbf{T}^{LinPh}(\alpha,\Delta_m)=\\&=\prod_{i=1}^{n}\mathbf{T}^{LinAm}(\alpha,P_i)\prod_{j=1}^{m}\mathbf{T}^{LinPh}(\alpha,\Delta_j)=\mathbf{T}^{LinAm}\left(\alpha,\prod_{i=1}^{n}P_i\right)\mathbf{T}^{LinPh}\left(\alpha,\sum_{j=1}^{m}\Delta_j\right).\end{aligned} \tag{4.27}$$

Thus, the arbitrary medium characterized by linear orthogonal eigenpolarizations can equivalently be represented as a combination of two polarization elements: linear retarder and linear partial polarizer with an equal azimuth of orientation α. Here, the values of linear phase Δ and amplitude P anisotropy are arbitrary and invariant with respect to the order of multiplication of the corresponding matrices Eqs.(4.1) and (4.3). This result can be considered as partial equivalence theorem [15,21,22,23].

4.1.2. Non-orthogonal linear eigenpolarizations

For the case of non-orthogonality of linear eigenpolarizations, we have:

$$\begin{cases}\chi_1=\tan\theta\\ \chi_2=\tan\eta\end{cases}. \tag{4.28}$$

By substitution of Eq.(4.28) in Eq.(4.19) and taking into account the arbitrariness of the eigenvalues Eq.(4.17), we obtaine the following Jones matrix :

$$\mathbf{T}^{Lin}=\begin{pmatrix}\cos\theta\sin\eta-P\exp(-i\delta)\sin\theta\cos\eta & -(1-P\exp(-i\delta))\cos\theta\cos\eta\\ (1-P\exp(-i\delta))\sin\theta\sin\eta & -\sin\theta\cos\eta+P\exp(-i\delta)\cos\theta\sin\eta\end{pmatrix} \tag{4.29}$$

The Jones matrix Eq.(4.29) is the model of an arbitrary medium characterized by linear eigenpolarizations. This reflects that Eq.(4.29) includes the case of orthogonal linear eigenpolarizations Eq.(4.21).

It should be noted that the important point here is following: the Jones matrix Eq.(4.29) cannot be represented by multiplication of the matrices of linear phase Eq.(4.1) and amplitude Eq.(4.3) anisotropy only.

4.1.3. Coinciding eigenpolarizations

In case of coincidence of linear eigenpolarizations, i.e., in the case of degenerate anisotropy, we have:

$$\chi_{1,2} = \tan\theta, \tag{4.30}$$

or in terms of matrix elements:

$$T_{22} - T_{11} = \pm 2i\sqrt{T_{12}T_{21}}\,. \tag{4.31}$$

It is evident that in this case, the Eq.(4.19) cannot be used to obtaine the corresponding Jones matrix. However, the Eq.(4.29) includes this case.

Next we use the fact that eigenpolarizations are linear, which in terms of the Jones matrix elements T_{ij} can be described as follows:

$$\frac{T_{11} - T_{22} \pm \sqrt{(T_{22} - T_{11})^2 + 4T_{12}T_{21}}}{2T_{21}} = \frac{T_{11} - T_{22} \pm \sqrt{0}}{2T_{21}} = \text{ctg}\theta\,, \tag{4.32}$$

or

$$T_{11} - T_{22} = 2T_{21}\text{ctg}\theta\,. \tag{4.33}$$

Conditions Eq.(4.31) and Eq.(4.33) have to be fulfilled simultaneously. As a consequence, we have one more additional condition:

$$T_{21} = -T_{12}\text{tg}^2\theta\,. \tag{4.34}$$

Thus, using Eq.(4.33) and (4.34), we have :

$$\mathbf{T}_{Deg}^{Lin} = \begin{pmatrix} T_{11} & T_{12} \\ -T_{12}\mathrm{tg}^2\theta & T_{11} - 2T_{21}\mathrm{ctg}\,\theta \end{pmatrix}. \tag{4.35}$$

Using designation $\xi = T_{12}/T_{11}$, after some algebra the Jones matrix of the medium characterized by degenerate anisotropy can be described in the form:

$$\mathbf{T}_{Deg}^{Lin} = \begin{pmatrix} \cos^2\theta & \xi\cos^2\theta \\ -\xi\sin^2\theta & (\cos\theta + 2\xi\sin\theta)\cos\theta \end{pmatrix}. \tag{4.36}$$

The Jones matrix Eq.(4.36) is the model of arbitrary medium characterized by degenerate linear anisotropy. In spite of the fact that the matrix elements depend on the azimuth θ of the linear amplitude anisotropy, nevertheless, one can easily verify that the rotation of this matrix by a certain angle β does not change the azimuth to $\theta + \beta$, as it is observed in the non-degenerate case. Therefore:

$$\mathbf{R}(-\beta)\mathbf{T}_{Deg}^{Lin}(\theta,\xi)\mathbf{R}(\beta) \neq \mathbf{T}_{Deg}^{Lin}(\theta+\beta,\xi) \tag{4.37}$$

The eigenvalues of the matrix Eq.(4.36) are:

$$V_1^{Deg} = V_2^{Deg} = (\cos\theta + \xi\sin\theta)\cos\theta \tag{4.38}$$

Eq.(4.36) is derived taking into account the fact that $T_{11} \neq 0$. However, the case $T_{11} = 0$ is also possible. The matrix, is similar to Eq.(4.36) in the case $T_{11} = 0$ and normalized to the element T_{12}, can be described in the form:

$$\mathbf{T}_{Deg}^{Lin} = \begin{pmatrix} 0 & \cos^2\theta \\ -\sin^2\theta & 2\cos\theta\sin\theta \end{pmatrix}. \tag{4.39}$$

Eigenvalues of this matrix are:

$$V_1 = V_2 = \cos\theta\sin\theta\,. \tag{4.40}$$

It should be emphasized that in this case the eigenvalues are the real values.

At the end of this section, let us note that the medium characterized by degenerate linear anisotropy Eq.(4.36) cannot be represented as a combination of the polarization elements with linear phase and linear amplitude anisotropy only.

4.2. Decomposition of the Jones matrices of linear anisotropy

For certain wavelength of input light and geometry of the experiment, the Jones matrices completely describe deterministic anisotropic medium [4,5,10]. In this section, we solve the spectral problem for a class of media with linear eigenpolarizations in the scope of generalized equivalence theorem Eq.(4.5), i.e., in terms of anisotropy parameters R, P, γ, Δ, α and φ, see Eqs. (4.1)-(4.4).

Without loss of generality, we assume that the azimuth of one of eigenpolarization coincides with the horizontal axis of the chosen Cartesian coordinate system. In this case, the azimuth of the second eigenpolarization Ω and angle between eigenpolarizations is assumed arbitrary:

$$\begin{cases} \chi_1 = 0 \\ \chi_2 = \tan\Omega \end{cases}. \tag{4.41}$$

This condition in terms of the Jones matrix elements has the form:

$$\begin{cases} T_{21} = 0 \\ T_{22} - T_{11} = T_{12}\mathrm{tg}\Omega \end{cases}. \tag{4.42}$$

For analysis in terms of anisotropy parameters, it is suitable to use so-called C-parameters (see Ref.24 and Appendix). For polarization basis Eq.(4.5), C-parameters are presented in Appendix: Eqs. (A4.1)-(A4.14), and Eqs. (A4.15-A4.16) present the explicit forms of eigenvalues and eigenpolarizations in terms of C-parameters.

After simple algebra system, Eq.(4.42) can be presented as follows:

$$\begin{cases} C_5 + C_7 = 0 \\ C_6 + C_8 = 0 \\ C_3 - C_5\mathrm{tg}\Omega = 0 \\ C_4 - C_6\mathrm{tg}\Omega = 0 \end{cases} \tag{4.43}$$

It should be noted that condition Eq.(4.43) is valid for any polarization bases. There is a difference in the relation between C and anisotropy parameters only. Taking into account the Eqs. (A4.1)-(A4.14), the condition for the medium characterized by linear eigenpolarizations (with the angle Ω between them) can be described in the form:

$$\begin{cases} R\mathrm{tg}\left(\frac{\Delta}{2}\right)\left(\cos(2\alpha-\varphi)+\frac{1-P}{1+P}\cos(\varphi-2(\alpha-\gamma))\right)=-\left(\frac{1-P}{1+P}\sin(2\gamma-\varphi)-\sin\varphi\right) \\ \mathrm{tg}\left(\frac{\Delta}{2}\right)\left(\sin(2\alpha-\varphi)-\frac{1-P}{1+P}\sin(\varphi-2(\alpha-\gamma))\right)=-R\left(\frac{1-P}{1+P}\cos(2\gamma-\varphi)+\cos\varphi\right) \\ R\mathrm{tg}\left(\frac{\Delta}{2}\right)\sin(2\alpha-\varphi-\Omega)=\frac{1-P}{1+P}\cos(2\gamma-\varphi-\Omega) \\ \mathrm{tg}\left(\frac{\Delta}{2}\right)\cos(2\alpha-\varphi-\Omega)=R\frac{1-P}{1+P}\sin(2\gamma-\varphi-\Omega) \end{cases} \tag{4.44}$$

The solution of Eq.(4.44) can be presented as follows:

$$\begin{cases} P=\dfrac{\cos(4\gamma-2\alpha-\Omega)+\cos 2(\alpha-\gamma)\cos(\Omega)\pm\sqrt{\sin^2(2\gamma-\Omega)-\cos^2 2(\alpha-\gamma)\cos^2\Omega}}{\cos(4\gamma-2\alpha-\Omega)-\cos 2(\alpha-\gamma)\cos(\Omega)\mp\sqrt{\sin^2(2\gamma-\Omega)-\cos^2 2(\alpha-\gamma)\cos^2\Omega}} \\ \Omega=2(\alpha-\varphi)-\frac{\pi}{2}-\pi k, \quad k\in Z \\ R=(-1)^n\sqrt{\mathrm{tg}\varphi\cdot\mathrm{ctg}(\varphi+\Omega-2\gamma)}, \quad n\in Z \\ \mathrm{tg}\left(\frac{\Delta}{2}\right)=(-1)^m\frac{1-P}{1+P}\sqrt{\frac{\sin 2(\varphi+\Omega-2\gamma)}{\sin 2\varphi}}, \quad m\in Z \\ (-1)^{n+m+k}=\mathrm{sgn}[\cos\varphi\cos(2\gamma-\varphi-\Omega)] \\ P, R, \Delta, \varphi, \alpha, \gamma\in\Re \end{cases} \tag{4.45}$$

These conditions together with the polarization basis Eq.(4.5) are another variant of the Jones matrix model of an arbitrary medium characterized by linear anisotropy. As can be seen in general case, the medium with linear eigenpolarizations is characterized by all four elementary types of anisotropy. The angle between linear eigenpolarizations Ω is determined by the azimuth α of linear phase anisotropy and the value φ of circular anisotropy only. These parameters and azimuth γ of linear amplitude anisotropy are independent parameters, the choice of which determines both the values of the remaining three anisotropy parameters P, R, Δ and the angle between eigenpolarizations Ω.

Let us consider the following numerical example. We choose the angle between eigenpolarizations $\Omega=45^o$ and three anisotropy parameters as $\alpha=73.2^o$ and $\varphi=\gamma=5.73^o$. The values of other anisotropy parameters (follow from

Eq.(4.45)) are $P \approx 0.14$, $R \approx 0.35$, and $\Delta \approx 242^o$. Then the corresponding Jones matrix is:

$$\begin{pmatrix} -0.6928 + 1.0864 i & 5.446 - 1.4584 i \\ 0 & 4.753 - 0.3720 i \end{pmatrix} \tag{4.46}$$

Solution of the spectral problem for the Jones matrix Eq.(4.46) gives for the eigenvalues:

$$V_1 = 4.768 \exp\left(-44.7^o i\right), \tag{4.47}$$

$$V_2 = 1.289 \exp\left(122.6^0 i\right), \tag{4.48}$$

and for eigenpolarizations :

$$\chi_1 = \begin{pmatrix} 1 & 1 \end{pmatrix}^T, \tag{4.49}$$

$$\chi_2 = \begin{pmatrix} 1 & 0 \end{pmatrix}^T. \tag{4.50}$$

As can be seen the Jones matrix Eq.(4.46) is indeed characterized by linear non-orthogonal ($\Omega = \pi / 4$) eigenpolarizations.

Condition Eq.(4.45) is also valid for the case of degenerate anisotropy. In this case, it can be used: $\Omega = 0$. Let us consider the following numerical example. We choose: $\gamma = 74.5^o$ and $\varphi = 57.3^o$. Other parameters obtained from Eq.(4.45) are $P \approx 0.606$, $R \approx 0.384$, $\Delta \approx 317.9^o$ and $\alpha \approx 102.3^o$. The corresponding Jones matrix is:

$$\begin{pmatrix} 0.6707 + 0.2577 i & 0.5511 - 0.4819 i \\ 0 & 0.6707 + 0.2577 i \end{pmatrix}. \tag{4.51}$$

The spectral problem solution for the matrix Eq.(4.51) gives for the eigenvalues:

$$V_1 = V_2 = 0.7185 \exp\left(21.0^o i\right), \tag{4.52}$$

and for the eigenpolarizations:

$$\chi_1 = \chi_2 = 0. \tag{4.53}$$

Both eigenpolarizations are linear horizontal, hence such medium is characterized by linear degenerate anisotropy.

One can easily verify that relations Eq.(4.44) gives the case of orthogonal linear eigenpolarizations, i. e., $\Omega = \pi/2$ taking into account the condition Eq.(4.41). This provids $R = 0$ and $\varphi = 0$, that corresponds to the case when the studied medium is characterized by equally oriented, $\alpha = \gamma$, linear phase and amplitude anisotropy.

4.3. Discussion and conclusions

In the previous sections, we developed a matrix model of an arbitrary medium characterized by linear anisotropy. The several important features of the developed model are also considered, namely, the case of orthogonal eigenpolarizations and the case of coincidences of eigenpolarizations, i. e., the case of degenerate anisotropy. In this section, we intend to consider the features of derived matrix models in more detail.

From Eq.(4.45) it follows that, in the general case, the angle between the eigenpolarizations Ω cannot be controlled by changing the value of only one of the anisotropy parameters. However, such an opportunity in practice would be of undoubted interest. On the other hand, in the problem of the synthesis of polarization systems with predetermined parameters, the practical implementation simplicity plays a very important role. In this context, an interesting question is whether it is possible to construct a polarization system characterized by linear eigenpolarizations and to allow the angle between the eigenpolarizations to be controlled by changing only one of the anisotropy parameters? At the same time, this polarization system would not include an element with circular amplitude anisotropy, which is very difficult to implement practically. In addition, in the case of linear eigenpolarizations being considered, one should set $\Delta = \pi$.

Thus the decomposition Eq.(4.5) can be described in the form:

$$\mathbf{T}^{Lin} = \mathbf{T}^{CirPh}(\varphi)\mathbf{T}^{LinPh}(\alpha, \pi)\mathbf{T}^{LinAm}(\gamma, P) \tag{4.54}$$

Thus, there are only the Jones matrices of circular phase, $\lambda/2$ linear phase, and linear amplitude anisotropy in the decomposition case.

One more feature should be noted here. One can directly verify that :

$$\mathbf{T}^{LinPh}(\alpha,\pi)=\begin{pmatrix}\cos(2\alpha) & \sin(2\alpha)\\ \sin(2\alpha) & -\cos(2\alpha)\end{pmatrix} \tag{4.55}$$

$$\mathbf{T}^{CirPh}(\varphi)\mathbf{T}^{LinPh}(\alpha,\pi)=\begin{pmatrix}\cos(2\alpha+\varphi) & \sin(2\alpha+\varphi)\\ \sin(2\alpha+\varphi) & -\cos(2\alpha+\varphi)\end{pmatrix} \tag{4.56}$$

This reflects that values of the parameters α and φ cannot be determined individually and the decomposition Eq.(4.54) is generally equivalent to the following:

$$\mathbf{T}^{Lin}=\mathbf{T}^{LinPh}(\alpha^{*},\pi)\mathbf{T}^{LinAm}(\gamma,P). \tag{4.57}$$

Eigenvalues and eigenpolarizations of the Jones matrix $\mathbf{T}^{Lin}$ Eq.(4.54) are:

$$V_{1,2}=\frac{1}{2}\left[(1-P)\cos(\varphi-2(\alpha-\gamma))\pm\sqrt{(1-P)^2\cos^2(\varphi-2(\alpha-\gamma))+4P}\right], \tag{4.58}$$

$$\chi_{1,2}=\frac{-(1+P)\cos(2\alpha-\varphi)\pm\sqrt{(1-P)^2\cos^2(\varphi-2(\alpha-\gamma))+4P}}{\sin(2\alpha-\varphi)+\sin(\varphi-2(\alpha-\gamma))+P[\sin(2\alpha-\varphi)-\sin(\varphi-2(\alpha-\gamma))]}. \tag{4.59}$$

As can be seen the eigenvalues and eigenpolarizations are real values. To illustrate these results, consider the following numerical example. Anisotropy parameters are chosen as: $P=0.5$, $\alpha=17.2^{o}$, $\gamma=40.1^{o}$ and $\varphi=74.5^{o}$. Corresponding Jones matrix is:

$$\begin{pmatrix}0.4474 & -0.2674\\ -0.6990 & -0.6998\end{pmatrix}. \tag{4.60}$$

The solution of spectral problem for the matrix Eq.(4.60) is
for the eigenvalues:

$$V_1=-0.8445\,, \tag{4.61}$$

$$V_2=0.5921\,, \tag{4.62}$$

and for the eigenpolarizations:

$$\chi_1=4.831\,, \tag{4.63}$$

$$\chi_2 = -0.5411\ . \tag{4.64}$$

The calculation of the angle between eigenpolarizations χ_1 and χ_2 gives $\Omega \approx 16.7^o$. Thus, this medium is caracterized by linear non-orthogonal eigenpolarizations.

The features of anisotropic behavior of the medium characterized by the Jones matrix Eq.(4.54) is examined by analyzing the ratio of eigenvalues (see Fig. (4.1)), and the angle between eigenpolarizations Ω as the functions of anisotropy parameters (see Eq.(4.65) and Fig. (4.2)):

$$\mathrm{tg}\Omega = \frac{\sqrt{(1-P)^2\cos^2(\varphi - 2(\alpha-\gamma)) + 4P}}{(1-P)\sin(\varphi - 2(\alpha-\gamma))}\ . \tag{4.65}$$

Anisotropy parameters are unrelated. Thus, it is possible to alter the angle between eigenpolarizations Ω by means of altering of any parameter from the set P, φ, α and γ. In practice, it is more convenient to alter either α or γ. Indeed, this reflects that the polarization elements rotate with linear phase or/and amplitude anisotropy.

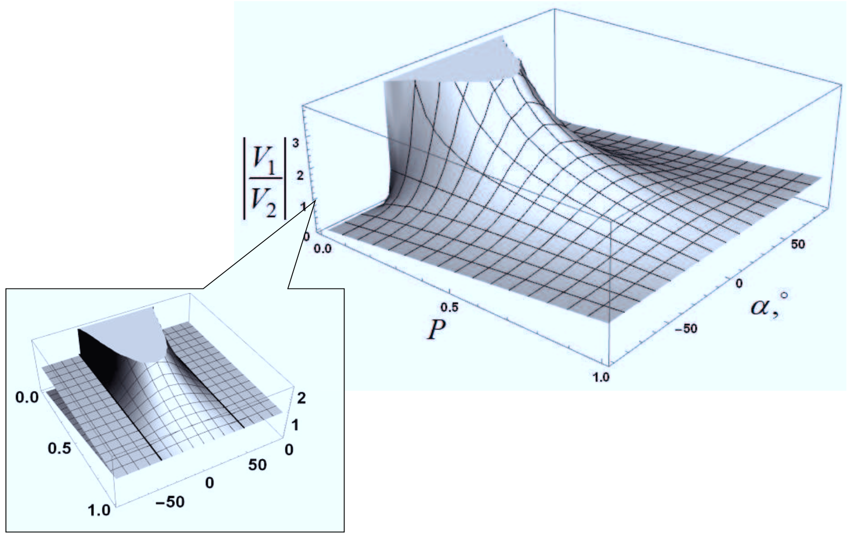

Fig.4.1. The dependence of the ratio of eigenvalues $|V_1/V_2|$ (see Eq.(4.58)) on the value P of linear amplitude anisotropy and azimuth α of linear phase anisotropy.

Insets to Fig.4.2 demonstrate the case of changing the value of the angle between the eigenpolarisations in the whole range: $0 \le \Omega \le 90^0$ with the change of either the value P of the linear amplitude anisotropy or azimuth α of the linear phase anisotropy.

When $|V_1/V_2| \ne 1$ the studied medium is characterized by amplitude anisotropy. Only in two cases the medium is characterized by orthogonal eigenpolarizations: when azimuths of linear phase and linear amplitude anisotropy are coinciding $\alpha = 0^0$ and orthogonal $\alpha = 90^0$. This is the case of Hermitian dichroism [24,25]. In all other cases of $|V_1/V_2| \ne 1$, i. e., when eigenpolarizations are non-orthogonal, the medium is characterized by non-Hermitian dichroism [24,25].

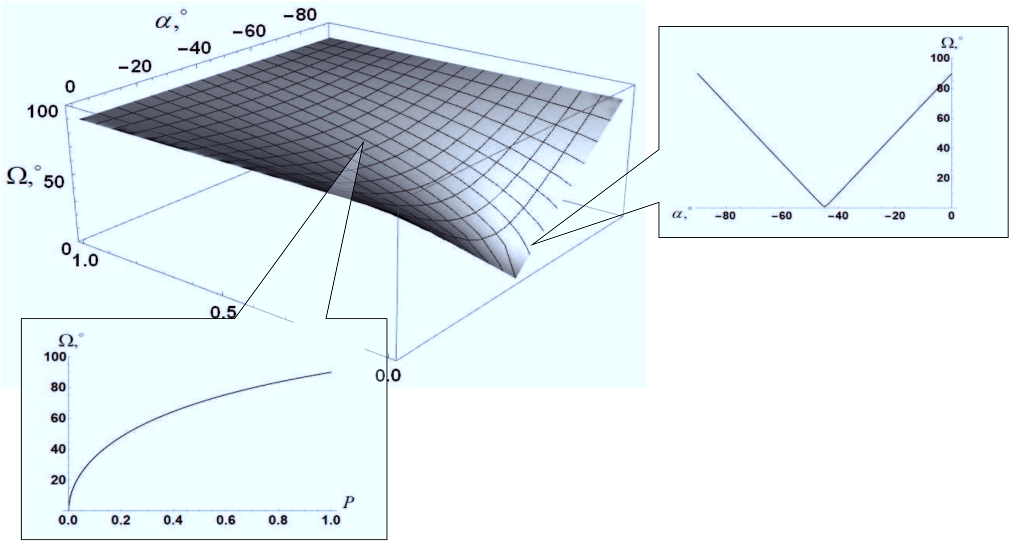

Fig.4.2. Dependence of the angle between the eigenpolarizations Ω Eq.(4.65) on the value P of linear amplitude anisotropy and azimuth α of linear phase anisotropy.

The case $|V_1/V_2| = 1$ is demonstrated by the inset in Fig.4.1. As can be seen the cross-section of the figure $|V_1/V_2|$ by the plane $|V_1/V_2| = 1$ is two line segments $\alpha = \pm\pi/4$.

This occurs when the following condition is fulfilled (see Eq.(4.58)):

$$\varphi = 2(\alpha - \gamma) + \frac{\pi}{2} + \pi l, \quad l \in \mathrm{Z} \qquad (4.66)$$

This gives for eigenpolarizations:

$$\chi_{1,2} = \frac{-(1+P)\cos\left(2\gamma - \frac{\pi}{2}\right) \pm 2\sqrt{P}}{\sin\left(2\gamma - \frac{\pi}{2}\right) + 1 + P\left(\sin\left(2\gamma - \frac{\pi}{2}\right) - 1\right)}, \tag{4.67}$$

and for eigenvalues:

$$V_{1,2} = \pm 2\sqrt{P} \tag{4.68}$$

Fig.4.3 shows the angle between eigenpolarizations Eq.(4.67).

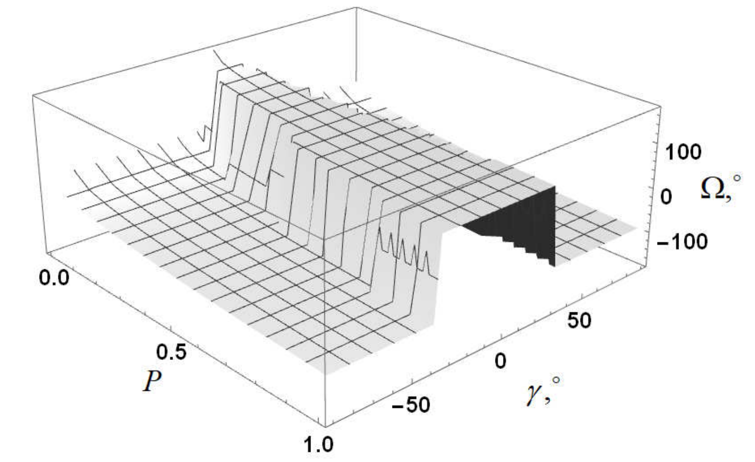

Fig.4.3. The dependence of the angle between eigenpolarizations Eq.(4.67) on the value P and azimuth γ of linear amplitude anisotropy.

As can be seen the angle between eigenpolarizations does not depend on the azimuth γ of the linear amplitude anisotropy. However, it can be changed by varying the value P of the amplitude anisotropy. Degenerate anisotropy, i. e., $\Omega = 0$ and $V_{1,2} = 0$, is realized when $P = 0$. The orthogonality of eigenpolarizations is achieved when $P = 1$, i. e., when linear amplitude anisotropy is absent.

We have performed the experimental examination of Eq.(4.54) as well. For this we derive theoretical and experimental dependences of Ω and V_2/V_1 on the azimuth α of linear phase anisotropy (see Fig.4.4 and Fig.4.5). The values and azimuth of linear amplitude anisotropy and the value of circular phase anisotropy are fixed and chosen to be equal to $P = 0.61$, $\varphi = -29^o$ and $\gamma = -2^o$, respectively.

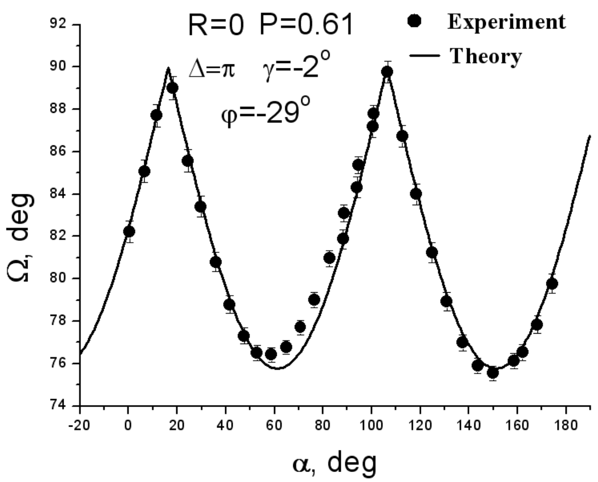

Fig.4.4. Theoretical and experimental dependences of the angle Ω between eigenpolarizations Eq.(4.65) on the azimuth α of linear phase anisotropy.

The exact value of linear amplitude anisotropy was obtained by selecting the angle of light ($\lambda = 630\ nm$) incident on a flat parallel sapphire plate with a thickness of $1\,mm$. The value of the circular phase anisotropy was obtained and changed by using a cuvette (length $5\,cm$) with a solution of sugar in distilled water. The Mueller matrices of this polarization system were measured using a polarimeter. Detailed description of the polarimeter can be found in Ref.25. Each experimental point shown in the figures below is the result of averaging over 500 single measurements. This ensures the measurement error does not exceed 1%.

The ratio V_2/V_1 is negative due to the presence of $\lambda/2$ retardation plate in the decomposition. Figs. (4.4) and (4.5) demonstrate that such an anisotropic sample has non-orthogonal linear eigenpolarizations.

As can be seen, the values of anisotropy parameters, at which the modulus of the ratio of the eigenvalues is equal to one, correspond to the minimum value of the angle between the linear eigenpolarizations.

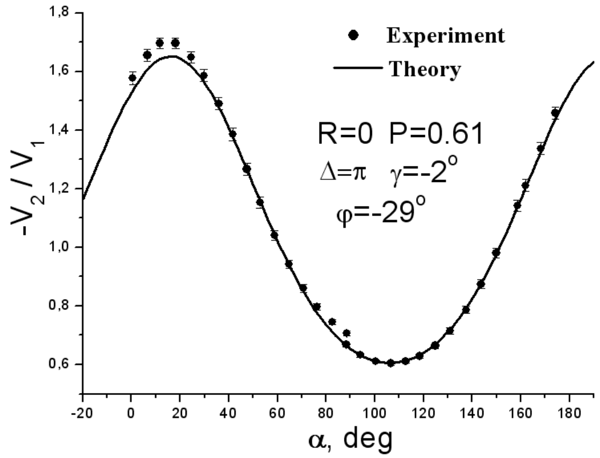

Fig.4.5. Theoretical and experimental dependences of the ratio V_2/V_1 of eigenvalues Eq.(4.58) on the azimuth α of linear phase anisotropy.

The case of degenerate anisotropy is of great interest as well. It follows from Eqs. (4.58) and (4.59) that the degeneracy condition for the decomposition Eq.(4.54) can be described in the form:

$$(1-P)^2\cos^2(\varphi-2(\alpha-\gamma))+4P=0\,, \tag{4.65}$$

or taking into account the non-negativity of the value P of the linear amplitude anisotropy:

$$P=0\,, \tag{4.70}$$

$$\varphi-2(\alpha-\gamma)=\frac{\pi}{2}+\pi p, \quad p\in Z\,. \tag{4.71}$$

Then for eigenvalues and eigenpolarizations we have:

$$V_{1,2}=0 \tag{4.72}$$

$$\chi_{1,2}=\tan\left(\gamma+\frac{\pi}{2}\right) \tag{4.73}$$

For this decomposition, the light with eigenpolarizations is completely absorbed and the azimuth of linear eigenpolarizations is orthogonal to the transmission axis of ideal polarizer. The Jones matrix for the case of degenerate anisotropy, Eqs.(4.72) and (4.73), can be obtained in the form:

$$\begin{pmatrix} \cos(\gamma)\sin(\gamma) & \sin^2(\gamma) \\ -\cos^2(\gamma) & -\cos(\gamma)\sin(\gamma) \end{pmatrix} \qquad (4.74)$$

This matrix is characterized by, a triple singularity. Indeed, on the one hand, the determinant of this matrix is zero. In this case, the Jones matrix Eq.(4.74) is an ideal linear degenerate polarizer. On the other hand, the singularity is associated with the double degeneracy of anisotropy, which is described by this matrix: (i) equality of eigenvalues and eigenpolarizations Eqs.(4.72) and (4.73) and (ii) linearity of eigenpolarizations, which (as a result of the degeneracy of the helicity) are singular [7].

Appendix: C-parameters

Indeed, the sums and differences of matrix elements can be represented as follows:

$$T_{22} + T_{11} = (C_1 + iC_2)\exp\left(-i\frac{\Delta}{2}\right) \qquad (A4.1)$$

$$T_{22} - T_{11} = (C_3 + iC_4)\exp\left(-i\frac{\Delta}{2}\right) \qquad (A4.2)$$

$$T_{21} + T_{12} = (C_5 + iC_6)\exp\left(-i\frac{\Delta}{2}\right) \qquad (A4.3)$$

$$T_{21} - T_{12} = (C_7 + iC_8)\exp\left(-i\frac{\Delta}{2}\right) \qquad (A4.4)$$

In addition, the determinant of the generalized Jones matrix Eq.(4.5) is:

$$|T| = T_{22}T_{11} - T_{21}T_{12} = Z\exp(-i\Delta) \quad , \qquad (A4.5)$$

where

$$C_1 = (1+P)\cos\left(\frac{\Delta}{2}\right)\cos\varphi + R(1-P)\sin\left(\frac{\Delta}{2}\right)\sin[\varphi - 2(\alpha-\gamma)] \tag{A4.6}$$

$$C_2 = R(1+P)\cos\left(\frac{\Delta}{2}\right)\sin\varphi + (1-P)\sin\left(\frac{\Delta}{2}\right)\cos[\varphi - 2(\alpha-\gamma)] \tag{A4.7}$$

$$C_3 = R(1+P)\sin\left(\frac{\Delta}{2}\right)\sin(2\alpha-\varphi) - (1-P)\cos\left(\frac{\Delta}{2}\right)\cos(2\gamma-\varphi) \tag{A4.8}$$

$$C_4 = -(1+P)\sin\left(\frac{\Delta}{2}\right)\cos(2\alpha-\varphi) + R(1-P)\cos\left(\frac{\Delta}{2}\right)\sin(2\gamma-\varphi) \tag{A4.9}$$

$$C_5 = R(1+P)\sin\left(\frac{\Delta}{2}\right)\cos(2\alpha-\varphi) + (1-P)\cos\left(\frac{\Delta}{2}\right)\sin(2\gamma-\varphi) \tag{A4.10}$$

$$C_6 = (1+P)\sin\left(\frac{\Delta}{2}\right)\sin(2\alpha-\varphi) + R(1-P)\cos\left(\frac{\Delta}{2}\right)\cos(2\gamma-\varphi) \tag{A4.11}$$

$$C_7 = -(1+P)\cos\left(\frac{\Delta}{2}\right)\sin\varphi + R(1-P)\sin\left(\frac{\Delta}{2}\right)\cos[\varphi - 2(\alpha-\gamma)] \tag{A4.12}$$

$$C_8 = R(1+P)\cos\left(\frac{\Delta}{2}\right)\cos\varphi - (1-P)\sin\left(\frac{\Delta}{2}\right)\sin[\varphi - 2(\alpha-\gamma)] \tag{A4.13}$$

$$Z = P(1-R^2) \quad . \tag{A4.14}$$

Then, in general case the eigenvalues and eigenpolarizations in terms of C-parameters can be described as:

$$V_{1,2} = \frac{1}{2}\left(C_1 + iC_2 \pm \sqrt{(C_1+iC_2)^2 - 4Z}\right)\exp\left(-i\frac{\Delta}{2}\right) \tag{A4.15}$$

$$\chi_{1,2} = \frac{C_3 + iC_4 \pm \sqrt{(C_1+iC_2)^2 - 4Z}}{C_5 - C_7 + i(C_6 - C_8)} \quad . \tag{A4.16}$$

References

1. P. Lankaster and M. Tismenetsky. The Theory of Matrices. 2nd ed., San Diego: Academic Press. – 1985.
2. R. Horn and Ch. Johnson. Matrix Analysis. Cambridge: Cambridge Univ. Press. – 1986. – 655 p.
3. M. Born and E. Wolf. Principles of Optics. Pergamon Press, Inc., New York. – 1981. – 885 p.
4. W. A. Shurcliff. Polarized light-production and use. Harvard: Harvard University Press. – 1962.
5. Ch. Brosseau. Fundamentals of polarized light. A statistical optics approach. New York: North-Holland Publishing Company. – 1998.
6. E. Collett. Polarized Light: Fundamentals and Applications. Marcel Decker, New York. – 1993.
7. M. V. Berry and M. R. Dennis. The optical singularities of birefringent dichroic chiral crystals. Proc. R. Soc. London, Ser. A, 459, 1261–1292 (2003).
8. S.-Y. Lu and R. A. Chipman. Homogeneous and inhomogeneous Jones matrices. J. Opt. Soc. Am. A, 11, 766–773 (1994).
9. S.-Y. Lu and R. A. Chipman. Interpretation of Mueller matrices based on polar decomposition. J. Opt. Soc. Am. A, 13, 1106–1113 (1996).
10. R. M. Azzam and N. M. Bashara. Ellipsometry and Polarized Light. North-Holland, New York. – (1987).
11. S. Pancharatnam. The propagation of light in absorbing biaxial crystals – I. Theoretical. Proc. Indian Acad. Sci. Sect. A, 42, 89–109 (1955).
12. S. Pancharatnam. The propagation of light in absorbing biaxial crystals – II. Experimantal. Proc. Indian Acad. Sci. Sect. A, 42, 235–248 (1955).
13. H. de Lang. Polarization properties of optical resonators passive and active. Ph.D. dissertation, Utrecht: University of Utrecht (1966).
14. R. C. Jones. A new calculus for the treatment of optical systems I. Description and discussion of the calculus. J. Opt. Soc. Am., 31, 488–493 (1941).
15. H. Hurwitz and C. R. Jones. A new calculus for the treatment of optical systems II. Proof of three general equivalence theorems. J. Opt. Soc. Am., 31, 493–499 (1941).
16. J. W. Hovenier. Structure of a general pure Mueller matrix. Appl. Opt. 33, 8318–8324 (1994).
17. J. W. Hovenier and D. W. Mackowski. Symmetry relations for forward and backward scattering by randomly oriented particles. J. Quant. Spectrosc. Radiat. Transfer. 60, 483–492 (1998).

18. V. V. Mar'enko and S. N. Savenkov. Representation of arbitrary Mueller matrix in the basis of matrices of circular and linear anisotropy. Opt. Spectrosc. 76, 94–96 (1994).
19. S. N. Savenkov, V. V. Marienko, E. A. Oberemok, and O. I. Sydoruk. Generalized matrix equivalence theorem for polarization theory. Phys. Rev. E. 74, 056607 (2006).
20. H. Poincare. Theorie Mathematique de la Lumiere. Gauthiers-Villars, Paris, Vol. 2 (1892).
21. C. Whitney. Pauli-algebraic operators in polarization optics. J. Opt. Soc. Am. 61, 1207–1213 (1971).
22. R. Barakat. Jones matrix equivalence theorems for polarization theory. Eur. J. Phys. 19, 209–216 (1998).
23. E. F. Dawson and N. O. Young. Helical Kerr Cell. JOSA 50, N2, 170-171 (1960).
24. S. N. Savenkov, O. I. Sydoruk, and R. S. Muttiah. Conditions for polarization elements to be dichroic and birefringent. J. Opt. Soc. Am. A., 22, N7, 1447–1452 (2005).
25. S. N. Savenkov, O. I. Sydoruk, and R. S. Muttiah. Eigenanalysis of dichroic, birefringent, and degenerate polarization elements: a Jones-calculus study. Applied Optics, 46, N27, 6700–6709 (2007).
26. S. N. Savenkov. Optimization and structuring of the instrument matrix for polarimetric measurements. Optical Engineering. 41, N5, 965–972 (2002).

Chapter 5

INTERACTION OF MICROWAVE RADIATION WITH NANOSTRUCTURED COMPOSITES: TOWARD EFFECTIVE SELECTIVE ABSORBES

V.I. Grygoruk, V.V. Oliynyk, V.V. Zagorodnii, L.Yu. Matzui, L.L. Vovchenko,
I.A. Gural’skiy, O.I. Kucheriv, M.O. Popov, V.L. Launets, A.L. Nikytenko,
S. Vitusevich

CONTENT

List of symbols and abbreviations

List of Symbols and Abbreviations

CNT	carbon nanotube;
MWCNT	multiwall carbon nanotube;
CM	composite material;
FMR	ferromagnetic resonance;
NFMR	natural ferromagnetic resonance;
Q	quality factor;
EMR	electromagnetic radiation;
SE_T	EMR attenuation;
S_R	power reflection factor;
S_A	power absorption factor;
S_{MR}	multiple reflection factor;
VSWR	voltage standing wave ratio;
AC	alternating voltage;
DAC	digital-to-analog converter;
DR	dielectric resonator;
AFC	amplitude-frequency characteristic;
ρ	density of states;
ω	cyclic frequency;

Introduction

This chapter describes the results obtained during research grant aimed at designing novel perspective materials for the efficient control of the microwave electromagnetic radiation parameters. The importance of such investigation is determined by the continuous progress in the fields of cellular communications, internet, digital data transmission networks, which demand the enhanced speed and volume of data transmision. This can be fulfilled by the transition from centimeter range of data transmission to the millimeter-wave band. The millimeter-wave band corresponds to signal frequencies in the range from 30 GHz to 300 GHz. Yet nowadays this transition is obstructed by the lack of proper materials for microwave electronic circuits providing efficient control of electromagnetic radiation characteristics in millimeter-wave band.

We performed the studies of several specific materials, demonstrating unique physical and electrodynamic properties. One of these area of research concerns to the basic mechanisms of interaction of millimeter-wave radiation with composites containing the admixture of the textured MWCNTs. The results of studies of the electrodynamic characteristics of substituted hexaferrite (with various dielectric cations such as Ga, Al, In) demonstrate that the the operating frequency band can be changed from 26 GHz to 80 GHz. The application of the molecular complexes with Fe(II) ions in millimeter-wave band was shown for the first time. These complexes are known as spin-crossovers. We show that their conductivity, permittivity, permeability, and absorption parameters can be abruptly changed under the influence of external factors.

The composite cell consisting of high-Q dielectric resonators and a layer of magnetically ordered material was investigated at microwave frequencies. The ferrite component was represented by two different classes of magnetic materials: ferromagnetic dielectric (nickel ferrite) and weak ferromagnet (iron borate). The electromagnetic properties of such bi-layer heterostructures were investigated both experimentally and theoretically in the X-band frequency range. A possibility of magnetic field control of their electromagnetic characteristics was demonstrated.

The texturing of carbon nanotubes in composites by their orientation under the influence of external electric field leads to a noticeable increase in the efficiency of composites interaction with electromagnetic radiation. This is result of the induced anisotropy of structural, electric and electrodynamic properties, such as: conductivity, dielectric constant, absorption and reflection coefficients of electromagnetic waves. The induced anisotropy effect can be enhanced with the increase of MWCNTs concentration.

The substitution of iron ions in barium hexaferrite with gallium, indium and aluminum ions results in substantial modification of FMR parameters and allows for effective modification of frequency range of hexaferrite application.

For the first time, we have instigated the interaction of microwave radiation with spin-crossovers of different chemical compositions as a function of temperature. This study opens the perspectives for applications of spin-crossovers as high-speed power switches and filters.

The results presented in this chapter were obtained at the at the Quantum Radiophysics department of the Faculty of Radiophysics, Electronics and Computer Systems of the National Taras Shevchenko University of Kyiv with financial support of the Ministry of Education and Science of Ukraine on the program 16BF052–04.

Textured composites and spin-crossovers were fabricated in collaboration with scientists from "The Laboratory of Physics of Solid Materials" of the Faculty of Physics and experts from the Physical Chemistry department of the Faculty of Chemistry. Substituted hexaferrite samples were fabricated and investigated by the multinational team of scientists from Belarus, Azerbaijan and Ukraine. Nanostructured nickel ferrite films were synthesized by the scientists from the Vernadsky Institute of General and Inorganic Chemistry of the Ukrainian National Academy of Sciences.

5.1. Effective control of the electromagnetic radiation parameters by structuring the MWCNTs in composites

5.1.1. Relevance of research

Carbon nanotubes represent an important class of nanomaterials with unique electrophysical properties due to their quasi-one-dimensional structure. The anisotropy of the atomic and electron structure of CNTs can be measured by the change in the EMR interaction efficiency depending on the angle between the EMR polarization vector beam and the axis of the nanotube. The structural parameters of CNTs (number of layers, defects, curvature, the presence of doped atoms) and their distribution in the sample may differently respond to the EMR of different wavelengths. For example, the orientation and defects of the graphene layers forming the walls of the CNTs can affect the elastic and nonelastic scattering of radiation with wavelengths of about ten nanometers (ultrasoft X-rays). In particular, the roentgen radiation propagation through the internal CNTs channels opens the prospects for developent of new elements for the X-ray devices. Investigation of X-ray radiation interaction with CNTs arrays can be used to determine the orientation of nanotubes in an array. In the optical and terahertz ranges, the spatial orientation of the CNTs and the degree of their curvature are important. The defects and lengths of the CNTs, their concentration and the spatial distribution in the dielectric matrix determine the dielectric properties of the electromagnetic properties, which are depending on the size, shape, concentration, and ordering of the matrix composite fillers.

5.1.2. Microwave measurements and dielectric properties of structured composites

The insertion of ordered spatially-oriented nanoparticles ensemble to the composite matrix enhances considerably the EMR-composite interaction efficiency. Special attention is given to the nanoparticles orientation method since this determines the structure quality and the EMR-composite interaction characteristic. To date, three nanoparticles orientation methods have been classified by different effects on the structure of nanoparticles, as it will be described below.

Composite materials (CMs) and are of great importance in the microwave range. The feasibility of desgning the CNT-based anisotropic CMs utilizing the superior orientation of nanotubes opens the prospects of their application in the nanoelectronics, computer industry, telecommunications, space and aircraft industries as tools to control microwave radiation. To fabricate new anisotropic CMs, a number of technical and technological problems such as ensuring the orientation of CNTs in the matrix, preventing agglomeration and destruction of nanotubes in the fabrication process have to be solved. The degree of CNTs structural orientation can be monitored by the electromagnetic response of the material (attenuation, absorption and reflection) when the CM is probed by the polarized EMR. Nanocomposite media is the base for new promising materials with predefined structural properties by:

1) the external electric field [1–3];
2) the external magnetic field [4];
3) external mechanical stress [5].

Each of these methods orients nanoparticles in the matrix by their specific effects. Therefore, the nanocomposites can be formed with desired macroscopic properties.

The induced anisotropy can improve the physical and mechanical properties of structured carbon nanocomposites, provide a unique combination of electrical, optical, mechanical, and electrodynamic parameters useful for various applications in technology, instrumentation, ecology.

a) Modeling of a nanotube orientation in an external electric field

Fig. 5.1 shows the scheme for a nanotube orientation calculation.

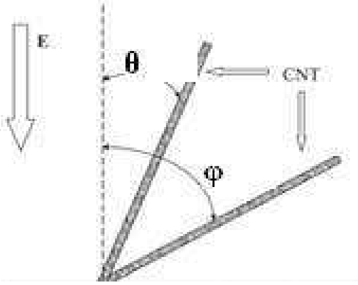

Fig. 5.1. MWCNT orientation under the external electric field:: φ is the initial nanotube tilt angle, Θ is the terminal tilt angle.

Let the MWCNT is oriented at the angle φ relative to the electric field *E*. Then the MWCNT is partially oriented at the angle θ as a result of the electric field effect. The value of the angle is determined by the mechanical balance of forces externally applied to the MWCNT.

The electric field E creates in a nanotube the electric polarization P equal to $P = \alpha_{\|} E cos\varphi$, where $\alpha_{\|}$ is the longitudinal polarization of the nanotube.

According to calculations performed in [6], the following relations are valid for the longitudinal and transverse electric polarizability of the MWCNT:

$$\alpha_{\|} = (0{,}23 + 0{,}135D)(L^2 + 52{,}5),$$
$$\alpha_{\perp} = (0{,}12D^2 + 1{,}76)(L + 4{,}65), \tag{5.1}$$

where α is the measured in cubic Angstrom ($Å^3$) units., D and L is the nanotube diameter and length in Angstrom (Å) units, respectively.

It is clear that the longitudinal polarization is approximately L / D times exceeding the transverse one. Thus, the transverse polarization is much smaller than the longitudinal one for nanotubes with a large aspect ratio $L/D \gg 1$.

The condition of the stable orientation of a particle in an electric field is following. The electric force has to exceed the Brownian motion effect (the latter excites random angular displacements of the nanotubes in a composite), i.e. the following condition has to be satisfied:

$$E > \frac{1}{\theta}\sqrt{\frac{4kT}{\varepsilon_0 \alpha\|}}\, ln|tg\theta|, \tag{5.2}$$

where E is the electric field strength, θ is the angle between the electric field and the induced dipole moment vectors, T is the absolute temperature of the composite, ε_0 is the electric constant.

Numerical estimations were performed for the case of MWCNTs in an epoxy resin polymer and the validity of calculations was demonstrated. The polarizability magnitudes of nanotubes (with 1–10 μm length and ~10 nm diameter) are estimated on the basis of known static electric polarizability tensors of MWCNTs, taking into account the effect of external field screening [7]. For instance, the orientation of nanotubes ensemble with polarizability of $\alpha_{II} \approx 10^4$ nm^3 will take time about 10 seconds in the field of E ~10^4 V / cm.

b) EMR screening efficiency provided by MWCNT composites

The composite-EMR interaction is characterized by the attenuation SE_T which is implemented by the composite under test [8,9]:

$$SE_T = S_R + S_A + S_{MR}, \tag{5.3}$$

where S_R is the power reflection factor at the input interface, S_A is the power absorption factor, S_{MR} is the factor of the multiple reflections to the output power decrement.

The reflection value in dB units can be calculated as:

$$S_R = 20lg\left|\frac{\text{VSWR}-1}{\text{VSWR}+1}\right|, \tag{5.4}$$

where VSWR is the voltage.

The absorption value S_A in dB is

$$S_A = 20lge^{d/\delta},\ \delta = \left(\sqrt{\pi f \mu \sigma}\right)^{-1}, \tag{5.5}$$

where d is the sample thickness, σ is the material conductivity.

The multiple reflection value S_{MR}

$$S_{MR} = 20lg\left|1 - e^{-2d/\delta}\right|. \tag{5.6}$$

Normally, the contribution of S_{MR} is small for the CMs with considered high-conductive filler concentrations and can be neglected.

5.1.3. Experimental investigation of the structured composites-EMR interaction.

a) Fabrication of structured CMs and the nanotubes distribution

Composite samples under study [9] were fabricated with following MWCNTs concentrations: sample 1 – 0.05wt.%, sample 2 – 0.4wt.%, sample 3 – 1.0wt.%, (all prepared without electric field application). Other 3 samples with the same set of concentrations were fabricated under the external electric field orienting the nanotubes: sample 4 – 0.05wt.%, sample 5 – 0.4wt.%, and sample 6 – 1.0wt.%. The dimensions of the samples fit for waveguide cross-sections: 7.2x3.4x3.4 mm^3 and 5.2x2.6x2.6 mm^3. The uniform-compzed samples provide for 90^o rotation inside the waveguide. This allows controlling the angle between the microwave electric field vector in the waveguide and the nanotubes axes of preferred orientation in the composite.

Images of the MWCNTs distribution in the composite matrix cured under the 15 kHz alternating electric field of 80 kV/m [10] were recorded by the optical microscope. The size of the actual image is 10.8x8.0 mm^2, the nanotubes concentration in the sample is 0.05wt.%.

As can be seen (Fig. 5.2a), the nanotubes distribution in the matrix without the application of orienting electric field is sufficiently homogeneous, no preferred orientation is visible. The sample is obtained by the ultrasonic dispersion. On the contrary, there is predefined nanotubes orientation along the external electric field direction (Fig. 5.2b).

Usual optical microscope is unsuitable for imaging the composite with MWCNTs concentration exceeding 0.05wt.%. For this reason, the near-field scanning microwave microscope, developed at the Department of Quantum Radiophysics of the Taras Shevchenko National University of Kyiv, was used to monitor the nanotubes ordering at higher concentrations.

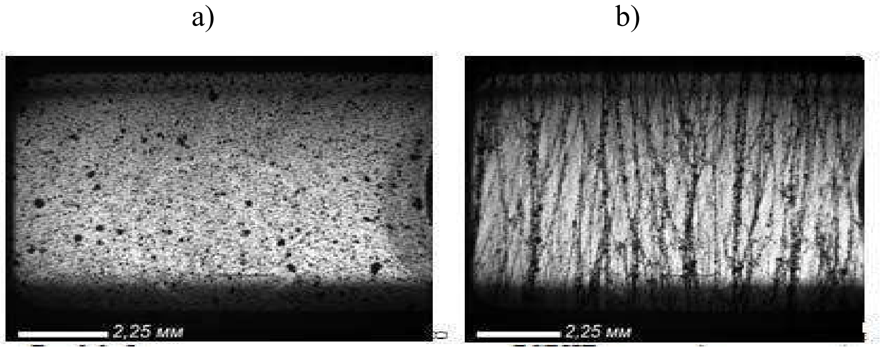

Fig. 5.2. Optical image of MWCNTs (0.05wt.%) introduced in the composite matrix: a) nanotubes distribution in the matrix without ordering; b) nanotubes ordering under the effect of the external electric field.

The analysis of MWCNTs distribution in the matrix volume was also performed by the near-field microwave microscope. Fig. 5.3 shows the scanned surface patches of the sample.

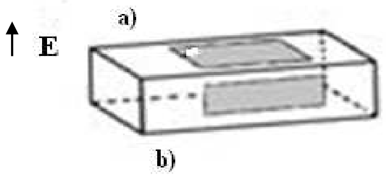

Fig. 5.3. The schematic of the scanned surface patches: a) and b) of the sample. The external AC electric field direction for MWCNTs ordering is labeled by the arrow.

Fig. 5.4 illustrates the MWCNTs ordering under the AC electric field. The MWCNTs concentration is 1wt.% (optical imaging is impossible because of the opacity of the samples).

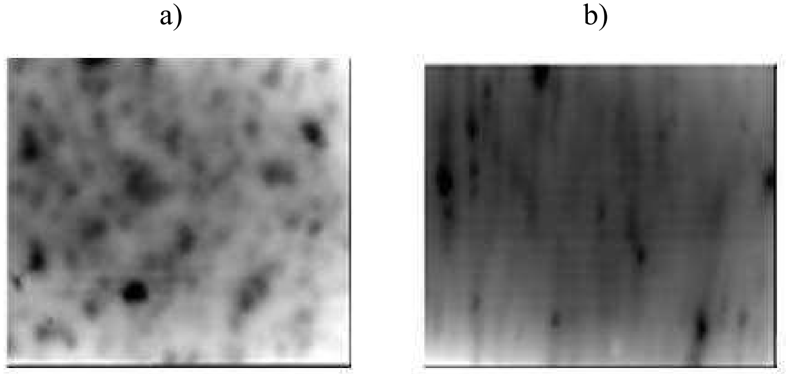

Fig. 5.4. Microwave near-field image of the MWCNTs distribution in the composite matrix for two cases: a) the nanotubes axes are perpendicular to the image plane; b) the nanotubes axes and the image are in the same plane.

The recorded images allow concluding that the nanotubes ordering occurs in the composite matrix with a wide range of MWCNTs concentrations. However, nanotubes tend to conglomerate (Fig.5.4) with an increase in concentration. In Fig. 5.4a the contrasting points are images of surface-embedded nanotubes while the blurry points are images of deeply-embedded nanotubes. Fig. 5.4b shows the preferred nanotubes arrangement in the in-plane of the image while black points indicate some nanotubes agglomerates oriented angularly to the sample surface. Better nanotubes ordering is attained by the increase of the electric field strength and the decrease of the composite matrix viscosity.

The structurization quality (i.e. the degree of nanotubes axes alignment in relation to the applied electric field direction) was examined by the specific resistivity measurements in parallel and perpendicular directions.

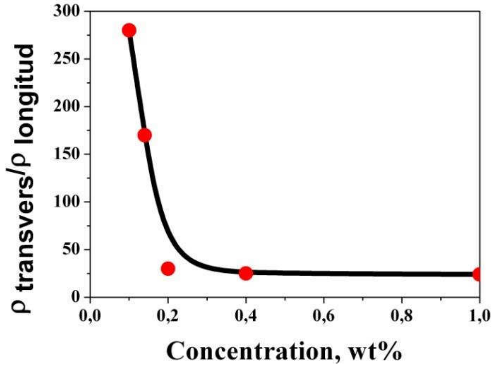

Fig. 5.5. The specific resistivity anisotropy in the structured samples

As estimated, the structured specimens show anomalous specific resistivity anisotropy. Fig. 5.5 demonstrates the ratio of transfer to longitudinal specific resistivities: ***ρ*** transvers/***ρ*** longitud .

However, the ratio rapidly decreases with increase of the MWCNTs concentration to ≈ 0.4wt.%. This is result of the MWCNTs assembly and conglomeration in the matrix. The conglomerational concentration increases with growth of the MWCNTs concentration.

The permittivity of the composite samples was measured in the microwave frequency range. The measurements were performed by the short-circuited waveguide method [11]. The schematic of the experimental setup is shown in Fig. 5.6.

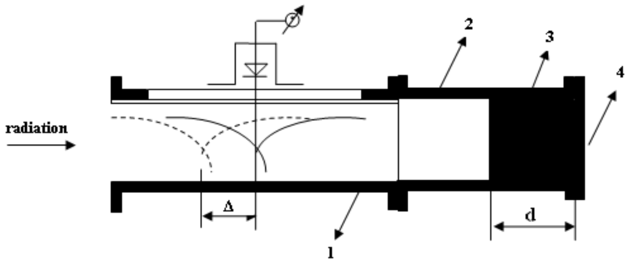

Fig. 5.6. Schematic representation of the permittivity measurement by the short-circuited waveguide method: 1 – measuring line; 2 – waveguide section; 3 – prismatic-shaped sample; 4 – shorting plug.

The prismatic-shaped sample (3) is inserted in the short-circuited waveguide section (2). The microwave measuring line (1) is attached to the short-circuited waveguide section. The sample's face surface has the area contact with the shorting plug (4). The length *d* of the sample has no fundamental restrictions, Δ is the standing wave minimum shift.

To perform the microwave dielectric characterization of the structured samples (Fig. 5.7.) microwave signal generators Г4-115 and Г4-141 were used with waveguide measuring lines P-31 and P-14, respectively.

Fig. 5.7. Experimental setup for permittivity measurements in the frequency range of 26 – 53 GHz.

The results of permittivity measurements at 26 GHz and 53 GHz are shown in Fig. 5.8.

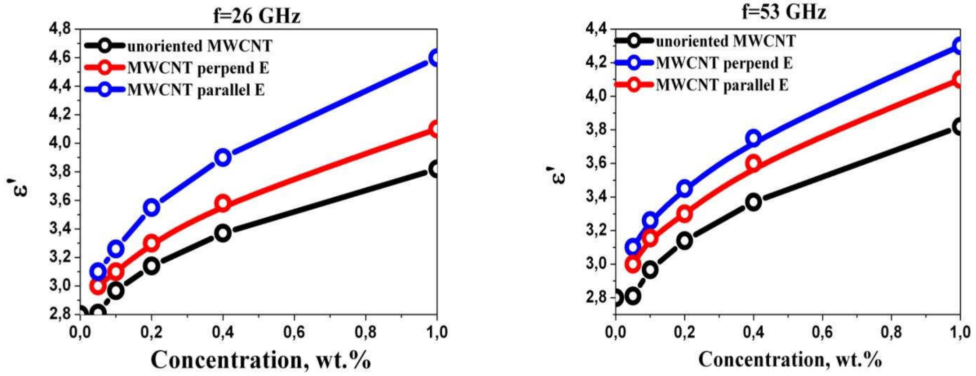

а)

б)

Fig. 5.8. The real part of CM permittivity versus MWCNTs concentration for different nanotubes orientations: (red)- ordered perpendicular E,(black)- unoriented, (blue) - ordered parallel to E, measured at different frequencies: a) at 26 GHz; b) at 53 GHz.

As can be seen a good coincidence of the permittivity concentration dependencies measured at 26 GHz and 53 GHz for the samples with unoriented nanotubes. However, structured samples show different permittivities at different frequencies. This reflects that interaction forces between EMR and nanotubes are different and depend on the angle between the electric field vector and the nanotube axis. Permittivity values at 26 GHz are higher compared to those, measured at 53 GHz.

Fig. 5.9 shows the imaginary part of the permittivity measured for the samples with 1wt.% MWCNTs for two different orientations of the nanotubes: transversal and longitudinal in relation to the EMR electric field vector ***E***. As can be seen, there is large difference in permittivity values. The value of imaginary permittivity ε"≈1 indicates the significant microwave EMR absorption.

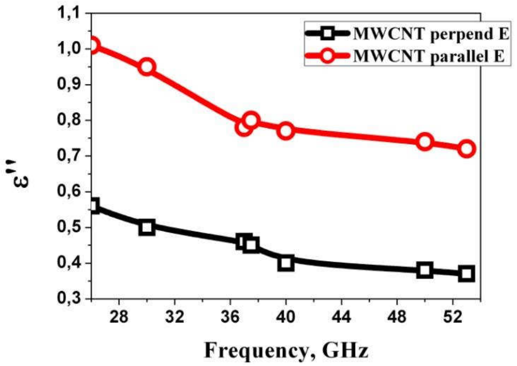

Fig. 5.9. Imaginary part of the structured CM permittivity versus frequency for different nanotubes axes orientations: parallel to E and perpendicular to E. MWCNTs concentration is 1wt.%.

b) microwave transmission/reflection spectra of the structured CMs

The spectral characteristics of the structured CMs were measured in Ka and U bands (26–37.5 and 37–53 GHz). Fig. 5.10 – 5.11 illustrate the experimental setup.

Microwave scalar network analyzers P2-65 and P2-69 were used to measure the transmission (S21) and reflection (S11) scattering parameters in the above-mentioned frequency ranges. CMs with 0.05, 0.4, and 1.0wt.% of MWCNTs were analyzed.

Fig. 5.10. The experimental setup for the frequency range of 26 – 37.5 GHz.

Fig. 5.1.1 The experimental setup for the frequency range of 37 – 53 GHz.

Fig. 5.12 shows the spectral characteristics of the CMs with different nanotube contents and orientations. The monotonic microwave attenuation increases with growth of MWCNT concentration in the case of unoriented MWCNTs in the composite [12–15]. The attenuation increases with EMR frequency. Note that the attenuation increases nonmonotonous in the CMs with nanotubes in parallel to the microwave electric field.

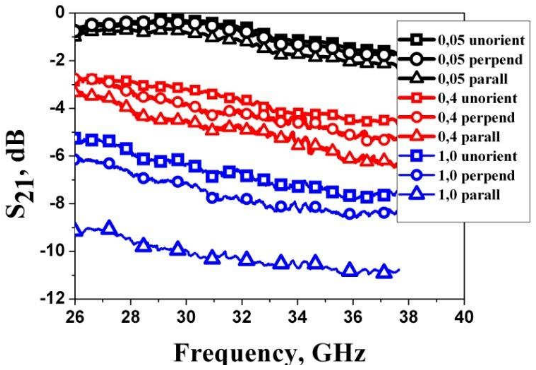

Fig. 5.12. Microwave attenuation spectra, measured for the structured CMs for different MWCNT contents and orientations.

The microwave reflection, in contrast, decreases with the increase of unoriented MWCNTs concentration and/or frequency increase (Fig. 5.13).

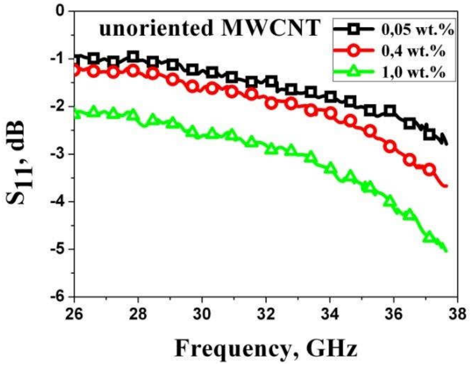

Fig. 5.13. Microwave reflection spectra depending on unoriented MWCNTs concentration in the CMs.

The completely different behavour as a function of the microwave reflection frequency is registered for oriented nanotubes in the CMs (Fig. 5.14).

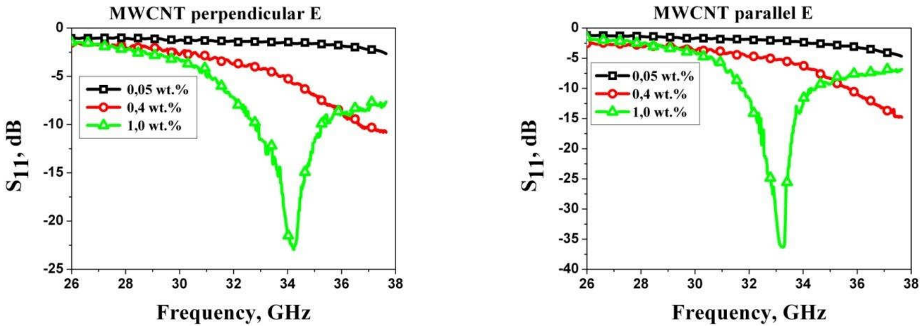

Fig. 5.14. Microwave reflection spectra, measured for different MWCNTs concentrations in the CMs.

Results reflect the resonant EMR interaction with the oriented CMs samples.Thus, MWCNTs orientation ordering in the composite matrix significantly depends on their interaction with microwave EMR and the composite matrix viscosity. The degree of nanotubes orientation can be changed by the driving electric field strength.

5.2. Frequency range expansion of barium hexagonal ferrite application by the iron cations substitution with diamagnetic cations

5.2.1. Relevance of research

The development of mobile communications, the Internet and other digital data networks requires an increase in the information transfer rate that can be achieved by the switch from cm to the millimeter wavelength range (with carrier frequencies of 30–300 GHz). Hexaferrites have high values of the magnetic anisotropy and hence are promising for operation in millimeter wavelength range as valves, circulators, phase shifters, elements of antennas, and can also be effective EMR absorbers. The latter is of importance to improve the control of electromagnetic waves [16–18]. Doping of hexagonal ferrites by various diamagnetic ions leads to a significant change in their magnetic characteristics [19–22] and allows shifting the operating frequency range.

The operating frequency range for hexagonal ferrites is determined by the natural FMR (NFMR) where the permeability values efficiently alter.

The physical effects determining the magnetic characteristics change at NFMR are the same as those in the induced FMR. These are additional oscillations of the nodes of a ferrite crystal lattice under the action of spin waves. Spin waves are excited by the microwave EMR. Thus, the interaction of the spin waves with the crystal lattice leads to the partial transformation of the external microwave field energy into the lattice thermal oscillations. In this case, the frequency of NFMR is determined by both the “rigidity” of the magnetization vector rotation in the plane of easy magnetization and the out-of-plane rotation “rigidity”.

The use of hexaferrite with high values of the crystalline magnetic anisotropy allows for the selective control of EMR characteristics by shifting the NFMR frequency. It is known that the NFMR frequency of the barium hexagonal ferrites ($BaFe_{12}O_{19}$) is located in the range of 47–50 GHz and depends on the particular value of the magnetic anisotropy field strength. Demagnetization shape-dependant magnetic fields also affect the NFMR frequency:

$$\omega = \gamma H_a, \tag{5.7}$$

where ω is the NFMR frequency, γ is the gyromagnetic ratio, H_a is the magnetic anisotropy field.

The NFMR frequency band in the polycrystalline ferrites is quite wide and may be controlled by introducing various diamagnetic ions into the ferrite, for example, aluminum [21,22]. Introduction of Al^{3+} ions into barium hexaferrite $BaFe_{12-x}Al_xO_{19}$ increases the magnetic anisotropy field from 17 kOe to 25 kOe by using material with with x = 1.5 [22]. Also, the resonant frequency change occurs under an external magnetic field H_0:

$$f = \gamma(H_0 + H_a - 4\pi M_s), \tag{5.8}$$

where $4\pi M_s$ is the demagnetizing factor.

The expression for the EMR energy absorbed in the material was obtained in [23]:

$$P = 2\pi f(\varepsilon'' E^2 + \mu'' H^2), \tag{5.9}$$

where f is the EMR frequency; ε'' and μ'' is the permittivity and permeability, respectively.

Thus, the microwave EMR absorption in material arises from magnetic losses, conduction currents losses, and the dielectric hysteresis. The latter two contributions are taken into account by the imaginary part of permittivity. It is shown [19] that the EMR energy absorption in ferromagnetic materials is determined mainly by magnetic losses resulted from NFMR and the domain boundaries resonance.

The obvious advantages of barium hexaferrite are a large crystalline magnetic anisotropy as well as high temperatures of ferromagnet-paramagnet phase transition. A collinear ferromagnetic ordering is formed as a result of strong sublattice exchange. The change in the number of magnetic bonds of iron cations in multicomponent oxide systems (due to the introduction of diamagnetic cations or the deviation from oxygen stoichiometry) allows controlling the functional properties of these ferrites.

5.2.2. Experimental studies

a) samples preparation

Barium hexaferrite microwave properties were changed for our research by the partial substitution of Fe cations with Ga^{3+} ($BaFe_{12-x}Ga_xO_{19}$ [24]), Al^{3+} ($BaFe_{12-x}Al_xO_{19}$ [25]), and In^{3+} [26] with different concentrations, x, in the range from 0.1 to 1.2.

The fabricated samples have dimensions corresponding to the waveguide cross-sections: 7.2 x 3.4 mm^2 for 25.8 – 37.5 GHz, 5.2 x 2.6 mm^2 for 37.5 – 53.5 GHz, and 3.6 x 1.8 mm^2 for 53.5 – 78.3 GHz frequency ranges. The sample thickness was 2 mm.

b) experimental setup schematic

The sample characterization was performed in the microwave frequency range by the scalar network analyzers P2-65, P2-68, P2-69. The external magnetic field was parallel to the microwave electric field vector in the waveguide. Fig. 5.15 shows the schematic of the experimental setup [27].

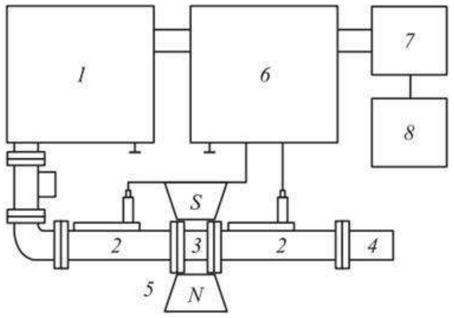

Fig. 5.15. Experimental setup: *1* — signal generator; *2* — waveguide directed couplers for the incident and reflected waves; *3* — waveguide section with the sample; *4* — matched load; *5* — magnet; *6* — indicator; *7* — DAC; *8* — computer.

c) $BaFe_{12-x}Ga_{x}O_{19}$ samples experimental characterization

EMR attenuation was measured in barium hexaferrites with different Ga^{3+} content in Ka and U frequency bands. A particular high-attenuation band is evident in any of measured absorption spectra (Fig. 5.16). The large attenuation bands are observed in all samples with different Ga^{3+} content and they are determined by NFMR.

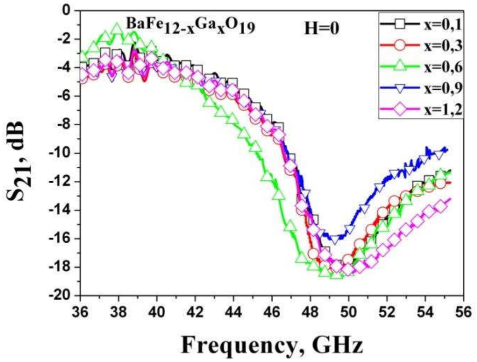

Fig. 5.16. EMR attenuation spectra for different Ga^{3+} content.

Fig. 5.17 shows nonmonotonic NFMR frequency dependence on the Ga^{3+} cations content [28]. The NFMR frequency decreases with increase of the Ga^{3+} content up to x = 0.6, for which the minimum NFMR frequency is observed.

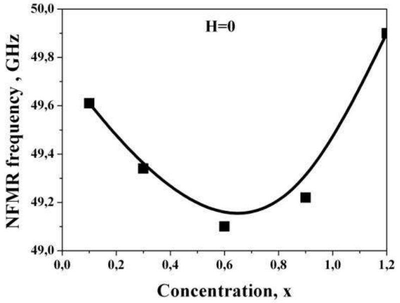

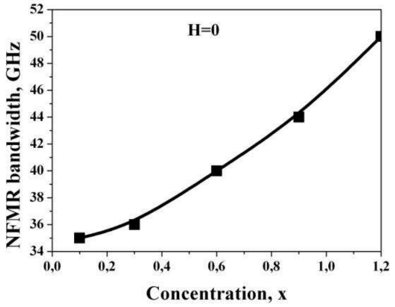

Fig. 5.17. NFMR frequency versus Ga^{3+} content

Fig. 5.18 NFMR bandwidth versus Ga^{3+} content.

The subsequent increase of Ga^{3+} content resuts in increase of the NFMR frequency up to the maximum value of 50.5 GHz observed at x = 1.2. The NFMR 3dB bandwidth also depends on the Ga^{3+} content (Fig. 5.18).

The increase of Ga^{3+} content allows increasing the NFMR bandwidth, i.e. the frequency range of high EMR absorption expands.

The EMR reflection coefficient was studied for hexaferrite samples with different Ga^{3+} content and different applied magnetic field strength. The corresponding dependencies are quite complicated. However, the reflection coefficient decreases with the increase of the magnetic field strength and reaches −33 dB (i.e. drops in 3 orders of intensity) at 5 kOe. The external magnetic field also changes the absorption spectra of the hexaferrite samples. Figure 5.19 shows the NFMR frequency change under the external magnetic field at different Ga^{3+} content.

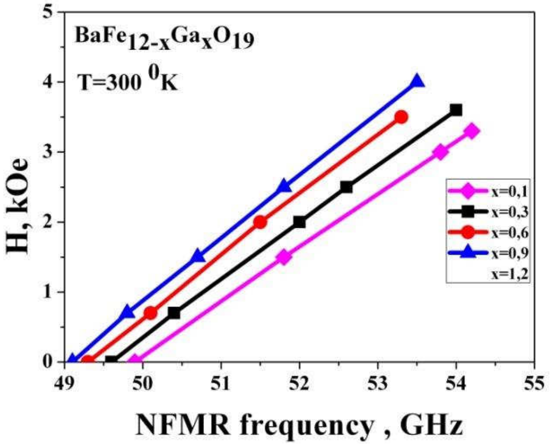

Fig. 5.19. Ga-substituted barium hexaferrite NFMR frequency as a function of applied magnetic field.

The experimental data show that all Ga-substituted samples are sensitive to the external magnetic field. When this field is applied, a resonance frequency shifts towards higher frequencies due to the higher effective internal magnetic field. These dependencies are almost linear for all samples [29].

d) $BaFe_{12-x}Al_xO_{19}$ samples experimental characterization

Fig. 5.20 shows EMR attenuation spectra in Al-substituted $BaFe_{12-x}Al_xO_{19}$ hexaferrite. Even at low Al^{3+} content, NFMR frequency shifts from 47 GHz (for pure barium ferrite) to 52 GHz at x = 0.1 and the shift increases with Al^{3+} content. The maximum observed NFMR frequency is 61 GHz at x = 1.2.

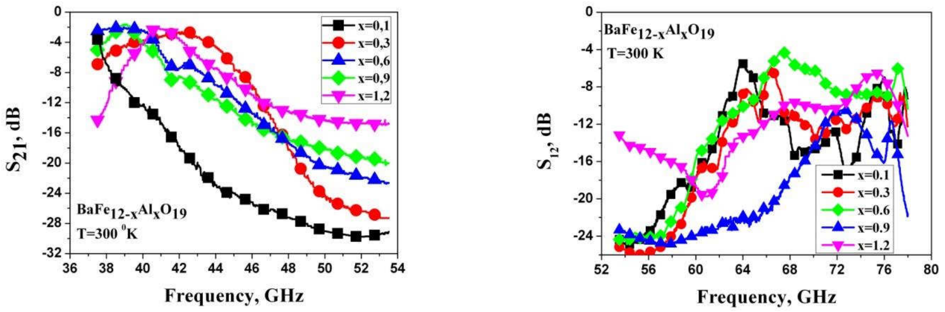
a) b)

Fig. 5.20. EMR attenuation spectra versus Al^{3+} concentration: a) in 36–54 GHz range; b) in 54–78 GHz range.

Fig. 5.21 illustrates a linear dependence of NFMR frequency on the Al^{3+} cations content.

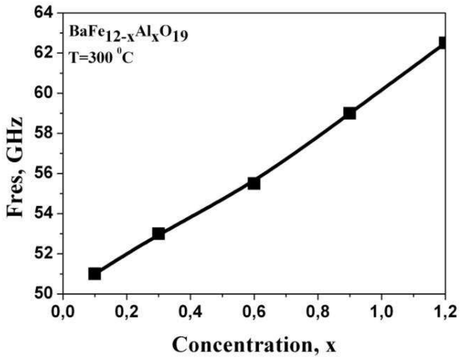

Fig. 5.21. NFMR frequency dependence on Al^{3+} concentration.

NFMR frequency also dependens on the external magnetic field strength (Fig.5.22).

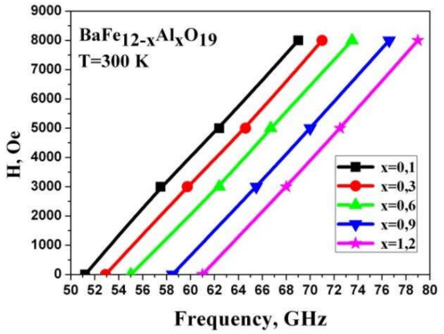

Fig.5.22. NFMR frequency as a function of external magnetic field at different Al^{3+} doping levels.

The change of external magnetic field results in a linear shift of the resonant frequency towards higher values.

Thus, the introduction of aluminum cations into the $BaFe_{12-x}Al_xO_{19}$ hexaferrite increases the magnetic anisotropy field from 16 kOe to 22 kOe, which in turn shifts the resonant frequency to 61 GHz; the external magnetic field strength of 10 kOe can tune the resonant frequency up to 80 GHz.

e) $BaFe_{12-x}In_xO_{19}$ samples experimental characterization

The third studied variant of substituted hexaferrite was In-doped, i.e. cations of indium In^{3+} were introduced hexaferrite instead of Fe^{3+} with contents of x = 0.3, 0.9, 1.2. EMR reflection characteristics were measured in a wide frequency range for hexaferrite with different In^{3+}content.

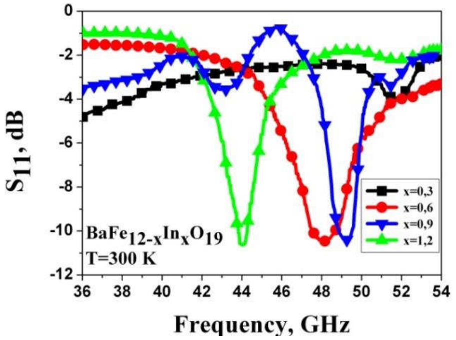

Fig. 5.23. EMR reflection spectra versus In^{3+} concentration.

As can be seen the reflection minimums (corresponding to absorption maximums) can be shifted towards lower frequencies (Fig. 5.23).

A linear dependence of NFMR frequency on the In^{3+} cations content is observed (Fig. 5.24) similarly to the above mentioned Ga- and Al-substituted hexaferrite. However, unlike in previous experiments, NFMR frequency shifts towards lower values when the content of ln^{3+} increases.

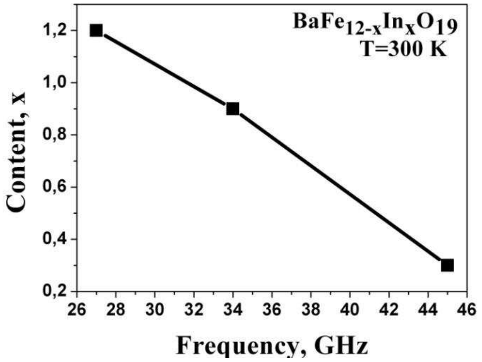

Fig. 5.24. NFMR frequency as a function of In^{3+} content in the hexaferrite.

Figure 5.25 shows the NFMR-field dependences for different In^{3+} contents in the hexaferrite. The significant influence of substituted cations on the frequency shift towards the lower values is observed. For instance, the frequency shift is 2 GHz at x = 0.3 and it is about 20 GHz at x = 1.2.

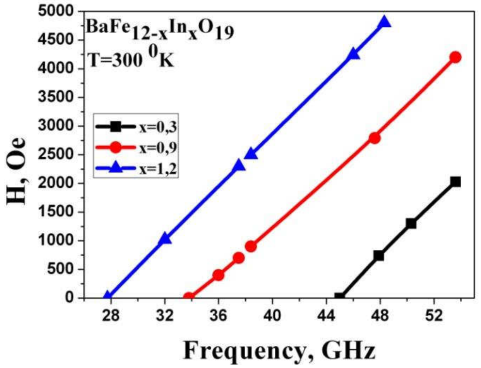

Fig. 5.25. NFMR frequency as a function of applied magnetic field for In^{3+}-substituted hexaferrite.

Thus, the introduction of diamagnetic cations significantly expands the frequency range of barium hexaferrite applications.

The replacement of Fe^{3+} with In^{3+} cations in the hexaferrite crystal lattice leads to a decrease in the saturation magnetization, coercivity and magnetic anisotropy fields due to a decrease in the number of magnetic cations. This causes a shift of the NFMR frequencies towards lower values up to 27.8 GHz at $x = 1.2$. When Fe^{3+} cations are partially replaced by Ga^{3+}, a nonmonotonic NFMR frequency shift occurs towards lower frequencies at low Ga content, but the subsequent increase in Ga content results in growth of the resonance frequency with the increase in the magnetic anisotropy field [30]. The substitution by Al^{3+} leads only to a rise in resonant frequency owing to an increase in the magnetic anisotropy field.

The introduction of diamagnetic cations allows operating the materials in the required frequency range without the application of external magnetic fields. In addition, material operating conditions can be changed by the content of diamagnetic cations. For example, it is possible to optimize the hexaferrite material for operation in phase shifters with minimal losses or to design the material with high losses and minimal reflection coefficient.

5.3. Application of spin-crossover materials for EMR parametric control

5.3.1. Relevance of research

In recent years increasing attention towards designing of molecular materials with properties attractive for practical applications is observed. To a great extent, this interest is caused by the need for miniaturization of devices [31]. Until recently, the tendency towards miniaturization was actively manifested in semiconductor technologies stimulating research in the fields of physics, solid-state chemistry, and technological developments in ever smaller sizes [32]. However, as known, semiconductor technologies are approaching their physical limit of miniaturization. A search for fundamentally new materials is required to reach a new level of miniaturization at a molecular scale. It is important to intergagrate these materials to obtain the components of electronic devices, to operate them as switches, memory units, gates, etc.

There are many classes of materials: organic, inorganic and coordination ones with potentially interesting electrical properties. Coordination compounds attract particular attention due to a huge variety of possible combinations of coordinating metals and organic ligands which allows synthesizing new materials with required physical properties. One of the promising classes of coordination compounds which can find numerous applications is represented by spin-crossover materials [31]. These compounds are $3d^4$–$3d^7$ metal complexes, among those Fe(II) compounds are the most studied. They are able to change their spin state from fully diamagnetic low-spin to paramagnetic high-spin. The change of spin state in spin-crossover compounds can be induced by various external factors: change of temperature or pressure, light irradiation, magnetic field, etc. Stability under repeated temperature cycles, low response time, hysteresis effects, and other features of spin-crossover compounds open a wide area for their potential applications: molecular electronics, spintronics, information storage, data displaying, and so on.

It should be noted that along with magnetic properties, the whole set of physical properties undergoes changes during the spin transition. The most significant changes concern optical (from strong absorption in the low-spin state to almost complete transmission in the HS state at selected wavelengths in UV-visible spectral range), mechanical and electrical properties of spin-crossover materials. As well, a distinct change of permittivity, permeability, EMR absorption/reflection coefficients, and other electrodynamic characteristics is observed [33]. These effects can be applied to design microwave switches, filters, radio-absorbing screening and other devices.

5.3.2. Experiment

Microwave scalar network analyzer P2-65 was used to measure the transmission (S_{21}) scattering parameters in the 25.8 – 37.5 GHz frequency range.

a) samples preparation

A powder sample of spin-crossover complex $[Fe(trz)(Htrz)_2]BF_4$ (Htrz = 1H-1,2,4-triazole, trz – deprotonated triazolato ligand) was obtained as previously described by Kroeber et al.[34]. A sample in the form of a pellet was inserted in the hollow rectangular waveguide. Dimensions of the spin-crossover samples were following: 7.2 x 3.4 x 2.5 mm^3.

b) measurements

Prior to the measurements of the microwave transmission scattering parameters, switchable properties of the obtained spin-crossover complex were studied using SQUID magnetometry. Measuring the magnetic susceptibility as a function of temperature allows following the spin transition in the material as the change in the number of unpaired electrons results in the dramatic change of χ. The magnetic measurements (Fig. 5.26a) show that at room temperature the complex is in the diamagnetic low-spin state ($\chi_M T \approx 0.5$ cm^3 K mol^{-1}). In heating mode upon reaching the temperature of spin transition the $\chi_M T$ values increase significantly at 377 K indicating the transition to the paramagnetic high-spin state ($\chi_M T \approx 3.2$ cm^3 K mol^{-1}). At further cooling, the transition back to the low-spin state occurs at 344 K revealing a 33 K wide hysteresis of spin transition. Fig. 5.26b additionally demonstrates the change of optical properties induced by the spin transition.

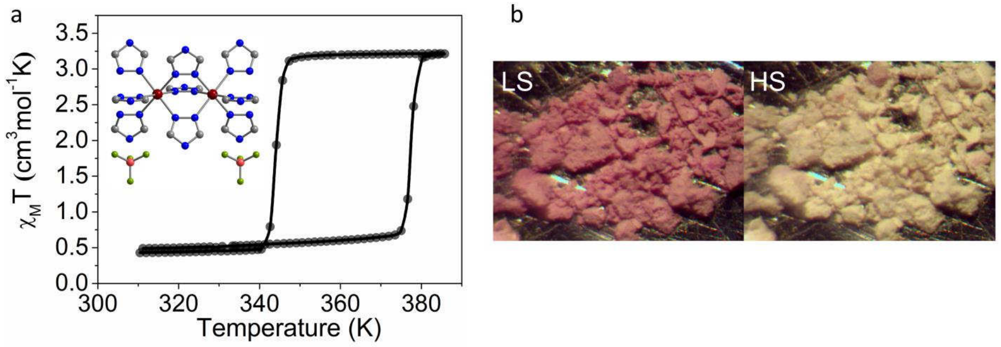

Fig. 5.26. (a) Magnetic measurements of $[Fe(trz)(Htrz)_2]BF_4$ demonstrating cooperative spin transition between diamagnetic and paramagnetic states. (b) Representation of the distinct color change upon transition from the low-spin (left) to the high-spin (right) state.

Microwave attenuation spectra were measured in the temperature range of 297 – 390 K in heating mode (Fig. 5.27).

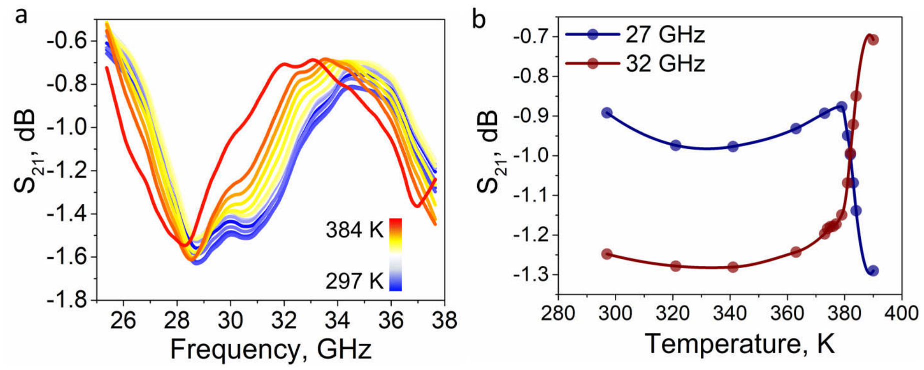

Fig. 5.27. Spin-crossover induced change of microwave transmission. (a) Temperature-dependent spectra of S_{21} measured in heating mode. (b) S_{21} vs. temperature at selected frequencies demonstrating the effect of microwave transmission switching upon spin transition.

At room temperature, two bands of S_{21} at 28.7 and 30.7 GHz can be identified in the investigated frequency range. Upon heating, a change of the transmission spectra associated with the spin transition is observed. First of all, the band at 30.7 GHz disappears completely with the transition to the HS, while the intensity of another band slightly decreases, additionally a minor shift of this band towards lower frequencies is registered.

In the temperature range of 295 – 375 K, S_{21} varies just slightly (Fig. 5.27b), however upon reaching the temperature of spin transition an abrupt change of transmission is observed. It should be noted that the direction of this change depends on the frequency of the wave, at which the analysis is performed. For example, in the case of 27 GHz wave analysis, a decrease of transmission from –0.9 dB to –1.3 dB is observed. However, at 32 GHz the opposite dependence can be found, namely an increase of transmission from –1.2 to –0.7 dB. Thus, the change of microwave transmission parameters itself is caused by the spin transition, while the direction of this change is determined by the correlation between the radiation wavelength and the size of the sample.

In order to understand the reason for these changes in microwave transmission parameters upon spin transition, temperature-dependence of dielectric properties of $[Fe(trz)(Htrz)_2]BF_4$ was investigated. The refraction index and absorption factor dependence on the temperature at 37 GHz were determined by the short-circuited waveguide method. The values of the absorption factor were calculated according to the transmission line theory using the thickness of the sample and input impedance of the waveguide filled with a sample.

At low temperatures the values of the absorption factor are about 0.0156 cm^{-1} (Fig. 5.28a). At heating the transition to the high-spin state and the absorption factor abruptly increase up to 0.0172 cm^{-1} were registered. With cooling (during the inverse transition to the low-spin state) the values of absorption factor switch back to the initial ones.

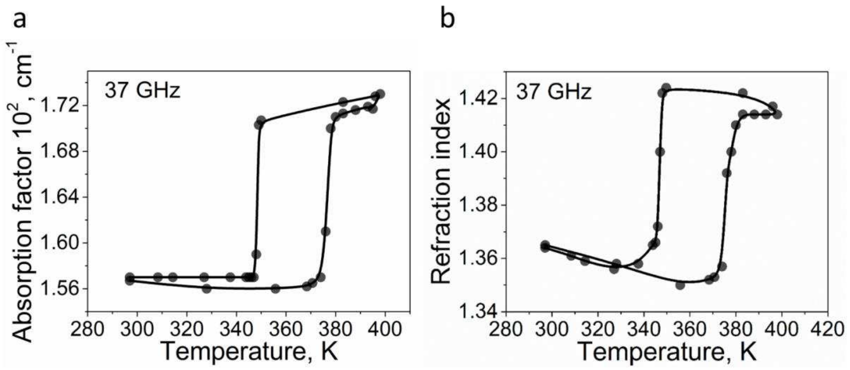

Fig. 5.28. (a) Temperature dependence of the absorption coefficient at 37 GHz; (b) Refraction index vs. temperature measured at the frequency of 37 GHz.

The obtained data allow calculating the refraction index of [Fe(trz)(Htrz)$_2$]BF$_4$. The dependence of the refraction index at 37 GHz on temperature is given in Fig.5.28b. Upon heating a minor decrease of refraction index can be observed, this effect can be associated with a slight thermal expansion of the sample. However, at the transition temperature from low-spin to high-spin state an abrupt increase of refraction index by ca. 6% is registered. Upon cooling the refraction index reverts to its initial values with the transition to the low-spin state. Thus, these experiments show considerable changes of dielectric properties of [Fe(trz)(Htrz)$_2$]BF$_4$ in the studied frequency range. This results in the change of microwave transmission parameters upon spin transition.

In summary, here a new efficient way of switching microwave radiation using molecular spin-crossover material is shown. The important finding is following. In spite of the huge variety of spin-transition complexes known for today, we demonstrate that there is a possibility to obtain spin-crossover-based microwave switches with required abruptness and hysteresis in the transistion region at any desired temperature.

5.4. Composite resonators “dielectric – magnetically ordered material” with magnetic field controlled microwave characteristics

5.4.1. Relevance of research

The microwave transceiver equipment for the modern telecommunication and radiolocation systems widely utilizes dielectric resonators (DR) for filters, solid-state oscillators, antenna systems etc. [35,36]. Such components are highly attractive due to low insertion losses, miniature size and high temperature stability [37], yet the lack of dynamical tuning of their characteristics (such as operating frequency or Q-factor) remains their crucial drawback.

At the same time, there is a demand for the frequency-selective microwave components which characteristics can be electronically adjusted accordingly to the incoming signal spectrum for their utilization as preselectors and matched filters or in cognitive radio systems [38].

In general, such electronic control can be realized if the microwave component includes some additional constituents, such as semiconductor varactors or diodes, various ferroelectrics etc.. This can be fulfilled via the electric field dependence of the added element’s dielectric properties (permittivity, conductance or capacitance) [39]. Another approach is based on the use of electromagnetically coupled to the DR ferrite with high-frequency magnetic permeability tunable by an external magnetic field [40,41].

The utilization of additional semiconductor or ferroelectric constituents usually results in degradation of the dielectric resonator’s Q factor and deterioration of its power handling capability and thermostability. On the other hand, high-quality ferrites, even polycrystalline ones, usually have relatively low dielectric losses and can withstand very high input power levels. Therefore the incorporation of magnetically ordered ferrite components with variable permeability seems more advantageous for the development of electronically tunable frequency-selective microwave devices with a high-quality factor, small dimensions, low cost and large dynamic range.

Here we considered the prototype composite heterostructures comprising the high-quality bulk dielectric resonator with a layer of magnetically ordered substance.

The latter was fabricated from two different kinds of magnetic materials: ferromagnetic dielectric (namely, nickel ferrite) and weak ferromagnet (iron borate).

Nickel ferrite $NiFe_2O_4$ is a traditional microwave material, known for his low conductivity, high room temperature saturation magnetization and low magnetic losses [42]. It was deposited in the form of a thick nanocrystalline film by the modified screen printing method, as described below, which is a simple and low-cost heterostructure fabrication technology.

Iron borate $FeBO_3$ belongs to a specific class of magnetically ordered materials known as weak ferromagnets or, alternatively, non-collinear antiferromagnets [43]. It has a rhombohedral crystallographic structure with “easy plane” type of anisotropy. The available theoretical models, allows using of the two-sublattice concept, predicting the existence of two distinct types of high-frequency magnetic oscillations in such materials [43,44]: quasi-ferromagnetic resonance (QFMR) mode, which manifests transversal oscillations of ferromagnetic vector and quasi-antiferromagnetic (QAFMR) mode. It is known that due to the presence of a rather large Dzyaloshinsky-Moriya field, causes decrease of the QFMR freqeuncy into Ku frequency band even for a moderate magnetic field of a few hundred Oe. However, the frequency of QAFMR is determined by a much larger intra-sublattice exchange field and it lies in the submillimeter-wave band.

Thus, the aim of the present studies is to develop fabrication technology for the two-layer “dielectric resonator-magnetic material” composite structures, investigate their microwave properties and demonstrate the feasibility of electronic control of heterostructure’s electromagnetic characteristics by an external static magnetic field.

5.4.2. Samples preparation and experimental methods

5.4.2.1. Composite structure „dielectric – weak ferromagnet”

Iron borate single crystals growth

High-quality single-crystal $FeBO_3$ basal platelets of hexagonal shape were grown by the solution-melt method with a boron-lead solvent [45]. By numerous growth experiments [46] the optimal melt composition for $FeBO_3$ synthesis was found to be (in wt. %): Fe_2O_3 – 6 %, PbF_2 – 30 %, PbO – 13 %, B_2O_3 – 51 %. The application of the differential-thermal analysis method allowed the rapid investigation of growth processes using extremely small amounts of starting batch components.

This approach allows optimizing the growth technology. The procedure, employed for the growth, enables obtaining good quality samples that were separated from the melt before it solidified as the temperature was decreased. This prevented the thermal deformation of crystals due to contact with solidifying solution-melt which could lead to the destruction of large crystals and the occurrence of mechanical stresses in smaller ones. The grown samples were optically transparent, have had a smooth surface and show a light-green color indicating the impurity-free crystals.

An experimental method for the investigation of the transmission characteristics of the "dielectric resonator-weak ferromagnet" composite structure

In order to fabricate the "dielectric resonator-weak ferromagnet" composite structure, a platelet of $FeBO_3$ with the thickness h=100 μm was epoxy bonded to the cylindrical DR with diameter D=5.1 mm and thickness S=3.1 mm fabricated from polycrystalline $Zr_xTi_ySn_{2-x-y}O_4$ (with dielectric constant $\varepsilon \approx 33$). $FeBO_3$ sample had roughly the same shape and diameter as a dielectric resonator.

This composite resonator was placed inside a rectangular X-band waveguide with 23×10 mm^2 cross-section. It was positioned on the waveguide wide wall, with iron borate in direct contact with metal. The lateral position of resonator L varied during the measurements (Fig. 1.30).

The external magnetic field from the solenoid coil was directed along the waveguide axis and applied in the sample plane. Microwave measurements in transmission mode were performed using an X-band scalar network analyzer P2-61.

The dielectric resonator was excited on the two lowest-order $EH_{\pm 11\delta}$ modes. These modes have identical spatial configurations and opposite rotation of their RF electric and magnetic field vectors (clockwise and counterclockwise). If the resonator is in free space, the eigenfrequencies of both modes are equal. However, due to the lack of cylindrical symmetry of waveguide metal walls, the frequency degeneracy increases and the deformation of modes' RF fields takes place.

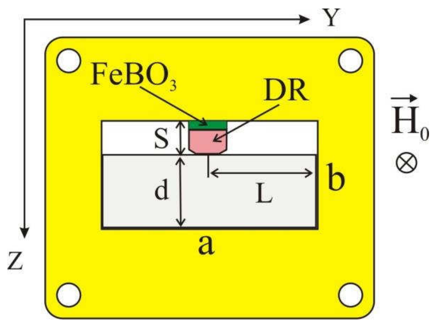

Fig. 5.30. Experimental measuring cell with composite resonator “dielectric – weak ferromagnetic”.

Our composite resonator consists of two parts, each of which represents a microwave resonator. The dielectric resonator has a discrete set of eigenmodes, with their resonant frequencies and Q factors depend on dielectric constant, resonator dimensions and position with respect to the metal waveguide walls, but both do not depend on the external magnetic field. On the contrary, weak ferromagnet constituent has a single resonant frequency (QFMR mode), which is almost independent of the sample’s dimension, but strongly depends on magnetic field. When both resonatrs are combined together, a relatively large area of contact between ferrite and dielectric causes tha following. The high-frequency electromagnetic fields of separate resonators in such heterostructure substantial overlap. This results in strong interaction and hybridization between dielectric and magnetic oscillations even for a small relative volume of the orthoferrite component.

5.4.2.2. Composite structure „dielectric-nickel ferrite”

A thermostable zinc-doped barium tetratitanate ceramics $(BaTi_4O_9)_{0.92}$-$(ZnO)_{0.08}$ [37] was selected as the dielectric component of the other composite heterostructure. In the microwave range this ceramics are characterized by Q-factor value $Q{\cdot}f \approx 70000$ GHz, dielectric constant $\varepsilon=34$ and temperature coefficient of dielectric permittivity $TC\varepsilon=10^{-6}$ K^{-1}. First, the cylindrical dielectric resonator with diameter D = 6.45 mm and thickness S = 1.70 mm was fabricated. Then a thick film of polycrystalline nickel ferrite was introduced on the top as it will be described below.

The powder precursors of the nickel ferrite $NiFe_2O_4$ with a spinel structure were obtained by the citrate sol-gel method. The analytically pure salts $Fe(NO_3)_3 \cdot 6H_2O$ and $Ni(NO_3)_2 \cdot 9H_2O$ and aqueous solutions of ammonia (25%) and citric acid (CA) were used as raw reagents. First, Fe^{3+} and Ni^{2+} nitrates were dissolved in the distilled water. Next, the citric acid was added to this aqueous solution in molar concentration in ratio = 1.5 with respect to the metal cations CA/M. Finally, a 25% aqueous solution of ammonia was added with continuous stirring until the solution has pH= 7. After that, the resulting suspension was heated to T = 353 K for 90 minutes until a viscous gel was formed. The gel was dried at T= 473 K until it transforms to the powder. The $NiFe_2O_4$ nanoparticles were synthesized after the sequential heating of this powder at 673 K (for 60 minutes) and 873–1173 K (for 120 minutes).

Synthesized powders of nickel ferrite were investigated by the X-ray phase and full-time X-ray phase analysis methods with a diffractometer ДРОН-4 (Cu Kα radiation). The size and morphology of powder particles have been determined using a SELMI 125 K transmission electron microscope.

This powder was deposited in the form of thick film using an original method developed by a modification of a well-known screen printing method. The latter is one of the most promising present-day techniques, which allows fabrication of high-quality uniform films with high density and large thicknesses. At the same time, it does not require expensive equipment, unlike LPE or PLD, hence the cost of produced films is low.

In the process of the film deposition, first, a uniform suspension from ferrite powder precursor and liquid hydroxypropyl methacrylate monomers was fabricated. The latter is a photopolymer which cures under the illumination by the ultraviolet (UV) radiation. A few different suspensions with various ferrite concentrations, namely 175, 350 and 525 g/l were prepared and then applied by the screen printing method on the dielectric resonator's top surface. Then the obtained films of different thicknesses (h=50, 70, 100, 200 μm) were cured under the UV light for 1 hour. Thus the thick polymer films with uniformly distributed ferrite nanoparticles were produced.

The method described above has a number of advantages over the traditional screen printing method. In particular, the additional thermal treatment at high temperatures, which can deteriorate the characteristics of a dielectric constituent of heterostructure and also may lead to the diffusion of ferrite’s chemical components into dielectric's surface layer, is not required. Moreover, it permits a fine control of the resulting ferrite layer's thickness, since the reduction of polymer volume during curing can be better controlled compared to the case of sintering in a muffle furnace.

Figure 5.31a shows the X-ray patterns of $NiFe_2O_4$ powders, calcinated from sol-gel precipitates. On the pattern recorded for the sample that was measured after thermal treatment at T = 873–1073 K the reflexes due to the presence of $\alpha - Fe_2O_3$ phase are visible beside the peaks of $NiFe_2O_4$. Single-phase $NiFe_2O_4$ with spinel structure is obtained after treatment at T = 1173 K (pattern number 4). The electron microscopy image of the single-phase samples shows that nickel ferrite powder has a laminar microstructure with nanoparticles average diameter equal to $d_{av.}$= 85 nm.

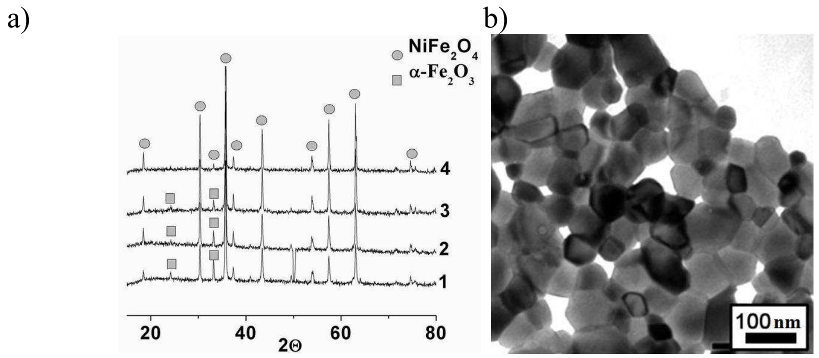

Fig. 5.31 a) X-ray patterns of thick nickel ferrite films after thermal treatment at the following temperature values: 1 – 873 K, 2 – 973 K, 3 – 1073 K, 4 – 1173 K; b) Microphotograph of nickel ferrite nanoparticles after thermal treatment at temperature T=1173 K

Measuring setup for the investigation of transmission characteristics of composite structures "dielectric resonator – thick film of nickel ferrite"

Absorption spectra of the manufactured composite heterostructures were measured in the X-band with Agilent N5230A PNA–L Vector Network Analyzer. The DR dimensions ensure that the main resonance mode of the free resonator is in the 10 – 12 GHz frequency range.

The dielectric resonator with deposited ferrite film was positioned on the glass substrate with a thickness of 0.2 mm inside the rectangular waveguide with the 23x10 mm^2 cross-section. The construction of a rectangular waveguide provides a complete shielding of measured samples (resonator radiation losses were excluded), and the glass substrate allows separation of the composite resonators from metal walls and reducing eddy currents losses. The coupling strength was adjusted whenever necessary by lateral displacement of composite resonator along the wide wall. A permanent magnet with a yoke frame was used to apply the external magnetic field directed perpendicularly to the sample surface (see Fig. 5.32).

The transmission characteristics of heterostructure were recorded in 8 – 12 GHz frequency band for different values of the magnetic field in a traveling wave mode. In such a way an effective excitation of both: dielectric resonator and ferromagnetic resonance in ferrite was assured. The characteristics of the hybrid resonance mode were then extracted from the recorded data.

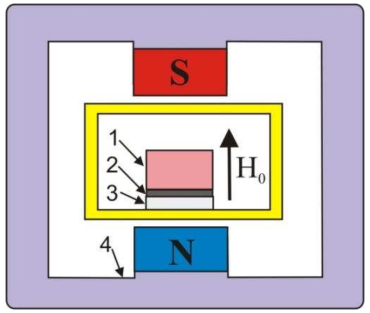

Fig. 5.32. Sketch of experimental measuring cell with composite resonator inside. 1 – dielectric resonator, 2 – thick ferrite nanocrystalline film, 3 – a glass substrate, 4 – permanent magnet with yoke frame.

5.4.3. Theoretical model.

Since the dielectric resonator volume is much larger than the resonator of ferrite, the perturbation theory can be used. We will treat DR eigen-oscillations as the unperturbed modes of the problem and ferrite film will be considered as a perturbation. In this case change of any DR mode's complex resonance frequency $\omega_r = 2\pi f_r(1 + i/(2Q))$ with the magnetic field H_0 can be written as [47,48]:

$$\frac{\omega_r(H_0) - \omega_r(H_0 = 0)}{\omega_r(H_0 = 0)} = -\frac{\int\limits_{V_F} \vec{m}\vec{h}_0^* dV}{2\int\limits_{V_{DR}} \vec{h}_0 \vec{h}_0^* dV} \ . \qquad (5.10)$$

Here $\vec{h}_0$ – is an unperturbed magnetic field vector of DR eigenmode, $\vec{m}$ – is a RF magnetization vector inside ferrite, V_F and V_{DR} is the volumes of ferrite layer and dielectric resonator, respectively. In expression (5.10) the numerator is proportional to the energy stored in perturbing volume, whereas the denominator is proportional to the total energy of the unperturbed dielectric resonator.

In fact, the complex dielectric constant of ferrite may also change hybrid mode complex resonant frequency, but since this effect does not depend on the magnetic field it will not be considered further.

We assumed that dielectric resonator lies on the metal plane (as shown in Fig. 5.10) and is surrounded by a perfect magnetic wall boundary. Then the spatial distribution of electromagnetic fields of the two circularly polarized azimuthally nonuniform $E_{\pm 1 1\delta}$ eigen-oscillations (those being the closest approximation to the actually excited $EH_{\pm 1 1\delta}$ modes) can be expressed in polar coordinates as [35]:

$$\begin{aligned}
&h_r^{\pm}(r,\phi,z) = A\frac{J_1(kr)}{kr}\cos(\beta z)e^{\pm i\phi}, && e_r^{\pm}(r,\phi,z) = \frac{\pm A\beta}{2\pi f\varepsilon_0\varepsilon k}\frac{\partial J_1(kr)}{\partial r}\sin(\beta z)e^{\pm i\phi},\\
&h_\phi^{\pm}(r,\phi,z) = \frac{\pm iA}{k}\frac{\partial J_1(kr)}{\partial r}\cos(\beta z)e^{\pm i\phi}, && e_\phi^{\pm}(r,\phi,z) = \frac{iA\beta}{2\pi f\varepsilon_0\varepsilon kr}J_1(kr)\sin(\beta z)e^{\pm i\phi},\\
&h_z^{\pm}(r,\phi,z) = 0, && e_z^{\pm}(r,\phi,z) = \frac{\pm Ak}{2\pi f\varepsilon_0\varepsilon}J_1(kr)\cos(\beta z)e^{\pm i\phi},
\end{aligned} \tag{5.11}$$

where $\beta = \sqrt{k_0^2\varepsilon - k^2}$, $k_0 = 2\pi f/c$, k is the transverse wave-vector, $J_1(kr)$ is the Bessel function of the first kind, A is the dimensionless amplitude. For the lowest-order $E_{\pm 1 1\delta}$ mode and perfect magnetic wall boundary condition, transverse wave-vector k is defined as $k = 3.682/D$.

Next, we expand the electromagnetic field inside DR in a Fourier series of DR eigenmodes $E_{\pm mn\delta}$. Since we consider frequencies close to $E_{\pm 1 1\delta}$ eigenfrequencies, it would be sufficient to keep only two terms, namely $\vec{h}_0 = A^{+}\vec{h}^{+} + A^{-}e^{i\theta}\vec{h}^{-}$, where $\vec{h}^{+}$ and $\vec{h}^{-}$ are given by Eq.(5.11), and θ is the phase difference between these two components.

On the other hand, high-frequency magnetization in magnetically ordered material can be expressed through the same RF magnetic field at the ferrite's position and ferrite's magnetic susceptibility: $\vec{m} = \hat{\chi}\vec{h}_0$.

For the QFMR mode in easy-plane weak ferromagnet, the magnetic permeability tensor in Cartesian coordinates with $X \parallel H_0$ (see Fig. 5.1) is given by [50]:

$$\hat{\chi} = \begin{pmatrix} 0 & 0 & 0 \\ 0 & \chi_1 & -i\chi_a \\ 0 & i\chi_a & \chi_2 \end{pmatrix}, \tag{5.12 a}$$

where $\chi_1 = -\dfrac{\gamma M(\omega_H + \omega_{DM})}{\omega^2 - \omega_H(\omega_H + \omega_{DM}) - \omega_\Delta^2}$, $\chi_2 = -\dfrac{\gamma M \omega_H}{\omega^2 - \omega_H(\omega_H + \omega_{DM}) - \omega_\Delta^2}$,

$\chi_a = \dfrac{\gamma M \omega}{\omega^2 - \omega_H(\omega_H + \omega_{DM}) - \omega_\Delta^2}$, $\omega_H = \gamma H_0$, $\omega_{DM} = \gamma H_{DM}$, $\omega_\Delta = \gamma H_\Delta$.

Note that expressions for χ_1 contains a very large multiplier ω_{DM} in the numerator. For the relatively low value of weak ferromagnetic saturation magnetization it compensates and as a result, this component of tensor susceptibility may easily reach the same magnitude as the susceptibility of the classical ferri- or ferromagnetic dielectrics [51]. On the other hand, χ_2 is much smaller than χ_1 and does not play any major role in interaction with the external electromagnetic field.

The external magnetic susceptibility tensor of nickel ferrite for the case when $Z \parallel H_0$ (see Fig. 5.32) in the Cartesian coordinate system is [42] can be described as:

$$\hat{\chi} = \begin{pmatrix} \chi & i\chi_a & 0 \\ -i\chi_a & \chi & 0 \\ 0 & 0 & 0 \end{pmatrix}. \tag{5.12 b}$$

In the expression (5.12b) $\chi = \gamma M \omega_H / (\omega_H^2 - \omega^2)$, $\chi_a = \gamma M \omega / (\omega_H^2 - \omega^2)$, $\omega_H = \gamma(H_0 - 4\pi M \cdot N_{zz} + H_a)$ is the internal magnetic field, γ is the gyromagnetic ratio, $4\pi M$ is the saturation magnetization of ferrite, H_a is the effective anisotropy field, N_{zz} is the demagnetizing factor. The susceptibility tensor components are complex if magnetic losses are not small and should to be taken into account.

Further, we will suppose that the spatial distribution of the microwave magnetic field inside the ferrite film is exactly the same as it was on the surface of DR without the film. Also, we will take into account that $h << S$ and hence assume that thickness distribution of both $\vec{m}$ and $\vec{h}_0$ across the ferrite film is uniform. After performing an evaluation of the right-hand-side of expression (5.10) one can find the explicit formulae for the magnetic field induced variations of resonance frequency and quality factor in both cases of interest (see below).

a) Weak ferromagnet

After perfoming calculations we obtaine:

$$\frac{\omega_{r0}-\omega_{r1}}{\omega_{r0}}=\frac{1}{2}\chi_1\left(1-1.837\frac{A^+A^-}{A^{+^2}+A^{-^2}}\cos\theta\right)\frac{V_F}{V_{DR}}, \tag{5.13}$$

which is correct for the multiplier of the order of unity. From Eq. (5.4) one can obtain that the strength of the interaction between dielectric's and weak ferromagnet's oscillations in composite resonator depends on the polarization of the electromagnetic field inside the dielectric resonator. For example, the perturbation effect would be identical for pure $E_{+11\delta}$ or $E_{-11\delta}$ modes (when either $A^+=0$ or $A^-=0$). In these cases, expression in brackets in the right-hand side of Eq. (5.13) becomes equal to 1. However, if the electromagnetic field comprises both of these modes with equal amplitudes and phases ($A^+=A^-$, $\theta=0$), this term will drastically reduce to value of 0.08. On the other hand, when participating modes of equal magnitude have an 180^0 phase shift, its value will increase to 1.92. Hence, the strength of interaction can change by a factor of 20.

When magnetic losses in $FeBO_3$ are taken into consideration, magnetic susceptibility becomes complex. Then, separating real and imaginary parts of Eq. (5.13) and assuming $Q>>1$, we get:

$$\frac{\Delta f_r}{f_{r0}}=\frac{1}{2}\chi_1'\left(1-1.837\frac{A^+A^-\cos\theta}{A^{+^2}+A^{-^2}}\right)\frac{V_F}{V_{DR}},\ \Delta\left(\frac{1}{2Q}\right)=\frac{1}{2}\chi_1''\left(1-1.837\frac{A^+A^-\cos\theta}{A^{+2}+A^{-2}}\right)\frac{V_F}{V_{DR}}, \tag{5.14}$$

where the real and imaginary parts of susceptibility are:

$$\chi_1'=-\frac{\gamma M\left(\left(\omega^2-\omega_H(\omega_H+\omega_{DM})-\omega_\Delta^2\right)(\omega_H+\omega_{DM})-(\alpha\omega)^2\omega_H\right)}{\left(\omega^2(1+\alpha^2)-\omega_H(\omega_H+\omega_{DM})-\omega_\Delta^2\right)^2+(\alpha\omega)^2(2\omega_H+\omega_{DM})^2},$$

$$\chi_1''=\frac{\alpha\omega\gamma M\left(\omega^2(1+\alpha^2)+(\omega_H+\omega_{DM})^2-\omega_\Delta^2\right)}{\left(\omega^2(1+\alpha^2)-\omega_H(\omega_H+\omega_{DM})-\omega_\Delta^2\right)^2+(\alpha\omega)^2(2\omega_H+\omega_{DM})^2}. \tag{5.15}$$

here α is the phenomenological Gilbert damping constant.

It should be noted that Eq. (5.14) can be presented as $\Delta Q/Q\propto -Q\chi'' V_F/V_{DR}$ which explicitly demonstrates that: (i) Q-factor of the composite resonator will always deteriorate in comparison to pure DR's one ($\chi''>0$, hence $\Delta Q<0$), since magnetic losses sum up with dielectric ones, and (ii) Q-factor fractional change is Q times ($Q>>1$) enhanced in comparison with fractional change of the resonant frequency.

Ferrimagnetic material

In this case, after similar calculations we get :

$$\frac{\Delta f_r}{f_{r0}} = -\left(\chi' \pm 0.837\,\chi'_a\right)\frac{V_F}{V_{DR}}, \quad \Delta\left(\frac{1}{2Q}\right) = \left(\chi'' \pm 0.837\,\chi''_a\right)\frac{V_F}{V_{DR}}. \tag{5.16}$$

Alternating signs in Eq.(5.16) correspond to different eigen-polarizations of dielectric mode. Namely, “+” corresponds to circularly polarized $E_{11\delta}$ mode with a right-hand rotation and “–” – to the mode with left-hand rotation. Since $\left(\chi' + 0.837\,\chi'_a\right) >> \left(\chi' - 0.837\,\chi'_a\right)$, the coupling between DR mode and ferromagnetic resonance (FMR) in ferrite layer is the most efficient when rotations of those modes are the same and are almost negligible in the opposite case.

The factor 0.837 in front of χ'_a appears due to the fact that $E_{11\delta}$ mode polarization is circular, i.e. only at the center of DR and transforms into elliptical one at the sidewall [48]. Hence, this coefficient, reflects the “spatially average” polarization state.

Real and imaginary parts of complex magnetic susceptibility are given by:

$$\chi' = \frac{\gamma M \omega_H\left(\omega_H^2 - \omega^2 + \left(\gamma\frac{\Delta H}{2}\right)^2\right)}{\left(\omega_H^2 - \omega^2 - \left(\gamma\frac{\Delta H}{2}\right)^2\right)^2 + \left(\gamma\Delta H\omega_H\right)^2}, \; \chi'' = \frac{\gamma M\left(\omega_H^2 + \omega^2 + \left(\gamma\frac{\Delta H}{2}\right)^2\right)}{\left(\omega_H^2 - \omega^2 - \left(\gamma\frac{\Delta H}{2}\right)^2\right)^2 + \left(\gamma\Delta H\omega_H\right)^2}\frac{\gamma\Delta H}{2},$$

$$\chi'_a = \frac{\gamma M \omega\left(\omega_H^2 - \omega^2 - \left(\gamma\frac{\Delta H}{2}\right)^2\right)}{\left(\omega_H^2 - \omega^2 - \left(\gamma\frac{\Delta H}{2}\right)^2\right)^2 + \left(\gamma\Delta H\omega_H\right)^2}, \; \chi''_a = \frac{\gamma M \omega\omega_H}{\left(\omega_H^2 - \omega^2 - \left(\gamma\frac{\Delta H}{2}\right)^2\right)^2 + \left(\gamma\Delta H\omega_H\right)^2}\gamma\Delta H, \tag{5.17}$$

where $\Delta H = 2\alpha\omega/\gamma$ is the full ferromagnetic resonance linewidth, α is the Gilbert damping constant.

Thus, from Eq.(5.16) the external field H_0 can induce changes in both resonance frequency and Q-factor of the composite resonator. Similarly, Q-factor modification is also expected to be more pronounced in comparison with modification of resonance frequency by assuming that the right-hand sides of Eq.(5.16) are of one order of magnitude.

An example of theoretical Δf_r and $\Delta(1/Q)$ vs. magnetic field curves for right-hand circularly polarized mode is shown in Fig. 5.33 for the following magnetic parameters: $4\pi M$ =3200 G, γ=3.1 MHz/Oe, ΔH =800 Oe, $V_F/V_{DR}=1/100$ and assuming DR unperturbed resonance frequency $f_r(H_0$=0) =11 600 MHz. For a thin solid ferrite film N_{zz}=1.

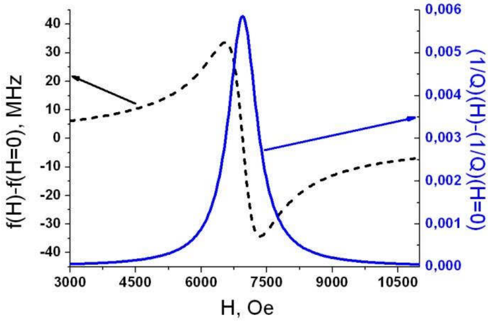

Fig. 5.33. Theoretical dependence of resonance frequency and inverse Q-factor shifts vs. magnetic field for the composite resonator fabricated on the basis of dielectric and nickel ferrite film.

Now, let's consider factors which affect the efficiency of coupling between components of composite resonators. From Eqs. (5.14)-(5.16) we obtain that changes in f_r and Q are directly proportional to the product of ferrite constituent fractional volume V_F/V_{DR} and saturation magnetization. Besides that, lower magnetic losses parameter ΔH results in larger χ' and χ'' values, which also enhances the effect. Finally, as can be seen from Fig. 5.33, the strongest coupling is for the field values around H_{FMR} (for which FMR or quasi-FMR frequency coincide with dielectric mode's unperturbed frequency). Indeed, in this case, the real and imaginary parts of $\hat{\chi}$ tensor attain the maximum values since the denominators of corresponding expressions become minimal.

Therefore, the largest magnetic field induced modification of hybrid oscillations' electrodynamics characteristics will take place for the ferrite film of the largest thickness, ferrite material with the largest saturation magnetization and the lowest magnetic losses and, noticeably, at the magnetic field close to FMR value for the frequency equal to dielectric resonator's unperturbed frequency.

5.4.4 Experimental results

5.4.4.1 Composite structure „dielectric – weak ferromagnet"

Results on the transmission characteristics for the composite resonator with iron borate and their modification with in-plane magnetic field are shown in Figs. 5.34-5.36 [49-53]. Figure 5.34 corresponds to the situation when the composite resonator was positioned in the middle of the waveguide's wide wall ($L = a/2$).

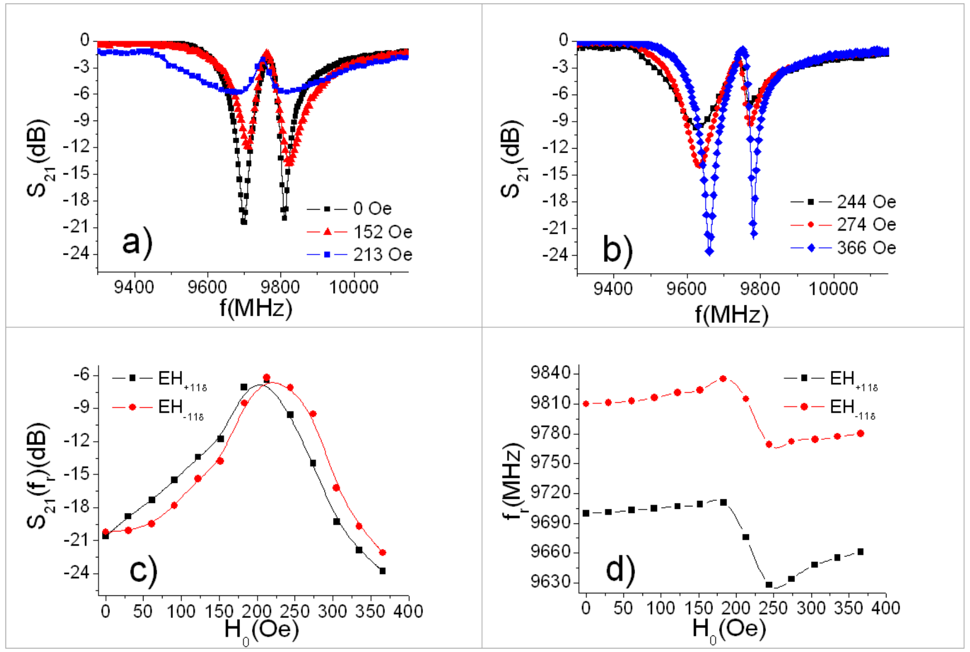

Fig. 5.34. (a) and (b) – transmission characteristics of the composite resonator as a function of magnetic fields H_0 showing the absorption due to resonance; (c) and (d) - transmission coefficient at resonance and resonance frequency vs. the magnetic field. The sample is positioned on the metal wall at $L = a/2$.

Fig. 5.35 shows results for the sample at the left circular polarization point (approximately $L = a/4$) and Fig. 5.36 presents results for the sample tightly pressed to the left sidewall ($L = a - D/2$). Investigations for the sample situated in symmetrical positions have shown qualitatively similar results and thus are not presented here.

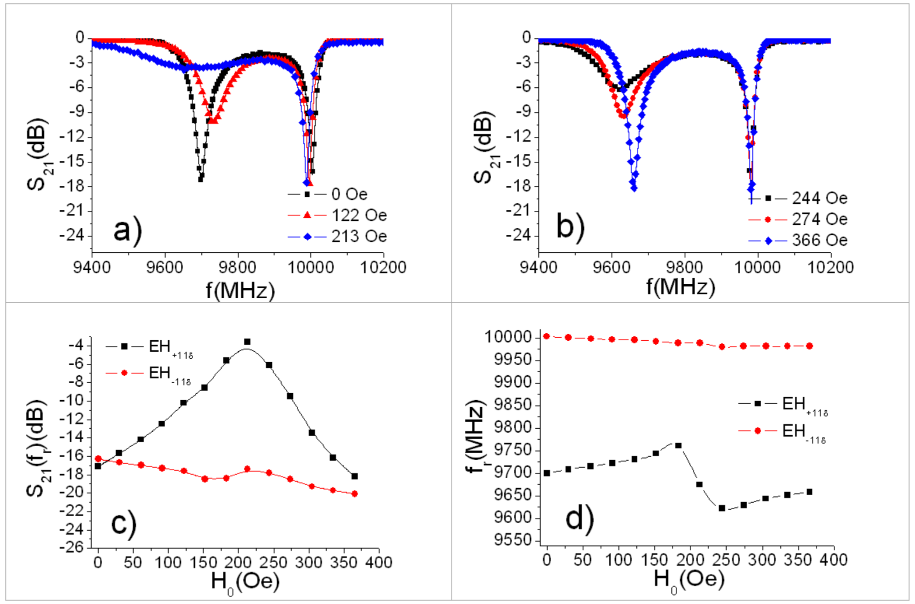

Fig. 5.35. Transmission characteristics as described in Fig. 5.34 obtained for the sample positioned at $L = a/4$.

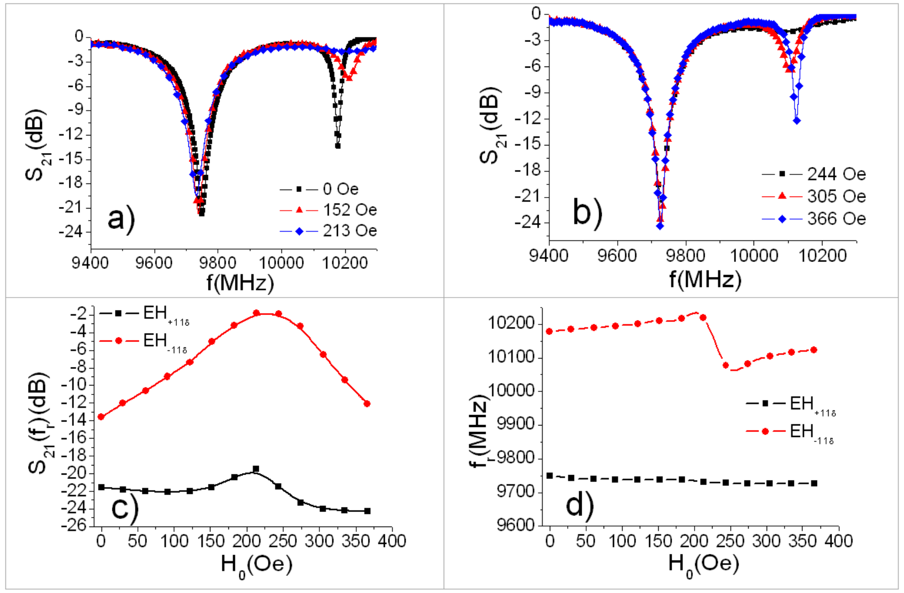

Fig. 5.36. Transmission characteristics as described in Fig. 5.34 obtained for the sample positioned at $L = a - D/2$.

These figures demonstrate the noticeable impact of FMR in $FeBO_3$ on the properties of hybrid oscillations, i.e. on eigenfrequency and Q-factor. The change in Q can be explained by transmission losses followed by change of the width of the resonance absorption line. Indeed, according to existing models [53], the linear transmission coefficient at resonance frequency is given by $S_{21}(f_r) = 20 \lg T(f_r)$, $T(f_r) = (1+K)^{-1} \approx K^{-1}, K >> 1$, where coupling coefficient K depends on the nature of transmission line, shape, size, and dielectric constant of the resonator. In addition, it is directly proportional to the unloaded Q-factor. Hence, we can treat $S_{21}(f_r)$ vs. H_0 profiles (see Fig. 5.34c-5.36c) as having qualitatively the same shape and behavior as $1/Q$ vs. H_0.

For the comparison between theoretical estimations and experimental data, let us consider the specific case of composite resonator positioned at $L = a/2$. This configuration is the closest to the theoretical model as the sample does not tached to the side metal walls. Figure 5.37 shows the measured values of the fractional resonance frequency shift $\Delta f_r / f_r$ for both DR modes as a function of the normalized magnetic field H_0 / H_{FMR}. These values were obtained from the results in Fig. 5.34. Theoretical estimations using Eq. (5.14) are also shown by a solid line.

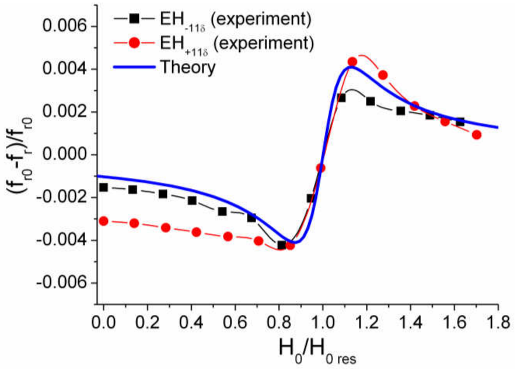

Fig. 5.37. Normalized composite resonance frequency shift vs. normalized magnetic field for the sample positioned at $L = a/2$.

Material properties of microwave dielectric were given earlier and for $FeBO_3$ we have assumed the following parameters: H_{DM} = 49.9 kOe, H_Δ=2.1 kOe, $4\pi M$ = 120 G [49], with the damping constant was taken to be $\alpha = 5.5 \cdot 10^{-3}$. As can be seen the experimental data agree qualitatively with predictions of the perturbation theory.

As was discussed earlier, $S_{21}(f_r)$ vs. H_0 curve should have qualitatively the same behavior as for $1/Q$ vs. H_0. The profile shown in Fig. 5.38c is bell-shaped which is typical for the imaginary part of the magnetic susceptibility, thus $1/Q$ actually behaves proportionally to the χ'', as it follows from Eq. (5.14).

Our experiments demonstrate that coupling between FMR mode and either of $EH_{\pm 11\delta}$ modes strongly depend on the position of composite resonator inside the waveguide. Specifically, when the sample is placed at the center, the strong hybridization with both DR modes is registered. The change of magnitudes of resonance frequency and insertion losses is about the same. On the contrary, at other positions, a preferable hybridization with either low-frequency or high-frequency mode can be obtained, whereas interaction with the other mode is negligible.

The data on the magnetic tuning of the composite resonator shows the following important characteristics. When the composite resonator is located at *L=a/2*, the maximum change in the transmission coefficient at resonance frequency is 16 dB and 15 dB for the $EH_{+11\delta}$ and $EH_{-11\delta}$ modes, whereas the resonance frequency changes by 85 MHz and 70 MHz, respectively. For this particular position, the actual electromagnetic field distribution is rather close to pure $E_{+11\delta}$ or $E_{-11\delta}$ mode configuration (at either $A^{+} >> A^{-}$ or $A^{+} << A^{-}$) and thus an almost equally strong coupling to both DR modes is provided. (ii) When the sample is moved to $L = a/4$ position, power absorption for the two modes changes by 14 dB and 4 dB, and frequency changes by 140 MHz and 10 MHz, respectively. This fact may be interpreted assuming $A^{+} \approx A^{-}, \theta = \pi$ and $A^{+} \approx A^{-}, \theta = 0$, respectively. For the case when the sample is in contact with the metal wall, the situation is almost exactly the opposite. We have 5 dB and 12 dB transmission loss variations and 10 MHz and 145 MHz frequency shifts, respectively. This situation is similar to the previous case, just the modes polarizations are reversed.

Finally, in this study, the composite resonator frequency tuning is accomplished for a nominal magnetic field H_0 below 250 Oe demonstrating attractive practical utilization. Indeed, such iron borate containing composite resonators may be used in the design of the microwave components operating under a relatively small, easily attainable magnetic field. Besides, according to Eq.(5.14) the frequency tuning range could be further increased by increasing the volume of $FeBO_3$.

5.4.4.2. Composite structure „dielectric – nickel ferrite film”.

Fig.5.38 demonstrates the transmission characteristics of the “$NiFe_2O_4$ thick film – $BaTi_4O_9$–ZnO” composite structures with different nickel ferrite films thicknesses (*h*=50, 70, 100, 200 μm) for the ferrite nanopowder concentration in the polymer suspension equal to C=175 g/l for few values of magnetic field H_0 [55-57]. During the measurements, the sample was positioned at the waveguide’s sidewall. This provides the optimal conditions for the excitation of the right-hand circularly polarized $E_{+11\delta}$ mode. Therefore for the theory, one should take expression (5.16) with the “+” sign.

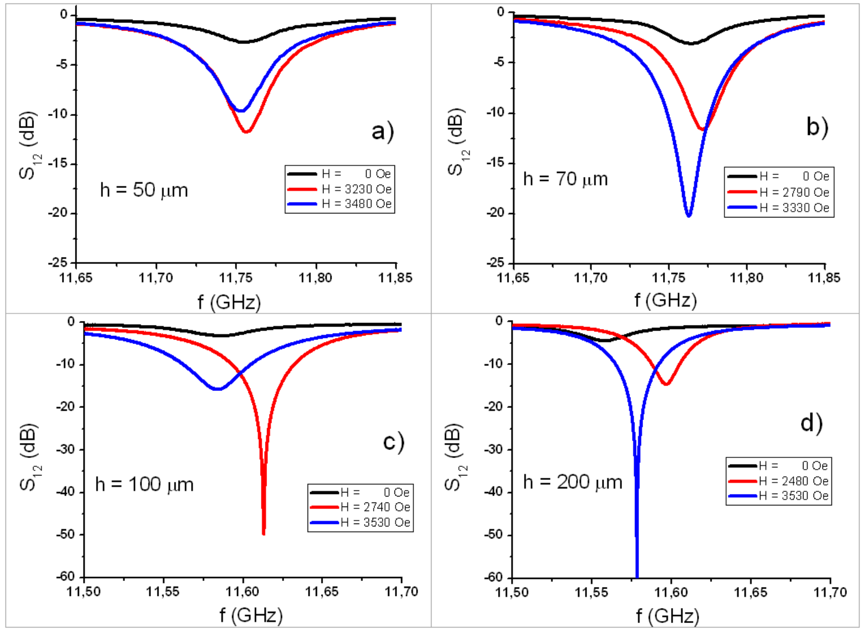

Fig. 5.38. Transmission characteristics of the composite nickel ferrite-dielectric resonator structure measured at different values of the external magnetic field, H (Oe): black-0; Red-about 2800, Blue – about 3600 and for different ferrite film thicknesses, h (μm): (a) – 50 μm, (b) – 70 μm, (c) – 100 μm, (d) – 200 μm. The concentration of ferrite in the film suspension was 175 g/l.

The application of the external magnetic field to the measurement cell with the composite resonator inside results in the noticeable modification of the hybrid structure’s resonance frequency and the insertion loss level at resonance. These effects are a direct consequence of the interaction between the electromagnetic field of the dielectric resonator and electromagnetic field of magnetization oscillations inside the ferrite component (see Section 5.3 for the details). Naturally, the largest change of resonator's characteristics take place for the external field close to the resonance field value H_{FMR}.

Fig. 5.29a shows that the frequency for field below resonance, $H < H_{FMR}$ increases and for field above resonance, $H > H_{FMR}$ decreases (in respect to the initial value) with increase of magnetic field. The reason for such behavior is the change of ferrite's magnetic susceptibility sign before and after the resonance (see Eq. (5.16)). The change of the absorption level at resonance (Fig. 5.38d) is obtained in the range from 9 dB (for the film with 50 μm thickness) to more than 60 dB (for h = 200 μm). The increase in the magnitude of absorbtion tuning with thickness can be explained by increased efficiency of interaction between the resonators. The efficiency is proportional to the volume of ferrite component.

The smallest shift of the resonance frequency with magnetic field was registered in the case of the composite resonators with ferrite film thickness equal to 50 μm (Fig. 5.39 a). The maximum frequency change with respect to the zero-field value for the 50 μm and 70 μm was 8.5 MHz and 7.5 MHz, respectively. For the case of resonators with 100 μm and 200 μm thick films, it was obtained to be 29 MHz and 12.5 MHz, respectively. In our experimental set-up magnetic field is restricted to 3600 Oe, therefore we the $f_r(H)$ dependence up to this value. Howevere, even the available experimental data were sufficient enough for the evaluation of magnetic parameters of the fabricated ferrite films.

Fig. 5.39 besides experimental data (dots) also shows the theoretical calculations performed using Eq. (5.16). The calculated data are shown by the solid lines. For the calculations, magnetic parameters: $4\pi M$, H_a and ΔH are used in the expressions for the components of the tensor magnetic susceptibility and as fitting parameters. The demagnetizing field effect was neglected, since the dipole-dipole interaction between ferrite nanoparticles dispersed in the photopolymer has to be rather weak in comparison with the solid ferrite films. The values for the above-mentioned parameters were chosen in order to provide the best possible agreement between experimental data and the theoretical curve.

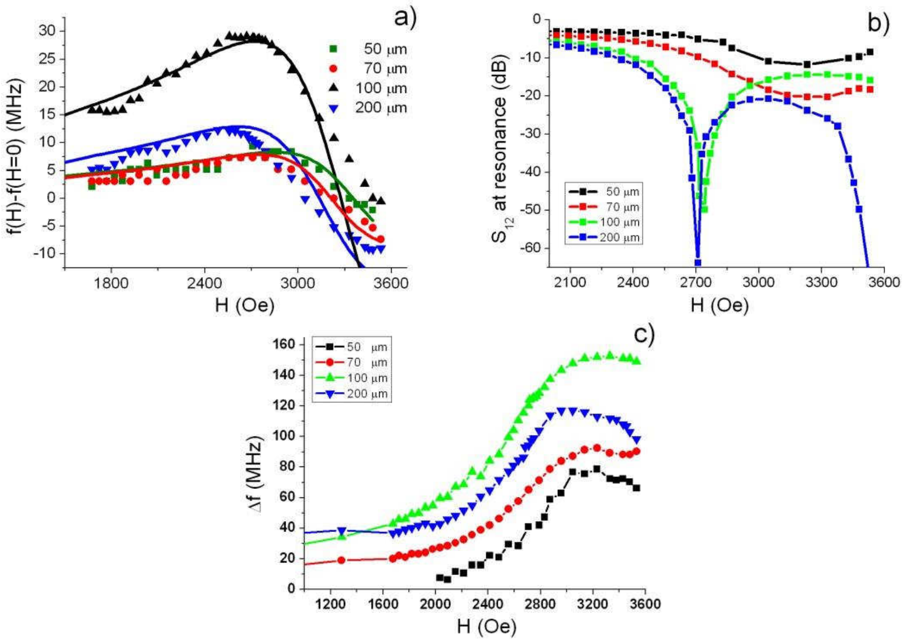

Fig. 5.39. (a) Resonance frequency shift, (b) maximum absorption level and (c) resonance linewidth at -3 dB level, obtained as a function of magnetic field for the composite ferrite-dielectric resonator with nickel ferrite films of different thicknesses, h (μm): 50- green, 70-red,100- black, 200- blue.

In should be noted that agreemtn between experimental and theoretical data for the thinner films (50 μm and 70 μm) is better compared to those obtained for the thicker ones. This can be explained by following reason: the initial assumption of minor perturbation is no longer valid with thickness growth and perturbation theory can be applied only for the case of small perturbations. In addition, in the thick films, the penetration of the UV curing radiation decreases due to the large absorption in ferrite particles; hence photopolymer curing might be incomlite.

The fitting magnetic parameters, used for plotting of the theoretical curves are listed in Table 5.1. As can be seen in all cases a similar H_a and ΔH values were obtained (although in general ΔH has a tendency to increase with increase of the thickness), whereas $4\pi M$ were significantly different. Rather small magnetization values in comparison with the bulk values can be explained by taking into account the fact that ferrite layer is not a solid material but a suspension of magnetic particles in a non-magnetic photopolymer. Therefore, after a proper volume averaging the resulting $4\pi M$ indeed becomes much smaller.

Further analyzing the data in Table 5.1 we can conclude that experimentally measured large resonance frequency tuning for the composite resonator with ferrite film with 100 μm thickness can be explained by a cumulative action of two factors: relatively large volume of ferrite constituent and high value of the effective saturation magnetization.

Table 5.1. Maximum resonance frequency shift and fitting magnetic parameters for the composite resonators with various ferrite film thicknesses.

Ferrite film thickness, μm	Maximum resonance frequency shift, MHz	Fit magnetic parameters		
		$4\pi M$, G	ΔH , Oe	H_a , Oe
50	8.5	490±30	1010±80	385±15
70	7.5	375±20	955±70	510±15
100	29.0	1330±100	1150±90	450±20
200	12.5	350±25	1260±80	550±20

Fig. 5.39c shows a variation of resonance linewidth of composite resonator hybrid mode measured at –3 dB level as a function of magnetic field. This important parameter determines the operating bandwidth of the various frequency-selective devices that can be designed on the basis of the hybrid resonators. On the other hand, for the given configuration of the measuring cell (with resonator-under-test cantaning a non-homogeneity) this parameter is inversely proportional to the loaded Q-factor. Indeed, for the large resonance absorption level (15 dB at least) we have $\Delta f_{-3dB} / f_r \approx 1/Q_L$ [57], thus the modification is proportional to the inverse Q-factor value.

From the experimental data, as can be seen the resonance linewidth increases as magnetic field approaches resonance value H_{FMR}. Therefore the loaded Q-factor decreases in a good agreement with the theoretical predictions. Moreover, the $\Delta f_{-3dB}(H)$ dependence has a specific bell-shape, which qualitatively corresponds to the theoretical H-field dependence for the imaginary part of the magnetic susceptibility (see also Fig. 5.34). As follows from Fig 5.40c, the largest linewidth modification is observed for the film with *h* = 100 μm and its value varied from ≈30 MHz to ≈150 MHz (i.e. fivefold). For the other film thicknesses, this variation is smaller compared to the variation registered for film with *h* = 100 μm.

Among the composite resonator's parameters considered above, two parameters: absorption level at resonance and resonance linewidth are defined not only by internal properties of the resonator itself, but also by external factor, such as the coupling coefficient [58]. Therefore, we can select the shift of resonator's resonance frequency f_r with the magnetic field as a measure of the coupling efficiency between dielectric resonator's eigen-oscillations and ferrite film's high-frequency magnetization in the composite heterostructure. From the measured experimental data (see Fig. 5.40 a), we can conclude that the strongest interaction between composite resonator's constituent components occurs in the case of ferrite film with 100 μm thickness compared to the interactions, obtained for investigated samples of other thicknesses.

Conclusions

The textured MWCNT in CM matrixes show the induced anisotropy of its electric and electrodynamic properties, such as conductivity, dielectric constant, absorption and reflection coefficients of electromagnetic wave at the applied external static electric field. The efficiency of textured CM interaction with electromagnetic radiation increases in the case of parallel orientation of electromagnetic wave electric field vector and MWCNT axis. The obtained characteristics of CM demonstrate their promising applications as effective screens for millimeter-wave radiation with minimum reflection and matched loads in waveguide structures.

The substitution of Fe^{3+} ions in barium hexaferrite by In^{3+}, Ga^{3+} and Al^{3+} diamagnetic ions results in a shift of the natural FMR frequency. Hence the introduction of diamagnetic cations drastically increases the frequency range of hexaferrite applications. Thus, the required properties of hexaferrite are obtained without the application of external magnetic field. The transition from one mode of operation to another one can be performed by changing the concentration of diamagnetic cations.

Molecular complexes with spin-active coordinated ions of transition metals from the group of iron demonstrate spin transition from low-spin to high-spin state followed by hysteresis. The spin transition leads to changes in physical and chemical properties of complexes, and, therefore in their main electrodynamic characteristics: dielectric permittivity, magnetic permeability, reflection and absorption coefficients. This opens the perspectives for future practical applications, such as high-speed phase and amplitude switches, tunable electromagnetic radiation protective screens, etc.

Results of studies of microwave properties of hybrid oscillations of a composite resonator comprising dielectric and iron borate parts demonstrate the electronic control of the resonator's frequency and quality factor.

We have established that application of magnetic field to the composite structures fabricated on the basis of high-quality microwave dielectrics and a thick film of nanocrystalline nickel ferrite materials results in the noticeable modification or resonator's transmission characteristics, including resonance frequency, transmission coefficient and resonance linewidth. For the structure with 100 µm thick ferrite film, the changes of resonance absorption level by more than 50 dB and almost fivefold variations of resonance linewidth were registered. The measured magnetic field characteristics for ferrite films of different thicknesses are in a good agreement with theoretical predictions performed in the frame of the perturbation theory.

A tunable variation of insertion losses by the amount of up to 16 dB as well as the change of resonance frequency of coupled oscillations by 145 MHz (or 1.5 %) were registered. The dependence of coupling between modes on the resonator's position inside the waveguide was analyzed. The characteristic behavior of f_r and $1/Q$ versus the magnetic field was investigated and qualitatively explained in the frame of the perturbation theory. Such composite resonators may find applications as a part of the microwave devices with tunable electrodynamic characteristics that can work in both centimeter wave band (quasi-FMR mode of iron borate) and submillimeter wave band (quasi-AFMR mode) with rather moderate magnitudes of magnetic field.

References

1. V. Launetz, L. Matzui, M. Melnichenko, V. Oliynyk, L. Vovchenko, O. Yakovenko. Electrodynamical properties of the nanocarbon/polymer composites with aligned by magnetic field secondary non-conductive component. Proc. SPIE, Nanotechnology VII, 1 June 2015, V. 9519. 951918 (2015).
2. V. L. Launets, L. Y. Matzui, V. V. Oliynyk, L. L. Vovchenko, O. S. Yakovenko, V. V. Zagorodnii. Conductive and shielding properties of MWCNTs/polymer nanocomposites with aligned filler distribution. Chapter 14, In book: NATO Science for Peace and Security, Series B: Physics and Biophysics, Springer. – 2016. 251–271, Code 173559.
3. V. L. Launets, L. Y. Matzui, V. V. Oliynyk, L. L. Vovchenko, O. S. Yakovenko, V. V. Zagorodnii. Microwave Properties and Conductivity Anisotropy of Oriented Multiwalled Carbon Nanotube Epoxy Composites. Metallofizika i noveishie tekhnologii. 38, N5, 657–668 (2016).
4. M. Al-Haik, E. Camponeschi, H. Garmestani, R. Vance. Properties of carbon nanotube-polymer composites aligned in a magnetic field. Carbon. 45, N10, 2037–2046 (2007).
5. S. Courty, J. Mine, A. R. Tajbakhsh, E. M. Terentjev. Nematic elastomers with aligned carbon nanotubes: New electromechanical actuators. Europhys. Lett. 64, N5, 654–660 (2003).
6. M. A. Shao-Jie, G. Wan-Lin. Mechanism of Carbon Nanotubes Aligning along Applied Electric Field. Chin. Phys. Lett. 25, N1, 270–273 (2008).
7. L. Lou, P. Nordlander, R. E. Smalley. Fullerene nanotubes in electric fields. Phys. Rev. B. 52, N3, 1429–1432 (1995).
8. V. L. Launets, O. O. Lazarenko, L. Y. Matzui, V. V. Oliynyk, L. L. Vovchenko, V. V. Zagorodnii. Electrical and Shielding Properties of Nanocarbon-Epoxy Composites. Capter 2 in book: Conductive Materials and Composites, Nova Science Publishers, New York. – 2016. 29–91.
9. L. Vovchenko, Yu. Perets, I. Ovsienko, L. Matzui, V. Oliynyk, V. Launetz. Shielding coatings based on carbon-polymer composites. Surface and Coatings Technology. 211, 196–199 (2012).
10. V. L. Launetz, L. Y. Matzui, V. V. Oliynyk, L. L. Vovchenko, O. S. Yakovenkoa, A. V. Trukhanov. Dielectric Properties of Composite Materials Containing Aligned Carbon Nanotubes. Inorganic Materials. 52, N11, 1198–1203 (2016).

11. V. Komarov, S. Wang, J. Tang. Permittivity and measurements. In Encyclopedia of RF and Microwave Engineering, John Wiley&Sons, Inc.: Hoboken, NJ, USA. – 2005. – 3693 – 3711.
12. O. Yakovenko, L. Matzui, G. Danylova, V. Zadorozhnii, L. Vovchenko, Yu. Perets, O. Lazarenko. Electrical properties of composite materials with electric field-assisted alignment of nanocarbon fillers. Nanoscale Research Letters. 12, 471 (2017).
13. O. Brusylovets, L. Vovchenko, L. Matzui, V. Launets, V. Oliynyk, A. Shames, O. Yakovenko, N. Skoryk. Synthesis and properties of ferrite nanopowders for epoxy-barium hexaferrite-nanocarbon composites for microwave applications. Mat.-wiss. Werkstofftechnik. 47, N2-3, 139–148 (2016).
14. Y. Mamunya, L. Matzui, L. Vovchenko, V. Oliynyk, B. Kumanek, U. Szeluga. Influence of conductive nano- and microfiller distribution on electrical conductivity and EMI shielding properties of polymer/carbon composites. Composites Science and Technology. 170, 51–59 (2019).
15. O. S. Yakovenko, L. Y. Matzui, L. L. Vovchenko, O. V. Lozitsky, O. I. Prokopov, O. A. Lazarenko, A. V. Zhuravkov, V. V. Oliynyk, V. L. Launets, S. V. Trukhanov, A. V. Trukhanov. Electrophysical properties of epoxy-based composites with graphite nanoplatelets and magnetically aligned magnetite. Molecular Crystals and Liquid Crystals. 661, N1, 68–80 (2018).
16. C. Daming, L. Yingli, L. Yuanxun, Y. Kai, Z. Huaiwu. Microstructure and magnetic properties of Al-doped barium ferrite with sodium citrate as chelate agent. Journal of Magnetism and Magnetic Materials. 37-38, 65–69 (2013).
17. V. Kostishyn, L. Matzui, V. Oleynik, L. Panina, S. Trukhanov, A. Trukhanov, V. Turchenko, E. Trukhanova, An. Trukhanov, E. Yakovenko. Microwave properties of the Ga-substituted $BaFe_{12}O_{19}$ hexaferrites. Material Research Express. 4, 076106 (2017).
18. I. Kazakevich, S. Trukhanov, V. Turchenko, V. Oleinik, E. Yakovenko, L. Matsui, V. Launets, L. Panina, L. Vovchenko. Magnetic and Absorbing Properties of M-type Substituted Hexafer-rites $BaFe_{12–x}Ga_xO_{19}$ ($0.1 < x< 1.2$). JETP. 123, N3, 461–469 (2016).
19. V. Kostishyn, L. Matzui, V. Oleynik, L. Panina, S. Trukhanov, A. Trukhanov, V. Turchenko, D. Tishkevich, An. Trukhanova, E. Yakovenko. Magnetic, dielectric and microwave properties of the $BaFe_{12-x}Ga_xO_{19}$ ($x \le 1.2$) solid solutions at room

temperature. Journal of Magnetism and Magnetic Materials. 442, N15, 300–310 (2017).

20. V. I. Kostenko, T. G. Chamor, L. V. Chevnyuk. Ferromagnetic Resonance in Epitaxial Films of Al-Substituted Barium Hexaferrite. Ukr. J. Phys. 50, N3, 265–267 (2005).
21. I. Bsoul, S. Mahmood. Structural and Magnetic Properties of $BaFe_{12-x}Al_xO_{19}$ Prepared by Milling and Calcination. Jordan Journal of Physics. 2, N.3, 171–179 (2009).
22. L. D. Landau, E. M. Lifshitz. Electrodynamics of Continuous Media. Gostexizdat, Moskau. – 1957. – 616 p.
23. I. S. Kazakevich, V. G. Kostishin, V. V. Oliynyk, S. V. Trukhanov, A. V. Trukhanov, L. V. Panina, V. A. Turchenko, E. S. Yakovenko, L. Yu. Magnetic and absorpion properties of substituted hexaferrites M-type $BaFe_{12-x}Ga_xO_{19}$ (0.1<x<1.2). Matsui. JETP. 150, N3, 536–545 (2016).
24. A. Trukhanov, S. Trukhanov, V. Kostishin, L. Panina, M. Salem, I. Kazakevich, V. Turchenko, V. Kochervinskii, D. Krivchenya. Multiferroic properties and structural features of M-type Al-substituted barium hexaferrites. Physics of the Solid State. 59, N4, 737–745 (2017).
25. S. Trukhanov, A. Trukhanov, A. Turchenko, V. Kostishin, L. Panina, I. Kazakevich, A. Balagurov. Crystal structure and magnetic properties of the $BaFe_{12-x}In_xO_{19}$ (x=0.1–1.2) solid solutions. Journal of Magnetism and Magnetic Materials. 417, 130–136 (2016).
26. L. L. Vovchenko, A. V. Trukhanov, S. V. Trukhanov, V. A. Turchenko, E. S. Yakovenko, L. Yu. Matsui, V. L. Launets., V. V. Oliynyk, I. S. Kazakevich. Crystal structure, magnetic and microwave properties $BaFe_{12-x}Ga_xO_{19}$ solid solutions ($0.1 \leq x \leq 1.2$). Fizika Tverdogo Tela. 58, N9, 1733–1738 (2016).
27. A. V. Trukhanova, S. V. Trukhanov, V. A. Turchenko, V. V. Oleinik, E. S. Yakovenko, L. Yu. Matsui, L. L. Vovchenko, V. L. Launets, I. S. Kazakevich, S. G. Dzhabarov. Crystal Structure, Magnetic, and Microwave Properties of Solid Solutions $BaFe_{12-x}Ga_xO_{19}$ ($0.1 \leq x \leq 1.2$). Physics of the Solid State, 58, N9, 1733–1738 (2016).
28. A. V. Trukhanov, S. V. Trukhanov, V. G. Kostishyn, V. V. Oleinik, E. S. Yakovenko, L. Yu. Matsui, D. I. Tishkevich, E. L. Trukhanova. Correlation of the atomic structure, magnetic properties and microwave characteristics in substituted

hexagonal ferrites. Journal of Magnetism and Magnetic Materials. 462, 127–135 (2018).

29. A. V. Trukhanov, S. V. Trukhanov, V. G. Kostishyn, V. V. Oleinik, E. S. Yakovenko, L. Yu. Matsui, D. I. Tishkevich, E. L Trukhanova. Mössbauer Studies and the Microwave Properties of Al^{3+}- and In^{3+}-Substituted Barium Hexaferrites. Physics of the Solid State. 60, N9, 1768–1777 (2018).
30. S. V. Trukhanov, A. V. Trukhanov, V. G. Kostishyn, N. S. Zabeivorota, L. V. Panina, An. V. Trukhanov, V. A. Turchenko, E. L. Trukhanova, V. V. Oleynik, O. S. Yakovenko, L. Yu. Matzui, V. E. Zhivulin. High-frequency absorption properties of gallium weakly doped barium hexaferrites. Philosophical Magazine. 99, N5, 585–605 (2019).,
31. Malcolm A. Halcrow. Spin-Crossover Materials: Properties and Applications. John Wiley&Sons. – 2013. – 564 p.
32. R. Schaller. Technological innovation in the semiconductor industry: a case study of the International Technology Roadmap for Semiconductors (ITRS). Management of Engineering and Technology. 195 (2001).
33. I. Gural'skiy, O. Kucheriv, V. Oliynyk, V. Launets, V. Zagorodnii.Spin-crossover materials towards microwave radiation switches. Scientific Reports. N6, 1–7 (2016).
34. J. Kroeber, J.-P. Audiere, R. Claude, E. Codjovi, O. Kahn, J. G. Haasnoot, F. Groliere, Jay Ch, A. Bousseksou, J. Linarès, F. Varret, A. Conthier-Vassal. Spin transitions and thermal hysteresis in the molecular-based materials $[Fe(Htrz)_2(trz)](BF_4)$ and $[Fe(Htrz)_3](BF_4)_2\cdot H_2O$ (Htrz = 1,2,4-4H-triazole; trz = 1,2,4-triazolato). Chemistry of Materials. 6, N8, 1404–1412 (1994).
35. D. Kajfez, P. Guillon. Dielectric resonators, 2nd ed., Atlanta: Noble Publishing Corporation. – 1998. – 561 p.
36. C. Kudsia, R. Cameron, W.-C. Tang. Innovations in microwave filters and multiplexing networks for communications satellite systems. IEEE Trans. Microwave Theory Tech. 40, N6, 1133–1149 (1992).
37. A. G. Belous. High-Q microwave dielectrics. Kyiv.: Naukova Dumka. – 2016.
38. P. W. Wong, I. Hunter. Electronically Tunable Filters. IEEE Microwave Magazine. 10, N6, 46–54 (2009).
39. R. R. Mansour. High-Q tunable dielectric resonator filters. IEEE Microwave Magazine. 10, N6, 84–98 (2009).

40. J. Krupka, A. Abramowicz, K. Derzakowski. Magnetically tunable filters for cellular communication terminals. IEEE Trans. Microwave Theory Tech. 54, 2329–3335 (2006).
41. I. V. Zavislyak, M. A. Popov, E. D. Solovyova, S. A. Solopan, A. G. Belous. Dielectric-ferrite film heterostructures for magnetic field controlled resonance microwave components. Materials Science and Engineering B. 197, 36–42 (2015).
42. Yu. M. Yakovlev, S. Sh. Gendelev. Ferrite monocrystals in radio electronics. Moscow: Soviet Radio (in Russian). – 1975.
43. E. A. Turov, A. V. Kolchanov, M. I. Kurkin, I. F. Mirsaev, V. V. Nikolaev. Symmetry and physical properties of antiferromagnetics. Cambridge: Cambridge International Science Publishing. – 2004.
44. L. V. Velikov, A. S. Prokhorov, E. G. Rudashevskiy, V. N. Seleznev. Antiferromagnetic resonance in $FeBO_3$. Sov. Phys. JETP. 39, N5, 909–915 (1974).
45. M. B. Strugatsky, S. V. Yagupov. Solution-in-melt synthesis of iron borate monocrystals. Sci. Notes of Taurida National University. Ser. Phys. 19, N58, No.1, 76–78 (2006).
46. S. V. Yagupov, M. B. Strugatsky, N. S. Postivey, S. S. Kostulin. Application of differential-thermal analysis for research of solution-in-melt crystallization. Sci. Notes of Taurida National University. Ser. Phys. 23, N62, No.1, 121–124 (2010).
47. L. F. Chen, C. K. Ong, C. P. Neo, V. V. Varadan, V. K. Varadan. Microwave Electronics: Measurement and Materials Characterization. Chichester: John Wiley & Sons. – 2004.
48. W. Von Aulock, J. H. Rowen. Measurement of dielectric and magnetic properties of ferromagnetic materials at microwave frequencies. The Bell System Technical Journal. 36, 427–448 (1957).
49. M. A. Popov, I. V. Zavislyak, H. L. Chumak, M. B. Strugatsky, S. V. Yagupov, G. Srinivasan. Ferromagnetic resonance in a single crystal of iron borate and magnetic field tuning of hybrid oscillations in a composite structure with a dielectric: Experiment and theory. J. of Appl. Phys. 118, N1, 013903-1– 9 (2015).
50. H. L. Chumak, I. V. Zavislyak, M. A. Popov. Hybrid oscillations in composite dielectric–weak ferromagnet resonator. Proceedings of the XIV International young scientists' conference on applied physics, 11-14 June 2014, Kyiv (Ukraine), 61–62 (2014).

51. M. A. Popov, H. L. Chumak. Spin-orbital enhancement of tensor magnetic susceptibility components in weak ferromagnet. Proceedings of the XI International conference "Electronics and applied physics", 21-24.October 2015, Kyiv (Ukraine), 47–48 (2015).
52. M. A. Popov, I. V. Zavislyak, M. B. Strugatsky, S. V. Yagupov, G. Srinivasan. Magnetic Field Controlled Microwave Hybrid Oscillations in Composite Resonator Dielectric-weak Ferromagnet. Progress In Electromagnetics Research Symposium Proceedings, 6-9 July 2015, Prague (Czech Republic), 2408–2412 (2015).
53. M. A. Popov, H. L. Chumak. Magnetic Field Tuning of Hybrid Modes in a Composite Microwave Resonator with Iron Borate. Proceedings of the International Young Scientists Forum on Applied Physics YSF-2015, September 29 – October 2, 2015, Dnipropetrovsk (Ukraine) (2015).
54. M. E. Ilchenko, E. V. Kudinov. Ferrite and dielectric microwave resonators. Kyiv: Kyiv University Publishing (in Russian). – 1973.
55. K. D. Solovyova, O. P. Fedorchuk, M. O. Popov, I. V. Zavislyak, A. G. Belous. Development the composite magnetically heterostructures based on "thick film of spinel nickel ferrite" – dielectric resonator α-Al_2O_3. Ukrainian Chem. J. 82, N5, 10–14 (2016).
56. M. A. Popov, O. P. Fedorchuk, E. D. Solovyova, A. G. Belous. Composite dielectric-ferrite film resonator with magnetic field tunable microwave characteristics. Proceedings of the XII International conference "Electronics and applied physics", 19-22 October 2016, Kyiv (Ukraine), 47–48 (2016).
57. O. P. Fedorchuk, M. A. Popov. Magnetically tuned composite elements on the base of the system "dielectric resonator/ferrite film". Electronics and Communications. 22, N1, 20–26 (2017).
58. F. J. Tischer. Mikrowellen-Messtechnik. Berlin: Springer-Verlag. – 1958.

CONCLUSIONS

The effects revealed as a result of the interaction of electric, magnetic and electromagnetic fields with nanostructured composites, semiconductor structures, anisotropic media, phonons of molecular nanocomplexes and nanoinhomogeneities are described in the monograph.

Fluctuations of the RTS type were registered in Si nanowire field-effect transistors fabricated with small characteristic sizes. The dynamic processes in the NW FET structures were studied in the temperature range from 200 K to 280 K. The results demonstrate the deviation of the single trap dynamics in Si NW from the classical Shockley-Reed-Hall law, not only before but also after γ-radiation treatment. The difference is explained in frame of the model taking into account the additional energy required for the charge carriers to overcome the effective barrier in the accumulation mode. The results show that low-dose γ-irradiation results in control of dynamic processes related to a single-trap phenomena in the gate oxide. It is established that the charge state changes from the neutral state before irradiation to the attractive state after treatment, although the additional energy remains unchanged. The results demonstrate that γ-irradiation is an effective tool to control the parameters of single traps.

The observed effects are important for a wide range of basic research and applications using single-trap phenomena, as well as for the development of memory devices based on single traps and biosensors with advanced functionalities. Si NW FETs with liquid gates were designed and used for the selective detection of human troponin (cTnl) as a cardiac biomarker which is the gold standard for early diagnosis of acute myocardial infarction. The transport and noise properties of fabricated liquid-gated NW FET samples were investigated. The high sensitivity of biosensors to pH was demonstrated. Detailed analysis of the measured noise spectra of Si NW FETs with liquid gates before and after binding of cTnl molecules indicates that the molecules lead to an increase in total noise, which can be used as a signal for the diagnostic of a cardiac disease.

It was established that electrostatic charges associated with biomolecular dynamic processes on the surface of nanowires play the role of effective voltage on the gate. These processes result in fluctuations in Si NW FET drain current. It was also shown that the use of glycine-HCl buffer with low pH leads to the dissociation of the antigen-antibody complex. This reflects that the initial state of sensors to be restored, which allows the multiple usage of fabricated sensors. Thus, the fabricated Si NW FETs with appropriate surface functionalization can be employed as reusable biological sensors and provide considerable potential as diagnostic bio-medical tools.

Spectroscopic features of Raman gain profiles in four types of single-mode fibers based on silica glass were analyzed by separating them from the experimental Raman spectra of spontaneous scattering using subsequent multimode decomposition into Gaussian-type components. The technique is analyzed on the basis of an oscillatory model of the Raman scattering of active vibrations of molecular nanocomplexes in amorphous glass, taking into account both quantum and semiclassical approaches. It is shown that the temperature changes of the Raman spectra are concentrated in the low-frequency region at $T = 300$ K. The spontaneous spectral density is more than an order of magnitude greater than the corresponding components of the Raman gain profile at frequencies ≤ 20 cm^{-1} . However, their difference became practically invisible at frequencies above 800 cm^{-1}.

It is shown that the dopant impurities more strongly perturb the nonlinear spectrum of Raman amplification (by an order of magnitude) compared to the change in linear parameters of the fiber core, since the corresponding changes in the refractive index are $\Delta n \sim 0.01$. The strong deformation of Raman gain profiles occurs due to the significant restructuring of the vibrational modes of molecular nanocomplexes of the fiber cores on the basis of the effect of relatively small concentrations of impurities.

The results of Gaussian decomposition for 12 components in pure SiO_2, P_2O_5, TiO_2 and for 11 components in GeO_2 doped fiber, demonstrate that the main vibrational modes of the glass matrix, which form Raman gain profiles in the fibers, vary significantly across all oscillation parameters – namely several times in amplitude, a few tens of cm^{-1} at the frequency position and constant attenuation. Therefore, the average relaxation time of Raman processes is τ_I = 300 fs. This fact provides prospects for practical applications in the form of Raman amplifiers and lasers, operating in the terahertz freqeuncy band. In addition, although this time interval corresponds to the fundamental limit of the applicability of quasi-stationary approximations, the applicability of basic coupled equations of nonlinear Raman interaction of waves demonstrates ways for modeling telecommunication systems with terabyte rates.

It was established that the evanescent field parameters at the quartz-vacuum interface depend on both the surface roughness parameters and the shape of this surface. In this way, if the spatial spectrum of the rough surface profile contain only one harmonic (the rough quartz surface was modeled using a sinusoidal surface shape), the evanescent field has a much lower level of intensity and contrast along the surface than for the case where the spatial spectrum has a more complex spectral composition.

It should be emphasized that the rough quartz surface was modeled using a surface with triangular shape profile. In particular, for the case of a sinusoidal shape of the surface profile, the field level and contrast were more than 2 times lower than for the case of a surface with triangular shape profile. In both cases, the field had maxima in the high regions and minima in the low regions of the surface. At the same time, for the triangular shape profile, the field maxima were more concentrated in the peaks of the high regions. This reflects the fact that the concentration of field maxima near the peaks increase with the increase of the spatial spectrum width, and the intensity level of the evanescent field and its contrast also increase accordingly. It was found that in inhomogeneous twisted media prevailing waves propagating in this optically active medium can be excited. In this case, the polarization ellipse of prevailing waves does not change the shape and direction of wave propagation. Only its azimuth changes linearly.

It was shown that for the existence of prevailing waves in inhomogeneous twisted media with linear phase and amplitude anisotropy, the azimuths of the axes of these types of anisotropy in an elementary layer have to coincide.

The relations for the parameters of anisotropy were found. The properties of this class of media are described by the first and second Jones equivalence theorems.

The anisotropy of the electrical and electrodynamic characteristics: resistivity, permittivity, attenuation and reflection of electromagnetic irradiation (EMI) is revealed as a result of structuring multi-walled carbon nanotubes (MWCNT) in the matrix of composite materials (CM) under the action of an external electric field.

The effect allows the electromagnetic radiation to be controlled using structured CM in a parallel orientation of the electric wave vector and the axis of MWCNT. The characteristics obtained for CM open prospects of their utilization as effective screens of millimeter radiation with minimal reflection and as matched loads in waveguide networks.

Results of research of the high-frequency properties of hybridized oscillations of a composite resonator consisting of dielectric and iron borate, demonstrate the electronic control of the frequency and quality of such a resonator. A controlled change in the insertion losses from 4 to 16 dB and the shifting the resonance frequency of coupled oscillations within 145 MHz (which is 1.5% of resonant frequency) was demonstrated.

The replacement of Fe^{3+} iron cations in barium hexaferrite by In^{3+}, Ga^{3+} and Al^{3+} diamagnetic cations leads to a shift in the resonance frequency of the NFMR. In this way, the introduction of diamagnetic cations significantly broadens the frequency range and allows advanced characteristics of hexaferrite to be obtained without the application of external magnetic fields as well as allows to switch the operation mode by changing the concentration of diamagnetic cations.

Molecular compounds containing spin-active coordinated ions of transition metals of the iron group were developed. They determine the spin transition: from high-spin state to low-spin one accompanied by hysteresis. The spin transition leads to a change in the physical and chemical properties of the complexes, first of all in their magnetic and basic electrodynamic characteristics: dielectric permittivity and magnetic permeability, reflection and absorption coefficients. This allows significant future practical applications such as the development of high-speed devices for phase and amplitude switching, as well as controlled radiation protective screens.

[*] Author to whom correspondence should be addressed: s.vitusevich@fz-juelich.de (S.Vitusevich, Forschungszentrum Juelich (FZJ), ICS-8: Bioelectronics, 52425 Germany)

Acknowledgments

The authors appreciate the technical staff of the Helmholtz Nano Facility (HNF) of Forschungszentrum Juelich, Germany for their assistance with the fabrication of nanowire sensor devices. The support from Ministry of Education and Science of Ukraine, for funding of project №16ВФ052-04 (reg. № 0116Ш02564) at the Quantum Radiophysics department of the Faculty of Radiophysics, Electronics and Computer Systems of the National Taras Shevchenko University of Kyiv, Ukraine is acknowledged. This work was partially supported EU within the Horizon 2020 project IMAGE (GA Nr. 778156) and by Deutsche Forschungsgemeinschaft (DFG) Project VI 456/3-1. Authors acknowledge Yu. Kutovyi from FZJ, ICS-8, Germany for collaboration.

Band / Volume 198
Shortcut to the carbon-efficient microbial production of chemical building blocks from lignocellulose-derived D-xylose
C. Brüsseler (2019), X, 62 pp
ISBN: 978-3-95806-409-6

Band / Volume 199
Regulation and assembly of the cytochrome bc_1-aa_3 supercomplex in *Corynebacterium glutamicum*
C.-F. Davoudi (2019), 135 pp
ISBN: 978-3-95806-416-4

Band / Volume 200
Variability and compensation in Alzheimer's disease across different neuronal network scales
C. Bachmann (2019), xvi, 165 pp
ISBN: 978-3-95806-420-1

Band / Volume 201
Crystal structures and vibrational properties of chalcogenides: the role of temperature and pressure
M. G. Herrmann (2019), xi, 156 pp
ISBN: 978-3-95806-421-8

Band / Volume 202
Current-induced magnetization switching in a model epitaxial Fe/Au bilayer
P. Gospodarič (2019), vi, 120, XXXVIII pp
ISBN: 978-3-95806-423-2

Band / Volume 203
Network architecture and heme-responsive gene regulation of the two-component systems HrrSA and ChrSA
M. Keppel (2019), IV, 169 pp
ISBN: 978-3-95806-427-0

Band / Volume 204
Spin-orbitronics at the nanoscale: From analytical models to real materials
J. Bouaziz (2019), 228 pp
ISBN: 978-3-95806-429-4

Band / Volume 205
Advanced methods for atomic scale spin simulations and application to localized magnetic states
G. P. Müller (2019), xx, 194 pp
ISBN: 978-3-95806-432-4

Schriften des Forschungszentrums Jülich
Reihe Schlüsseltechnologien / Key Technologies

Band / Volume 206
Different growth modes of molecular adsorbate systems and 2D materials investigated by low-energy electron microscopy
J. E. Felter (2019), vi, 114, XXXIV pp
ISBN: 978-3-95806-434-8

Band / Volume 207
NADPH-related studies performed with a SoxR-based biosensor in *Escherichia coli*
A. Spielmann (2019), IV, 73 pp
ISBN: 978-3-95806-438-6

Band / Volume 208
Chemisorption aromatischer Moleküle auf Übergangsmetalloberflächen: Bildung molekularer Hybridmagnete
S. Schleicher (2019), 109 pp
ISBN: 978-3-95806-442-3

Band / Volume 209
Regulatory interactions between *Corynebacterium glutamicum* and its prophages
M. Hünnefeld (2019), IV, 209 pp
ISBN: 978-3-95806-445-4

Band / Volume 210
Quantum Technology
Lecture Notes of the 51st IFF Spring School 2020
23 March – 03 April 2020, Jülich, Germany
ed. by H. Bluhm, T. Calarco, D. DiVincenzo (2020), ca. 700 pp
ISBN: 978-3-95806-449-2

Band / Volume 211
Interaction of physical fields with nanostructured materials
(2020), 255 pp
ISBN: 978-3-95806-450-8

Weitere ***Schriften des Verlags im Forschungszentrum Jülich*** unter
http://wwwzb1.fz-juelich.de/verlagextern1/index.asp

Schlüsseltechnologien / Key Technologies
Band / Volume 211
ISBN 978-3-95806-450-8

JÜLICH
Forschungszentrum